Analysis of Nonlinear Spatio-temporal Partial Differential Equations: Applications to Host-Parasite Systems and Bubble Growth

by

Aoibhinn Maire Bradley

A Thesis submitted to
The University of Strathclyde
for the degree of

Doctor of Philosophy

Department of Mathematics and Statistics
University of Strathclyde

2014

Declaration

This thesis is the result of the author's original research. It has been composed by the author and has not been previously submitted for examination which has led to the award of a degree.

Signed: .... Date:.................

Abstract

The mountain hare population currently appears to be under threat in Scotland. The natural population cycles exhibited by this species are thought to be, at least in part, due to its infestation by a parasitic worm. We seek to gain an understanding of these population dynamics through a mathematical model of this system and so determine whether low population levels observed in the field are a natural trough associated with this cycling, or whether they point to a more serious decline in overall population densities.

A generic result, that can be used to predict the presence of periodic travelling waves (PTWs) in a spatially heterogeneous system, is reported. This result is applicable to any two population host-parasite system with a supercritical Hopf bifurcation in the reaction kinetics. Application of this result to two examples of well studied host-parasite systems, namely the mountain hare and the red grouse systems, predicts and illustrates, for the first time, the existence of PTWs as solutions for these reaction advection diffusion schemes.

One method for designing bone scaffolds involves the acoustic irradiation of a reacting polymer foam resulting in a final sample with graded porosity. The work in this thesis represents the first attempt to derive a mathematical model, for this empirical method, in order to inform the experimental design and tailor the porosity profile of samples. We isolate and study the direct effect of the acoustic pressure amplitude as well as its indirect effect on the reaction rate.

We demonstrate that the direct effect of the acoustic pressure amplitude is negligible due to a high degree of attenuation by the sample. The indirect effect, on reaction rate, is significant and the standing wave is shown to produce a heterogeneous bubble size distribution. Several suggestions for further work are made.

Acknowledgements

I am deeply grateful to my supervisor Dr Anthony Mulholland for all his help, advice and especially for his unshakeable faith in my ability to complete this thesis.

I also want to thank Dr Steven Webb, my second supervisor, for his encouragement and continued support with this work since leaving Glasgow.

I would also like to acknowledge the help and co-operation of Dr Carmen Torres-Sanchez, Dr Sunny Townsend and Professor Jonathan Sherratt.

My special thanks goes to my parents, who have supported me in whatever I do, and to my brothers who are always there with helpful advice when needed.

A particular thank you to my flatmate Dawn, also a PhD student. Thankfully, although we both experienced the usual ups and downs of PhD life, we were always out of phase and, therefore, able to motivate each other when necessary.

And finally, I thank Andy for his patience and love, and for giving me the space necessary to finish this thesis.

Preface

The work in this thesis is divided into two distinct parts. The first five chapters relate to research carried out, on host-parasite systems, in the first year and a half of my PhD programme. The second part of the thesis, contained in Chapters 7 to 9, is a study of some of the effects of acoustic irradiation on a reacting polymer foam. The study of this second subject arose as a result of my attendance at a Mathematics in Medicine Study Group at the University of Strathclyde in 2010.

Contents

Chapter 1

Introduction: Host-Parasite Systems

1.1 Motivation

Interest in the mountain hare, *Lepus timidus*, has resurfaced in the media [21], in recent months, with parliamentary questions being lodged at the Scottish parliament regarding its conservation status, abundance and distribution in Scotland [73]. Despite the fact that it has been listed in Annex V of the EC Habitats Directive (1992) for many years [97], there are currently renewed concerns about the perceived decline in the population and more specifically about the effect of culls (both legal and illegal) on the mountain hare population [21]. There have been reports of localised declines and possible extinctions but given the lack of up to date information on abundance and distribution in the field, coupled with the fact that the mountain hare populations exhibit natural cyclical fluctuations in density, it is hard to ascertain whether observed low levels and possible localised extinctions are the result of environmental factors or are simply due to the inherent peaks and troughs in population levels associated with such cyclic population dynamics [43]. It is hoped that a greater understanding of the population dynamics of the mountain hare species along with a knowledge of the causative factors for population fluctuations will help to inform the management of the population which is thought to be currently under threat. In this thesis we build on work produced by the former Macauley Institute, Aberdeen in conjunction with the University of Glasgow [97]. This work was both empirical and theoretical and looked, in particular, at the specific effect associated with the mountain hare's intestinal parasite, *Trichostrongylus retortaeformis*. In this study, reaction kinetic models were developed with an aim to understanding the population fluctuations observed in the data. We seek to examine the effect of a spatial extension of this kinetic model as well as probing it analytically to derive some generic results that can be applied to a specific sub-category of host-parasite systems.

1.2 Background

Many natural species exhibit some oscillatory behaviour in population density with cycles that are characterised by their amplitude and period [83]. Examples include Snowshoe hares [46], field voles [48], grouse [37, 98] and mountain hares [36, 62, 63, 65, 97]. These population cycles can either be the result of spatially homogeneous oscillations predicted by the associated reaction kinetic model or the observed spatiotemporal cycles are formed by periodic travelling waves (PTWs) [95], which oscillate in space and time. There are many possible reasons why temporal or spatial cycling could occur and they vary for individual systems. In some cyclic systems, a number of factors need to interplay to produce oscillations [46]. Example mechanisms can include habitat heterogeneity, seasonal forcing, interaction with other populations, climatic forcing and landscape obstacles [83]. In other systems, interspecies interactions are thought to result in cycling [39, 48]. This interaction may take different forms depending on the species involved. For example, predator-prey interactions have been extensively studied since the work of Lotka and Volterra in the 1920s [6], and predation has been shown to be an established cause of cycling in the prey species [80].

Another example is the host-parasite interaction, regarded by Anderson and May as a ‘particular manifestation of the general predator-prey interaction’ [6]. In [6], the authors show theoretically that where the parasite is loosely aggregated in the host population, and where its effect on survival is small compared to its effect on host fecundity, the parasite population will tend to destabilise the system resulting in population cycling. Indeed, field studies of red grouse and their intestinal nematode exhibit spatiotemporal oscillations in host-parasite densities [68,102] and further investigation has also shown that it is the parasite that is responsible for this cycling effect [39]. With other host parasite studies, however, observed spatiotemporal oscillations in the field data have not yet been explained [96] and many other factors outwith parasite effects, for example predation [46], food limitation [42], culling [35], territoriality [36] have been proposed as possible drivers of these cycles, but as yet nothing has been proved empirically or theoretically.

An important aim of population dynamics is to develop a better understanding of the cause and effect of such cyclic behaviour so that species that are under threat, or those of economic importance, may be better managed. For example, a system that we will study in the main body of this thesis is the mountain hare *Lepus timidus* in Scotland. This is the only lagomorph species native to the UK with 99% of the population residing in Scotland [57]. Lagomorphs are members of the taxonomic order *Lagomorpha* and include hares and rabbits. The mountain hare population is believed to be under threat from a number causes and as such has been listed in Annex V of the EC Habitats Directive (1992) [97] requiring the UK to ensure its conservation and sustainable management. In 2007, due to a perceived decline in mountain hare numbers the Scottish Government’s wildlife conservation agency Scottish Natural Heritage (SNH) made the mountain hare a UK biodiversity action plan species [97]. Field data measurements show that this population exhibits cyclic dynamics [63] with 7-10 year fluctuations in abundance [36]. Its associated intestinal nematode *Trichostrongylus retortaeformis* has been proposed as a possible driver of these cycles [63, 97]. Based on these propositions, Townsend *et al.* [97] derived a non-spatial reaction kinetic model (ordinary differential equations, ODEs) to describe these cycles but concluded that it did not completely describe the effects of parasites on the mountain hare demography. Specifically, the parameter set required to generate oscillations with the properties observed in the field data resulted in unrealistically high parasite burdens. The authors [97] proposed a number of possible reasons for this. First, they highlighted the fact that several of the plausible parameter ranges were based on small sample sizes or indirect data sources and were therefore possibly inaccurate. It was further suggested that the effects of the parasites on the system may extend beyond mortality and fecundity and that other parasitic effects may need to be included in the reaction kinetic model. Finally, they proposed a secondary role for parasites in the reaction kinetics and in a later paper [96] the same authors go on to suggest population dispersal, harvesting and population control as areas of ongoing investigation. In this thesis, we focus on the area of population dispersal and employ a spatially extended model for the mountain hare - parasite system.

Another species which has been modelled using similar non-spatial ODEs (e.g. see [18]) is the red grouse, *Lagopus lagopus scoticus*. As the favourite game bird of Britain [98], there is an abundance of long-term data describing grouse population dynamics. In common with the mountain hare, it is subject to parasitism by the intestinal nematode *Trichostrongylus tenuis*, which has proven to be one of the two main mechanisms proposed for red grouse cycles [98].

By modelling both these host-parasite systems in space and time we hope to gain some insight into the population cycling observed in the field. We will also derive a result for the spatial host-parasite system, analagous to a result presented by Koppell and Howard [45] for predator-prey reaction-diffusion systems.

We then show how this generic result may be used to predict the existence of PTW solutions in general two population cyclic host-parasite reaction-advection-diffusion systems which contain a supercritical Hopf bifurcation in the reaction kinetics.

1.3 Overview

This part of the thesis may be loosely divided into four sections. Chapter 2 introduces the necessary theory required to tackle the problem of cyclic host-parasite systems, both temporal and spatiotemporal. Chapter 3 describes the motivation and background for studying population dynamics of the mountain hare and its intestinal parasite *Trichostrongylus retortaeformis*, looking at both the spatially homogeneous system as well as a model incorporating spatial heterogeneity. In Chapter 4, a new result is derived for a general two population host-parasite reaction-advection-diffusion model containing a supercritical Hopf bifurcation in the reaction kinetics. This generic result is then applied to two host-parasite studies of particular interest, namely the mountain hare-*Trichostrongylus retortaeformis* system and the red grouse-*Trichostrongylus tenuis* system. Chapter 5 proposes areas of further investigation and some conclusions are drawn. Specifically the chapters may be summarised as follows:

Chapter 2 presents an overview of the mathematical theory that underpins the study of periodic travelling waves in a spatiotemporal domain, as well as the reaction kinetics of generic two population predator - prey systems. The analysis of Koppell and Howard [45] on general two population predator-prey reaction diffusion models characterised by a supercritical Hopf bifurcation in the reaction kinetics is elucidated. The form and properties of '$\lambda - \omega$' systems are studied. These are a simple class of reaction diffusion equations proposed by [45] and are a very useful tool in the analysis of cyclic reaction-diffusion systems.

Chapter 3 describes the particular host-parasite model for the mountain hare-*Trichostrongylus retortaeformis* system proposed by Townsend *et al.* [95, 97]. First, the temporal model is investigated and the global and localised behaviour of the system is analysed before illustrating numerically the possibility of PTW solutions for the associated reaction-advection-diffusion system.

Chapter 4 derives a new result predicting the presence of PTW solutions, given the existence of limit cycle solutions in the reaction kinetics, for a certain class of reaction-advection-diffusion equations. This result is tested on two published reaction kinetic models describing different host-parasite systems.

Chapter 5 summarises the results for Chapters 3 and 4 and draws some conclusions before outlining possible areas of advance in the study of this class of host-parasite systems. It also proposes a linear stability analysis study on the PTW solutions derived in previous Chapters.

1.4 Key Contributions

The principal original contributions of the author for this section of the thesis may be summarised:

- In Section 3.8 we present the analysis of the spatially augmented mountain hare-*Trichostrongylus retortaeformis* model originally proposed by [95] and the result that spatial extension does not extend the limit cycle behaviour beyond that observed in the temporal model.

- The spatial extension of the red grouse-parasite model published in [18], using Fickian diffusion to model host dispersal, and an advection term to describe parasite dispersal is proposed in Section 4.4.2.

- The illustration of PTWs, in the spatiotemporal domain, as possible solutions for the spatially heterogeneous red grouse-*Trichostrongylus tenuis* model proposed in [18].

- In Chapter 4, the proposition of a generic result that can be applied to the spatially heterogeneous model of any two population, cyclic, host-parasite reaction-advection-diffusion system containing a supercritical Hopf bifurcation in the reaction kinetics. This generic result can also predict the minimun speed of the PTW solution; the particular wave speed is dictated by initial and boundary conditions.

Chapter 2

Mathematical Background

2.1 Periodic travelling waves

The term ‘periodic travelling wave’ (PTW) refers to a particular type of solution, in which the model variables vary periodically in space, as well as in time. They are a fundamental solution form for reaction-diffusion systems with a stable limit cycle in the kinetics [45] and have been studied extensively, typically, in cyclic two population predator-prey systems [78–83, 85, 86]. In their review, Sherratt and Smith [83] tabulate details of a number of field studies reporting periodic travelling waves in populations undergoing multi-year cycles. According to Sherratt and Smith [83], the significance of a PTW is the correlated spatial and temporal density variations that it implies. The synchrony in population dynamics associated with PTWs has been attributed to a number of different factors, for example, population dispersal, large scale perturbations in the environment or multi-year oscillations in some important environmental factor, for example climatic forcing or sunspot activity [83]. The two main mechanisms known to generate such PTWs in predator-prey systems are boundary effects and the invasion of a predator population into a prey population [83].

One of the aims of this work is to study theoretically the existence of PTW solutions in cyclic, two population host-parasite systems. Not only are there fundamental differences in the reaction kinetics of host-parasite systems (as opposed to the predator-prey models) but the spatial augmentation of the temporal model will now involve advection as well as diffusion since, in many cases, the parasites travel on, or in, their associated host population for all or part of their life cycle. Before examining two population host-parasite systems, we first summarise the PTW theory associated with predator-prey systems.

2.2 Predator-prey systems

There are numerous examples of predator-prey interactions in nature and, in these cases, the predator, in effect, kills and eats the prey. Lotka-Volterra [9] developed the first mathematical model to study these predator-prey systems and demonstrated that simple predator-prey reactions can lead to oscillatory behaviour of the populations. Since then, predator-prey interactions have been widely studied and spatially heterogeneous systems are often modelled using reaction-diffusion equations with constant diffusion coefficients to model population dispersal [60]. An example of a predator-prey reaction kinetic (non-spatial) system is [83],

$$\frac{du}{dt} = \overbrace{\frac{\sigma uv}{(\kappa + v)}}^{\text{benefit from predation}} - \overbrace{\mu u}^{\text{death}}, \tag{2.1}$$

$$\frac{dv}{dt} = \underbrace{v(1-v)}_{\text{intrinsic birth and death}} - \underbrace{\frac{uv}{(\kappa + v)}}_{\text{predation}}. \tag{2.2}$$

where u and v represent the predator and prey population densities respectively, μ is the predator death rate, σ is the prey to predator conversion rate and κ is the half-saturation constant in the rate of prey consumption term by predators. Note that the benefit from predation is taken to be proportional to the predation term in the prey equation and this is thought to be a key driver for temporal oscillations in population densities in this system [60]. The reaction kinetics of these type of systems have been studied extensively and it is often shown that predators introduced into a prey population can induce a stable limit cycle about an unstable co-existence steady state. In 1973, Koppell and Howard produced a seminal paper on two population cyclic systems of this form [45]. They considered a spatiotemporal version where population dispersal is modelled by Fickian diffusion, for both predator and prey, with predator and prey populations having associated constant diffusion coefficients D_u and D_v, respectively. They showed that all oscillatory reaction-diffusion equations, of the form

$$\frac{\partial u}{\partial t} = f(u,v) + D_u \frac{\partial^2 u}{\partial x^2}, \tag{2.3}$$

$$\frac{\partial v}{\partial t} = g(u,v) + D_v \frac{\partial^2 v}{\partial x^2}, \tag{2.4}$$

where $f(u,v)$ and $g(u,v)$ describe the reaction kinetics of the non-spatial system, have a one parameter family of periodic travelling wave solutions; here the word 'oscillatory' indicates that the reaction diffusion kinetics have a stable limit cycle [101]. They proved that there is a family of small amplitude waves provided that the dispersal coefficients for the two populations are sufficiently close. To do this, they showed that the travelling wave variable ODE system

$$\frac{du}{dz} = f(u,v) + \frac{D_u}{s^2}\frac{d^2 u}{dz^2}, \tag{2.5}$$

$$\frac{dv}{dz} = g(u,v) + \frac{D_v}{s^2}\frac{d^2 v}{dz^2}, \tag{2.6}$$

where $z = t - x/s$, has a Hopf bifurcation at some positive value of the wave speed, s_{Hopf}, and then used the Hopf theorem to imply a one-parameter family of periodic solutions as s increases above this minimum value, s_{Hopf}. This limit cycle solution in z corresponds to the birth of PTW solutions in the associated PDE system in the (x,t) plane. These solutions are 'one parameter' in the sense that if we select a parameter set producing a travelling wave solution characterised by a speed, s, then, for this parameter set, the values of amplitude, wavelength and period for the PTW are fixed; similarly if we choose an amplitude then the speed, period and wavelength of the resulting PTW are determined [83].

The wave amplitude can range between zero to that of the amplitude of the spatially homogeneous oscillations of the reaction kinetics. Similarly, the wave speed can range from some minimum speed given by s_{Hopf}, to infinity, which corresponds to the spatially homogeneous oscillations of the reaction kinetics. The period ranges from a minimum related to the minimum wave speed to a maximum value equal to the period of the limit cycle solution in the reaction kinetics.

In addition, Koppell and Howard [45] introduced and developed the analysis of the simple class of reaction-diffusion equations known as '$\lambda-\omega$' systems; these have since been used extensively in prototype studies of cyclic reaction-diffusion systems [60] and for this reason we will summarise the form and properties of these systems in the next section.

2.3 $\lambda - \omega$ systems

We will start with the full $\lambda-\omega$ reaction-diffusion system, introducing some basic assumptions, and then initially consider the spatially homogeneous limiting case before going on to predict the presence and form of periodic plane waves as solutions to the spatial system.

A $\lambda - \omega$ system is a simple type of reaction-diffusion system taking the form

$$\frac{\partial u}{\partial t} = \frac{\partial^2 u}{\partial x^2} + \lambda(r)u - \omega(r)v, \tag{2.7}$$

$$\frac{\partial v}{\partial t} = \frac{\partial^2 v}{\partial x^2} + \omega(r)u + \lambda(r)v, \tag{2.8}$$

where $r = (u^2 + v^2)^{1/2}$, u and v are real-valued functions of space x and time t, and $\lambda(0)$ and $\omega(0)$ are both strictly positive. An important property of this system is that any isolated zero of $\lambda(.)$ corresponds to a limit cycle in the reaction kinetics. In theory, any two population cyclic system near to a supercritical Hopf bifurcation can, by reduction to normal form, be described by a $\lambda - \omega$ system [83]. The reaction kinetics of the original system will determine the form of $\lambda(r)$ and $\omega(r)$. The beauty of the $\lambda - \omega$ system is that analytical expressions, in terms of system parameters, may be derived for the PTW solution form and its stability. For general reaction-diffusion systems, however, unless the reaction kinetics of the system are very simple, the reduction to normal form to obtain the functions $\lambda(r)$ and $\omega(r)$ can be cumbersome and time consuming and, because of this, for the two systems considered in the main body of the thesis, we will obtain the properties and stability of the PTW solutions using the numerical bifurcation analysis package, AUTO [19]. The $\lambda - \omega$ system illustrated in (2.7) and (2.8) is a generic system for PTWs for equations that have a supercritical Hopf bifurcation in the reaction kinetics. We will now introduce the analysis for this generic system before investigating our own specific host-parasite system.

2.3.1 Spatially homogeneous $\lambda - \omega$ systems

In the spatially homogeneous case, the temporal $\lambda - \omega$ system is simply stated as [60]

$$\frac{du}{dt} = \lambda(r)u - \omega(r)v, \tag{2.9}$$

$$\frac{dv}{dt} = \omega(r)u + \lambda(r)v, \tag{2.10}$$

$$r = \sqrt{u^2 + v^2}, \tag{2.11}$$

where r is a function of t only. In order to fulfil the conditions necessary for a supercritical Hopf bifurcation we need $\lambda(r_0) = 0$ and $\lambda'(r_0) < 0$: that is, $\lambda(r)$ is positive for $0 \leq r \leq r_0$ and negative for $r > r_0$, and $\omega(r)$ is a positive function for all r [60]. This simple system has an exact limit cycle solution which can be derived explicitly. In the spatially homogeneous system, the two variables u and v are functions of t only and their form depends on the system parameters, and r_0, which turns out to be the amplitude for the limit cycle solution.

If we express the variables u and v in the complex form, namely

$$c = u + iv, \qquad \text{so that,} \qquad |c| = \sqrt{u^2 + v^2} = r, \tag{2.12}$$

and

$$\begin{aligned}\frac{dc}{dt} &= \frac{du}{dt} + i\frac{dv}{dt}, \\ &= \lambda(r)u - \omega(r)v + i(\omega(r)u + \lambda(r)v), \\ \Rightarrow \frac{dc}{dt} &= [\lambda(|c|) + i\omega(|c|)]c. \qquad (2.13)\end{aligned}$$

The rate of change of the modulus, $|c|$, is given by,

$$\frac{d|c|}{dt} = \frac{u}{|c|}\frac{du}{dt} + \frac{v}{|c|}\frac{dv}{dt}. \qquad (2.14)$$

Substituting for the rate equations (2.9) and (2.10),

$$\begin{aligned}\frac{d|c|}{dt} &= \frac{u}{|c|}\left[\lambda(|c|)u - \omega(|c|)v\right] + \frac{v}{|c|}\left[\omega(|c|)u + \lambda(|c|)v\right], \qquad (2.15) \\ &= \frac{\lambda(|c|)}{|c|}\left(u^2 + v^2\right), \qquad (2.16) \\ &= \lambda(|c|)|c|. \qquad (2.17)\end{aligned}$$

A steady state solution is observed when the above rate equation is equal to zero, that is, when $\lambda(|c|)|c| = 0$. But by our earlier definition, $\lambda(r_0) = 0$ and therefore our steady state is a limit cycle solution described by the circle, $|c| = r_0$, in the (u, v) plane. Rewriting the system in polar co-ordinates we have,

$$c = re^{i\theta} \qquad \Rightarrow \frac{dr}{dt} = r\lambda(r), \qquad \frac{d\theta}{dt} = \omega(r),$$

so that the limit cycle solution can be described by

$$r(t) = r_0, \qquad \theta(t) = \omega(r_0)t + \theta_0, \qquad \text{where } \theta_0 \text{ is a constant.}$$

The spatially homogeneous system thus has a limit cycle solution in the $u - v$ plane given, in polar co-ordinates, by

$$(u, v) = (r_0 \cos[\theta_0 + \omega(r_0)t], r_0 \sin[\theta_0 + \omega(r_0)t]).$$

2.3.2 Spatially heterogeneous $\lambda - \omega$ systems

To obtain travelling wave solutions in the spatially extended system we substitute for the polar co-ordinates into (2.7)-(2.8) to get,

$$\frac{\partial}{\partial t}\begin{pmatrix} r\cos\theta \\ r\sin\theta \end{pmatrix} = \begin{pmatrix} \lambda(r) & -\omega(r) \\ \omega(r) & \lambda(r) \end{pmatrix}\begin{pmatrix} r\cos\theta \\ r\sin\theta \end{pmatrix} + \frac{\partial^2}{\partial x^2}\begin{pmatrix} r\cos\theta \\ r\sin\theta \end{pmatrix}, \qquad (2.18)$$

where now $u(x,t) = r(x,t)\cos(\theta(x,t))$ and $v(x,t) = r(x,t)\sin(\theta(x,t))$. Differentiating $r\cos\theta$ and $r\sin\theta$ with respect to t,

$$\begin{aligned} \frac{\partial}{\partial t}(r\cos\theta) &= r_t\cos\theta - r\theta_t\sin\theta, & (2.19)\\ \frac{\partial}{\partial t}(r\sin\theta) &= r_t\sin\theta + r\theta_t\cos\theta & (2.20)\end{aligned}$$

and twice with respect to x,

$$\begin{aligned} \frac{\partial^2}{\partial x^2}(r\cos\theta) &= r_{xx}\cos\theta - 2r_x\theta_x\sin\theta - r\theta_{xx}\sin\theta - r\theta_x^2\cos\theta, & (2.21)\\ \frac{\partial^2}{\partial x^2}(r\sin\theta) &= r_{xx}\sin\theta + 2r_x\theta_x\cos\theta + r\theta_{xx}\cos\theta - r\theta_x^2\sin\theta. & (2.22)\end{aligned}$$

Substitution of these into (2.18) and simplification yields (for $r \neq 0$)

$$\theta_t = \omega(r) + \frac{1}{r^2}\left(r^2\theta_x\right)_x. \qquad (2.23)$$

In a similar way we can obtain an expression for r_t, namely

$$r_t = r\lambda(r) + r_{xx} - r\theta_x^2. \qquad (2.24)$$

Our $\lambda - \omega$ system for reaction diffusion systems with limit cycles can, therefore, be now restated as

$$\begin{aligned} r_t &= r\lambda(r) + r_{xx} - r\theta_x^2, & (2.25)\\ \theta_t &= \omega(r) + r^{-2}\left(r^2\theta_x\right)_x. & (2.26)\end{aligned}$$

In section 2.3.1 we showed that if $r_0 > 0$ exists and $\lambda'(r_0) < 0$ then the asymptotically stable limit cycle solution for the non-spatial system is

$$r = r_0, \qquad \theta = \theta_0 + \omega(r_0)t. \qquad (2.27)$$

In other words the limit cycle solutions u and v are

$$u = r\cos\theta = r_0\cos\left[\theta_0 + \omega(r_0)t\right], \tag{2.28}$$

$$v = r\sin\theta = r_0\sin\left[\theta_0 + \omega(r_0)t\right]. \tag{2.29}$$

In the inhomogeneous system, we look for a travelling plane wave of the form

$$\mathbf{u}(x,t) = \mathbf{U}(z), \qquad z = \sigma t - kx,$$

where σ is the frequency and k the wavenumber. Therefore, in the polar form

$$r = \alpha, \qquad \theta = \sigma t - kx \tag{2.30}$$

where α is a given constant value of $r(x,t)$.

If we substitute for this form of solution into the system (2.25) and (2.26) we can determine necessary and sufficient conditions, for the single parameter α, such that the solutions are travelling plane waves. Since α is a constant value of r then for each solution $\alpha_t = \alpha_x = 0$, $\theta_t = \sigma$, $\theta_x = -k$ and from (2.25) and (2.26)

$$0 = \alpha\lambda(\alpha) - \alpha k^2, \qquad \Rightarrow \lambda(\alpha) = k^2, \tag{2.31}$$

$$\sigma = \omega(\alpha). \tag{2.32}$$

We therefore have a one parameter family of travelling plane wave solutions given by

$$u = \alpha\cos\left[\omega(\alpha)t - x\lambda^{\frac{1}{2}}(\alpha)\right], \tag{2.33}$$

$$v = \alpha\sin\left[\omega(\alpha)t - x\lambda^{\frac{1}{2}}(\alpha)\right], \tag{2.34}$$

with wave speed c

$$c = \frac{\sigma}{k} = \frac{\omega(\alpha)}{\lambda^{\frac{1}{2}}(\alpha)}. \tag{2.35}$$

As an example, we will consider a particular simple case of a λ-ω system with $\lambda(r)$ and $\omega(r)$ such that the kinetics of the system satisfy the supercritical Hopf bifurcation requirements but are also such that they are amenable to analysis. We take

$$\omega(r) \equiv \omega_0 - r^2, \qquad \lambda(r) = \lambda_0 - r^2. \tag{2.36}$$

Substituting these forms for $\lambda(r)$ and $\omega(r)$ into the dynamics in (2.7) and (2.8) we have a steady state solution at $u = v = 0$, the nature of which is governed by the values λ_0 and ω_0.

For $u = v = 0$ it follows that $r = 0$, $\lambda(0) = \lambda_0$ and $\omega(0) = \omega_0$. The dynamic system then becomes

$$\frac{\partial}{\partial t}\begin{pmatrix} u \\ v \end{pmatrix} = \begin{pmatrix} \lambda_0, & -\omega_0 \\ \omega_0, & \lambda_0 \end{pmatrix}\begin{pmatrix} u \\ v \end{pmatrix}, \tag{2.37}$$

and the corresponding eigenvalues, $\eta_\pm$ are given by,

$$\begin{vmatrix} \lambda_0 - \eta, & -\omega_0 \\ \omega_0, & \lambda_0 - \eta \end{vmatrix} = 0. \tag{2.38}$$

Solving the auxiliary equation yields the eigenvalues,

$$\eta = \lambda_0 \pm \omega_0 i, \tag{2.39}$$

so that for

$$\lambda_0 < 0 \rightarrow \text{steady state solution is stable}, \tag{2.40}$$

$$\lambda_0 = 0 \rightarrow \text{Hopf bifurcation value giving } \eta = \pm\omega_0 i, \tag{2.41}$$

$$\lambda_0 > 0 \rightarrow \text{steady state solution is unstable}. \tag{2.42}$$

We would therefore expect small amplitude limit cycle solutions for small positive $\lambda_0 = \gamma$ where $r_0 = \sqrt{\gamma}$ where $0 < \gamma \ll 1$. The spatially homogeneous limit cycle solutions are therefore,

$$u = \sqrt{\gamma}\cos[\omega(\sqrt{\gamma})t + \theta_0], \qquad v = r_0 \sin[\omega(\sqrt{\gamma})t + \theta_0], \qquad \gamma > 0. \tag{2.43}$$

Now considering the reaction diffusion system for these particular $\lambda(.)$ and $\omega(.)$, we substitute for travelling plane wave solutions of the form

$$r = \alpha, \qquad \theta = \sigma t - kx,$$

where now

$$\begin{aligned}\sigma &= \omega(\alpha) = \omega_0 - \alpha^2,\\ k &= \lambda^{\frac{1}{2}}(\alpha) = (\sqrt{\gamma} - \alpha^2)^{\frac{1}{2}},\end{aligned}$$

so that the corresponding spatial PTW solutions are therefore

$$u = \alpha \cos\left[(\omega_0 - \alpha^2)t - \left(\gamma - \alpha^2\right)^{\frac{1}{2}} x\right], \tag{2.44}$$

$$v = \alpha \sin\left[(\omega_0 - \alpha^2)t - \left(\gamma - \alpha^2\right)^{\frac{1}{2}} x\right]. \tag{2.45}$$

where the amplitude of the PTWs, $\alpha < \sqrt{\gamma}$. In other words the amplitude of the PTW is less than the amplitude of the limit cycle solution in the reaction kinetics and as $\alpha \to r_0$ the speed (2.35) tends to infinity and we retrieve the spatially homogeneous limit cycle solution. The above solutions are illustrated in Figure 2.1. One parameter set, illustrated in Figure 2.1(a), results in PTWs moving from right to left across the spatial domain; in (b) the parameters chosen produce PTWs moving in the opposite direction across the domain. These solutions will only persist if they are stable; unstable waves cannot be a long term solution and numerical analysis indicates that instability results in irregular spatio-temporal oscillations [78, 83]. A detailed description of the stability analysis of travelling wave solutions of $\lambda - \omega$ systems is described in [60].

2.4 General Host-parasite systems

Until the work carried out by Anderson [5] and Anderson & May [6, 56] relatively little theoretical work was done on the effects of parasites on their host population. Anderson [5] defined parasitism in terms of the parasite's influence on the growth rate of its host population and suggested that this effect is related to the average parasite burden per host which is governed by the statistical distribution of the parasite population within the host population. Anderson [5] cites a number of important population processes including overdispersion and

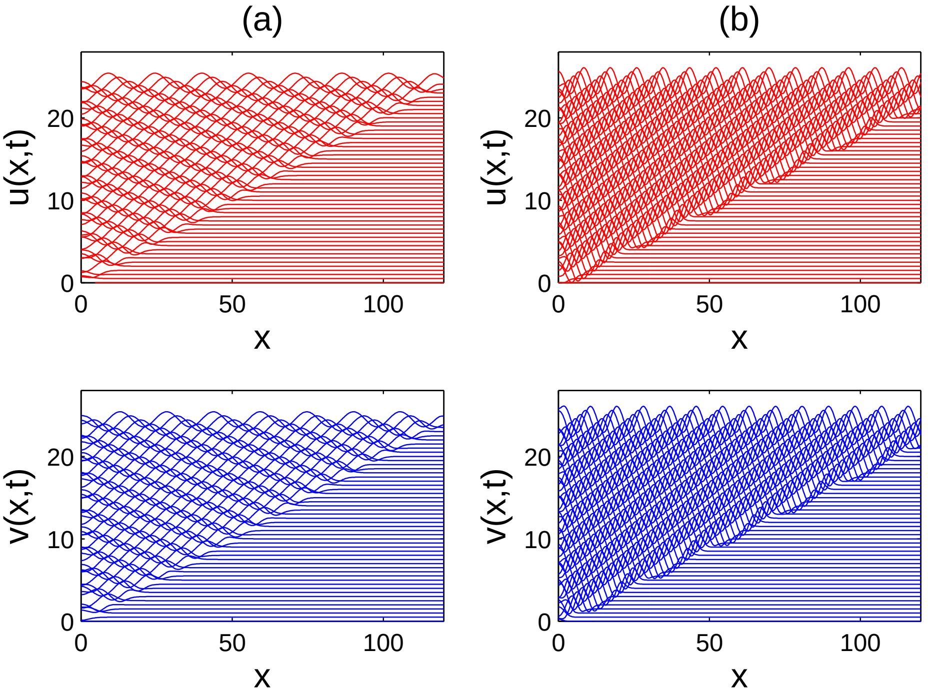

Figure 2.1: Typical numerical solutions of (2.7,2.8), with $\lambda(r) = \lambda_0 - r^2$ and $\omega(r) = \omega_0 - r^2$. It shows a front moving across the domain at constant speed, with periodic wave trains behind this wave. In (a) the wave trains move in the negative x direction, while in (b) they move in the positive x direction. The solutions for $u(x,t)$ and $v(x,t)$ are plotted as functions of space x at successive times t, with the vertical separation of solutions proportional to the time interval. We consider the system on the semi-infinite domain $[0,\infty)$ with initial data of the form $u(x,0) = v(x,0) = A\exp(-\xi x)$. The parameter A affects the time course of the evolution, but has no effect on the ultimate behaviour; we take $A = 0.1$. The remaining parameter values are: (a) $\xi = 0.8$, $\lambda_0 = 1$, $\omega_0 = 2$, $0 < t < 60$; (b) $\xi = 4$, $\lambda_0 = 3$, $\omega_0 = 1$,$0 < t < 40$.

density dependence in parasite mortality or reproduction. At that time, most theoretical work in ecology concentrated on predator-prey systems where the predator kills and eats its prey. Anderson and May [6] first defined 'parasitism' broadly as 'an ecological association between species in which one, the parasite, lives on or in the body of the other, the host' for all or part of its life cycle. The parasite relies on the host production of nutrients as being vital to its own survival so that, where the relationship is obligatory for the parasite, it is harmful to the host. Three conditions are proposed that must be fulfilled in order that a species is classified as a parasite: (1) the host provides the parasite's habitat; (2) the parasite is nutritionally dependent on the host; and (3) the parasite is harmful to the host [6]. One of the basic reaction kinetic models presented by Anderson and May [56] is

$$\begin{aligned} \frac{dH}{dt} &= (a-b)H-(\alpha+\delta)P, && (2.46)\\ \frac{dP}{dt} &= P\left(\frac{\lambda H}{H+H_0}-(\mu+b+\alpha)-\alpha\left(\frac{k+1}{k}\right)\frac{P}{H}\right), && (2.47)\end{aligned}$$

where H is the host population density and P is the parasite population density. It must be noted that this system fails mathematically when $H = 0$ as the parasite equation blows up due to the singularity in the third term. However, we use this model to describe the parasite burden per host and therefore make the assumption that when $H = 0$, P is necessarily zero. The first term in the host rate equation (2.46), gives the net contribution of hosts per unit time by subtracting the intrinsic host mortality rate, b, from the intrinsic host fecundity rate, a. α and δ are the effect, per parasite, on host mortality and fecundity, respectively. Therefore, the effects per host are $\alpha P/H$ and $\delta P/H$, respectively giving the total number of hosts killed due to parasite infection, αP, and the net reduction in host fecundity due to the parasites, δP.

For the parasite rate equation (2.47), λ is defined as the rate of production of transmission stages per parasite, giving a net reproduction rate of λP for a parasite population P. In many natural systems these transmission stages pass out in the faeces to the environment where, in time, they hatch and migrate up blades of grass to be ingested by foraging hosts. As a result, only a certain proportion of these transmission stages will infect the host population. The density of free stages in the habitat in relation to the density of hosts per unit area is important in determining the transmission rate. The term, $H/(H+H_0)$, describing the effective transmission factor, determines the proportion of transmission stages produced that infect the host population in a given time interval, so that the total number of stages infecting the host population in this time is given by $\lambda PH/(H+H_0)$. As H increases with respect to H_0 the transmission rate tends to unity so that all transmission stages produced infect the host population. If H_0 is large with respect to H then only a small proportion of transmission stages are converted to adult parasites. The total number of adult parasite deaths due to the combined effects of adult parasite mortality, μ, the total host mortality rate given by the sum of the intrinsic rate, b, and the parasite induced rate, α is $-(\mu+\alpha+b)P$. The third term, $\alpha P(k+1)/kH$, reflects the effect of the statistical distribution of parasites within the host population on the number of parasites removed at each time point. In most natural systems, the parasite tends to be overdispersed within the host population and the negative binomial probability model is commonly used to model this distribution [5]. A random distribution is often described by the Poisson model which is defined by the single parameter of mean parasite burden, P/H, and is given by $P/H+(P/H)^2$. An overdispersed population, on the other hand, is described by the two parameter binomial probability distribution defined by the mean and, k, the inverse measure of the degree of parasite aggregation within the host. It is modelled by $P/H+(P/H)^2(k+1)/k$. If k is small, the parasite population is 'highly aggregated', with a small number of hosts containing the majority of the parasite population. As such the parasite population tends to have less regulatory effect on the host population; if k is large then the population is 'loosely aggregated' and as $k\to\infty$ we approach a random distribution.

Anderson and May [56] showed that where the parasite was loosely aggregated in the host population and where its effect on host fecundity was greater than that on host mortality, it tended to be a destabilising influence on the reaction kinetics of the system, resulting in stable limit cycle solutions. These are exactly the properties associated with the two natural cyclic host-parasite systems (mountain hare and red grouse) that we go on to investigate in the next sections.

Chapter 3

Mountain Hare, Parasite System

3.1 Background and motivation

The mountain hare (see Figure 3.1), *Lepus timidus*, is indigenous to Scotland and 99% of the UK population resides at altitudes above 500m [33]. Mountain hares are thought to be less fussy about the quality of their forage than brown hares and this gives them a competitive edge especially at high altitudes. In 1995 the total population was of the order of 350,000 [34] with population densities varying tenfold, reaching a peak approximately every ten years [33]. This same study [34], however, did recognise that the value proposed may be over/underestimated by as much as 50% [43]. The mountain hare population is currently thought to be under threat with densities approaching extinction levels in certain parts of Scotland [43]. As a result, the species is listed in Annex V of the EC Habitats Directive [97] requiring its conservation status and sustainable management to be ensured. There are a number of hypothesised contributory factors to their low densities, including predation, food limitation, territoriality, parasite infestation and culling [97].

Field studies in Scotland, Finland and elsewhere demonstrate cycling in the mountain hare population densities [65]. The form of the cycling varied between studies and different causative factors have been suggested. For example, in Scandanavian countries, predation is thought to play an important role [37, 62],

Figure 3.1: Mountain hare, *Lepus timidus*, in its winter coat which provides excellent camoflage on those snowy Scottish peaks.

however, in Scotland, where most of the mountain hare population resides on estates land managed for red grouse, predation is not thought to be an issue [62]. Other contributory factors have been suggested including food limitation and territoriality. But observations suggest that mountain hares tend to be non-territorial [30, 36, 97] and food limitation is not thought to be an issue [42, 97]. Mountain hares have been implicated in the transmission of louping ill virus to red grouse [35] and, as a result, they have become victims of culling, though it is hard to quantify this effect since, in many cases, the culling is carried out illegally [43]. Scottish Natural Heritage (SNH) published the results of a questionnaire-based survey carried out in 2006/07 giving a figure of 24529 mountain hares culled across 90 estates in Scotland [43]. This report also pointed to the fact that the naturally occuring cyclic dynamics of the mountain hare may complicate analysis of long term patterns of abundance and that the factors causing these fluctuations remain unknown [43]. We seek to address this point by mathematically modelling the population dynamics of the mountain hare and its associated parasite to see if this interaction is responsible for the population cycling observed in the field.

Though theoretical evidence abounds to support the hypothesis of parasite induced cycling in a host population in general [5, 6, 18, 38, 39, 56], empirical evidence for parasite induced cycling in the mountain hare population is lacking. Properties associated with field oscillations in mountain hare populations recorded across large areas of Scotland are listed in Table 3.1 and illustrate the variation in dynamics observed at a range of different locations [65].

Period	4-15 years
Mean hare density	20-200km^{-2}
Amplitude of oscillations	Coefficient of variation 0.39-1.80
Mean parasite burden	200-5000 worms per hare

Table 3.1: Characteristics of the highly variable dynamics of mountain hare populations across Scotland [65, 95].

The mountain hare parasite, *Trichostrongylus retortaeformis*, is a worm found in the intestines of mountain hares (see Figure 3.2). The females produce eggs in the gut which then pass out in the hare faeces. After hatching, the larvae climb up blades of grass where they are then ingested by foraging hares and the cycle recommences [32]. This worm has little effect on hare mortality but dramatically reduces its fecundity [64]. Empirical evidence suggests that, in most host-parasite systems in the field, the parasites are over-dispersed (or loosely aggregated) in their host populations [5], where only a small number of hosts contain the majority of the total parasite population.

Simple mathematical models predict that parasites that are loosely aggregated in the host population and which have a stronger effect on host fecundity

Figure 3.2: The mountain hare intestinal nematode *Trichostrongylus retortaeformis*.

than on host mortality should destabilise the system and induce cycling [18, 56]. Newey and Thirgood measured the effect of *Trichostrongylus retortaeformis* on female mountain hares and concluded that the experimental reduction of parasites was associated with an increase in fecundity [64]. A later paper [63] by the same authors demonstrated that *Trichostrongylus retortaeformis* is indeed loosely aggregated in the mountain hare population and they hypothesise that this factor along with the parasites' influence on fecundity demonstrate that it is this intestinal parasite that is responsible for the fluctuating levels of mountain hares observed in the field. In light of these experimental results, Townsend *et al.* [97] derived a mathematical model that incorporates these effects and then probed it numerically and analytically to see if it can predict the cyclic population densities observed in the field [97]. The model they developed is a purely temporal reaction-kinetic model (i.e. spatial dispersal of hosts is neglected) and a fuller description and analysis of this system will be the subject of Sections 3.2-3.7. Their results, however, were inconclusive in that cycles of the required amplitude and period could only be produced using parameters which produced an unrealistic mean parasite burden. A number of reasons were suggested for this, including doubts about the reliability of certain parameter values determined from ‘small sample size or indirect data sources’ [97]. It was also proposed to be due to the fact that spatial heterogeneity and host dispersal was lacking in the original model [97]. The aim of this part of the thesis is to examine if, by adding spatial heterogeneity, we may be able to theoretically predict cycles with more realistic mean parasite burdens.

Addressing this point, we model the system in the spatiotemporal field using the reaction kinetics of [97] and adding diffusion and advection terms for the host and parasite populations, respectively, to determine if oscillations of realistic amplitude and period can be predicted in the spatial system with more realistic parasite burdens.

First, for completeness, we will look at the temporal dynamics only and assume a spatially homogeneous system in Sections 3.2 to 3.7 before considering the effects of spatial heterogeneity in Section 3.8.

3.2 Reaction kinetics

Townsend *et al.* [97] use a variant of the classic Anderson & May macroparasite model (introduced in [17]) which describes continuous growth equations for a host population of density, H, interacting with a parasite population, P. In the first instance we will describe the case when the population densities are time dependent only in which case the ODE system is,

$$\frac{dH}{dt} = -\alpha P - bH + aH\left(\frac{kH}{\delta P + kH}\right)^k, \tag{3.1}$$

$$\frac{dP}{dt} = P\left[\frac{\lambda H}{H_0 + H} - (\mu + \alpha + b) - \alpha\left(\frac{k+1}{k}\right)\frac{P}{H}\right]. \tag{3.2}$$

Parameter descriptions can be found in Table 3.2. Comparing the original Anderson & May model, described by (2.46) and (2.47), to (3.1) and (3.2) we can see that the parasite rate equations are the same. In the hare rate equations the terms describing the net death rate are also the same and given by $(-bH - \alpha P)$. The difference between these two systems pertains to the description of the net birth rate of the host population. In Anderson & May [56] the parasite induced effect on host fecundity is assumed to act linearly so that the total host birth rate is given by $(aH - \delta P)$. This allows for a biologically unrealistic negative net host fecundity. In (3.1) the net host fecundity is modelled using the non-linear term introduced by Diekmann & Kretchsmar [17] which takes into account the negative binomial distribution of the parasite population within the host population and its effect on the net host fecundity. Here δ also acts to reduce the host fecundity, as in (2.46), but it now acts non-linearly and the host fecundity is always a positive quantity. As δ increases for a fixed k the host fecundity decreases, however, as k increases for a fixed δ, the net host fecundity increases.

3.3 Parameter estimation

Ranges of the model parameters are also presented in Table 3.2. These ranges were calculated by Townsend *et al.* [97] to be the most practical based on the best available empirical information. Where possible, field data from the mountain hares in Scotland were used [65], otherwise data were drawn from closely related systems [97]. For our analysis, we use the following set of parameter val-

Symbol	Parameter	Unit	Lower Limit	Upper Limit
a	Intrinsic fecundity of adult hares	yr^{-1}	1.8	2.8
δ	Parasite reduced induction in hare fecundity	$\text{parasite}^{-1}\text{yr}^{-1}$	0	0.0001
b	Intrinsic mortality of adult hares	yr^{-1}	0.08	0.61
α	Parasite-induced hare mortality	$\text{parasite}^{-1}\text{yr}^{-1}$	0	0.0001
λ	Parasite fecundity	yr^{-1}	80	2800
H_0	Transmission inefficiency constant		13500	66800
μ	Adult parasite mortality	yr^{-1}	0	1.2
k	Degree of overdispersion		0.5	2

Table 3.2: Parameter ranges based on empirical information [97].

ues, unless stated otherwise in the text: $k = 1$, $\delta = 1.5 \times 10^{-5}$ parasite^{-1}yr^{-1}, $\alpha = 8 \times 10^{-6}$ parasite^{-1}yr^{-1}, $b = 0.61$ yr^{-1}, $a = 1.8$ yr^{-1}, $\lambda = 100$ yr^{-1}, $\mu = 1$ yr^{-1}, $H_0 = 3.82 \times 10^4$. These values lie within the lower and upper limits proposed by [97] (Table 3.2); they result in a limit cycle solution in the reaction kinetics for this system.

3.4 System rescaling

For our analysis, we rescale the system variables so that all computed quantities are of relatively similar magnitude; this aids numerical integration and also reduces the number of parameters in the governing equations. We let $H = H_0\bar{H}$ and $P = P_0\bar{P}$ where H_0 and P_0 are characteristic host and parasite densities. We then set $P_0/H_0 = b/\alpha$ so that, with $k = 1$, (3.1) and (3.2) can be restated as

$$\begin{aligned} \frac{d\bar{H}}{dt} &= -b(\bar{H} + \bar{P}) + \frac{a\bar{H}^2}{c_1\bar{P} + \bar{H}}, & (3.3) \\ \frac{d\bar{P}}{dt} &= \bar{P}\left[\frac{\lambda\bar{H}}{1 + \bar{H}} - (\mu + b + \alpha) - \frac{2b\bar{P}}{\bar{H}}\right], & (3.4) \end{aligned}$$

where we take $c_1 = \delta b/\alpha$.

3.5 Global behaviour

First we investigate the global properties of the system by deriving its nullclines, which are found by setting the rate equations (3.3) and (3.4) equal to zero. Example solutions of the zero rate equations, in the $\bar{H} - \bar{P}$ plane, are shown in Figure 3.3. Along each nullcline the corresponding dependent variable remains constant in time. The steady state solutions of the system then occur where the $\bar{H}$ and $\bar{P}$ nullclines intersect in the $\bar{H} - \bar{P}$ space.

3.5.1 $\bar{H}$ Nullcline

The $\bar{H}$ nullcline (i.e. $d\bar{H}/dt = 0$) is given by,

$$-b(\bar{H} + \bar{P}) + \frac{a\bar{H}^2}{c_1\bar{P} + \bar{H}} = 0, \tag{3.5}$$

For $\bar{H} \ll 1$, $d\bar{P}/dt$ approximates to

$$\frac{d\bar{P}}{dt} \sim -\frac{2b\bar{P}^2}{\bar{H}},$$

so that the rate of change of $\bar{P}$ along the $\bar{H}$ nullcline is in the negative $\bar{P}$ direction for $\bar{H} \ll 1$. Conversely, for $\bar{H}$ large (i.e. $1/\bar{H} \ll 1$)

$$\frac{d\bar{P}}{dt} \sim \lambda\bar{P},$$

since $\bar{H}/(1 + \bar{H}) \to 1$. Therefore, the rate of change of $\bar{P}$ along the $\bar{H}$ nullcline is in the positive $\bar{P}$ direction. The arrows in Figure 3.3 illustrate, qualitatively, these changes in $\bar{P}$ along the $\bar{H}$ nullcline.

3.5.2 $\bar{P}$ Nullcline

Similarly we can determine how $\bar{H}$ changes along the $\bar{P}$ nullclines which are given by $d\bar{P}/dt = 0$, namely

$$\bar{P}\left[\frac{\lambda\bar{H}}{1 + \bar{H}} - (\mu + b + \alpha) - \frac{2b\bar{P}}{\bar{H}}\right] = 0.$$

There are therefore two $\bar{P}$ nullclines; the trivial one, $\bar{P} = 0$, and the non-trivial one defined by

$$\frac{\lambda\bar{H}}{1 + \bar{H}} - (\mu + b + \alpha) - \frac{2b\bar{P}}{\bar{H}} = 0.$$

Along the trivial $\bar{P}$ nullcline

$$\frac{d\bar{H}}{dt} = (a - b)\bar{H}.$$

Typically $a > b$, otherwise in the parasite free case the host density will decay to zero. So the rate of change of $\bar{H}$ along this trivial $\bar{P} = 0$ nullcline is in the positive direction. The non trivial $\bar{P}$ nullcline is given by

$$\bar{P} = \frac{\bar{H}}{2b}\left(\frac{\lambda \bar{H}}{1+\bar{H}} - (\mu + b + \alpha)\right).$$

For $\bar{P} \ll 1$ on the non-trivial nullcline

$$\frac{d\bar{H}}{dt} \sim \frac{a\bar{H}^2}{c_1\bar{P} + \bar{H}},$$

which is always positive. Whereas, for $\bar{P}$ large (i.e. $1/\bar{P} \ll 1$),

$$\frac{d\bar{H}}{dt} \sim -b\bar{P},$$

which is negative. These two results then give the arrow structure for the non-trivial nullcline as shown in Figure 3.3 illustrating the possibility of limit cycle solutions.

Indeed, the bifurcation analysis package, AUTO [19], was used to confirm the existence of a Hopf bifurcation for this system, for the set of parameters listed in Section 3.3, and illustrates the presence of stable limit cycle solutions (see Figure 3.4). AUTO is a software package for continuation and bifurcation problems in ODEs.

We can see from the AUTO plots in Figure 3.4 that the system is linearly unstable for values of δ above the Hopf bifurcation (denoted by δ_{HB}) and stable limit cycles are observed; for values of δ less than the Hopf bifurcation value the steady state is linearly stable and, following a small perturbation, the populations will quickly return to their equilibrium. Illustrations of these two types of behaviour are shown in the $P-H$ phase plane, in Figure 3.5, and temporally in Figures 3.6 and 3.7. The bifurcation shown is a supercritical Hopf bifurcation.

Having investigated the global behaviour of the system, we now look at the steady state solution and the behaviour of the system local to this point.

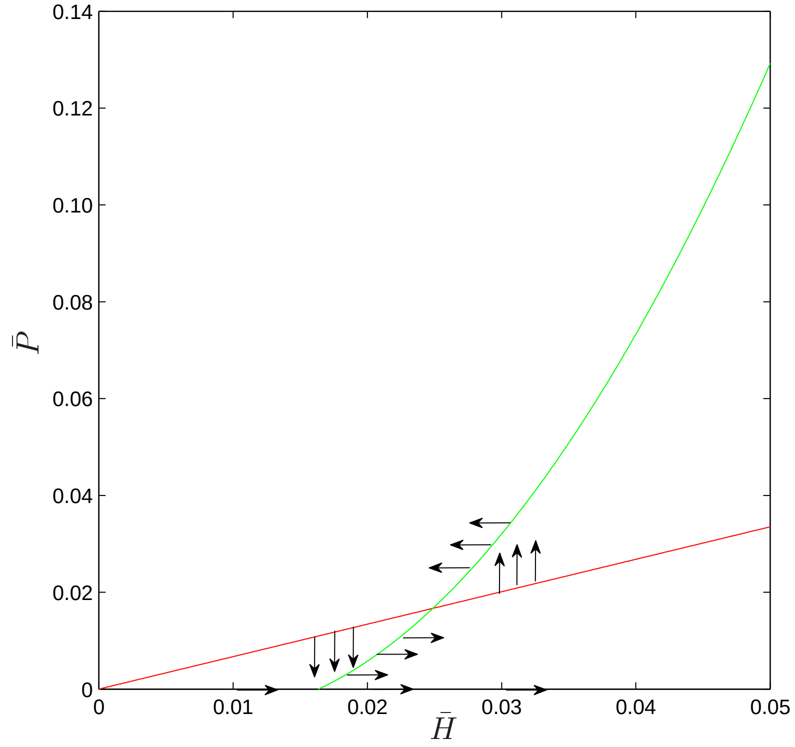

Figure 3.3: Nullcline plot for $\alpha = 8 \times 10^{-6}$, $\delta = 1.5 \times 10^{-5}$ and the remaining parameters as stated in Section 3.3. The $\bar{H}$ (red line) and $\bar{P}$ (green line) nullclines plotted in the $\bar{H} - \bar{P}$ plane; the arrows on the $\bar{H}, \bar{P}$ nullclines show the direction of the rate of change of $\bar{P}(t)$ and $\bar{H}(t)$ with time, respectively. The $\bar{H}$ axis is the trivial $\bar{P}$ nullcline. The arrow configuration indicates the possibility of limit cycle solutions.

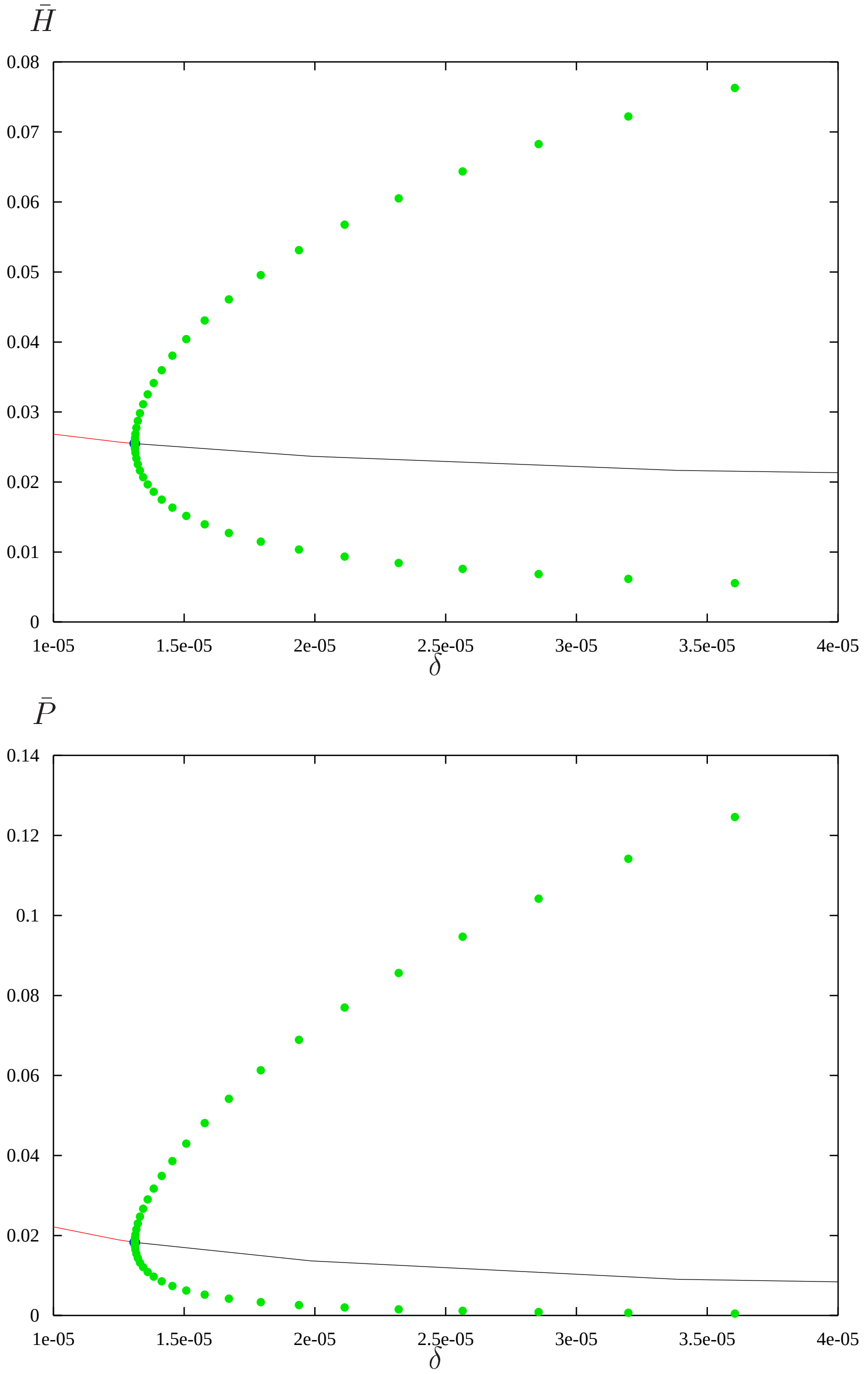

Figure 3.4: AUTO [19] plots of scaled host population density, $\bar{H}$ and scaled parasite population density, $\bar{P}$ versus δ. $\alpha = 8 \times 10^{-6}$ and all other parameters are as described in Section 3.3. The red line indicates a stable fixed point $(\bar{H}^*, \bar{P}^*)$. For, $\delta > \delta_{\mathrm{HB}}$, the steady state solution is unstable (black line). For reference, the unscaled variables are $H = H_0\bar{H}$ and $P = P_0\bar{P}$, where $H_0 = 3.82 \times 10^4$ and $P_0 = 2.91 \times 10^9$, so that, for example, with $\delta = 2.5 \times 10^{-5}$ the host population density oscillates between approximate maximum and minimum values of 2300 and 382, respectively and the parasite population density oscillates between approximate maximum and minimum values of 2.6×10^8 and 5.8×10^6, respectively.

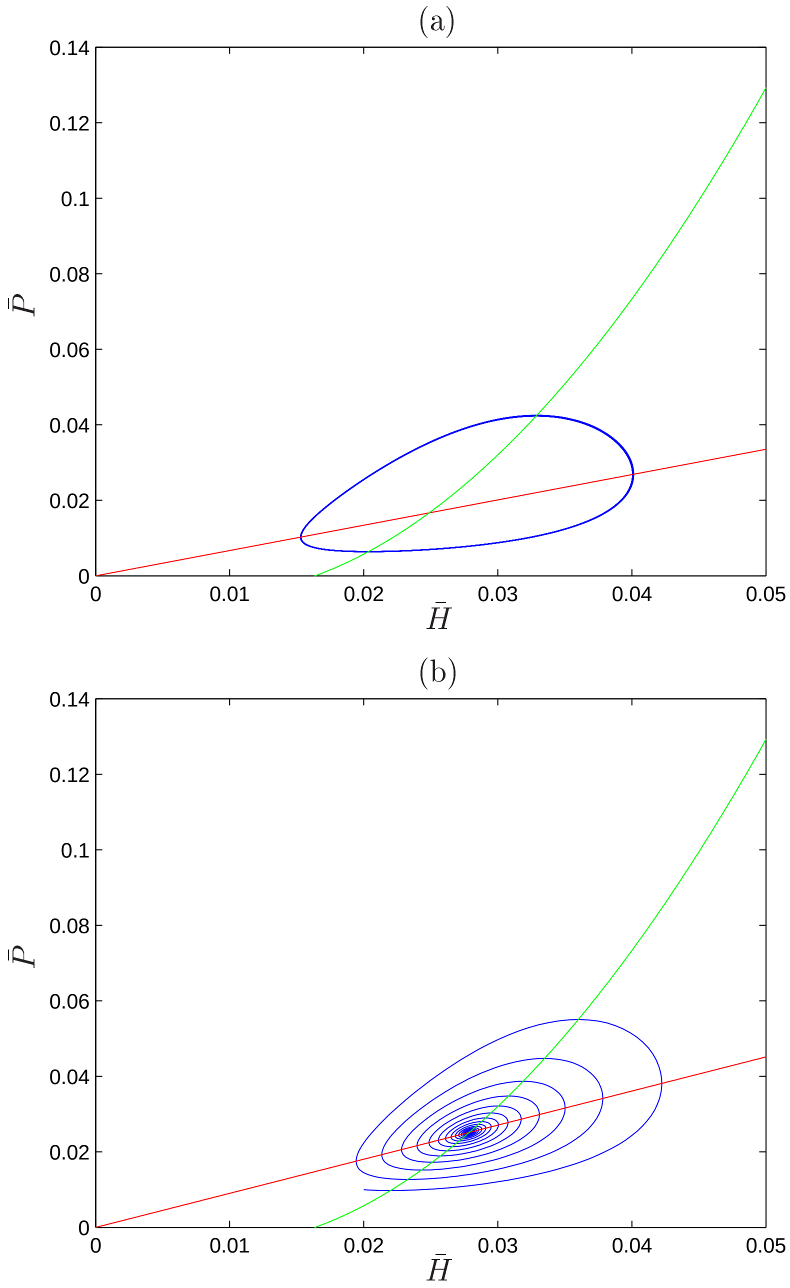

Figure 3.5: Nullcline and phase plane plots for $\alpha = 8 \times 10^{-6}$, with (a) $\delta = 1.5 \times 10^{-5}$ (limit cycle solution) and (b) $\delta = 8 \times 10^{-6}$ (fixed point steady state). The remaining parameters as stated in Section 3.3. The $\bar{H}$ (red line) and $\bar{P}$ (green line) nullclines are shown and the $\bar{H}$ axis is the trivial $\bar{P}$ nullcline.

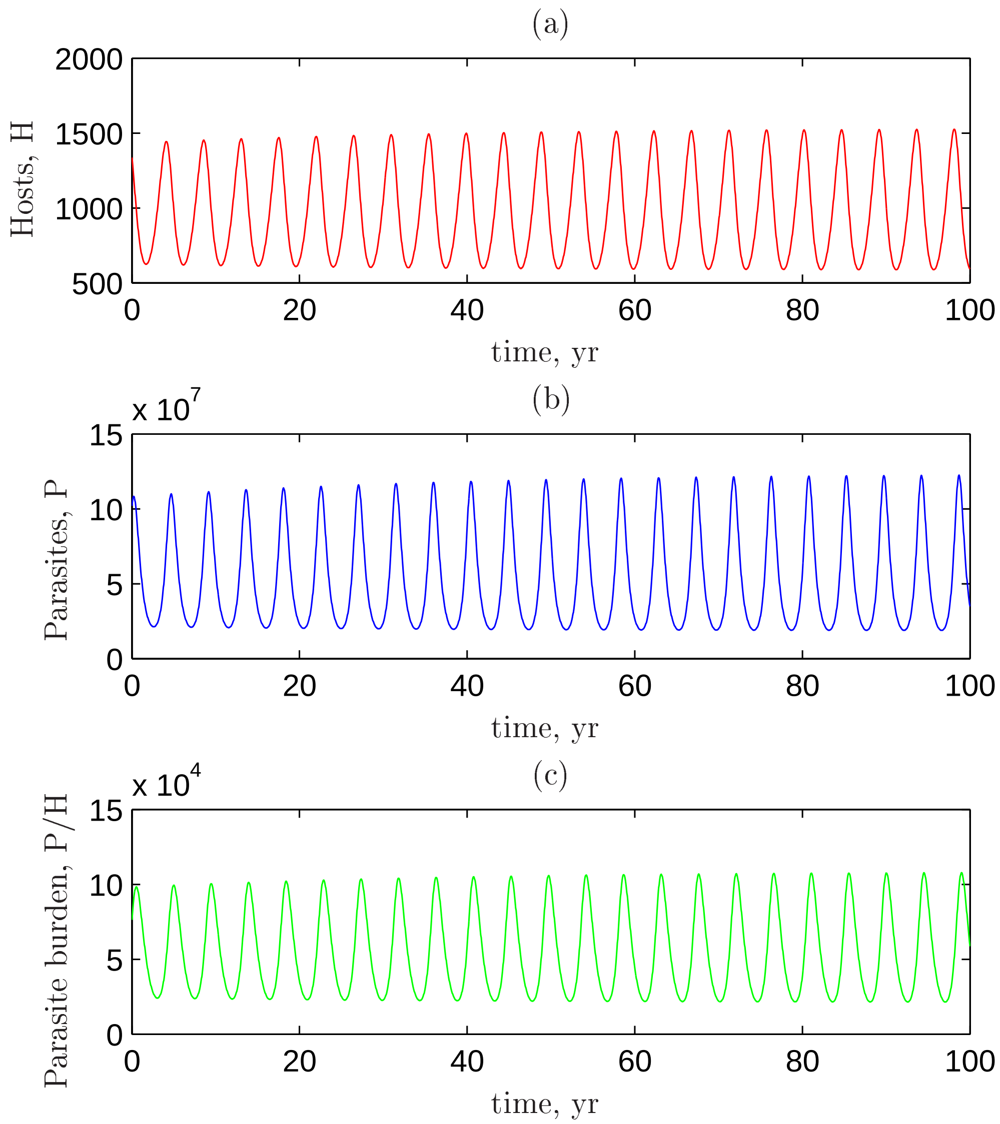

Figure 3.6: Temporal variation in unscaled (a) host, H, (b) parasite, P and (c) mean parasite burden, P/H, population densities for the given parameter set (see Section 3.3) with $\delta = 1.5 \times 10^{-5}$. In this case we observe limit cycle solutions for H and P. The initial conditions are $H(0) = 1337, P(0) = 1 \times 10^{8}$.

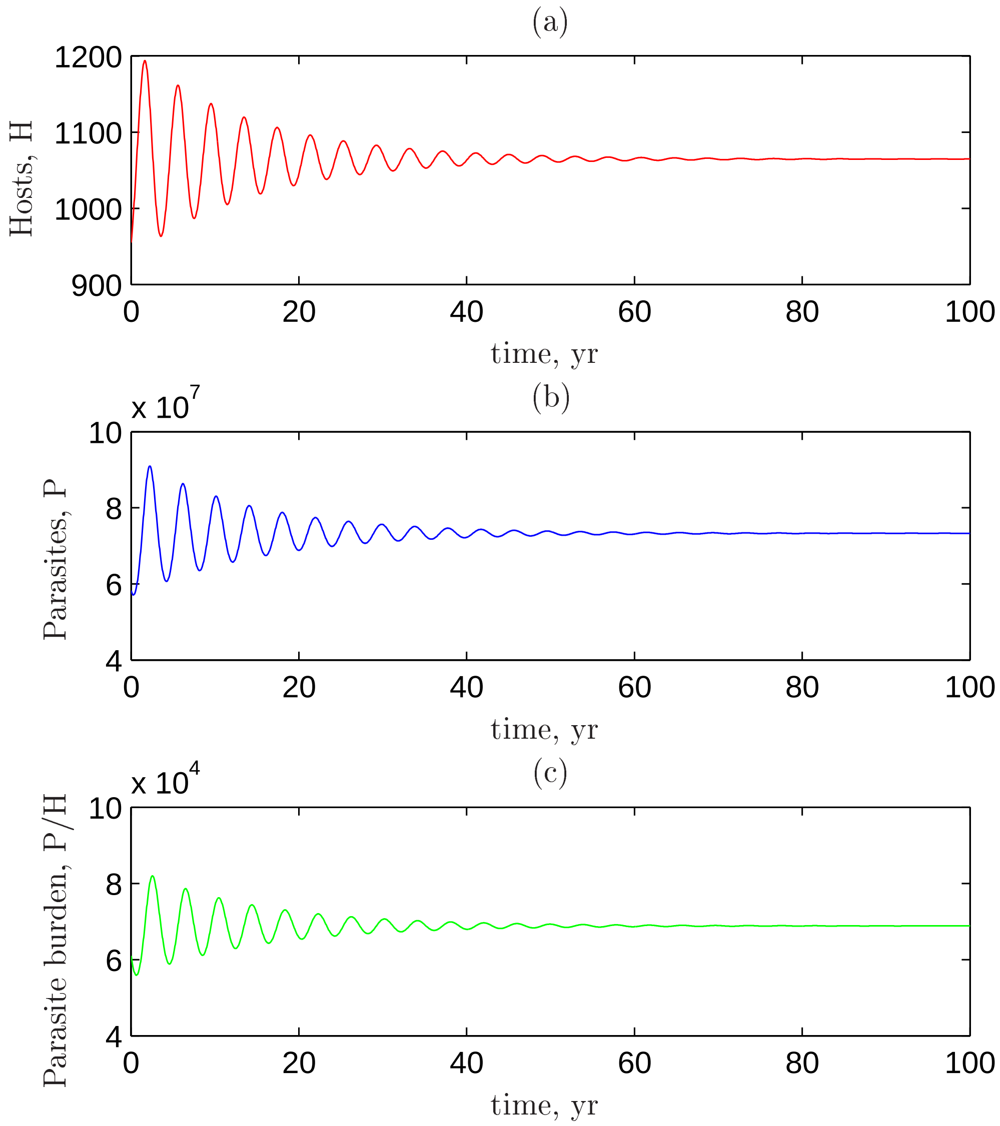

Figure 3.7: Temporal variation in unscaled (a) host, H, (b) parasite, P and (c) mean parasite burden, P/H, population densities for the given parameter set (see Section 3.3) with $\delta = 8 \times 10^{-6}$. In this case we observe decay to a stable, fixed point steady state. The initial conditions are $H(0) = 955$, $P(0) = 5.8 \times 10^{7}$.

3.6 The steady state solution

At the steady state solution, $(\bar{H}^*, \bar{P}^*)$, $d\bar{H}/dt = 0 = d\bar{P}/dt$ so that

$$\begin{aligned} -b(\bar{H}^* + \bar{P}^*) + \frac{a\bar{H}^{*2}}{c_1\bar{P}^* + \bar{H}^*} &= 0, & (3.6)\\ \bar{P}^*\left[\frac{\lambda\bar{H}^*}{1+\bar{H}^*} - c_2 - \frac{2b\bar{P}^*}{\bar{H}^*}\right] &= 0, & (3.7)\end{aligned}$$

where we write $c_2 = (\mu + b + \alpha)$. This predicts a trivial steady state solution $(0,0)$ and a non-trivial steady state solution which satisfies

$$\frac{\lambda\bar{H}^*}{1+\bar{H}^*} - c_2 - \frac{2b\bar{P}^*}{\bar{H}^*} = 0. \tag{3.8}$$

By eliminating ${\bar{H}^*}^2$ from the simultaneous equations (3.6) and (3.7), we can derive the following expression for the host population density at the non-trivial steady state

$$\bar{H}^* = \frac{\bar{P}^*\left(\chi_1\bar{P}^* - \chi_2\right)}{\chi_3 + \chi_4\bar{P}^*}, \tag{3.9}$$

where,

$$\begin{aligned} \chi_1 &= bc_1(\lambda - c_2),\\ \chi_2 &= 2b(a-b),\\ \chi_3 &= c_2(a-b),\\ \chi_4 &= 2b(a-b) - b(1+c_1)(\lambda - c_2).\end{aligned}$$

$\bar{P}^*$ is determined by substituting for $\bar{H}^*$ into the host rate equation at steady state (3.6)

$$(a-b)\bar{P}^{*2}\left(\frac{\chi_1\bar{P}^* - \chi_2}{\chi_3 + \chi_4\bar{P}^*}\right)^2 - b(1+c_1)\bar{P}^{*2}\left(\frac{\chi_1\bar{P}^* - \chi_2}{\chi_3 + \chi_4\bar{P}^*}\right) - bc_1\bar{P}^{*2} = 0. \tag{3.10}$$

Multiplying across by $(\chi_3 + \chi_4\bar{P}^*)^2/\bar{P}^{*2}$, where $\bar{P}^{*2} \neq 0$

$$(a-b)(\chi_1\bar{P}^* - \chi_2)^2 - b(1+c_1)(\chi_1\bar{P}^* - \chi_2)(\chi_3 + \chi_4\bar{P}^*) - bc_1(\chi_3 + \chi_4\bar{P}^*)^2 = 0.$$

Collecting together powers of $\bar{P}^*$ and rearranging gives the following analytic expression

$$\bar{P}^* = \frac{-\kappa_B \pm \sqrt{\kappa_B^2 - 4\kappa_A\kappa_C}}{2\kappa_A}, \tag{3.11}$$

where,

$$\begin{aligned}
\kappa_A &= (a-b)\chi_1^2 - b(1+c_1)\chi_1\chi_4 - bc_1\chi_4^2, \\
\kappa_B &= -2(a-b)\chi_1\chi_2 - b(1+c_1)(\chi_1\chi_3 - \chi_2\chi_4) - 2bc_1\chi_3\chi_4, \\
\kappa_C &= (a-b)\chi_2^2 + b(1+c_1)\chi_2\chi_3 - bc_1\chi_3^2.
\end{aligned}$$

The steady state $\bar{P}^*$ value must be positive and so we are only interested in the positive root. Substitution of $\bar{P}^*$ into (3.9) then gives the full, non-trivial, steady state solution $(\bar{H}^*, \bar{P}^*)$. The unscaled host and parasite steady state densities ($H^* = H_0\bar{H}^*$, $P^* = P_0\bar{P}^*$) in the $\alpha - \delta$ plane are depicted in Figure 3.8. For fixed α, as we increase δ, the host and parasite steady state population densities both decrease. On the other hand, if we fix δ and increase α the steady state host population increases while the parasite steady state density decreases. δ is a measure of the effect of the parasites on the host fecundity and we would indeed expect that fixing α and increasing δ, would result in a decreased host population.

3.7 Linear stability analysis

In order to analytically understand the $\bar{H} - \bar{P}$ phase space close to the steady state solutions $(\bar{H}^*, \bar{P}^*)$, it helps to approximate the non-linear system, in this region, by a linear one. That is, we perform linear stability analysis. We let $h = \bar{H} - \bar{H}^*$ and $p = \bar{P} - \bar{P}^*$ where $\bar{H}$ and $\bar{P}$ are taken to be near to the steady state, $(\bar{H}^*, \bar{P}^*)$, and therefore h and p are small, that is, $h, p << 1$. Applying the Taylor series expansion about the point $(\bar{H}^*, \bar{P}^*)$, retaining only linear terms and noting that $\partial\bar{H}/\partial t \equiv f(\bar{H}, \bar{P}) = 0$ and $\partial\bar{P}/\partial t \equiv g(\bar{H}, \bar{P}) = 0$ at $(\bar{H}^*, \bar{P}^*)$,

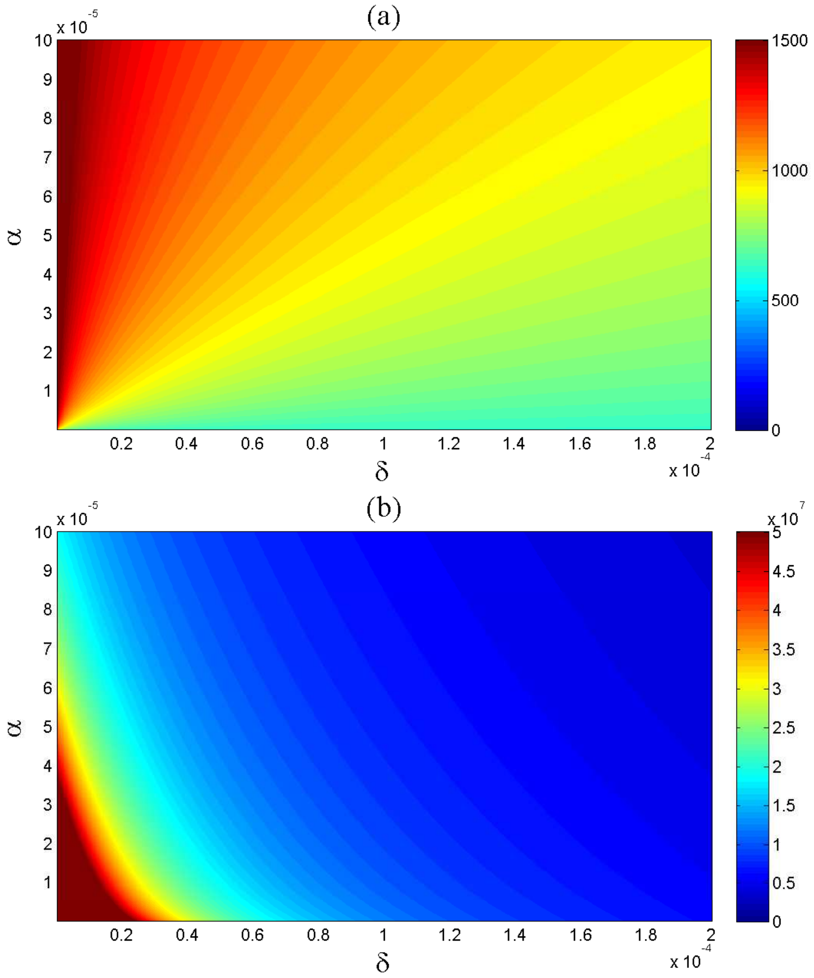

Figure 3.8: Plots illustrating the unscaled non-trivial steady state population densities for (a) hosts, H^* and (b) parasites, P^* in the $\alpha - \delta$ plane. The parameters are quantified in Section 3.3.

we can then describe the behaviour of the transformed co-ordinates (h, p) about the steady state by the linear system

$$\begin{pmatrix} h' \\ p' \end{pmatrix} = \begin{pmatrix} A & B \\ C & D \end{pmatrix} \begin{pmatrix} h \\ p \end{pmatrix}.$$

where,

$$A = \tfrac{\partial f}{\partial \bar{H}}(\bar{H}^*, \bar{P}^*), \quad B = \tfrac{\partial f}{\partial \bar{P}}(\bar{H}^*, \bar{P}^*),$$

$$C = \tfrac{\partial g}{\partial \bar{H}}(\bar{H}^*, \bar{P}^*), \quad D = \tfrac{\partial g}{\partial \bar{P}}(\bar{H}^*, \bar{P}^*),$$

so that,

$$\begin{aligned} A &= \frac{2(a-b)\bar{H}^* - b(1+c_1)\bar{P}^*}{(c_1\bar{P}^* + \bar{H}^*)}, \\ B &= \frac{-b(\bar{H}^*(1+c_1) + 2c_1\bar{P}^*)}{(c_1\bar{P}^* + \bar{H}^*)}, \\ C &= \frac{\lambda\bar{P}^*(2+\bar{H}^*)}{(1+\bar{H}^*)^2} - \frac{c_2\bar{P}^*}{\bar{H}^*}, \\ D &= \frac{2b(c_1\bar{P}^* + \bar{H}^*) - 2a\bar{H}^*}{(c_1\bar{P}^* + \bar{H}^*)}. \end{aligned}$$

The trace of the Jacobian matrix, $\mathrm{tr}J = (A + D)$, is an indicator of a Hopf bifurcation of the system. That is, a Hopf bifurcation occurs when there are complex eigenvalues and the trace changes sign (i.e. the eigenvalues are purely imaginary). The trace of our system is

$$(A + D) = \frac{2(a-b)\bar{H}^* - b(1+c_1)\bar{P}^*}{(c_1\bar{P}^* + \bar{H}^*)} + \frac{2b(c_1\bar{P}^* + \bar{H}^*) - 2a\bar{H}^*}{(c_1\bar{P}^* + \bar{H}^*)}, \quad (3.12)$$

$$= \frac{b(c_1 - 1)\bar{P}^*}{(c_1\bar{P}^* + \bar{H}^*)}. \quad (3.13)$$

The quantities $\bar{H}^*$ and $\bar{P}^*$ are strictly positive as are the parameters b and c_1. Consequently, the sign of the trace will change only according to the sign of the term $(c_1 - 1)$. In other words, the Hopf bifurcation for the linear system in the region of the steady state, lies along the line $c_1 = 1$ in the $\alpha - \delta$ phase plane, or in terms of α and δ,

$$\begin{aligned} c_1 - 1 &= 0, \\ \iff \frac{\delta b}{\alpha} &= 1, \end{aligned}$$

so that the Hopf bifurcation line is described by $\alpha = b\delta$ in the $\alpha - \delta$ plane. For $\mathrm{tr}J(\bar{H}^*, \bar{P}^*) > 0$, $\alpha < b\delta$ and limit cycle solutions, such as those in Figure 3.6(a) and (b) are observed; when the trace is less than zero, so that $\alpha > b\delta$ the system decays to a stable fixed point solution as illustrated in Figure 3.6(c),(d). Figure 3.9 shows a plot of the negative $\mathrm{tr}J(\bar{H}^*, \bar{P}^*)$ values (that is, solutions with a stable fixed steady state in $\bar{H} - \bar{P}$ densities); all positive trace values have been denoted as white (that is, oscillations in $\bar{H} - \bar{P}$ densities).

3.8 The spatial model

In the previous section, we considered the change in population densities with respect to time only, effectively assuming a homogeneous spatial distribution. However, field studies [47, 59, 62] have shown that the spatial distribution of these populations are in fact heterogeneous and so, if we want to understand better how they interact in the field then our model should account for these spatio-temporal variations. The initial motivation for this section of work was a study carried out by Townsend *et al.* [97] on the kinetics of the host-parasite mechanism for the Scottish mountain hare. We have since extended this work and carried out a numerical analysis of the spatially extended system and observed PTWs for certain parameter sets. We seek (in Chapter 4) to probe this spatially extended model and derive some analytical results that can be used to predict the properties of the PTWs, but first we illustrate the PTWs associated with this host-parasite system.

For simplicity, we assume a spatial distribution in one dimension only so that $\bar{H} = \bar{H}(x,t)$ and $\bar{P} = \bar{P}(x,t)$ and $x \in \mathbb{R}$. We assume that the hosts move

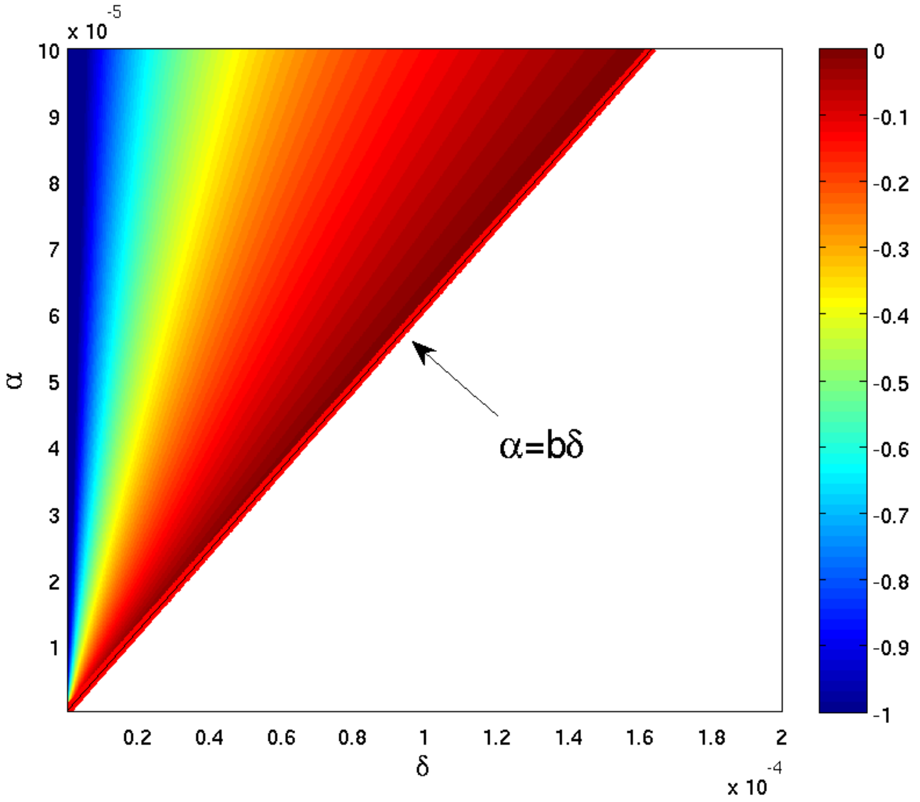

Figure 3.9: Hopf bifurcation in $\alpha - \delta$ phase space. Below the Hopf bifurcation line, $\alpha = b\delta$, the trace values are all positive indicating a limit cycle solution below this line, as in Figure 3.6. Above this line we would observe a stable fixed point solution such as that in Figure 3.6(c),(d). The parameterisation is described in Section 3.3.

through the spatial domain according to Fickian flux, $J_{\bar{H}} = -D_H \partial \bar{H}/\partial x$, where D_H is the diffusion constant for the hosts. The mean parasite burden, $\bar{P}/\bar{H}$, is now a function of x as well as t. At any given spatial point in the domain the parasite flux is given by the host flux times the number of parasites per host, since the parasite population lives in the host population. To illustrate, consider a fixed point in the spatial domain where we can measure the rate at which the host population density changes in one direction or the other. Since the parasites live in the host population then the rate at which parasite population density changes is equal to the rate at which the host population changes times the number of parasites per host. The spatial gradient of the parasite flux term, $\bar{P}J_{\bar{H}}/\bar{H}$, then gives the final advection term in (3.15). The governing equations are

$$\begin{aligned}
\frac{\partial \bar{H}}{\partial t} &= -b(\bar{H}+\bar{P}) + \frac{a\bar{H}^2}{c_1\bar{P}+\bar{H}} - \frac{\partial J_{\bar{H}}}{\partial x}, && (3.14)\\
\frac{\partial \bar{P}}{\partial t} &= \bar{P}\left[\frac{\lambda \bar{H}}{1+\bar{H}} - (\mu+b+\alpha) - \frac{2b\bar{P}}{\bar{H}}\right] - \frac{\partial}{\partial x}\left(\frac{\bar{P}J_{\bar{H}}}{\bar{H}}\right). && (3.15)
\end{aligned}$$

This describes a reaction advection diffusion system. This system can be solved numerically using the method of lines to reduce it to a coupled system of ordinary differential equations (ODEs). A central difference approximation is used for the diffusion term in the hare equation and flux limiters for the advection term in the parasite equation. The flux limiters are designed to ensure physically realistic solutions, in this case, to ensure positivity of the population densities. Further discussion on their construction and effects can be found in Appendix A along with full details of the numerical scheme. No-flux boundary conditions are applied at each end of the spatial domain and the resulting system is solved using a fourth order Runge-Kutta method. The initial spatial distributions for both populations are described by

$$\bar{H}(x,0) = \bar{P}(x,0) = A\exp(-\xi x), \qquad (3.16)$$

where A and ξ are positive constants, which we take to be 0.03 and 1, respectively. Application of the parameter set detailed in Section 3.3 generates a travelling wave front, followed by PTWs, where oscillations in hare and parasite densities occurred in both space and time. These spatiotemporal oscillations are illustrated in Figures 3.10 to 3.14. This is the first time that PTW solution behaviours have been observed in a host-parasite system; normally such mathematical solution forms are observed and analysed in predator-prey reaction-diffusion systems, where the movement of predators and prey are independent of each other. As a quick, initial comparison, studying Figures 3.6 and 3.10 we can compare the results from the spatially homogeneous and heterogeneous models and note the effect on the amplitude and temporal period of the oscillations. In the ODE model, the host population oscillates between a density value of approximately 625 to 1500 for the base parameter set used by Townsend *et al.* [97]. In the spatial model, this amplitude is slightly reduced with minimum/maximum values of 700/1400. The temporal period is 4.5 years in both cases and the mean parasite burden, P/H is of similar magnitude to the spatially homogeneous case, that is $O(10^4)$. The speed of the PTWs, illustrated in Figure 3.11, is calculated to be 1.2km/yr for this particular parameter set and initial and boundary conditions, and the waves travel in the positive x-direction.

When considering the governing system (3.14) and (3.15), it is important to note that the alternative scheme,

$$\frac{\partial \bar{H}}{\partial t} = -b(\bar{H}+\bar{P}) + \frac{a\bar{H}^2}{c_1\bar{P}+\bar{H}} - \frac{\partial J_{\bar{H}}}{\partial x}, \tag{3.17}$$

$$\frac{\partial \bar{P}}{\partial t} = \bar{P}\left[\frac{\lambda\bar{H}}{1+\bar{H}} - (\mu+b+\alpha) - \frac{2b\bar{P}}{\bar{H}}\right], \tag{3.18}$$

using Fickian flux for the hosts and omitting the explicit parasite flux term, can be used to produce almost identical results. In this case the diffusion of the host population coupled with the reaction kinetics and the assumption that the parasite population exists only in the host population, appears to be sufficient to

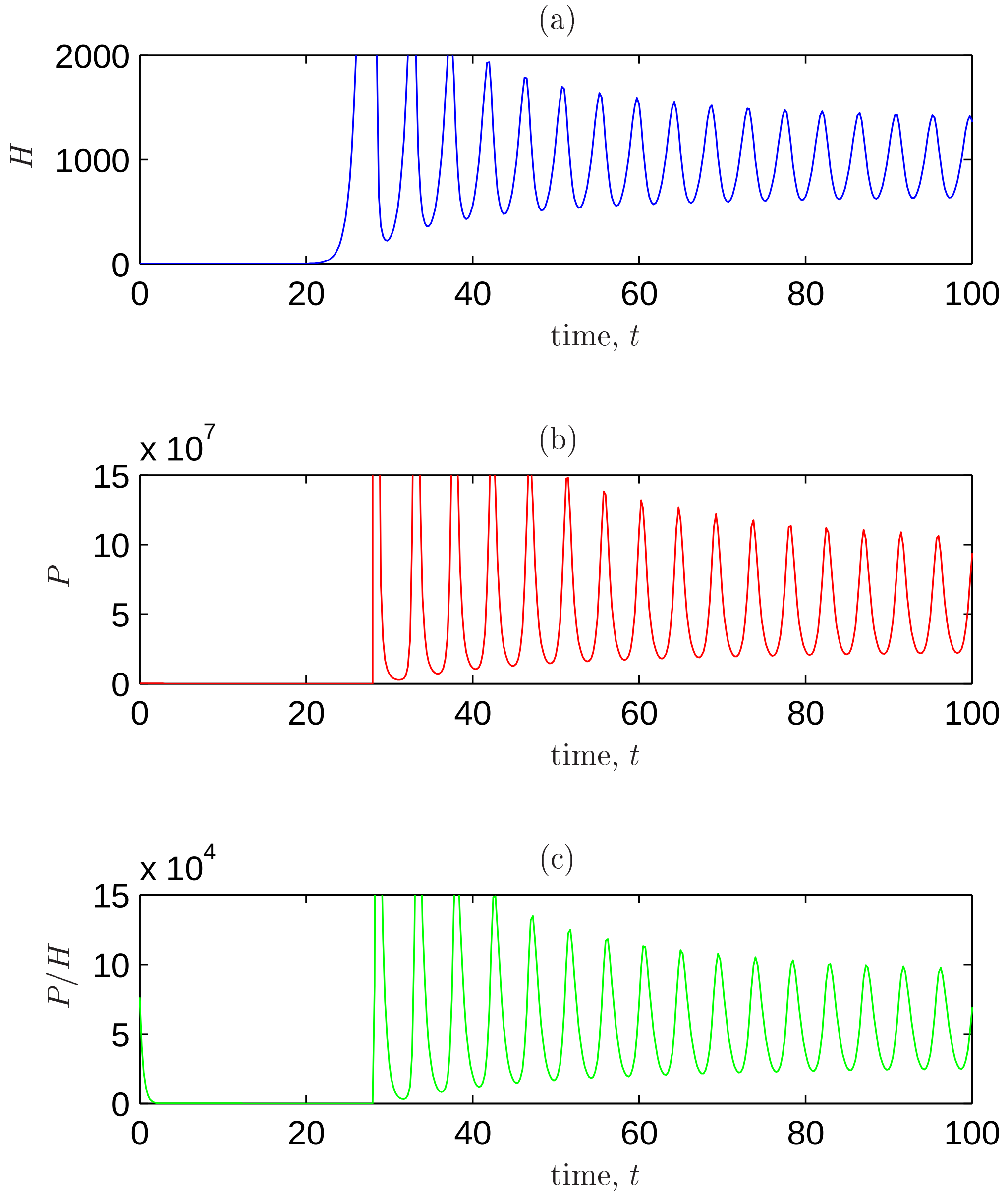

Figure 3.10: Temporal oscillations in population densities (a) H, (b) P and (c) P/H at a fixed point in space ($x = 30$km). The diffusion coefficient, $D_H = 0.01$, $\delta = 1.5 \times 10^{-5}$ and all other parameters are as in Section 3.3. The initial spatial distribution of both H and P are described by $A \exp(-\xi x)$, where $A = 1146$ and $\xi = 1$.

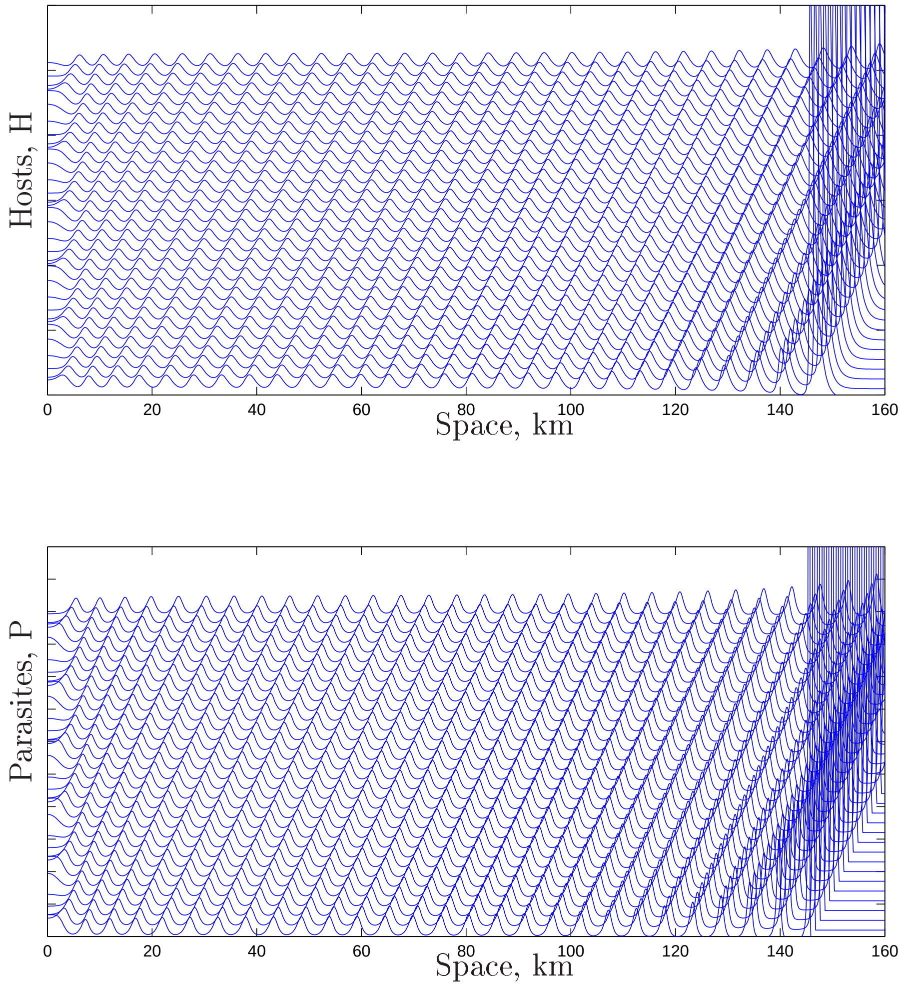

Figure 3.11: Numerical solutions of the system (3.14), (3.15) for $\delta = 1.5\text{x}10^{-5}$ and $D_H = 0.01$. The periodic wave trains, for both host and parasite populations, move in the positive x direction. The solutions for $\bar{H}$ and $\bar{P}$ are plotted as functions of space x at successive times t, with the vertical separation of solutions proportional to the time interval. We consider the system on the semi-infinite domain $[0, \infty)$ with initial data of the form $\bar{H}(x, 0) = \bar{P}(x, 0) = Aexp(-\xi x)$. The parameter A affects the time course of the evolution, but has no effect on the ultimate behaviour; we take $A = 1146/H_0$ and $\xi = 1$. The wave speed for this parameter set with given initial and boundary conditions is 1.2km/yr.

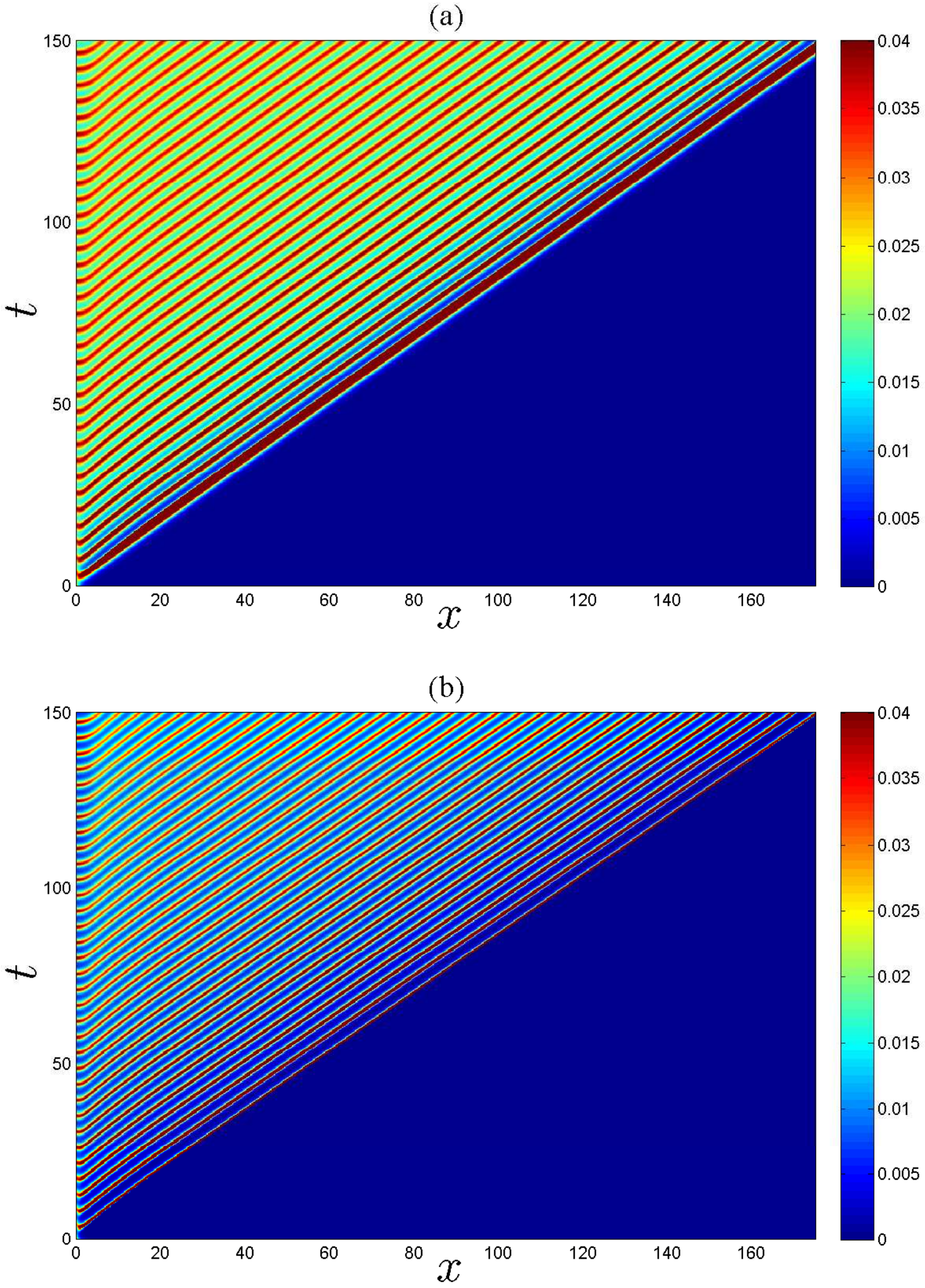

Figure 3.12: Colour plot showing the variation in (a) scaled host, $\bar{H}$, and (b) scaled parasite, $\bar{P}$, population densities in the spatiotemporal plane. These are numerical solutions of the system (3.14) - (3.15) for $\delta = 1.5 \times 10^{-5}$ and $D_H = 0.01$. The solutions for $\bar{H}$ and $\bar{P}$ are plotted in the space-time domain with the colour plot indicating population density levels at a given point of space and time. We consider the system on the semi-infinite domain $[0, \infty)$ with initial data of the form $\bar{H}(x, 0) = \bar{P}(x, 0) = A \exp(-\xi x)$. The parameter A affects the time course of the evolution, but has no effect on the ultimate behaviour; we take $A = 1146/H_0$ and $\xi = 1$. The wave speed is 1.2 km/yr and the remaining parameter values are detailed in Section 3.3.

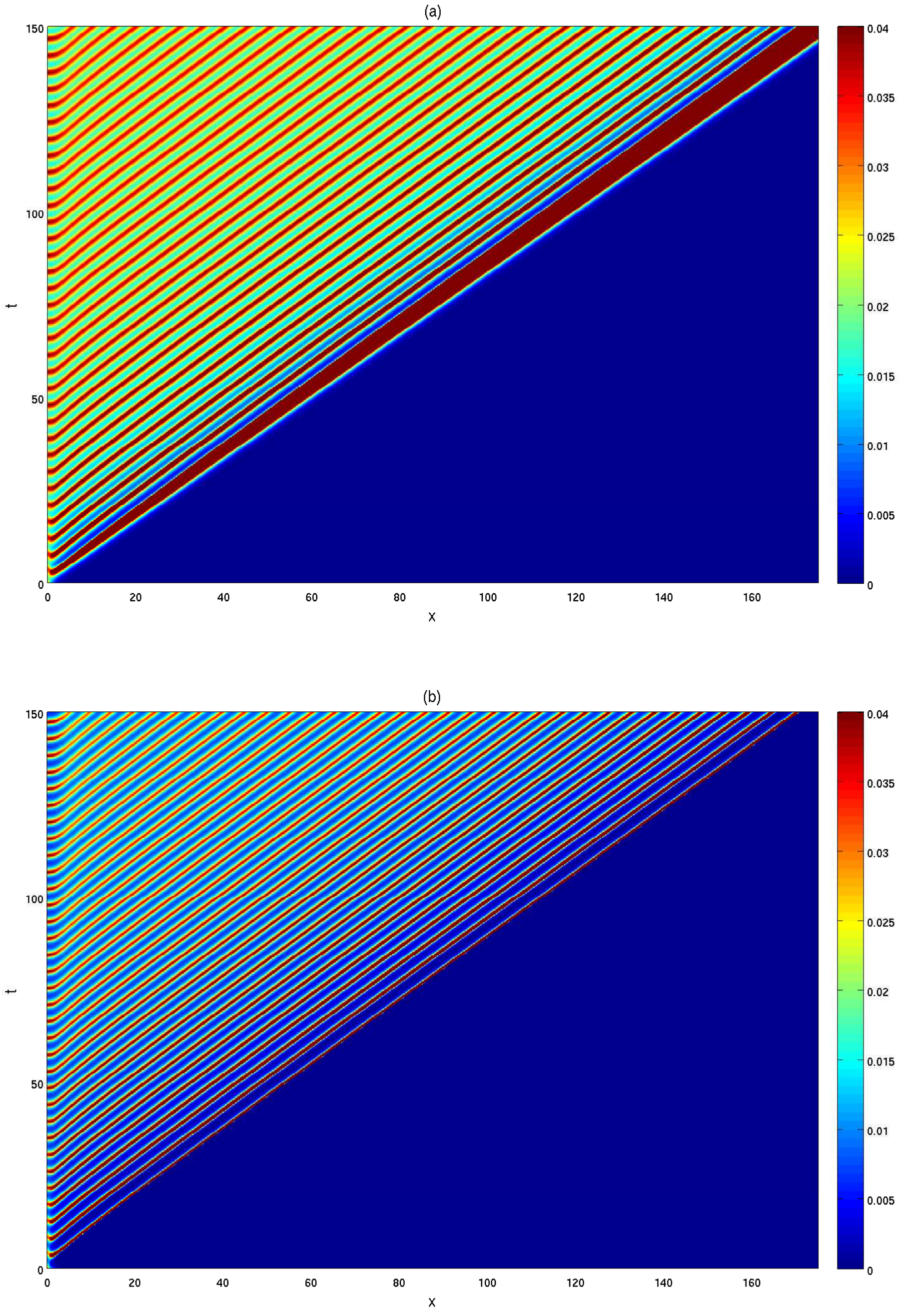

Figure 3.13: Colour plot showing the variation in (a) scaled host, $\bar{H}$, and (b) scaled parasite, $\bar{P}$, population densities in the spatiotemporal plane. These are numerical solutions of the system (3.17) - (3.18) for $\delta = 1.5 \times 10^{-5}$ and $D_H = 0.01$. The solutions for $\bar{H}$ and $\bar{P}$ are plotted in the space-time domain with the colour plot indicating population density levels at a given point of space and time. We consider the system on the semi-infinite domain $[0, \infty)$ with initial data of the form $\bar{H}(x, 0) = \bar{P}(x, 0) = A\exp(-\xi x)$. The parameter A affects the time course of the evolution, but has no effect on the ultimate behaviour; we take $A = 1146/H_0$ and $\xi = 1$. The wave speed is 1.2 km/yr and the remaining parameter values are detailed in Section 3.3.

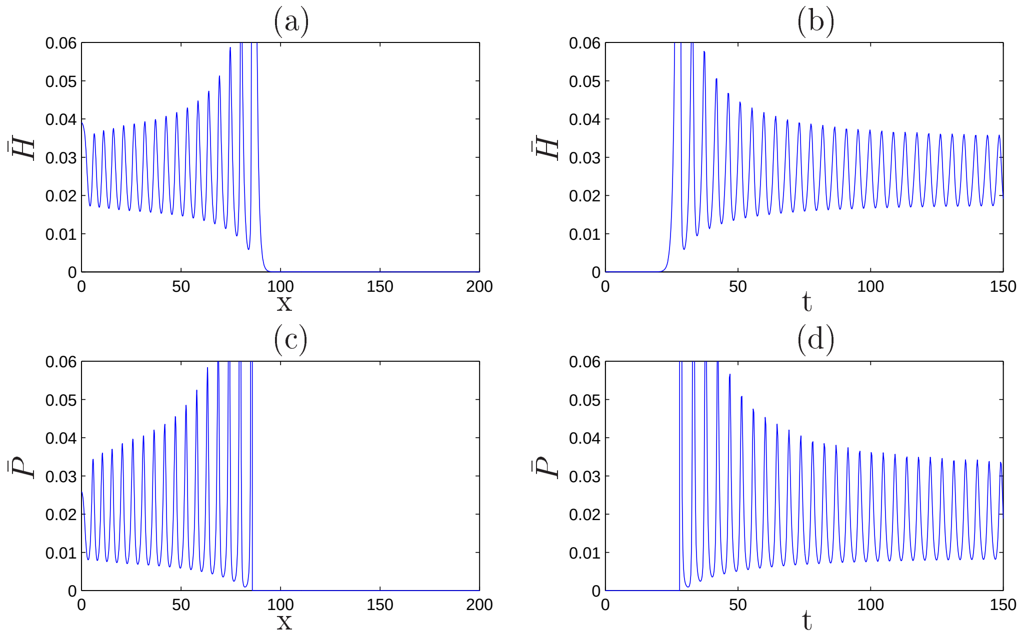

Figure 3.14: Spatial and temporal oscillations in scaled population densities $\bar{H}$ and $\bar{P}$. Spatial oscillations are illustrated in (a) $\bar{H}$ and (c) $\bar{P}$ at the fixed time point $t = 75$yrs. Temporal oscillations in (b) $\bar{H}$ and (d) $\bar{P}$ at the fixed spatial point $x = 30$km are also shown. The parameter set and initial conditions are as described in Figure 3.12.

model the spatial change in host and parasite densities. This can be observed for our particular parameter set by comparing Figures 3.12 and 3.13 which illustrate PTW solutions for (3.14) - (3.15) and (3.17) - (3.18), respectively. In both cases the wave speed is the same and the only slight difference can be observed near the transition wavefront where the host population is moving into empty space. In the former model, as the host moves into empty space the parasite advection term ensures a non-zero parasite density as well. In the latter case, as the host moves into empty space, initially the parasite density is zero there because there has been no corresponding flux of parasites. But then the kinetic terms cause the parasite density to quickly adjust to a non-zero level. These two models have only been compared for this particular parameter set so no general comment can be made about their equivalence in different regimes. This would be worth investigating in the future but is not explored further in this thesis.

Having shown, numerically, the presence of PTWs as a possible solution form for this particular host-parasite system, we will now try to obtain a generic result to predict PTWs in two population cyclic host parasite systems with a supercritical Hopf bifurcation in the reaction kinetics.

3.9 Discussion

In this Chapter, we investigated the mountain hare-*Trichostrongylus retortaeformis* system model derived by Townsend *et al.* [96, 97]. First we studied the reaction kinetics before going on to derive some numerical solutions to the spatially extended model and were able to illustrate, for the first time in a system of this type, PTWs. We derived analytical solutions for the homogeneous steady state population levels and performed a linear stability analysis which yielded an equation describing the Hopf bifurcation in the phase plane of two parasite related parameters, α and δ. The partial derivatives of the reaction kinetics derived in this section will be used again in Chapter 4 when we apply a new generic result to this particular host-parasite system.

We introduced the spatially heterogeneous mountain hare-parasite model and obtained some numerical solutions illustrating the possibility of PTWs with this system. We made a quick comparison of the amplitude and period of the temporal oscillations in the temporal and spatial systems and found only a slight reduction in the amplitude of the temporal oscillation associated with the spatial model, with the period remaining unchanged. Also, the parasite burden was of a similar magnitude in both systems. This suggests, therefore, that simply accounting for population dispersal in the model is not enough to produce PTW solutions of the amplitude and period observed in the field for parameter sets that give realistic parasite burdens.

In the following Chapter, we derive a generic result, for the spatially heterogeneous model, based on work done by Koppell and Howard [45], that gives conditions on the parameter set describing the associated reaction kinetic system resulting in PTW solutions.

Chapter 4

A generic host-parasite reaction advection diffusion system

A generic host-parasite reaction advection diffusion system can be modelled by

$$\frac{\partial H}{\partial t} = f(H,P) - \frac{\partial}{\partial x}\left(J_H\right), \tag{4.1}$$

$$\frac{\partial P}{\partial t} = g(H,P) - \frac{\partial}{\partial x}\left(\frac{P}{H}J_H\right), \tag{4.2}$$

where f and g describe the reaction kinetics of the host, H, and parasite, P, system and the spatial derivatives relate to the dispersal effects of the host; The population densities, $H = H(x,t)$ and $P = P(x,t)$, now depend on their spatiotemporal co-ordinates and we assume Fickian diffusion for the hosts, $J_H = -D_H \frac{\partial H}{\partial x}$. Expanding the spatial derivatives we therefore have,

$$\frac{\partial H}{\partial t} = f(H,P) + D_H \frac{\partial^2 H}{\partial x^2}, \tag{4.3}$$

$$\frac{\partial P}{\partial t} = g(H,P) + \frac{D_H}{H}\left(\frac{\partial P}{\partial x}\frac{\partial H}{\partial x} + P\frac{\partial^2 H}{\partial x^2} - \frac{P}{H}\left(\frac{\partial H}{\partial x}\right)^2\right). \tag{4.4}$$

We are interested in periodic plane wave solutions and therefore rewrite the above system in terms of the travelling wave variable, $z = t - x/s$, where s is the speed of the periodic plane wave. Noting the following relationships between the two co-ordinate systems,

$$\frac{\partial}{\partial t} = \frac{\partial}{\partial z}, \qquad \frac{\partial}{\partial x} = \frac{1}{s}\frac{\partial}{\partial z}, \qquad \frac{\partial^2}{\partial x^2} = \frac{1}{s^2}\frac{\partial^2}{\partial z^2},$$

the system of PDEs with respect to (x, t) can be reduced to a system of ODEs with respect to z as shown:

$$\begin{aligned} \frac{dH}{dz} &= f(H,P) + \frac{D_H}{s^2}\frac{d^2H}{dz^2}, && (4.5) \\ \frac{dP}{dz} &= g(H,P) + \frac{D_H}{s^2H}\left(\frac{dP}{dz}\frac{dH}{dz} + P\frac{d^2H}{dz^2} - \frac{P}{H}\left(\frac{dH}{dz}\right)^2\right). && (4.6) \end{aligned}$$

Rearranging (4.5) and assigning $V = \frac{dH}{dz}$ we obtain three first order ODEs,

$$\begin{aligned} H' &= V, && (4.7) \\ V' &= \frac{s^2}{D_H}\left(V - f(H,P)\right), && (4.8) \\ P' &= \frac{s^2H}{s^2H - D_HV}\left(g(H,P) + \frac{P}{H}(V - f(H,P)) - \frac{D_HV^2P}{s^2H^2}\right). && (4.9) \end{aligned}$$

where the $'$ indicates differentiation with respect to z.

4.1 Linearising the reaction advection diffusion system

We want to investigate the behaviour of the reaction advection diffusion system in the region of the non-trivial steady state solution predicted by the reaction kinetics, (H^*, P^*). The system co-ordinates are transformed relative to the steady state values and linearised, assuming that the perturbations from the steady state are small. The new system variables are $h = H - H^*$, $p = P - P^*$ and $v = V - V^*$ where (H^*, V^*, P^*) denotes the co-ordinates of the non-trivial steady state solution. The relationship in this region between the new co-ordinates and their derivatives with respect to z is then approximated by the Jacobian matrix as shown:

$$\begin{bmatrix} h' \\ v' \\ p' \end{bmatrix} = J \begin{bmatrix} h \\ v \\ p \end{bmatrix}$$

where we define

$$\begin{aligned}\frac{dH}{dz} &= l(H,V,P),\\ \frac{dV}{dz} &= m(H,V,P),\\ \frac{dP}{dz} &= n(H,V,P),\end{aligned}$$

and the Jacobian matrix, J is defined by

$$J = \left[\begin{array}{ccc} \frac{\partial l}{\partial H} & \frac{\partial l}{\partial V} & \frac{\partial l}{\partial P} \\ \frac{\partial m}{\partial H} & \frac{\partial m}{\partial V} & \frac{\partial m}{\partial P} \\ \frac{\partial n}{\partial H} & \frac{\partial n}{\partial V} & \frac{\partial n}{\partial P} \end{array}\right]\Bigg|_{(H^*,V^*,P^*)} . \tag{4.10}$$

Computing the entries for J and noting that at the non-trivial steady state, (H^*, V^*, P^*), we have

$$V^* = \frac{\partial H}{\partial z}\left(H^*, V^*, P^*\right) = 0, \tag{4.11}$$

and the reaction kinetics of the system, namely $f(H^*, P^*)$ and $g(H^*, P^*)$ go to zero so that

$$\frac{\partial n}{\partial H}\left(H^*, P^*\right) = \frac{\partial g}{\partial H}\left(H^*, P^*\right) - \frac{P^*}{H^*}\frac{\partial f}{\partial H}\left(H^*, P^*\right), \tag{4.12}$$

$$\frac{\partial n}{\partial V}\left(H^*, P^*\right) = \frac{P^*}{H^*}, \tag{4.13}$$

$$\frac{\partial n}{\partial P}\left(H^*, P^*\right) = \frac{\partial g}{\partial P}\left(H^*, P^*\right) - \frac{P^*}{H^*}\frac{\partial f}{\partial P}\left(H^*, P^*\right). \tag{4.14}$$

The linearised system, about the steady state can, therefore, be restated as

$$\left[\begin{array}{c} h' \\ v' \\ p' \end{array}\right] = \left[\begin{array}{ccc} 0 & 1 & 0 \\ -\frac{s^2 A}{D_H} & \frac{s^2}{D_H} & -\frac{s^2 B}{D_H} \\ C - A\frac{P^*}{H^*} & \frac{P^*}{H^*} & D - B\frac{P^*}{H^*} \end{array}\right] \left[\begin{array}{c} h \\ v \\ p \end{array}\right] \tag{4.15}$$

where we assign

$$\frac{\partial f}{\partial H}\left(H^*, P^*\right) = A, \qquad \frac{\partial f}{\partial P}\left(H^*, P^*\right) = B,$$
$$\frac{\partial g}{\partial H}\left(H^*, P^*\right) = C, \qquad \frac{\partial g}{\partial P}\left(H^*, P^*\right) = D.$$

The eigenvalues η of the transformed co-ordinate system are found by solving $\det(J - I\eta) = 0$, that is

$$\begin{vmatrix} -\eta & 1 & 0 \\ -\frac{s^2 A}{D_H} & \frac{s^2}{D_H} - \eta & -\frac{s^2 B}{D_H} \\ C - A\frac{P^*}{H^*} & \frac{P^*}{H^*} & D - B\frac{P^*}{H^*} - \eta \end{vmatrix} = 0. \tag{4.16}$$

Multiplying and collecting coefficients of powers of η, we then obtain the eigenvalue equation

$$\eta^3 - \eta^2 \left(\frac{s^2}{D_H} + D - B\frac{P^*}{H^*} \right) + \eta \left(\frac{s^2}{D_H}(A + D) \right) - \left(\frac{s^2}{D_H}(AD - BC) \right) = 0. \tag{4.17}$$

We are seeking PTW solutions to the original PDE system. These solutions arise at the Hopf bifurcation of the associated ODE system in the travelling wave variable z, which can be found by solving the eigenvalue equation (4.17).

4.2 Conditions for PTWs

Comparing (4.17) with the general form for a cubic polynomial

$$a_3\eta^3 + a_2\eta^2 + a_1\eta + a_0 = 0, \tag{4.18}$$

and noting that a Hopf bifurcation is associated with purely imaginary eigenvalues, $\eta = \pm pi$ say with $p \neq 0$, we factorise the cubic polynomial as follows,

$$\left(\eta^2 + p^2\right)(q\eta + r) = 0, \qquad \text{where } q, r \neq 0. \tag{4.19}$$

Comparing (4.18) and (4.19) then gives rise to the following relations

$$a_3 = q, \qquad a_2 = r, \qquad a_1 = p^2 q, \qquad a_0 = p^2 r. \tag{4.20}$$

Therefore, we have

$$a_0 a_3 = a_1 a_2, \tag{4.21}$$

$$a_1 a_3 = p^2 q^2 > 0, \tag{4.22}$$

$$a_0 a_2 = p^2 r^2 > 0. \tag{4.23}$$

where, in our case,

$$\begin{aligned} a_0 &= -\frac{s^2}{D_H}(AD - BC), \\ a_1 &= \frac{s^2}{D_H}(A + D), \\ a_2 &= -\left(\frac{s^2}{D_H} + D - B\frac{P^*}{H^*}\right), \\ a_3 &= 1, \end{aligned}$$

and the eigenvalue equation at the Hopf bifurcation then becomes

$$\left(\eta^2 + \frac{s^2}{D_H}(A + D)\right)\left(\eta - \left(\frac{s^2}{D_H} + D - B\frac{P^*}{H^*}\right)\right) = 0, \tag{4.24}$$

with eigenvalues

$$\eta_{1,2} = \pm is\sqrt{\frac{(A + D)}{D_H}}, \tag{4.25}$$

$$\eta_3 = \frac{s^2}{D_H} + D - B\frac{P^*}{H^*}. \tag{4.26}$$

Substituting for a_i into equations (4.21) - (4.23) then gives three conditions on the minimum speed, s_{Hopf}, of the PTW, namely,

Condition I

The condition $a_0 a_3 = a_1 a_2$ implies that

$$-\frac{s^2}{D_H}(A + D)\left(\frac{s^2}{D_H} + D - B\frac{P^*}{H^*}\right) = -\frac{s^2}{D_H}(AD - BC). \tag{4.27}$$

Rearranging gives

$$\frac{s^2}{D_H}\left[\frac{s^2}{D_H}(A + D) + \left(D^2 + BC - \frac{P^*}{H^*}B(A + D)\right)\right] = 0, \tag{4.28}$$

which leads to the following solutions for s^2: $s^2 = 0$, corresponding to zero temporal frequency for the periodic plane wave, and the non-trivial case where,

$$s^2 = D_H\left(\frac{P^*}{H^*}B - \left(\frac{D^2 + BC}{A + D}\right)\right). \tag{4.29}$$

Condition II

The inequality $a_1 a_3 > 0$ implies that

$$\frac{s^2}{D_H}(A+D) > 0, \tag{4.30}$$

and since $\frac{s^2}{D_H} > 0$ we retrieve the condition for instability in the linearised reaction kinetic system, namely

$$A + D > 0, \tag{4.31}$$

that is, the eigenvalues of the Jacobian matrix of the reaction kinetics have a positive real part and the resultant steady state solution is unstable, with an associated stable limit cycle.

Condition III

The third condition, $a_0 a_2 > 0$, gives

$$\frac{s^2}{D_H}(AD - BC)\left(\frac{s^2}{D_H} + D - B\frac{\bar{P}^*}{\bar{H}^*}\right) > 0.$$

and since $\frac{s^2}{D_H} > 0$ is defined by (4.29) we have

$$(AD - BC)\left(\left(B\frac{\bar{P}^*}{\bar{H}^*} - \frac{D^2 + BC}{A+D}\right) + D - B\frac{\bar{P}^*}{\bar{H}^*}\right) > 0.$$

Rearranging gives the inequality condition

$$(AD - BC)^2 > 0. \tag{4.32}$$

To summarise, the three conditions on the system parameters for the presence of (non-trivial) PTW solutions are,

$$s^2 \;=\; D_H\left(B\frac{P^*}{H^*} - \frac{(D^2 + BC)}{A+D}\right), \tag{4.33}$$

$$A + D > 0, \tag{4.34}$$

$$(AD - BC)^2 > 0. \tag{4.35}$$

From here on we shall use s_{Hopf} for s in (4.33) to denote the minimum speed of the PTW at the Hopf bifurcation. In their paper, Koppell & Howard [45] assumed the condition that the linearised system contained an unstable focus; this does not appear to be a necessary condition required by our analysis. Condition III indicates that the determinant of the linear system, $AD - BC$ may be negative or positive, indicating an unstable node or focus.

Following the line adopted by Koppell & Howard [45] for a spatially heterogeneous cyclic, two population predator-prey system, we have here produced an analagous result for the spatially heterogeneous host-parasite system, which gives conditions for the presence/absence of PTW solutions for a given set of parameters. This result is generic and can be applied to any two population host-parasite reaction kinetic system containing a supercritical Hopf bifurcation. The Koppell & Howard [45] result applied to predator-prey systems where the populations necessarily move independently of each other, but whose dispersal coefficients are similar. With the host-parasite system the parasite lives on or in the host and therefore the dispersal coefficients for both populations are exactly the same, that is, the parasite moves with the same velocity as the host.

Having produced this new generic result for host-parasite systems we will test it against two sample models to confirm that we can predict and then numerically confirm the existence of PTW solutions in these systems.

4.3 Mountain hare, trichostronglyus retortaeformis system

A detailed study of the properties of the non-spatial version of this system was carried out in Chapter 3. The full spatial version reads

$$\begin{aligned} \frac{\partial H}{\partial t} &= f(H,P) - \frac{\partial J_H}{\partial x}, && (4.36) \\ \frac{\partial P}{\partial t} &= g(H,P) - \frac{\partial}{\partial x}\left(\frac{PJ_H}{H}\right), && (4.37) \end{aligned}$$

where $J_H = -D_H \partial H/\partial x$ and D_H is the dispersion constant for the host population, and $f(H,P)$ and $g(H,P)$ describe the reaction kinetics of the hare and parasite populations, respectively. For the numerical analysis described in this section, we use an alternative, but equivalent rescaling of the system equations, in order to make the numerical analysis more tractible; the rescaling of this system is described in Appendix B and the rescaled system is given by

$$\begin{aligned} \frac{\partial \bar{H}}{\partial t} &= -\bar{\alpha}\bar{P} - b\bar{H} + \frac{a\bar{H}^2}{\bar{\delta}\bar{P} + \bar{H}} - \frac{\partial \bar{J}_H}{\partial x}, && (4.38) \\ \frac{\partial \bar{P}}{\partial t} &= \bar{P}\left[\frac{\lambda \bar{H}}{1+\bar{H}} - \mu - \bar{\alpha}\epsilon - b + 2\bar{\alpha}\frac{\bar{P}}{\bar{H}}\right] - \frac{\partial}{\partial x}\left(\frac{\bar{P}\bar{J}_H}{\bar{H}}\right), && (4.39) \end{aligned}$$

where $H = H_0\bar{H}$, $P = P_0\bar{P}$, $\alpha = \epsilon\bar{\alpha}$, $\delta = \epsilon\bar{\delta}$ and $\epsilon = H_0/P_0 = 3.82 \times 10^{-4}$. The scaling factor H_0 is the transmission inefficiency constant as in (3.2) and is quantified in Section 3.3. The scaling factor P_0 is chosen to ensure that the scaled population densities lie in the range zero to one. In this particular case $P_0 = 1 \times 10^8$. The reaction kinetics of the spatially homogeneous system are given by

$$\begin{aligned} f(\bar{H},\bar{P}) &= -\bar{\alpha}\bar{P} - b\bar{H} + \frac{a\bar{H}^2}{\bar{\delta}\bar{P} + \bar{H}}, && (4.40) \\ g(\bar{H},\bar{P}) &= \bar{P}\left[\frac{\lambda \bar{H}}{1+\bar{H}} - \mu - \bar{\alpha}\epsilon - b - 2\bar{\alpha}\frac{\bar{P}}{\bar{H}}\right]. && (4.41) \end{aligned}$$

In order to apply the results from the analysis of the generic reaction diffusion system (Section 4.2) we first need to compute the required derivatives of the reaction kinetics.

$$\begin{aligned} A &= \frac{\partial f}{\partial \bar{H}}(\bar{H},\bar{P}), \\ &= -b + \left(\frac{a\bar{H}^{*2} + 2a\bar{\delta}\bar{P}^*\bar{H}^*}{\left(\bar{\delta}\bar{P}^* + \bar{H}^*\right)^2}\right), && (4.42) \\ B &= \frac{\partial f}{\partial \bar{P}}(\bar{H},\bar{P}), \\ &= -\left(\bar{\alpha} + \frac{\bar{\delta}a\bar{H}^{*2}}{\left(\bar{\delta}\bar{P}^* + \bar{H}^*\right)^2}\right), && (4.43) \end{aligned}$$

$$\begin{aligned} C &= \frac{\partial g}{\partial \bar{H}}(\bar{H},\bar{P}), \\ &= \bar{P}^{*}\left(\frac{\lambda}{\left(1+\bar{H}^{*}\right)^{2}}-\frac{2\bar{\alpha}\bar{P}^{*}}{\bar{H}^{*2}}\right), \end{aligned} \tag{4.44}$$

$$\begin{aligned} D &= \frac{\partial g}{\partial \bar{P}}(\bar{H},\bar{P}), \\ &= \frac{\lambda\bar{H}^{*}}{1+\bar{H}^{*}}-(\mu+b+\bar{\alpha}\epsilon)-4\bar{\alpha}\frac{\bar{P}^{*}}{\bar{H}^{*}}. \end{aligned} \tag{4.45}$$

We can insert these expressions for A, B, C, D into (4.29) and investigate numerically how the minimum wave speed s_{Hopf} varies with different ranges of the parameters α and δ. The red line, calculated analytically, in Figure 4.1 is the Hopf bifurcation line for the non-spatial system, namely, $\alpha = b\delta$. The region of the plot under this line is the phase space for $\alpha < b\delta$ where there are limit cycle solutions in the non-spatial kinetics. The shading indicates the predicted minimum PTW speed calculated from (4.33) using (4.42) - (4.45). For increasing values of α ($< b\delta$), the greyscale plot indicates that the minimum speed of the PTW increases and approaches infinity as we approach the non-spatial Hopf bifurcation line. This corresponds to the limiting case of infinite wave speed associated with spatially homogeneous oscillations [83]. Stationary steady states are predicted in the white region above the bifurcation line ($\alpha > b\delta$). We also plot the minimum speed of the periodic plane wave at the Hopf bifurcation, s_{Hopf}, against the parameter α for constant δ (see Figure 4.2). As α approaches the Hopf bifurcation point, from the reaction kinetics, the speed s_{Hopf} tends to infinity (indicated by the vertical dashed line).

To investigate the one parameter family of PTW solutions further, we use the bifurcation analysis package AUTO [19]. We choose a set of parameter values that result in PTW solutions according to the above analysis. The fixed parameter values we choose are given in Table 4.1. For the purpose of this analysis we also choose several combinations of the parameters α and δ from the region of space for which the model predicts PTWs. We then explore how the

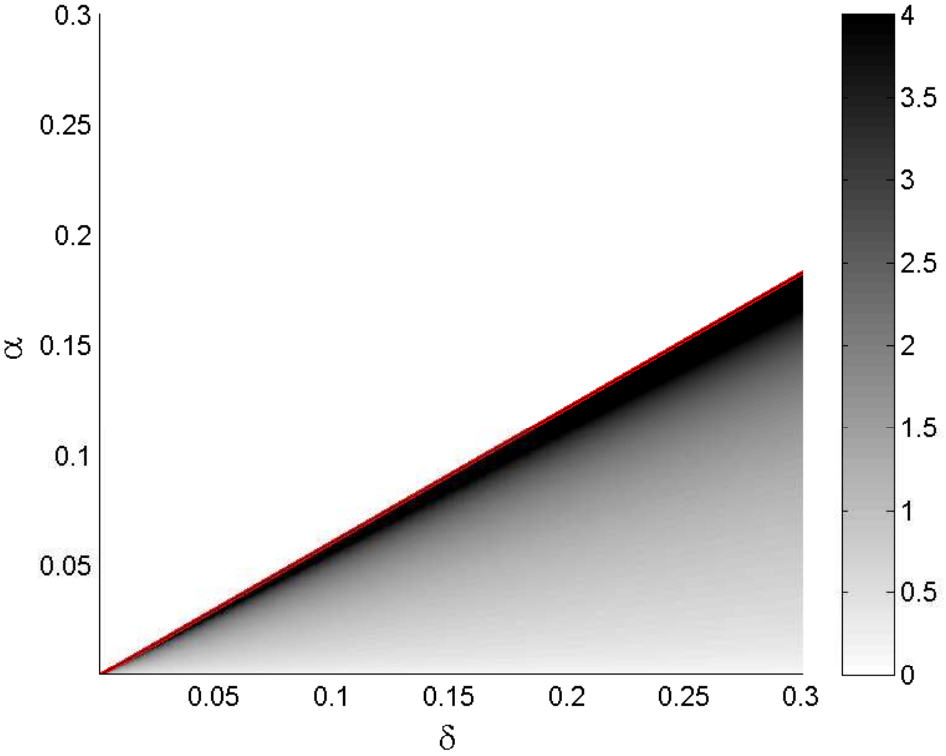

Figure 4.1: Minimum speed, s_{Hopf}, of the periodic plane wave, at the Hopf bifurcation of the ODE system in z, in the α-δ phase plane. The remaining parameters are fixed and the same as in Section 3.3 with $D_H = 0.5$. The shading indicates the predicted minimum PTW speed calculated from (4.33) using (4.42) - (4.45). The red line indicates the Hopf bifurcation line, $\alpha = b\delta$ in the α-δ phase plane. As we approach this line the minimum speed s_{Hopf} approaches infinity. However, in order to illustrate this we choose the finite greyscale range $[0, 4]$.

Parameter	Value
a	1.8
b	0.61
λ	100
ϵ	3.82×10^{-4}
μ	1
D_H	0.5

Table 4.1: Fixed parameter values for AUTO [19] continuation analysis chosen from within the parameter ranges stated in Table 3.2 with the exception of D_H which, in the absence of any data, we take to be equal to 0.5.

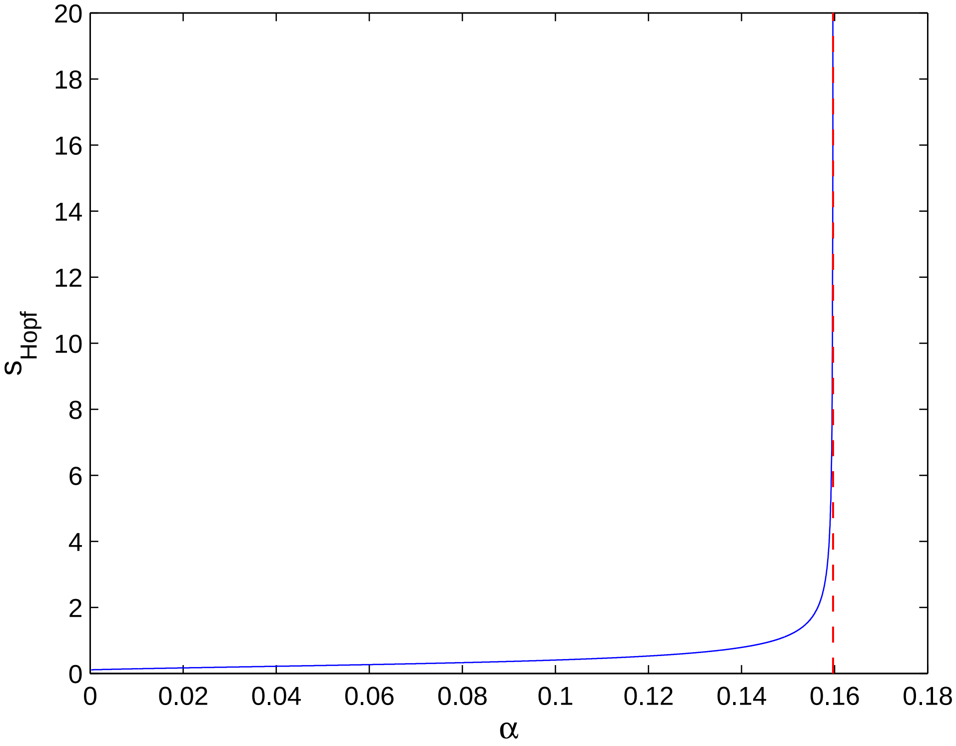

Figure 4.2: The minimum speed of the PTW at the Hopf bifurcation (of the ODE system in spatial variable z), s_{Hopf}, versus α for fixed $\delta = 0.2618$. The vertical dashed line indicates the Hopf bifurcation of the ODE in the reaction kinetics.

amplitude and period of these waves vary as we approach the Hopf bifurcation of the reaction kinetics. These parameter values, their associated steady state solutions (H^*, V^*, P^*) and the Hopf bifurcation value of δ for the given α value, i.e. δ_{Hopf} are listed in Table 4.2.

α	δ	H^*	V^*	P^*	δ_{Hopf}	s_{Hopf}
2	5	0.0237	0	0.0041	3.28	3.02
0.5	3	0.0206	0	0.0083	0.82	1.58
0.0209	0.2618	0.0188	0	0.1058	0.0343	1.19

Table 4.2: Parameter sets for AUTO [19] continuation analysis

We choose firstly $\alpha = 2$ and $\delta = 5$ and starting from the associated steady state solution and a small value for PTW speed, we increase s keeping all other parameters fixed to track the birth of limit cycles, which occurs at $s_{\text{Hopf}} = 3.0235$ in this case. Then starting from this speed and keeping α fixed we vary δ towards δ_{Hopf} of the non-spatial system and track the speed s of the PTWs and their period. An example of the results can be seen in Figure 4.3. This figure displays the family of PTW solutions associated with this parameter set.

We then select a particular speed from this family of PTWs (in the example shown, we choose $s = 52.566$) and with α and s fixed we alter δ and track the effect on the amplitude and period of the associated wave as δ approaches δ_{Hopf} of the non-spatial system. We carried out this procedure for two other values of α (indicated in Table 4.2) and all of the results are depicted in Figure 4.4. This figure illustrates that the wave amplitude decreases to zero as δ approaches the Hopf bifurcation value for the reaction kinetics, δ_{Hopf}, and the period tends to some limiting value which is dictated by the speed which gives rise to the onset of the oscillatory solution, s_{Hopf}. Importantly, this indicates that the oscillations die out in the spatially extended system at the same parameter values as in the non-spatial system. Therefore, cycles are still predicted in the same parts of parameter space and, therefore, only predicted using parameters which produce

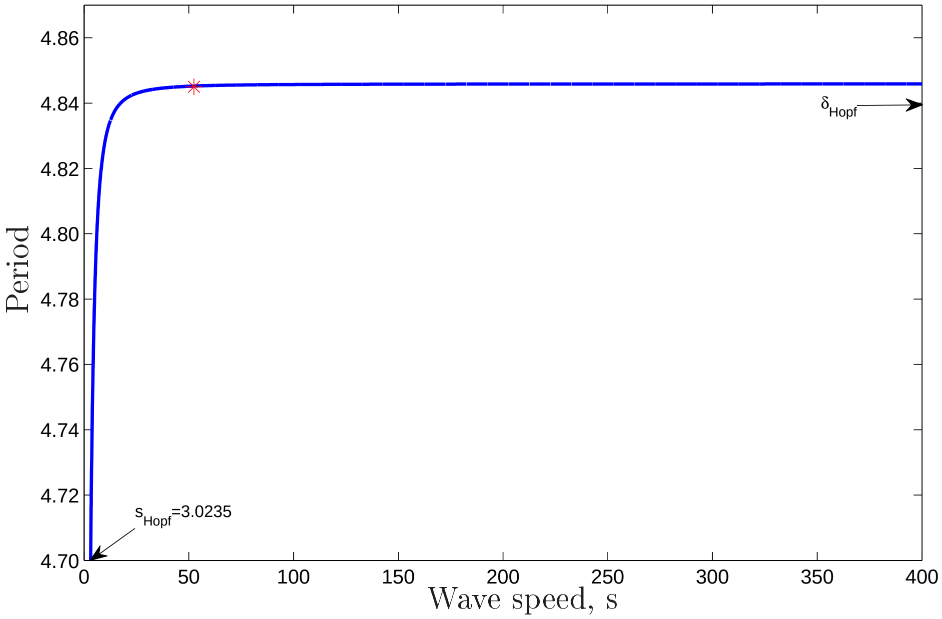

Figure 4.3: Tracking wave speed and period of associated PTW solutions when $\alpha = 2$ and δ is varied from $\delta = 5$ towards $\delta_{\text{Hopf}} = 3.28$. As $\delta \to \delta_{\text{Hopf}}$ the wavespeed tends to infinity and the period approaches a constant value. The red marker indicates the chosen speed, $s = 52.566$ which we then employ in the continuation shown in Figure 4.4.

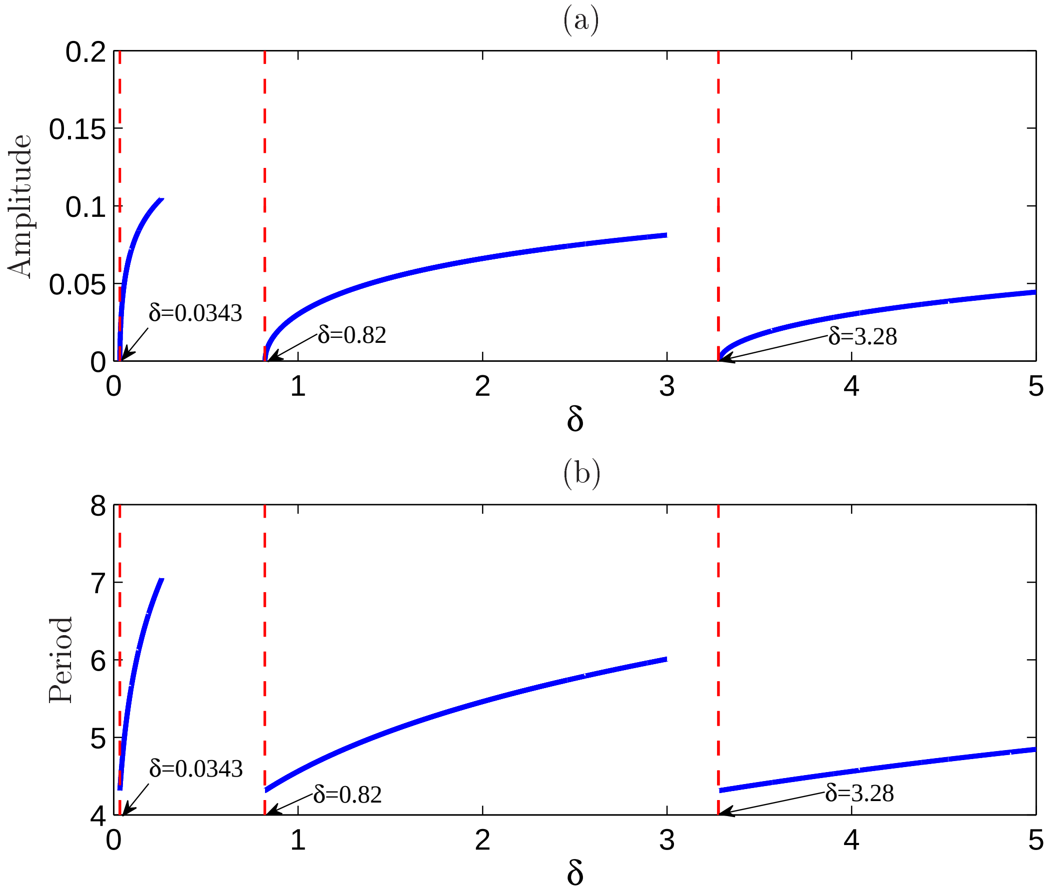

Figure 4.4: Continuation plots produced by AUTO [19] for three combinations of α and initial value of δ. The period and amplitude of the PTW solutions are tracked, in (a) and (b) respectively, as δ tends from the value given in Table 4.2 to the associated Hopf bifurcation value δ_{Hopf} of the non-spatial system. In each case, as δ tends to δ_{Hopf}, the amplitude of the PTW goes to zero and the period tends to some limiting value.

unrealistic parasite burdens as found initially by Townsend *et al.* in [97]. Thus, the key missing factor in this host-parasite system appears not to be spatial variations in host-parasite densities, although, landscape heterogeneity or non-Fickian diffusion terms may yield different results.

Considering the PTWs for the parameter set and initial/boundary conditions as illustrated in Figures 3.11 and 3.12 we can calculate the predicted minimum wave speed for the one parameter family of PTW solutions. The s_{Hopf} given by (4.29) is 0.78km/yr. It is important to note that this minimum speed for the family of PTW solutions for this parameter set does not take into account the initial and boundary conditions and it is therefore not surprising that the wave speed measured in Figure 3.11 is 1.2km/yr, that is, it is greater than s_{Hopf} as expected.

4.4 Red grouse, trichostrongylus tenuis system

The mountain hare-parasite system, described and studied in the previous section, predicts PTW solutions for the theoretical reaction advection diffusion model. Although spatiotemporal oscillations are observed in the field data, there is no concrete evidence to suggest that the parasites are driving the oscillations in this particular system. In the Red grouse system, however, there is evidence that points to the parasites as drivers of the spatiotemporal oscillations observed [39].

The red grouse population has been extensively studied for many years due to its status as a game bird on Scottish estates and there is a plethora of data regarding population densities of this species and its associated parasite, *Trichostrongylus tenuis*, gathered from many land managed estates in Scotland. This spatio-temporal field data demonstrates asynchronous cycles in space for both of these populations [59]. For this reason, we want to apply our generic result to this well established system to see if the model predicts PTW solutions that reflect those observed in the field. In addition, non-spatial mathematical models of this system do indeed predict limit cycle solutions about an unstable steady state in the associated reaction-kinetic equations.

A number of grouse species, including *Lagopus lagopus scoticus* are known to exhibit cyclic fluctuations in population densities where factors such as predation, food, cover and shooting mortality are not thought to be driving these cycles [59]. Dobson and Hudson [39] proposed three possible parasite induced components causing this behaviour, the parasite being *Trichostrongylus tenuis*. They hypothesised that 'reduced host breeding production, a low degree of aggregation of parasites with the host population and developmental time delays due to larval arrestment' were the causative factors for the population cycles observed in the grouse population [39]. A second theoretical paper by these authors [18] deals with the developement of a series of non-spatial reaction kinetic models to illustrate and predict this cyclic behaviour of the red grouse system.

Similarly to the life cycle of *Trichostrongylus retortaeformis* in the mountain hare, the parasite, *Trichostrongylus tenuis*, inhabits the large caecum of the red grouse where it reproduces; eggs are then passed in the red grouse faeces. Under the right conditions, the eggs hatch and the larvae migrate to the growing tips of heather which constitute the main food plant for foraging red grouse. In this way, the larvae enter the caecum of the red grouse and the cycle continues. The infective larvae that migrate from the passed faeces to the tips of heather are known as the free living parasite stage.

4.4.1 Reaction kinetics

A number of theoretical models, with different properties, were defined and explored by Dobson and Hudson [18]. We choose their third model which includes a density dependent term, gH, in the host rate equation, to model the territorial behaviour of the red grouse. This particular model was chosen as this extra term is thought to reduce the propensity for unstable cycles and limit the size of the host population [18]. The model has three rate equations for the red grouse host population, H, adult parasite population, P, and the free living parasite, W:

$$\begin{aligned}
\frac{dH}{dt} &= (a-b-gH)H-(\alpha+\delta)P, && (4.46)\\
\frac{dW}{dt} &= \lambda P-\gamma W-\beta WH, && (4.47)\\
\frac{dP}{dt} &= \beta WH-(\mu+b+\alpha)P-\alpha\frac{P^2}{H}\left(\frac{k+1}{k}\right), && (4.48)
\end{aligned}$$

and the parameter set used by Dobson and Hudson [18] is described in Table 4.3. The introduction of a separate rate equation for the free living parasite, W, is one approach used to model the effects of a developmental time delay in the ecological system. The time delay occurs between the production of the transmission stage (i.e. free living larvae) and its readiness for reinfection [56]. Here, the third rate equation in W follows the dynamics of the free living infective stages. The rate of production of infectives is given by λP. A proportion of these, βWH, will be taken up into the host, where β determines the rate at which the host picks up infective stages and is assumed to be proportional to the density of both hosts and free living stages; the remainder, γW represents the loss of infective stages due to any process that prevents host reinfection, including death of free larvae due to harsh environmental conditions, for example. The adult parasite population density, P, is the population residing in the caecum of the red grouse. The free living parasite stage, W, are the larvae that have hatched and migrated from the passed faeces to the tips of heather. Under optimal conditions, the life span of the free living larval stage, W, is roughly seven days [39] which is relatively short compared to the life span of the host population. Therefore we can apply the following quasi steady state assumption for W, namely $dW/dt = 0$, thereby reducing the three equation system to two equations and enabling us to apply our generic two-variable result of Section 4.2. Thus, (4.47), gives the

Symbol	Parameter	Unit	Value
a	Intrinsic fecundity of adult grouse	yr^{-1}	1.8
δ	Parasite reduced induction in grouse fecundity	$P^{-1}\mathrm{yr}^{-1}$	0.000388
b	Intrinsic mortality of adult grouse	$\mathrm{yr}^{-}1$	1.05
α	Parasite-induced grouse mortality	$P^{-1}\mathrm{yr}^{-1}$	0.000300
λ	Parasite fecundity	$\mathrm{yr}^{-}1$	11
γ	Mortality of free living parasite stages	yr^{-1}	13
β	Transmission rate	$H^{-1}\mathrm{yr}^{-1}$	0.1
μ	Adult parasite mortality	yr^{-1}	1.0
k	Degree of overdispersion		1.0
g	Density dependent coefficient		0.002

Table 4.3: Parameter values chosed from ranges quoted by Dobson and Hudson in Table 2 of their paper [18], where H denotes host and P denotes parasite. We have chosen δ in order that PTW solutions can be illustrated. The density dependent coefficient, g, was based on information in Hudson *et al.* [38].

following expression for W in terms of H and P

$$\begin{aligned} \lambda P - \gamma W - \beta W H &= 0, \\ \Rightarrow W &= \frac{\lambda P}{\gamma + \beta H}. \end{aligned} \tag{4.49}$$

Substituting for W into (4.48) then yields the following two equation system,

$$\frac{dH}{dt} = (a-b)H - (\alpha+\delta)P - gH^2, \tag{4.50}$$

$$\frac{dP}{dt} = P\left[\frac{\lambda H}{H_0 + H} - (\mu + b + \alpha) - \alpha\frac{P}{H}\left(\frac{k+1}{k}\right)\right], \tag{4.51}$$

where we set $H_0 = \gamma/\beta$. We now (for convenience) rescale the system according to $H = H_0\bar{H}$, $P = P_0\bar{P}$, where $P_0 = (a-b)H_0/(\alpha+\delta)$ so that

$$\frac{d\bar{H}}{dt} = (\bar{H} - \bar{P}) - c_4\bar{H}^2, \tag{4.52}$$

$$\frac{d\bar{P}}{dt} = \bar{P}\left[\frac{\lambda\bar{H}}{1+\bar{H}} - c_2 - c_3\frac{\bar{P}}{\bar{H}}\right], \tag{4.53}$$

where we write $c_2 = (\mu + b + \alpha)$, $c_3 = \alpha(a-b)k'/(\alpha+\delta)$, $c_4 = g\gamma/\beta(a-b)$ and $k' = (k+1)/k$.

4.4.1.1 Global behaviour

We now perform a nullcline analysis to get a qualitative understanding of the global behaviour of this non-spatial system. The results of our nullcline analysis are shown in Figure 4.5 and indicate the possibility of limit cycle solutions which are confirmed by a numerical parameter continuation performed in AUTO [19] (shown in Figure 4.6). In Figure 4.5, the steady state solutions, which are determined in the following section, are descibed by

$$
\begin{aligned}
(\bar{H}_1^*, \bar{P}_1^*) &= (0,0), & (\bar{H}_2^*, \bar{P}_2^*) &= (c_2/(\lambda - c_2), 0),\\
(\bar{H}_3^*, \bar{P}_3^*) &= (\bar{H}_3^*, \bar{H}_3^*(1 - c_4 \bar{H}_3^*)), & (\bar{H}_4^*, \bar{P}_4^*) &= (1/c_4, 0).
\end{aligned}
$$

where $(\bar{H}_3^*, \bar{P}^*)$ is the positive solution given by (4.55) and (4.60).

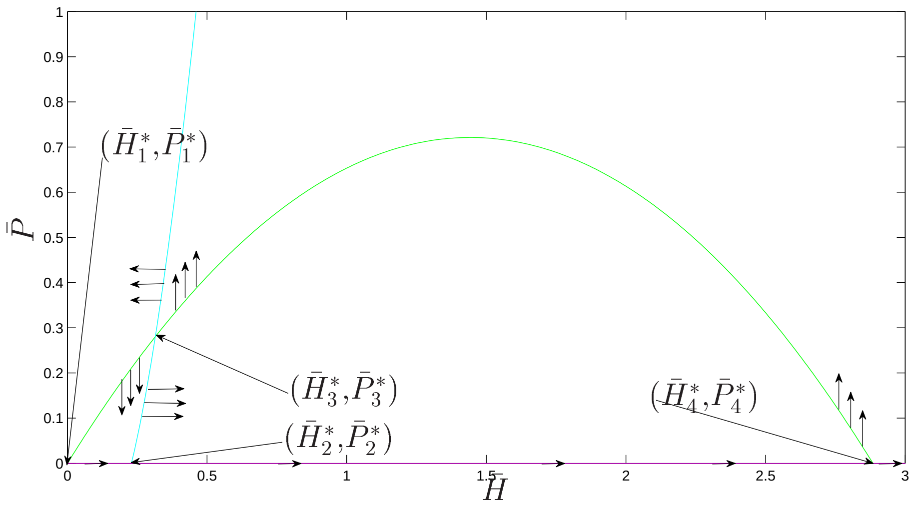

Figure 4.5: The $\bar{H}$ (green line) and $\bar{P}$ (cyan line and magenta line) nullclines plotted in the $\bar{H} - \bar{P}$ plane; the arrows on the $\bar{H}/\bar{P}$ nullclines show the direction of the rate of change of $\bar{P}(t)$ and $\bar{H}(t)$ with time, respectively. The $\bar{H}$ axis is the trivial $\bar{P}$ nullcline. The arrow configuration indicates the possibility of limit cycle solutions. The parameters can be found in Table 4.3.

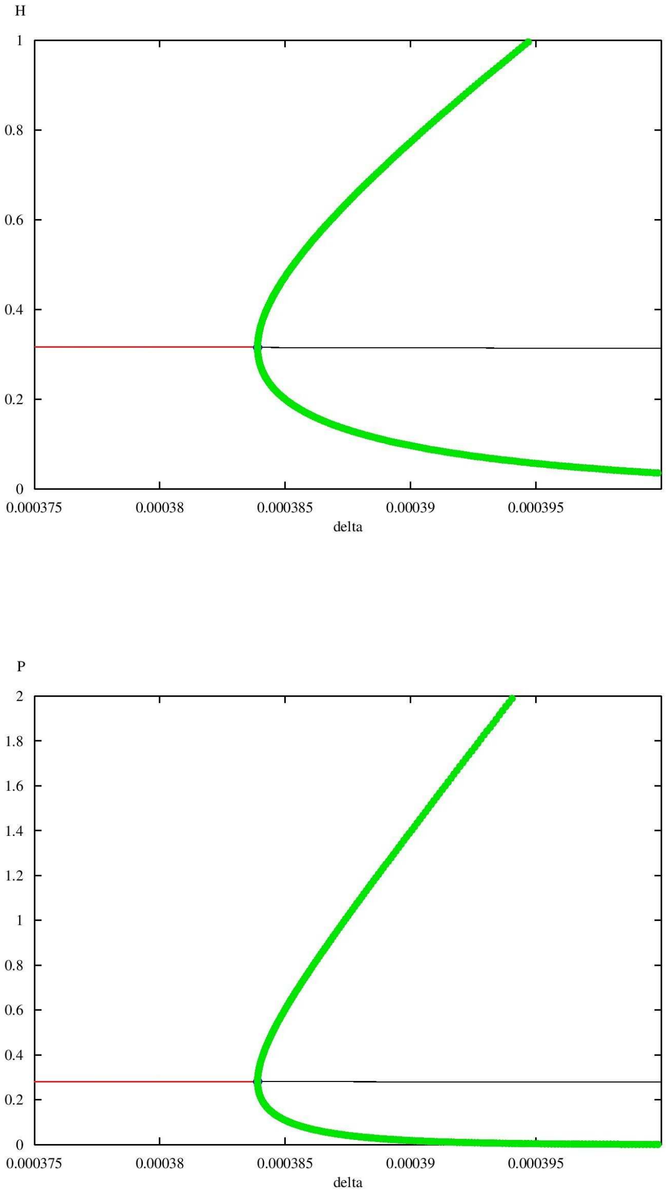

Figure 4.6: AUTO [19] plot of scaled host population density, $\bar{H}$, and scaled parasite population density, $\bar{P}$ versus δ. $\alpha = 3 \times 10^{-4}$ and all other parameters are as described in Table 4.3. The red line before the Hopf bifurcation indicates that the fixed point steady state solution is stable. Beyond the Hopf bifurcation the steady state solution is unstable, indicated by the black line, and AUTO [19] plots the upper and lower limits of the limit cycle solution. For the upper plot, the scaling factor is H_0 so that, for example, with $\delta = 3.9 \times 10^{-4}$, the host population density oscillates between approximate maximum and minimum values of 83 and 17, respectively. For the lower plot, the scaling factor is P_0 so that, for example, with $\delta = 3.9 \times 10^{-4}$, the host population density oscillates between approximate maximum and minimum values of 14×10^4 and 9.5×10^4, respectively.

4.4.1.2 Steady state solutions

The steady state solutions are determined by setting the rate equations equal to zero,

$$\left.\frac{d\bar{H}}{dt}\right|_{(\bar{H}^*,\bar{P}^*)} = \left.\frac{d\bar{P}}{dt}\right|_{(\bar{H}^*,\bar{P}^*)} = 0,$$

so that, from (4.52)

$$(\bar{H}^* - \bar{P}^*) - c_4\bar{H}^{*2} = 0, \tag{4.54}$$

so that rearranging for $\bar{P}^*$ we have

$$\bar{P}^* = \bar{H}^*\left(1 - c_4\bar{H}^*\right). \tag{4.55}$$

Firstly, this places a restriction on $\bar{H}^*$, to ensure positivity, such that,

$$1 - c_4H^* \geq 0 <=> \bar{H}^* < \frac{\beta(a-b)}{g\gamma}, \tag{4.56}$$

since for this system $(a-b) > 0$ and the remaining parameters are assumed to be positive. Now, from (4.53), we get the trivial steady state solution, $\bar{P}^* = 0$, and the non-trivial steady state solution given by

$$\frac{\lambda\bar{H}^*}{1+\bar{H}^*} - c_2 - c_3\frac{\bar{P}^*}{\bar{H}^*} = 0. \tag{4.57}$$

Substitution of $\bar{P}^*$ from (4.55) into (4.57) then gives,

$$\frac{\lambda\bar{H}^*}{1+\bar{H}^*} - c_2 - c_3\left(1 - c_4\bar{H}^*\right) = 0. \tag{4.58}$$

After rearranging we then get a quadratic in $\bar{H}$:

$$\Phi_A\bar{H}^{*2} + \Phi_B\bar{H}^* + \Phi_C = 0, \tag{4.59}$$

where we define,

$$\Phi_A = c_3c_4, \qquad \Phi_B = (\lambda - c_2) - c_3(1 - c_4), \qquad \Phi_C = -(c_2 + c_3).$$

Grouped parameter	Formula
H_0	γ/β
P_0	$\gamma(a-b)/\beta(\alpha+\delta)$
k'	$(k+1)/k$
c_1	$b\delta/\alpha$
c_2	$\mu+b+\alpha$
c_3	$\alpha k'(a-b)/(\alpha+\delta)$
c_4	$g\gamma/\beta(a-b)$

Table 4.4: Definitions of grouped parameters used in the analysis.

A full list of grouped parameters are given in Table 4.4. The steady state host population solutions are, therefore, simply

$$\bar{H}^* = \frac{-\Phi_B \pm \sqrt{\Phi_B^2 - 4\Phi_A\Phi_C}}{2\Phi_A}. \tag{4.60}$$

The scaled parasite steady state density, $\bar{P}^*$, is then obtained by substituting for $\bar{H}^*$ in (4.55). We then choose the steady state solution that is positive for both $\bar{H}^*$ and $\bar{P}^*$.

4.4.2 Spatial extension of the red grouse system

The generic form of the spatial governing equations,

$$\frac{\partial \bar{H}}{\partial t} = f(\bar{H},\bar{P}) + D_H\frac{\partial^2 H}{\partial x^2}, \tag{4.61}$$

$$\frac{\partial \bar{P}}{\partial t} = g(\bar{H},\bar{P}) + D_H\frac{\partial}{\partial x}\left(\frac{P}{H}\frac{\partial H}{\partial x}\right), \tag{4.62}$$

is the same as the mountain hare-parasite model, in Section 4.3 but the reaction kinetics for the grouse-parasite model are different, so that, now

$$f(\bar{H},\bar{P}) = (\bar{H}-\bar{P}) - c_4\bar{H}^2, \tag{4.63}$$

$$g(\bar{H},\bar{P}) = \bar{P}\left[\frac{\lambda\bar{H}}{1+\bar{H}} - c_2 - c_3\frac{\bar{P}}{\bar{H}}\right]. \tag{4.64}$$

Conversion from the (x,t) system to the wave variable, $z = t - x/s$, means that the results from Section 4.2, for the generic spatial model, can be applied

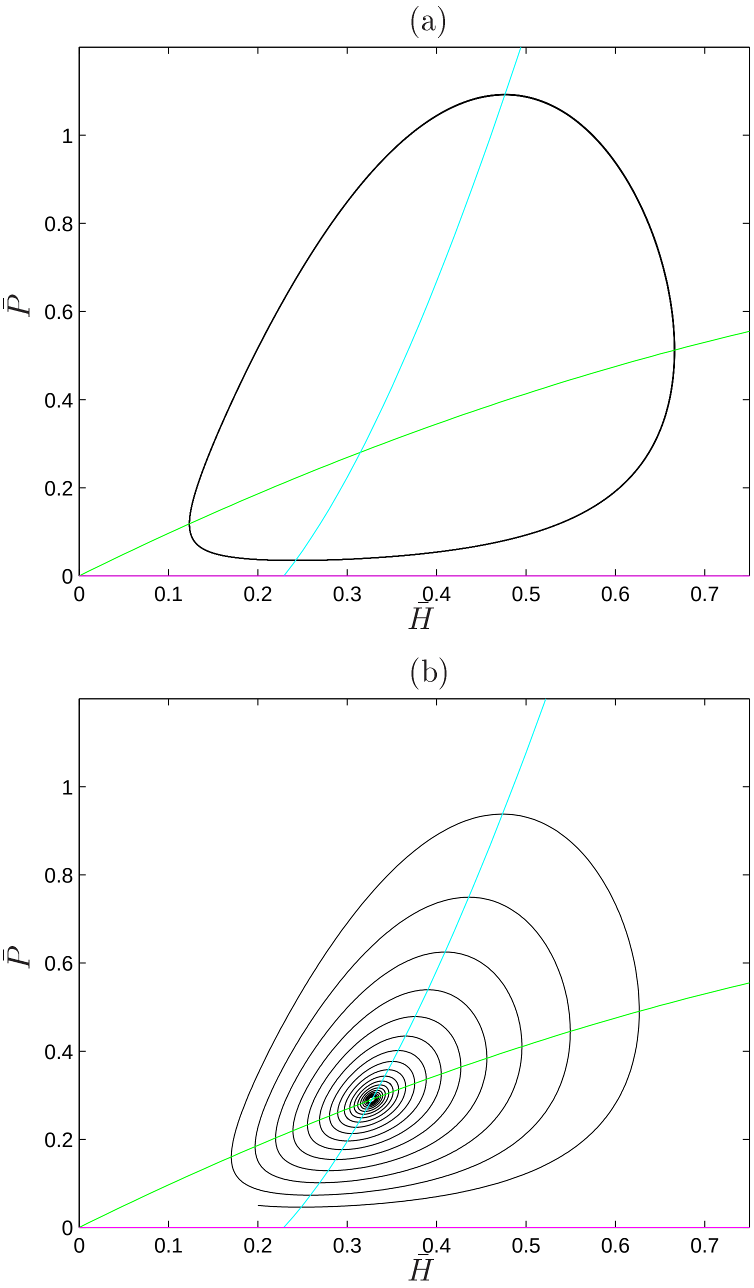

Figure 4.7: Nullcline and phase plane plots for $\alpha = 3 \times 10^{-4}$, with (a) $\delta = 3.88 \times 10^{-4}$ (limit cycle solution) and (b) $\delta = 3 \times 10^{-4}$ (fixed point steady state). The remaining parameters as stated in Table 4.3. The $\bar{H}$ (green line) and $\bar{P}$ (cyan line and magenta line) nullclines are also shown.

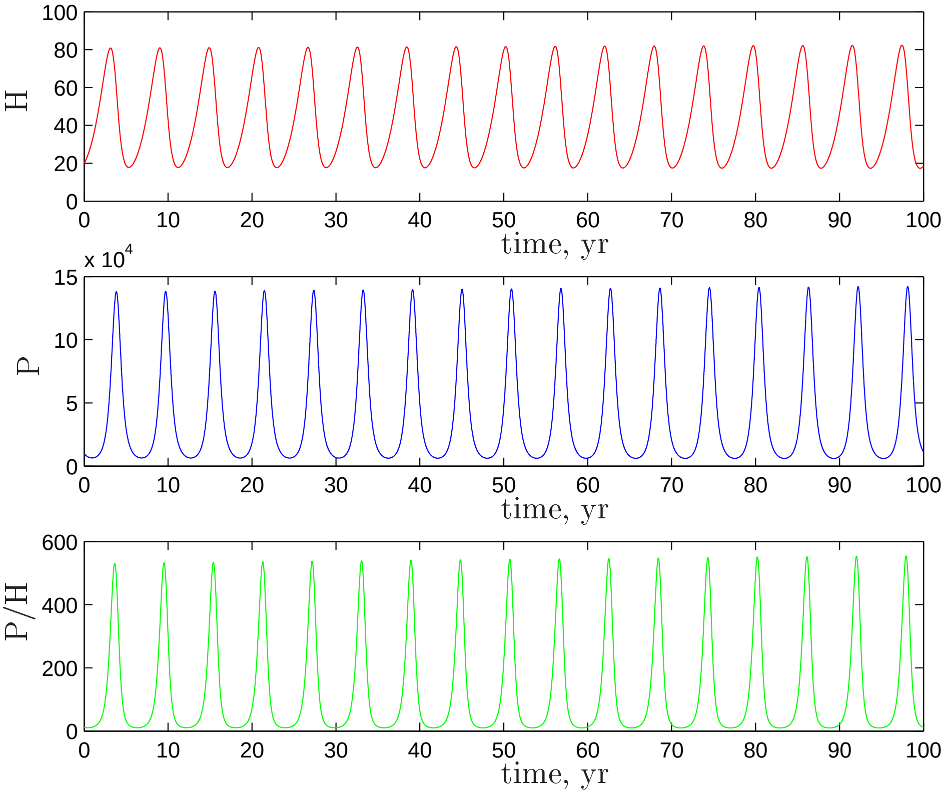

Figure 4.8: Limit cycle solutions of the ODE system described by (4.50)-(4.51) showing how the host, H, and parasite, P, population densities vary with time, as well as the mean (per host) parasite burden P/H. The host population oscillates between minimum and maximum densities of approximately 20 and 80, respectively. Parameter values for this plot are listed in Table 4.3.

directly. The entries for the Jacobian matrix are given by

$$\begin{aligned}
A &= \frac{\partial f}{\partial \bar{H}}|_{(\bar{H}^*,\bar{P}^*)} = 1 - 2c_4\bar{H}^*, && (4.65)\\
B &= \frac{\partial f}{\partial \bar{P}}|_{(\bar{H}^*,\bar{P}^*)} = -1, && (4.66)\\
C &= \frac{\partial g}{\partial \bar{H}}|_{(\bar{H}^*,\bar{P}^*)} = \left(1 - c_4\bar{H}^*\right)\left[\frac{\lambda\bar{H}^*}{(1+\bar{H}^*)^2} + c_3\left(1 - c_4\bar{H}^*\right)\right], && (4.67)\\
D &= \frac{\partial g}{\partial \bar{P}}|_{(\bar{H}^*,\bar{P}^*)} = -c_3\left(1 - c_4\bar{H}^*\right). && (4.68)
\end{aligned}$$

Applying the three conditions, (4.33)-(4.35) presented in Section 4.2 to the above system, and substituting for A, B, C, D, above and the base set parameter values adopted by Dobson and Hudson [18] (see Table 4.3), we have,

Condition I:

$$\begin{aligned}
s^2_{\text{Hopf}} &= (1 - c_4\bar{H}^*)D_H\left(\frac{\left(\frac{\lambda\bar{H}^*}{(1+\bar{H}^*)^2} + c_3(1 - c_4\bar{H}^*)\right) - c_3^2(1 - c_4\bar{H}^*)}{(1 - c_3) + c_4(c_3 - 2)} - 1\right),\\
&= 11.40,
\end{aligned}$$

so that taking the square root gives a minimum PTW wave speed of $s_{\text{Hopf}} =$ 3.38km/yr. Since we have chosen a parameter set that produces a limit cycle solution in the reaction kinetics (see Figure 4.8), the second, (4.34), and third, (4.35), conditions are also satisfied.

Although this parameter set supports the PTWs with $s_{\text{Hopf}} = 3.38$km/yr, we were not able to illustrate them numerically. This is most likely due to the fact that this parameter set is close to the Hopf bifurcation in the ODE system and the resultant PTWs are necessarily of small amplitude. Choosing a value of $\delta = 8 \times 10^{-4}$, that is, further away from the Hopf bifurcation, results in PTWs of higher amplitude which we are able to illustrate numerically in Figures 4.9 and 4.10. In this case Condition I (4.33) gives $s_{\text{Hopf}} = 0.40$km/yr with Condition II and III also satisfied.

Figures 4.9 and 4.10 illustrate a travelling wave front of hosts and parasites, from left to right, which after a period of time is followed by a regular spatiotemporal oscillation over the spatial domain. The wave speed s is calculated to be 0.8km/yr which is greater than the minimum wave speed, s_{Hopf} predicted by Condition I. This is to be expected since Condition I predicts only the minimum wave speed possible for the family of PTWs generated by a given parameter set. It is the initial and/or boundary conditions that will determine which particular 'member' of this family will be chosen as a solution. Having described and illustrated a PTW solution for this system we now discuss wave stability. For any given parameter set, generating a one parameter family of PTW solutions, not all solutions will be stable. Unstable waves cannot be a long term solution and numerical simulations of unstable PTWs indicate irregular spatio-temporal oscillations as the long term behaviour [83]. Behind the regular spatiotemporal oscillations illustrated in Figure 4.9 instabilities gradually grow and overwhelm these waves leading to irregular spatiotemporal oscillations. Sherratt *et al.* [83] have shown that in some cases the instability of the predicted wave is such that they are never seen. This may explain why we were not able to illustrate PTWs for the wave speed solution $s_{\text{Hopf}} = 3.38$km/yr described above.

In this section we have taken a parameter set for this system which is shown to produce a limit cycle solution in the reaction kinetics (i.e.those generating the temporal oscillations shown in Figure 4.8) and applied the generic PTW conditions previously described, which predict the presence and properties of the PTW solution associated with the spatially extended system.

4.5 Discussion

We have used a result derived by Koppell and Howard [45] for a two population, cyclic system with a supercritical Hopf bifurcation in the reaction kinetics. Koppell and Howard derived their result for a spatially extended generic predator - prey reaction kinetic system where Fickian diffusion is used to describe the independent population dispersal of both species. A condition of their result

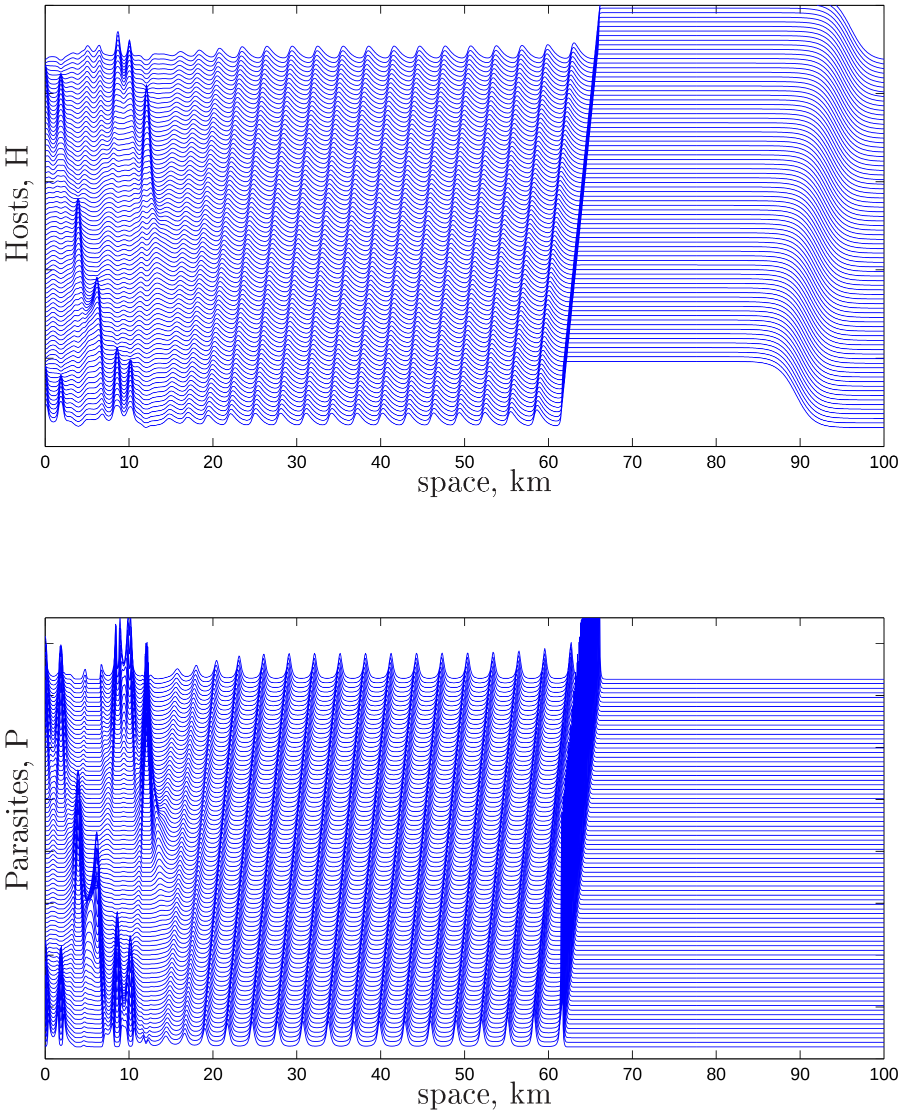

Figure 4.9: The solutions H and P plotted as a function of space x at successive times t, from $t = 117$yrs to $t = 125$yrs, for the generic governing system (4.61) - (4.62) with reaction kinetics described by (4.63)-(4.64). The vertical separation of solutions proportional to the time interval. The parameter values are listed in Table 4.3 with the exception of $\delta = 8 \times 10^{-4}$ and $D_H = 0.03$. The initial conditions are given by $H(0) = 0.78H_0 \exp(-\xi x)$, $P(0) = 0.28P_0 \exp(-\xi x)$, where $\xi = 1$, and the grouped parameters H_0, P_0 are described in Table 4.4. Zero flux boundary conditions at each boundary are imposed for both populations. The host population density oscillates between a minimum of approximately 20 and maximum of approximately 80 as can be seen in Figure 4.10.

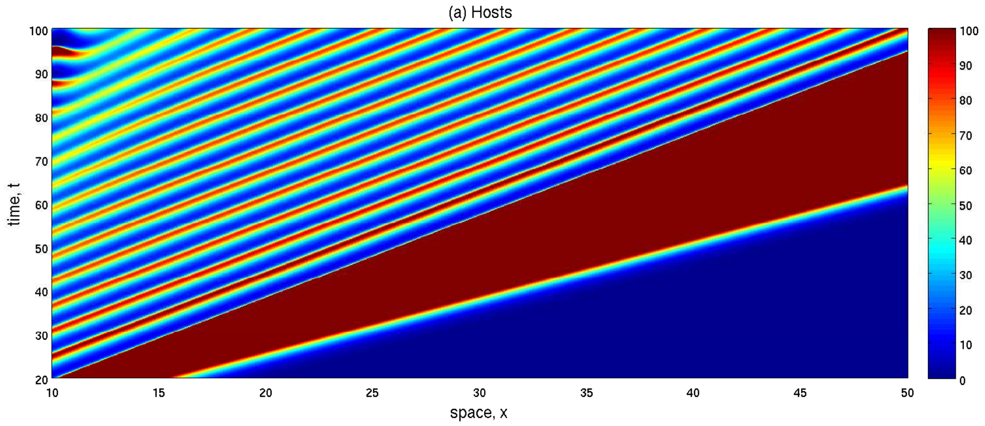

(a) Hosts

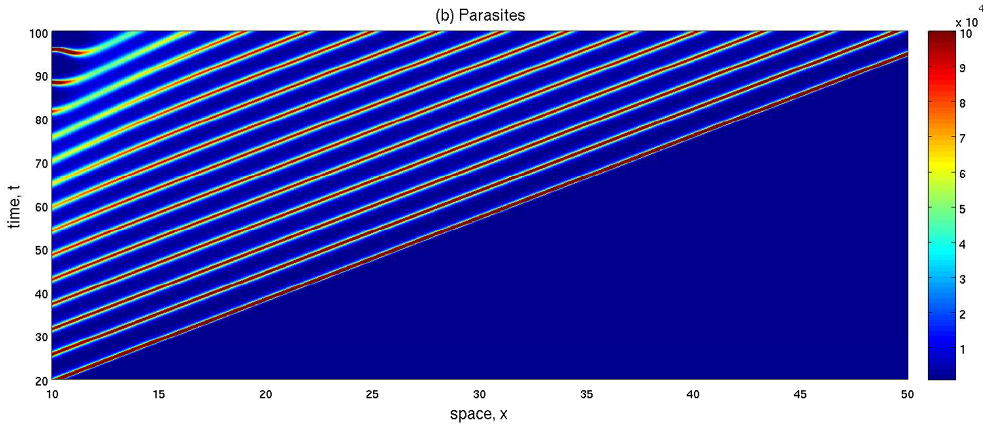

(b) Parasites

Figure 4.10: Colour plot illustrating the peaks and troughs of (a) the host population density, H, and (b) the parasite population density, P, across the space-time plane. The generating system and parameterisation, boundary and initial conditions are as described for Figure 4.9.

was that the diffusion coefficients for each population had to be similar. Our analagous result pertains to a cyclic host-parasite system with a supercritical Hopf bifurcation in the reaction kinetics and assumes that the parasite population lives on or in the host population and travels with the same host velocity. Therefore, the spatially extended system is described by a single diffusion coefficient. We have derived three equivalent conditions on the reaction kinetics of the associated temporal system that are predictors of PTWs in the spatially extended system. This is the first time that such a result has been proposed for a host-parasite system.

We went on to test this new result on two specific host-parasite systems that are of particular interest. The first is the mountain hare-*Trichostrongylus retortaeformis* system and the second is the red grouse-*Trichostrongylus tenuis* system. Cyclical oscillations in host/parasite numbers in both systems have been reported in the field [43]. Townsend *et al.* [97] showed that a reaction kinetic model for the mountain hare-parasite system can predict limit cycle solutions. However, the parameter set used to generate these solutions resulted in unrealistic parasite burdens and it was not possible therefore to conclude that it was the parasites that were inducing such cycling in the mountain hare population. We investigated the effect of spatially augmenting this system on the oscillatory behaviour observed and sought to ascertain whether or not the spatially heterogeneous system resulted in oscillations for more realistic parasite burdens or for a wider range of system parameters. Comparison of Figures 3.9 and 4.1 shows that the emergence of PTWs with a finite minimum speed, s_{Hopf}, occur only in the $\alpha - \delta$ plane bounded by the line $\alpha = b\delta$. This coincides exactly with the limit cycle solutions observed in the reaction kinetics which are also contained by the same Hopf bifurcation line in the $\alpha - \delta$ plane (see Figure 3.9). The continuation analysis performed using AUTO [19] in Section 4.3 confirms this result and Figure 4.4 shows that the amplitude of the PTW tends to zero as the $\alpha - \delta$ parameter set approach their Hopf bifurcation values. We conclude, therefore, that the spatial augmentation, that we have considered, of the mountain hare-parasite system does not alter the parameter set displaying oscillatory behaviour.

The red grouse-*Trichostrongylus tenuis* system has been the subject of extensive study over the years given its position as Britain's favourite game bird [98]. Field data pertaining to this species is much more prolific than that of the mountain hare due to its commercial importance and a number of theoretical studies have shown that the red grouse-parasite reaction kinetics are responsible for the oscillations observed in the field [18]. To date though, no spatial extension of this temporal model has been proposed or investigated. The models suggested by Dobson and Hudson [18] are three population models describing the reaction kinetics of the host, the adult parasite and the parasite larvae. We make a quasi steady state assumption for the parasite larvae thus reducing the system to a two population model and then apply our spatial extension and generic result. Numerical analysis of the spatially extended simplified two population system predicts PTWs for the parameter sets used in [18]. This is the first time that a spatial system has been proposed for the red grouse-parasite system and the first time PTWs have been predicted as solutions to the system. We were then able to take the generic result derived via the Koppell and Howard [45] analysis and use it to test for PTW solutions for this parameter set.

We illustrated PTW solutions for both the mountain hare and red grouse systems. The mountain hare system exhibited a wave speed of 1.2km/yr and the red grouse system a wave speed of 0.8km/yr. These are not unrealistic values given that the range of wave speeds observed empirically in other dynamic systems varies greatly. For example, Lambin *et al.* [47] reported a wave speed of 19km/yr in the field vole population in Kielder Forest. Recent studies on the dynamics of larch budmoth populations show that these cycles organise into travelling waves with speeds of approximately 250km/yr [83]. At the slower end of the scale Moss *et al.* reveal travelling waves in red grouse population abundance, in Scotland, moving at speeds of 2-3km/yr. The minimum possible wave speeds of the wave family predicted by our mathematical models, s_{Hopf}, depend on the parameterisation of the system; the wave speeds of the particular numerical solutions illustrated are dictated by the initial and boundary conditions and we cannot predict them analytically for these systems. Currently there are no published results on PTW wave speeds measured in the field for the Scottish mountain hare, however, the results produced here give some indication of the potential wave speeds that may be observed and could be used to direct the structure and scope of future field studies on the Scottish mountain hare.

Chapter 5

Conclusions and Further Work

5.1 Conclusions

One of the main aims of this work was to investigate the spatially heterogeneous mountain hare-*Trichostrongylus retortaeformis* system to see if this extension of the temporal reaction kinetic model resulted in oscillatory behaviour for a wider parameter phase space and more realistic parasite burdens than the kinetic model alone. However, the results of our analysis show that the oscillatory behaviour is only exhibited where the temporal kinetics contain limit cycle solutions. The amplitude of the temporal oscillations is only slightly lower in the spatial case and the period remains the same.

A result was derived that is applicable to general two population host-parasite reaction advection diffusion systems. This result is analagous to the Koppell and Howard [45] result for predator-prey systems and pertains to the spatial augmentation of the reaction kinetic model, where a diffusion term models host dispersal in the environment and parasite movement is governed by an advection term. The new result predicts the presence of PTW solutions in the spatial model given a particular parameterisation of the reaction kinetics. If PTWs are possible, the calculated value, s_{Hopf}, gives the minimum speed possible for an emerging PTW.

A second host-parasite system of interest was the red grouse-*Trichostrongylus* *tenuis* system. A three population model proposed by [18] was reduced to a two population model via a quasi steady state assumption, and diffusion and advection terms were added for the host and parasite populations, respectively. Our generic result was then applied to a particular parameterisation of the system and a finite minimum wave speed for emerging PTWs was predicted. PTWs were plotted using this same parameterisation. This is the first time PTWs have been illustrated in a theoretical model of the red grouse-*Trichostrongylus tenuis* system.

5.2 Further Work

We propose the following avenues for further investigation. For the mountain hare-parasite system it may be worth modelling the free larvae as a separate population. In Chapters 3 and 4 we made a quasi steady state assumption for the free living larvae stage, which is valid under favourable environmental conditions. However, larvae development may be retarded under harsher environmental conditions, for example, and the time delay for parasite development is no longer short in comparison with changes in host population density changes. Inclusion of a free living parasite population in the mountain hare-*Trichostrongylus retortaeformis* system is analagous to the three population red grouse-parasite models proposed by [18]. In both the spatial mountain hare and red grouse models numerical analysis could be performed in order to find parameterisations yielding PTW solutions. It may be possible to extend the result obtained for the general two population cyclic reaction advection diffusion model to a three population system. This would provide a more realistic model than the two population model derived by assuming a quasi steady state for the parasite larvae.

Another area of interest for the mountain hare model, originally developed by Townsend *et al.* [97], is the parameter values proposed for the system. They suggested that some of the parameter values chosen were based on small sample sizes or indirect data sources [97]. It would be useful if more studies could be carried out to obtain more confidence in the kinetic parameters.

Seasonal and climatic changes have also been shown to be driving mechanisms for spatiotemporal oscillations [83] via temporal oscillations in parameters associated with the system. For example, in the mountain hare system, Newey *et al.* [63] demonstrated in their empirical data that the degree of aggregation of the parasite population in the host population, described by the parameter k, varied from month to month. A model that incorporated this form of seasonal variation in the parameter k would be of interest.

Although we have illustrated numerical PTW solutions for two host-parasite reaction advection diffusion models we have said nothing about the stability of these solutions. It is worth striving to obtain an analytic expression to describe the stability of emerging PTW solutions as well as studying the effect of the boundary and initial conditions on the PTW speed observed.

Chapter 6

Introduction: Functionally graded polymer foams

6.1 Background and motivation

An empirical method developed by Torres Sanchez *et al.* [93] for designing bone scaffolds uses acoustic irradiation of a reacting polyurethane foam to tailor the porosity profile within the final cured sample. The aim of this section of the thesis is to present the first attempt at modelling mathematically some of the mechanisms involved in this complex reaction. In Chapter 7 we look at the effect of inertia on the growth of a single bubble within an Oldroyd B fluid. This effect would be of interest if considering mass transfer of gas into the bubble, from the surrounding liquid, by rectified diffusion [13]. In Chapter 8 we are interested in the direct effect of the acoustic pressure amplitude of the irradiating standing wave on the bubble growth dynamics of a single bubble. We then consider the indirect effect of the acoustic pressure amplitude on the local reaction rate within the sample and the bubble distribution profiles observed within a multibubble distribution across the sample. The aim is to compare the results from the mathematical model with the experimental observations of Torres Sanchez *et al.* [93] that as the pressure amplitude increases across the sample domain, the porosity increases, that is the bubble size increases.

6.1.1 Tissue Engineering

Generally tissue engineering involves the combination of living cells and a scaffold or support structure [29]. Progenitor cells are seeded onto the scaffold which then slowly degrades as the tissue structure grows [12]. This technique can be used to replace portions of, or whole tissues, for example, bone, blood vessels, bladder etc [29,40,55]. In this particular case we are interested in the production and structure of bone scaffolds which will ultimately be used to replace bone tissue. Bone is a natural structure exhibiting a functionally graded porosity, being fairly dense on the periphery and more porous at its centre [8]. This heterogeneous porosity is one of the factors giving this structure its strength and functionality, and in the area of tissue engineering it is a feature we would like to mimic [93]. The best grafts and bone substitutes are thought to be those with biomechanical and biological properties most closely resembling the non-uniform graded porosity distribution observed in natural bone [8]. Due to ongoing scientific advances it has been possible to fabricate tissues in the laboratory by combining the use of engineered scaffolds and stem cells with one of the aims of tissue engineering being the incorporation of added functionality and biomechanical stability into these laboratory grown tissues in order to improve the success rate for transplantation [29].

To achieve the goal of tissue reconstruction, scaffolds must meet some specific requirements. There needs to be a balance between larger and smaller pores in the scaffold due to the nature of the roles played by different pore sizes. Larger pores promote better flow transportation of nutrients and metabolic waste while smaller pores provide sufficient surface area for cell attachment and proliferation [12]. Biodegradability is often an essential factor since scaffolds should preferably be absorbed by the surrounding tissues without the necessity of a surgical removal [29].

A number of different approaches to the design and manufacture of bone scaffolds have been reported [12] with some authors using rapid prototyping (RP) to produce novel scaffolds with controllable porosity and channel size that can be achieved by varying processing parameters [105]. Tai *et al.* [90] studied the effect of polymer chemical composition, molecular weight and processing parameters (including temperature and pressure) on the final pore size and structure and demonstrated that the pore size and structure of the supercritical scaffolds can be tailored by careful control of processing conditions.

The method employed by Torres-Sanchez *et al.* [93] that we seek to model involves another empirical approach but this time an acoustic standing wave is used to irradiate a sample of polymerising polyurethane foam with the aim of tailoring the porosity profile of the final sample to a particular porosity specification. Torres-Sanchez *et al.* [93] demonstrated experimentally a relationship between the pressure amplitude of the irradiating sound wave and the porosity value at a given position in the sample. One of the aims of this thesis is to provide the first stages of a mathematical model of this experiment so that in the future scaffolds may be produced with strictly defined and controlled porosity profiles.

6.1.2 Polymer foams

A polymeric foam is a particular example of a viscoelastic, heterogeneous material and such materials have been used widely in a number of fields including biomaterials, tissue engineering and structural mechanics [93]. The polymer foam is composed of at least two phases, one solid plus voids whose size distribution can be varied [93]. They possess a number of properties that make them particularly suited to the field of tissue engineering including their low density, chemical inertness, high wear resistance, biodegradability and thermal and acoustic insulation.

Similar to natural bone, the structure of a foam is characterised by the distribution, size and wall thickness of cells in the bulk material. That distribution has a direct correlation with the mechanical properties of the solid foam. Therefore, when a foamed material's behaviour needs to be engineered, its cellular structure is an obvious starting point. Torres-Sanchez *et al.* [93] demonstrated that it was possible to tailor the porosity profile of a polymerising polyurethane foam by altering its position within an acoustic field. Although this was done empirically, they managed to identify 'sensitive stages' during the reaction where ultrasound was observed to have an impact and hypothesized that this was due to the fact that diffusion and convection were predominant effects during these stages.

The polymerisation reaction is very complex involving bubble dynamics, evolving rheology [26,58], two phases, rectified diffusion [13,14,22,23,51], Bjerknes forces [3,49] and Ostwald ripening [54,75] to name but a few. In addition we want to add ultrasonic irradiation and model its effects as well.

Ultrasonic irradiation of liquids has been shown experimentally to result in a number of unusual phenomena including rectified diffusion and increased reaction rates [31,44,92]. We seek to strip the problem back by making many assumptions and concentrate on the bubble evolution, post nucleation, in a viscoelastic fluid and ignore the effects of rectified diffusion, Bjerknes forces and Ostwald ripening. We look at the direct effect of the ultrasound pressure amplitude on the long term growth of the bubble and not on its oscillatory effects. We do, however, seek to incorporate the effects of inertia into an existing model in order to provide a tool to investigate this oscillatory behaviour in the future.

A number of articles in the literature document the empirical effect observed of ultrasound enhancing the polymerisation reaction rate. Price *et al.* [69] demonstrated an increased polymerisation reaction rate when a reacting polymer sample was irradiated with ultrasound and further demonstrated that increasing the intensity of the ultrasound lowered the reaction time. Although their work was inconclusive they suggest that this effect is due to the 'extremely efficient mixing of the components enhanced by ultrasound'. Torres-Sanchez *et al.* demonstrate a similar effect through their experimental technique using resistivity measurements to monitor reaction progression [92].

6.1.3 Bubble dynamics

Much work has been done to study and model the nucleation [28, 76, 88] and subsequent single bubble growth [7, 24–28, 66, 77, 88, 89, 91, 100] in viscoelastic materials including polymer foams, both reacting [26] and non-reacting [24–27, 106]. The effects of ultrasound on nucleation [107] and subsequent growth of a single bubble via rectified diffusion in an aqueous fluid [50, 53, 61, 70, 71] have been studied extensively. Bubble distributions have been studied with an aim to predict and describe heterogeneous porosity profiles in polymer foam samples [11,66,76,77] but no attempt has been made to tailor the profile directly. The effect of an acoustic field on bubble populations within a non-viscous liquid was studied numerically in [49] but we are not aware of any attempt to model analytically the effect of an acoustic standing wave on a multi bubble distribution in a viscoelastic liquid. Numerical studies have been carried out on the evolving bubble distributions in a polymer foam in the absence of acoustic irradiation [24, 25, 106]. Empirical studies have been done on the effect of ultrasound on the nucleation of bubbles in a polymer foam and the resulting final bubble size distributions [107] but here we seek to look at the effect of ultrasound on bubble growth post nucleation and assume homogeneous bubble nucleation through the sample.

There have been a number of studies of the nucleation and subsequent growth of a single spherical gas bubble in a surrounding fluid due to diffusion of gas through the fluid and into the bubble. Amon and Denson [4] proposed a cell model for the analysis of bubble growth in an expanding polymer foam with each cell containing a spherical gas bubble surrounded by a concentric liquid envelope containing a limited supply of gas. Their model takes account of heat transfer and inertia and couples bubble growth to the changing foam density. Street *et al.* [89] and Ting *et al.* [91] both used the Oldroyd B fluid model to describe the viscoelasticity of the surrounding fluid layer which they assumed to be infinite. This resembles the case of early time foaming where bubble size is small and bubbles are spaced at large distances from each other, remaining spherical and not interfering with each other. They demonstrated that the viscoelasticity of the melt as well as the diffusivity of the gas determined the initial growth rate. Arefmanesh *et al.* [7] considered the case of a spherical gas bubble surrounded by a finite shell of viscoelastic fluid which they modelled using the upper convected Maxwell model. They introduced a Lagrangian transformation to describe the moving bubble/liquid interface and substituted a concentration potential to aid numerical solution. Their model serves to describe the case where a large number of bubbles exist in close proximity to each other which we would expect in an expanding polymer foam. Other authors [76, 77] looked at bubble growth in polymer foams in conjunction with nucleation and concluded that the most sensitive parameters to final bubble size distribution are those associated with nucleation. They conclude that while growth dynamics can alter the distribution this is only a secondary effect. Feng [28] also looks at the effect of nucleation but proposes a model for heterogeneous nucleation and its effect on the final bubble size distribution. Venerus [99, 100] developed and evaluated transport models of diffusion induced bubble growth in viscous liquids of both finite and infinite extent and compared results with Amon and Denson [4] and Arefmanesh *et al.* [7]. Both models agree at early stages of the growth process and differ at later stages when the equilibrium bubble radius is approached for the finite liquid model.

Everitt *et al.* [26], building on the above work, proposed a model to capture the changing fluid rheology and gaseous phase for a reacting polymer foam. The evolving fluid is treated as a multimode Oldroyd B system and the Lagrangian transformation is used to describe the moving bubble boundary with a concentration potential proposed by [7] employed to aid numerical solution near to the liquid/gas boundary. They include an additional equation to model gas produced by the reaction and propose additional terms for the diffusion and mass conservation equations to account for the reaction effects on gas concentration. This reacting polymerisation model contains the majority of the elements that we needed to model the experimental polymerisation reaction that Torres Sanchez *et al.* had published [93], except for the application of ultrasonic irradiation. We, therefore, settled on this model as a foundation for the work in this section of the thesis and manipulate it to model the additional ultrasound effect.

6.2 Overview

This section of the thesis examines two different effects of ultrasonic irradiation on the bubble size distribution in an expanding polymer foam. Chapter 7 seeks to model the effect of inertia on a non-reacting polymer foam, and inner and outer leading order asymptotic solutions are proposed. Chapter 8 presents the first mathematical model of the experiment carried out in the laboratory by Torres-Sanchez *et al.* [93], with an aim to illustrate mathematically the same qualitative effects of an irradiating acoustic signal on the porosity distribution of the final polymerised sample, as observed in the laboratory [93], and to ascertain the magnitude/signifance of this effect, in isolation. The chapters may be summed up as follows:

Chapter 7 presents and expounds a model proposed by Everitt *et al.* [26] for a non-reacting polymer foam. The original model assumed the effect of inertia to be negligible and did not include an acoustic irradiation term. The non-reacting model is re-derived to include inertia as well as an additional term to describe the acoustic pressure amplitude. An assumption of instantaneous diffusion is then made in order to partially decouple the system and an asymptotic analysis is performed so that a leading order outer and first order inner solution are presented. The dependence of the accuracy of the inner asymptotic solution on the surrounding fluid volume is discussed and different approximations are proposed for different regimes. An analytic leading order and first order inner solution are presented for the case when this fluid volume is large and tending to infinity. In the case when it is not, an approximate analytic form is suggested that minimises the error.

Chapter 8 introduces and builds on the model derived by Everitt *et al.* [26] for the expanding single bubble in a free-rising, reacting polymer foam. This numerical model is employed to follow the evolution of a single bubble in a given parameterised system. We look at the indirect effect of ultrasound irradiation on the local reaction rate of the sample and the combined effect of bubble-bubble interaction to explain the heterogeneous bubble distributions observed experimentally in [93]. Details of the experimental set up published by Torres-Sanchez *et al.* [93] are presented and parameter values are derived. A one dimensional multi bubble system is considered and rules for bubble-bubble interactions are proposed. As opposed to Chapter 7, the effect of ultrasound is modelled indirectly through its suggested effect on the reaction rate [69, 92]. The ultrasound signal is modelled by a standing wave function and the localised pressure amplitude is then calculated. This means that single bubble evolution at each spatial point through the sample can be calculated by assuming that the spatially distributed reaction rate across the domain directly correlates with the local pressure amplitude.

6.3 Key contributions

The principal original contributions of the author for this second section of the thesis may be summarised:

- A new mathematical model is derived to describe single bubble growth in a free rising, non-reacting polymer foam irradiated by an acoustic standing wave and incorporating the effects of inertia in Chapter 7.
- Leading and first order asymptotic inner solutions in the temporal domain are presented, in Section 7.5, for the case of instantaneous diffusion. Two scenarios are discussed; the first describes the case when the fluid volume surrounding the bubble is large compared to the bubble volume and the second describes the case when both volumes are of the same order.
- In Section 7.6 the leading order asymptotic outer solution, for the case of instantaneous diffusion, is described analytically using the first iteration of the Picard iteration method. A numerical solution for the leading order outer equation is also presented.
- A first mathematical model of an experiment described by Torres-Sanchez *et al.* [93] is proposed in Sections 8.3 to 8.6. The model isolates the effect of the acoustic pressure amplitude on the local reaction rate of the sample and can be used to illustrate different heterogeneity profiles for final bubble distributions through the sample domain, given an initial homogeneous bubble distribution. A relationship between intial bubble spacing through the sample and the resultant final heterogeneity of the sample is discussed.

Chapter 7

A mathematical model of the growth of a bubble in a non-reacting polymer foam incorporating inertia

A paper written by Everitt *et al.* [26] on bubble dynamics in reacting and non-reacting polymer foams presents two models for individual bubble expansion in curing polymer foams. The first model is for a non-reacting solidifying polymer foam with constant elastic modulus; the second models the gas production due to the reaction and the evolving rheology of the viscoelastic material in the reacting polymer foam. Everitt *et al.* [26] neglect the effects of inertia since parameterisation of the system results in a very small Reynolds number, and their model does not include an acoustic forcing term.

In this chapter the non-reacting model proposed by Everitt *et al.* [26] is extended to include inertia effects and this original derivation is described in detail in Section 7.2. Also included in this model is a term to account for the effects of a standing acoustic wave insonifying the polymerising sample. We derive inner and outer asymptotic solutions in Sections 7.5 and 7.6, respectively.

The model equations are derived by consideration of an Oldroyd B polymeric fluid [103]. Once the governing equations, initial and boundary conditions are obtained, an instantaneous diffusion assumption is made in order to partially decouple the system which is then probed in an effort to derive an approximate analytic solution using asymptotic expansions. An inner and outer asymptotic solution are proposed; the former to first order and the latter to leading order. Two different regimes are investigated for the inner asymptotic solution. In the first case the bubble volume is much smaller than the surrounding fluid volume whereas in the second case these two volumes are assumed to be of the same order. The first instance may describe the situation at early time in the polymerising sample when bubbles have just nucleated and are at large distances from each other so that they are effectively surrounded by an infinite fluid volume. We may assume that the second case describes a regime where the bubbles are larger and more closely packed so that the fluid volume available to each individual bubble is reduced. We discuss the accuracy of the first order asymptotic inner solutions in each regime before deriving a leading order analytic solution for the outer temporal variable. A numerical scheme is produced to test the accuracy of the analytic solution and the limitations of the analytic solution are discussed before using the numerical scheme to predict the effects of changing viscosity and acoustic pressure amplitude on the outer solution.

7.1 Description of non-reacting model

In the non-reacting case a polymeric liquid containing a foaming agent is subjected to a sudden reduction in pressure and foaming commences as the foaming agent comes out of solution [26]. This is a two phase system with the foam considered to be a system of identical, spherical bubbles of gas, each surrounded by a layer of viscoelastic fluid containing a quantity of dissolved gas. The model concerns a single bubble with initial volume, $4\pi u_0/3 = 4\pi R^3/3$, with bubble radius R and initial gas pressure p_{g0}. The fluid surrounding the bubble is assumed to be incompressible, viscoelastic and containing a limited supply of dissolved ideal gas. The initial bubble volume is the volume when the bubble gas pressure is p_{g0} and is larger than the nucleation volume. It is further assumed that the bubble undergoes spherically symmetric expansion driven by the pressure difference across the bubble-fluid interface, $(p_{g0} - p_a)$, where p_a is the ambient gas pressure. The conditions are isothermal and the bubble-fluid interface is in thermodynamic equilibrium [26]. First, the dynamics of the fluid layer are considered; the system is modelled using the Oldroyd B system of equations for a viscoelastic medium [103]. Subsequently, the gaseous phase, its concentration in, and diffusion through, the fluid, and its transport across the bubble-fluid interface are modelled.

7.2 Liquid phase

A solution of polymer molecules in a Newtonian liquid exhibits both viscous and elastic behaviour [104] and can be modelled as an Oldroyd B fluid [103]. This is derived by considering how polymers behave at the microscopic level and then scaling upwards to predict the macroscopic effects. The general governing equations are

$$\begin{aligned} \boldsymbol{\nabla} \cdot \mathbf{q} &= 0, & (7.1) \\ -p\mathbf{I} + \mu\left(\boldsymbol{\nabla}\mathbf{q} + (\boldsymbol{\nabla}\mathbf{q})^T\right) + G(\mathbf{A} - \mathbf{I}) &= \boldsymbol{\sigma}, & (7.2) \\ \rho\left(\frac{\partial \mathbf{q}}{\partial t} + \mathbf{q} \cdot \boldsymbol{\nabla}\mathbf{q}\right) &= \boldsymbol{\nabla} \cdot \boldsymbol{\sigma}, & (7.3) \\ \frac{\partial \mathbf{A}}{\partial t} + (\mathbf{q} \cdot \boldsymbol{\nabla})\mathbf{A} - \mathbf{A} \cdot \boldsymbol{\nabla}\mathbf{q} - (\boldsymbol{\nabla}\mathbf{q})^T \cdot \mathbf{A} &= -\frac{1}{\tau}(\mathbf{A} - \mathbf{I}). & (7.4) \end{aligned}$$

where $\mathbf{q}$ is the velocity vector, $\boldsymbol{\sigma}$ is the stress tensor, μ is the solvent viscosity, ρ is the fluid density, G is the relaxation modulus associated with the polymer stress, $\mathbf{A}$ the orientation tensor, $\mathbf{I}$ the identity matrix and τ represents the relaxation time of a polymer molecule.

Substituting for $\mathbf{q} = q_r\mathbf{e}_r + q_\theta\mathbf{e}_\theta + q_\phi\mathbf{e}_\phi$ into the continuity equation (7.1) and

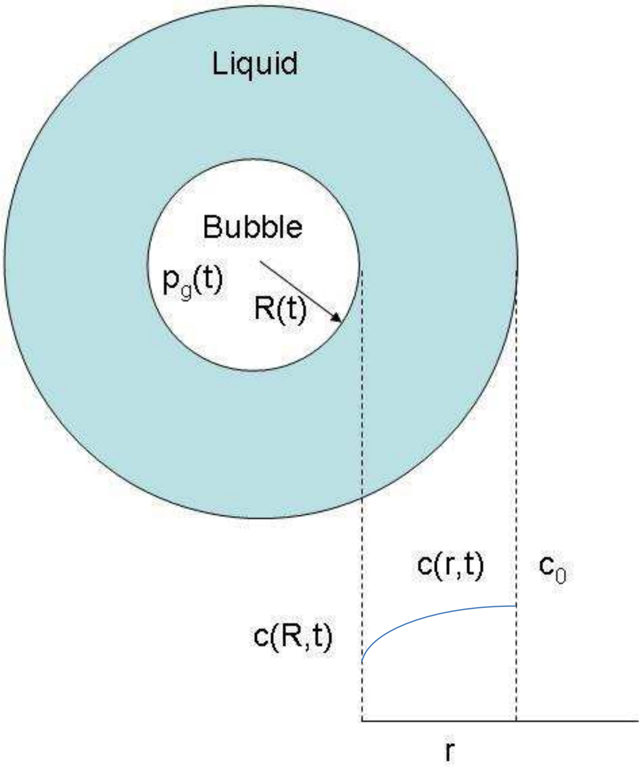

Figure 7.1: Schematic illustrating an expanding single bubble in a finite liquid volume. The bubble radius is denoted by $R(t)$ and the bubble gas pressure by $p_g(t)$. The gas concentration at the bubble surface is $c(R,t)$; the concentration profile within the liquid, $c(r,t)$ depends on time t and the radial co-ordinate r where the origin is at the bubble centre. The concentration at the outer fluid boundary is given by the constant c_0.

expressing the divergence of the velocity vector, $\mathbf{q}$, in spherical polar co-ordinates gives

$$\begin{aligned} \nabla \cdot \mathbf{q} &= \frac{1}{r^2}\frac{\partial}{\partial r}(r^2 q_r) + \frac{1}{r\sin\theta}\frac{\partial}{\partial\theta}(\sin\theta q_\theta) + \frac{1}{r\sin\theta}\frac{\partial q_\phi}{\partial\phi}, \qquad (7.5) \\ &= \frac{1}{r^2}\frac{\partial}{\partial r}(r^2 q_r), \qquad (7.6) \end{aligned}$$

since the spherically symmetric bubble expansion means $q_\theta = q_\phi = 0$ and q_r is dependent on r and t only. Therefore,

$$\frac{\partial}{\partial r}(r^2 q_r) = 0 \qquad \text{for } r \geq R, \qquad (7.7)$$

where R is the radial co-ordinate of the bubble-fluid interface. Integration with respect to r gives $r^2 q_r = C$ where C is an arbitrary constant. Letting $q_r(R) = \dot{R}$ gives $C = \dot{R}R^2$ and,

$$\begin{aligned} \mathbf{q} &= q_r \mathbf{e}_r, \qquad (7.8) \\ &= \frac{\dot{R}R^2}{r^2}\mathbf{e}_r. \qquad (7.9) \end{aligned}$$

In order to substitute for $\mathbf{q}$ in equation (7.2) the gradient of this first order cartesian tensor is evaluated as [41]

$$\nabla\mathbf{q} = \begin{pmatrix} \frac{\partial q_r}{\partial r} & \frac{1}{r}\left(\frac{\partial q_r}{\partial\theta} - q_\theta\right) & \frac{1}{r\sin\theta}\frac{\partial q_r}{\partial\phi} - \frac{q_\phi}{r} \\ \frac{\partial q_\theta}{\partial r} & \frac{1}{r}\left(\frac{\partial q_\theta}{\partial\theta} + q_r\right) & \frac{1}{r\sin\theta}\left(\frac{\partial q_\theta}{\partial\phi}\right) - \frac{\cot\theta}{r}q_\phi \\ \frac{\partial q_\phi}{\partial r} & \frac{1}{r}\left(\frac{\partial q_\phi}{\partial\theta}\right) & \frac{1}{r\sin\theta}\frac{\partial q_\phi}{\partial\phi} + \frac{q_r}{r} + \frac{\cot\theta}{r}q_\theta \end{pmatrix}. \qquad (7.10)$$

As above $q_\theta = q_\phi = 0$, q_r is dependent on r and t only and therefore $\nabla\mathbf{q} = (\nabla\mathbf{q})^T$ so that

$$\nabla\mathbf{q} + (\nabla\mathbf{q})^T = \frac{2\dot{R}R^2}{r^3}\begin{pmatrix} -2 & 0 & 0 \\ 0 & 1 & 0 \\ 0 & 0 & 1 \end{pmatrix}. \qquad (7.11)$$

Equation (7.2) can now be expanded as

$$\boldsymbol{\sigma} = \begin{pmatrix} -p & 0 & 0 \\ 0 & -p & 0 \\ 0 & 0 & -p \end{pmatrix} + \frac{2\mu\dot{R}R^2}{r^3}\begin{pmatrix} -2 & 0 & 0 \\ 0 & 1 & 0 \\ 0 & 0 & 1 \end{pmatrix} + G\begin{pmatrix} A_{rr} & 0 & 0 \\ 0 & A_{\theta\theta} & 0 \\ 0 & 0 & A_{\theta\theta} \end{pmatrix}, \qquad (7.12)$$

since in the spherically symmetric expansion all the off-diagonal components of the orientation tensor $\mathbf{A}$ are equal to zero and $A_{\theta\theta} = A_{\phi\phi}$. The only non-zero components of the stress tensor $\boldsymbol{\sigma}$ are,

$$\begin{aligned}
\sigma_{rr} &= -p - 4\mu\frac{\dot{R}R^2}{r^3} + GA_{rr}, && (7.13)\\
\sigma_{\theta\theta} &= -p + 2\mu\frac{\dot{R}R^2}{r^3} + GA_{\theta\theta}, && (7.14)\\
\sigma_{\phi\phi} &= \sigma_{\theta\theta}. && (7.15)
\end{aligned}$$

Having determined $\boldsymbol{\sigma}$, the momentum equation (7.3) can be tackled. The individual components of the divergence of the second order cartesian tensor $\boldsymbol{\sigma}$ in spherical polar co-ordinates are [41]

$$\begin{aligned}
(\boldsymbol{\nabla}\cdot\boldsymbol{\sigma})_r &= \frac{1}{r^2}\frac{\partial}{\partial r}\left(r^2\sigma_{rr}\right) + \frac{1}{r\sin\theta}\frac{\partial}{\partial\theta}\left(\sin\theta\sigma_{\theta r}\right) + \frac{1}{r\sin\theta}\frac{\partial\sigma_{\phi r}}{\partial\phi} - \frac{\sigma_{\theta\theta}+\sigma_{\phi\phi}}{r},\\
(\boldsymbol{\nabla}\cdot\boldsymbol{\sigma})_\theta &= \frac{1}{r^2}\frac{\partial}{\partial r}\left(r^2\sigma_{r\theta}\right) + \frac{1}{r\sin\theta}\frac{\partial}{\partial\theta}\left(\sin\theta\sigma_{\theta\theta}\right) + \frac{1}{r\sin\theta}\frac{\partial\sigma_{\phi\theta}}{\partial\phi} + \frac{\sigma_{\theta r}}{r} - \frac{\cot\theta}{r}\sigma_{\phi\phi},\\
(\boldsymbol{\nabla}\cdot\boldsymbol{\sigma})_\phi &= \frac{1}{r^2}\frac{\partial}{\partial r}\left(r^2\sigma_{r\phi}\right) + \frac{1}{r\sin\theta}\frac{\partial}{\partial\theta}\left(\sin\theta\sigma_{\theta\phi}\right) + \frac{1}{r\sin\theta}\frac{\partial\sigma_{\phi\phi}}{\partial\phi} + \frac{\sigma_{\phi r}}{r} + \frac{\cot\theta}{r}\sigma_{\phi\theta},
\end{aligned}$$

so that in the spherically symmetric case the only non-zero component of the divergence is the radial one. Substituting for σ_{rr}, $\sigma_{\theta\theta}$ and $\sigma_{\phi\phi}$ gives

$$\begin{aligned}
(\boldsymbol{\nabla}\cdot\boldsymbol{\sigma})_r &= \frac{1}{r^2}\frac{\partial}{\partial r}\left(r^2\sigma_{rr}\right) - \frac{2\sigma_{\theta\theta}}{r},\\
&= \frac{1}{r^2}\left(2r\sigma_{rr} + r^2\frac{\partial}{\partial r}\sigma_{rr}\right) - \frac{2\sigma_{\theta\theta}}{r},\\
&= \frac{2}{r}(\sigma_{rr} - \sigma_{\theta\theta}) + \frac{\partial\sigma_{rr}}{\partial r},\\
&= \frac{2}{r}\left(-p - 4\mu\frac{\dot{R}R^2}{r^3} + GA_{rr} + p - 2\mu\frac{\dot{R}R^2}{r^3} - GA_{\theta\theta}\right) + \frac{\partial\sigma_{rr}}{\partial r},
\end{aligned}$$

from (7.13) and (7.14). That is

$$\begin{aligned}
(\boldsymbol{\nabla}\cdot\boldsymbol{\sigma})_r &= \frac{2}{r}\left(-6\mu\frac{\dot{R}R^2}{r^3} + G(A_{rr} - A_{\theta\theta})\right) + \frac{\partial}{\partial r}\left(-p - 4\mu\frac{\dot{R}R^2}{r^3} + GA_{rr}\right),\\
&= -12\mu\frac{\dot{R}R^2}{r^4} + \frac{2G}{r}(A_{rr} - A_{\theta\theta}) - \frac{\partial p}{\partial r} + 12\mu\frac{\dot{R}R^2}{r^4} + G\frac{\partial A_{rr}}{\partial r},\\
&= -\frac{\partial p}{\partial r} + G\frac{\partial A_{rr}}{\partial r} + \frac{2G}{r}(A_{rr} - A_{\theta\theta}). && (7.16)
\end{aligned}$$

Using (7.9) and (7.10), the inertia term on the left hand side of equation (7.3) is given by

$$\begin{aligned}
\rho\left(\frac{\partial \mathbf{q}}{\partial t}+\mathbf{q}\cdot\boldsymbol{\nabla}\mathbf{q}\right) &= \rho\left(\frac{\partial}{\partial t}\left(\frac{\dot{R}R^2}{r^2}\right)\mathbf{e_r}+\frac{\dot{R}R^2}{r^2}\left(\frac{\partial q_r}{\partial r}\right)\mathbf{e_r}\right), && (7.17)\\
&= \rho\left(\frac{\ddot{R}R^2+2R\dot{R}^2}{r^2}+\frac{\dot{R}R^2}{r^2}\left(\frac{-2\dot{R}R^2}{r^3}\right)\right)\mathbf{e_r}, && (7.18)\\
&= \rho\left(\frac{\ddot{R}R^2+2R\dot{R}^2}{r^2}-\frac{2\dot{R}^2R^4}{r^5}\right)\mathbf{e_r}. && (7.19)
\end{aligned}$$

Equation (7.3) can therefore be stated as,

$$\rho\left(\frac{\ddot{R}R^2+2R\dot{R}^2}{r^2}-\frac{2\dot{R}^2R^4}{r^5}\right)=-\frac{\partial p}{\partial r}+G\frac{\partial A_{rr}}{\partial r}+\frac{2G}{r}(A_{rr}-A_{\theta\theta}). \qquad (7.20)$$

The boundary conditions require continuity of stress to be applied at the inner and outer fluid boundaries, and this is discussed in the following section.

7.2.1 Lagrangian reference frame

The inner and outer boundary conditions are to be defined at the bubble-fluid interface and the outer fluid layer, respectively (see Figure 7.1). In the current co-ordinate system these interfaces are both moving with time, and therefore, would need to be updated at consecutive time points. In order to simplify the analyses, both numerical and analytical, the system is transformed to the Lagrangian volume co-ordinate system. This can be done since the fluid volume is conserved. In the Lagrangian volume scheme the frame of reference moves with the bubble-fluid interface. Due to the spherically symmetric expansion we only need consider the radial co-ordinate in the analysis. The Lagrangian volume transformation is described below and illustrated in Figure 7.2.

Since the fluid volume is conserved then $4\pi\left(r_{f,0}^3-r_{b,0}^3\right)/3=4\pi\left(r_{f,t}^3-r_{b,t}^3\right)/3$. Letting this conserved fluid volume equal $4\pi X/3$ we can restate the equations and variables using the general fluid volume variable x which ranges from $x=0$

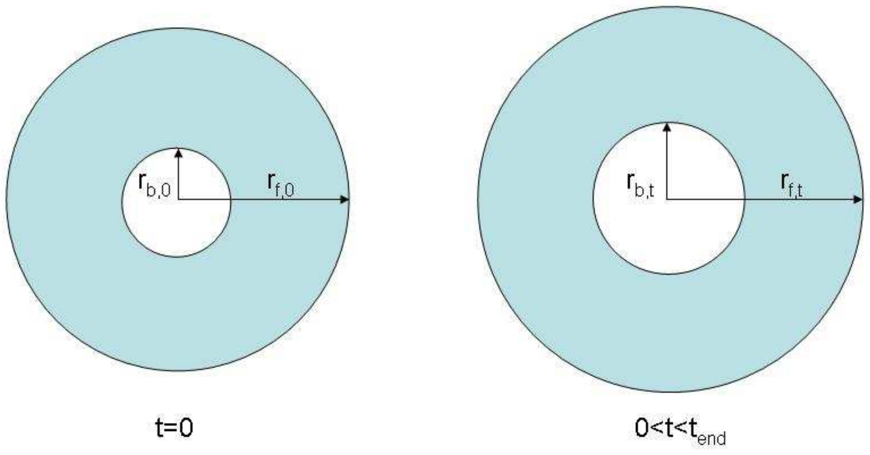

Figure 7.2: Schematic demonstrating the properties of the Lagrangian volume transformation. The unit cell is made up of the bubble volume and the fluid volume. At $t = 0$ the bubble radius is $r_{b,0}$ and the unit cell radius is $r_{f,0}$ so that the fluid volume is $\frac{4}{3}\pi\left(r_{f,0}^3 - r_{b,0}^3\right)$. At all subsequent time points, $(0 < t < t_{\text{end}})$, this fluid volume is conserved so that $\left(r_{f,t}^3 - r_{b,t}^3\right) = \pi\left(r_{f,0}^3 - r_{b,0}^3\right)$ for all t. In this way the frame of reference is given by the bubble-fluid boundary and boundary conditions do not need to be updated at consecutive time points.

	$t = 0$	$0 < t < t_{\text{end}}$
Bubble volume	$\frac{4}{3}\pi r_{b,0}^3$	$\frac{4}{3}\pi r_{b,t}^3$
Total volume	$\frac{4}{3}\pi r_{f,0}^3$	$\frac{4}{3}\pi r_{f,t}^3$
Fluid volume	$\frac{4}{3}\pi\left(r_{f,0}^3 - r_{b,0}^3\right)$	$\frac{4}{3}\pi\left(r_{f,t}^3 - r_{b,t}^3\right)$

Table 7.1: Volumes associated with the spherically symmetric bubble expansion in a finite fluid volume as illustrated in Figure 7.2

at the bubble surface to $x = X$ at the outer fluid volume limit. We can do this since the variables are symmetric in the θ and ϕ directions and depend on r and t only. If we let the general bubble volume $4\pi u(t)/3 = 4\pi R(t)^3/3$ then at a generic volume co-ordinate $4\pi u/3 + 4\pi x/3$, we can determine the associated radial position in the fluid relative to the origin at the centre of the bubble as $4\pi r^3/3 = 4\pi(u+x)/3$, or simply $r = (u+x)^{\frac{1}{3}}$. This transformation means that we can follow the bubble-liquid interface as the bubble expands so our boundary condition at the bubble surface does not have to be recalculated at each successive time point.

Transformation of (7.20) to the Lagrangian volume co-ordinate, x, where $\partial/\partial r = 3r^2\partial/\partial x$, results in

$$\rho\left(\frac{\ddot{R}R^2 + 2R\dot{R}^2}{r^2} - \frac{2\dot{R}^2R^4}{r^5}\right) = -\frac{\partial p}{\partial x}3r^2 + G\frac{\partial A_{rr}}{\partial x}3r^2 + \frac{2G}{r}(A_{rr} - A_{\theta\theta}), \quad (7.21)$$

Division by $3r^2$ and substitution for the following relations,

$$\dot{u} = 3R^2\dot{R}, \quad (7.22)$$

$$\dot{u}^2 = 9R^4\dot{R}^2, \quad (7.23)$$

$$\ddot{u} = 3(\ddot{R}R^2 + 2R\dot{R}^2), \quad (7.24)$$

$$r = (x+u)^{\frac{1}{3}}, \quad (7.25)$$

into (7.21) yields,

$$\rho\left[\frac{\ddot{u}}{9(x+u)^{\frac{4}{3}}} - \frac{2\dot{u}^2}{27(x+u)^{\frac{7}{3}}}\right] = -\frac{\partial p}{\partial x} + G\frac{\partial A_{rr}}{\partial x} + \frac{2G}{3(x+u)}(A_{rr} - A_{\theta\theta}). \quad (7.26)$$

Integration with respect to x gives,

$$\rho\left[-\frac{\ddot{u}}{3(x+u)^{\frac{1}{3}}} + \frac{\dot{u}^2}{18(x+u)^{\frac{4}{3}}}\right] = -p(x) + GA_{rr} + \frac{2}{3}G\int^{x}\frac{(A_{rr} - A_{\theta\theta})}{(x'+u)}dx' + C_1, \quad (7.27)$$

where C_1 is an arbitrary constant of integration to be determined by application of the boundary conditions. These boundary conditions are derived by considering the stresses acting on each boundary, that is, at the bubble/fluid interface

$$\begin{array}{c}\text{isotropic}\\ \text{pressure}\end{array} + \begin{array}{c}\text{Newtonian}\\ \text{stress}\end{array} + \begin{array}{c}\text{polymer}\\ \text{stress}\end{array} = \begin{array}{c}\text{bubble}\\ \text{pressure}\end{array} + \begin{array}{c}\text{surface}\\ \text{tension}\end{array},$$

and at the outer fluid surface we have

$$\begin{array}{c}\text{isotropic}\\ \text{pressure}\end{array} + \begin{array}{c}\text{Newtonian}\\ \text{stress}\end{array} + \begin{array}{c}\text{polymer}\\ \text{stress}\end{array} = \begin{array}{c}\text{atmospheric}\\ \text{pressure}\end{array} + \begin{array}{c}\text{ultrasound}\\ \text{pressure}\\ \text{excitation}\end{array}.$$

This results in the following two boundary conditions, at $x = 0$ and $x = X$, in the Lagrangian frame,

$$\begin{aligned} -p(0) - \frac{4\mu\dot{u}}{3u} + GA_{rr}(0) &= -p_g + \frac{2S}{u^{\frac{1}{3}}}, \qquad \text{at } x = 0, && (7.28) \\ -p(X) - \frac{4\mu\dot{u}}{3(X+u)} + GA_{rr}(X) &= -p_a - p_u, \qquad \text{at } x = X, && (7.29) \end{aligned}$$

where S is the surface tension, p_g is the bubble gas pressure, X is the Lagrangian volume co-ordinate for the outer fluid boundary and p_u is the pressure amplitude of the applied ultrasound signal. Evaluation of (7.27) at $x = 0$ and $x = X$ gives,

$$\begin{aligned} \frac{2}{3}G\int_0^X \frac{(A_{rr} - A_{\theta\theta})}{x' + u}dx' &= \rho\left(-\frac{\ddot{u}}{3(X+u)^{\frac{1}{3}}} + \frac{\dot{u}^2}{18(X+u)^{\frac{4}{3}}} + \frac{\ddot{u}}{3u^{\frac{1}{3}}} - \frac{\dot{u}^2}{18u^{\frac{4}{3}}}\right) \\ &\quad + p(X) - p(0) - GA_{rr}(X) + GA_{rr}(0), \qquad (7.30) \end{aligned}$$

and substitution for $p(0) - GA_{rr}(0)$ and $p(X) - GA_{rr}(X)$ from boundary conditions (7.28) and (7.29) respectively, gives the definite integral

$$\begin{aligned} \frac{2}{3}G\int_0^X \frac{(A_{rr} - A_{\theta\theta})}{x' + u}dx' &= \rho\left(-\frac{\ddot{u}}{3(X+u)^{\frac{1}{3}}} + \frac{\dot{u}^2}{18(X+u)^{\frac{4}{3}}} + \frac{\ddot{u}}{3u^{\frac{1}{3}}} - \frac{\dot{u}^2}{18u^{\frac{4}{3}}}\right) \\ &\quad - \frac{4\mu\dot{u}}{3(X+u)} + p_a + p_u + \frac{4\mu\dot{u}}{3u} - p_g + \frac{2S}{u^{\frac{1}{3}}}. \qquad (7.31) \end{aligned}$$

Rearranging (7.31) gives the momentum equation,

$$\begin{aligned} \frac{4}{3}\mu\dot{u}\left(\frac{1}{u} - \frac{1}{X+u}\right) &+ \rho\left[\frac{\ddot{u}}{3}\left(\frac{1}{u^{\frac{1}{3}}} - \frac{1}{(X+u)^{\frac{1}{3}}}\right) - \frac{\dot{u}^2}{18}\left(\frac{1}{u^{\frac{4}{3}}} - \frac{1}{(X+u)^{\frac{4}{3}}}\right)\right] \\ &= p_g - p_a - p_u + \frac{2}{3}G\int_0^X \frac{(A_{rr} - A_{\theta\theta})}{(x' + u)}dx' - \frac{2S}{u^{\frac{1}{3}}}. \qquad (7.32) \end{aligned}$$

The only remaining unknown, in the Oldroyd B system (7.1) - (7.4), is the orientation tensor $\mathbf{A}$ which is described by (7.4). The total derivative

$$\frac{D\mathbf{A}}{Dt} = \frac{\partial \mathbf{A}}{\partial t} + (\mathbf{q} \cdot \boldsymbol{\nabla})\mathbf{A}, \tag{7.33}$$

however, in the Lagrangian frame, reduces (7.4) to

$$\frac{\partial \mathbf{A}}{\partial t} = \mathbf{A} \cdot \boldsymbol{\nabla}\mathbf{q} + (\boldsymbol{\nabla}\mathbf{q})^T \cdot \mathbf{A} - \frac{1}{\tau}(\mathbf{A} - \mathbf{I}), \tag{7.34}$$

since the convection term $(\mathbf{q} \cdot \boldsymbol{\nabla})\mathbf{A}$ is now zero. Substitution for $\boldsymbol{\nabla}\mathbf{q}$ from (7.10) therefore,

$$\begin{aligned}
\begin{pmatrix} \frac{\partial A_{rr}}{\partial t} & 0 & 0 \\ 0 & \frac{\partial A_{\theta\theta}}{\partial t} & 0 \\ 0 & 0 & \frac{\partial A_{\theta\theta}}{\partial t} \end{pmatrix} &= \frac{\dot{R}R^2}{r^3} \begin{pmatrix} -2 & 0 & 0 \\ 0 & 1 & 0 \\ 0 & 0 & 1 \end{pmatrix} \begin{pmatrix} A_{rr} & 0 & 0 \\ 0 & A_{\theta\theta} & 0 \\ 0 & 0 & A_{\theta\theta} \end{pmatrix} \\
&\quad + \frac{\dot{R}R^2}{r^3} \begin{pmatrix} A_{rr} & 0 & 0 \\ 0 & A_{\theta\theta} & 0 \\ 0 & 0 & A_{\theta\theta} \end{pmatrix} \begin{pmatrix} -2 & 0 & 0 \\ 0 & 1 & 0 \\ 0 & 0 & 1 \end{pmatrix} \\
&\quad - \frac{1}{\tau} \begin{pmatrix} A_{rr} - 1 & 0 & 0 \\ 0 & A_{\theta\theta} - 1 & 0 \\ 0 & 0 & A_{\theta\theta} - 1 \end{pmatrix},
\end{aligned}$$

so that the rate equations for A_{rr} and $A_{\theta\theta}$ are described by

$$\frac{\partial A_{rr}}{\partial t} = -4\frac{\dot{R}R^2}{r^3} A_{rr} - \frac{1}{\tau}(A_{rr} - 1), \tag{7.35}$$

$$\frac{\partial A_{\theta\theta}}{\partial t} = 2\frac{\dot{R}R^2}{r^3} A_{\theta\theta} - \frac{1}{\tau}(A_{\theta\theta} - 1). \tag{7.36}$$

Transformation to the Lagrangian co-ordinate system gives the evolution equations

$$\frac{\partial A_{rr}}{\partial t} = -\frac{4\dot{u}}{3(u+x)} A_{rr} - \frac{1}{\tau}(A_{rr} - 1), \tag{7.37}$$

$$\frac{\partial A_{\theta\theta}}{\partial t} = \frac{2\dot{u}}{3(u+x)} A_{\theta\theta} - \frac{1}{\tau}(A_{\theta\theta} - 1). \tag{7.38}$$

Subtracting (7.37) from (7.38) gives the first normal difference rate equation

$$\frac{\partial (A_{rr} - A_{\theta\theta})}{\partial t} = \frac{2\dot{u}}{3(u+x)}[(A_{rr} - A_{\theta\theta}) - 3A_{rr}] - \frac{1}{\tau}(A_{rr} - A_{\theta\theta}), \tag{7.39}$$

where the initial conditions are given by $A_{rr} = A_{\theta\theta} = 1$ everywhere at $t = 0$.

7.3 Gaseous phase

Next we consider the gas concentration in the liquid, its diffusion through the fluid and its transport across the bubble-fluid interface. The fluid initially contains a finite concentration, c_0, of dissolved gas, distributed homogeneously throughout the layer. For $t > 0$, gas is transported across the bubble-fluid interface at a rate governed by Henry's law [2]. This sets up a concentration gradient through the liquid layer and gas diffuses through the liquid in the direction of decreasing concentration gradient, according to the diffusion equation [52]. Henry's law relates the gas concentration at the bubble surface, ($x = 0$), to the pressure inside the bubble, via

$$c(0,t) - c_0 = (p_g(t) - p_{g_0})H, \tag{7.40}$$

where p_{g_0} is the initial bubble gas pressure, $p_g(t)$ is the bubble gas pressure at subsequent $t > 0$ and H is the Henry's law constant. The gas concentration in the fluid, $c(x,t)$, is governed by the convection-diffusion equation [106] which is derived from the assumption of mass conservation in the liquid, to give

$$\frac{\partial c}{\partial t} + \mathbf{q} \cdot \nabla c = \nabla \cdot (D \nabla c), \tag{7.41}$$

where D is the diffusion coefficient. In a spherically symmetric system, therefore

$$\frac{\partial c}{\partial t} + q_r \frac{\partial c}{\partial r} = D \frac{1}{r^2} \frac{\partial}{\partial r} \left(r^2 \frac{\partial c}{\partial r} \right), \tag{7.42}$$

and in the Lagrangian frame the convection term disappears [7] to give

$$\begin{aligned} \frac{\partial c}{\partial t} &= D(x+u)^{-\frac{2}{3}} 3(x+u)^{\frac{2}{3}} \frac{\partial}{\partial x} \left((x+u)^{\frac{2}{3}} 3(x+u)^{\frac{2}{3}} \frac{\partial c}{\partial x} \right), & (7.43) \\ &= 9D \frac{\partial}{\partial x} \left((x+u)^{\frac{4}{3}} \frac{\partial c}{\partial x} \right). & (7.44) \end{aligned}$$

The initial gas concentration throughout the liquid layer is $c(x,0) = c_0$. As the bubble expands for $t > 0$ the pressure drops and a steep concentration gradient is set up in the thin boundary layer surrounding the bubble and propagates through the fluid causing gas to diffuse into the bubble. This steep concentration gradient at early t makes numerical analysis difficult and consequently a concentration potential $\phi(x,t)$, such that $\partial\phi/\partial x = c - c_0$, is introduced to overcome this problem [26]; the diffusion of this potential is

$$\frac{\partial}{\partial t}\left(\frac{\partial\phi}{\partial x}\right) = 9D\frac{\partial}{\partial x}\left((x+u)^{\frac{4}{3}}\frac{\partial}{\partial x}\left(\frac{\partial\phi}{\partial x}\right)\right).$$

Changing the order of integration

$$\frac{\partial}{\partial x}\left(\frac{\partial\phi}{\partial t}\right) = 9D\frac{\partial}{\partial x}\left((x+u)^{\frac{4}{3}}\frac{\partial^2\phi}{\partial x^2}\right)$$

and integrating with respect to x the diffusion equation can now be writen as

$$\frac{\partial\phi}{\partial t} = 9D(x+u)^{\frac{4}{3}}\frac{\partial^2\phi}{\partial x^2}, \tag{7.45}$$

with $\partial\phi/\partial x = (p_g - p_{g_0})H$ at the bubble surface. If we assume that there is no transport across the outer fluid boundary (ensuring that gas supply is limited) then $\partial^2\phi/\partial x^2 = 0$ at the outer fluid boundary. The bubble volume, u, can be related to the bubble gas pressure p_g and the concentration potential at the bubble surface, $\phi(0,t)$, by application of the principle of mass conservation. From the ideal gas law [2], where R_g is the universal gas constant and T is the temperature, then from (7.45)

$$\begin{aligned}\frac{d}{dt}\left(\frac{p_g u}{R_g T}\right) &= 9Du^{\frac{4}{3}}\left.\frac{\partial^2\phi}{\partial x^2}\right|_{x=0}, \\ &= \left.\frac{\partial\phi}{\partial t}\right|_{x=0}.\end{aligned}$$

Integrating with respect to time gives

$$p_g u = R_g T\phi(0,t) + C_1, \tag{7.46}$$

and application of initial conditions, $u(0) = u_0, p_g(0) = p_{g_0}, \phi(0,0) = 0$ retrieves the constant of integration, C_1, so that,

$$p_g u = p_{g_0}u_0 + R_g T\phi(0,t). \tag{7.47}$$

The system is now fully described by (7.32), (7.37), (7.39), (7.45) and (7.47). Non-dimensionalisation of the governing equations and boundary conditions results in the following system,

$$\begin{aligned}
&\frac{4}{3}\dot{u}\left(\frac{1}{u}-\frac{1}{(X+u)}\right)+\mathcal{R}\left[\ddot{u}\left(\frac{1}{u^{\frac{1}{3}}}-\frac{1}{(X+u)^{\frac{1}{3}}}\right)-\frac{\dot{u}^2}{6}\left(\frac{1}{u^{\frac{4}{3}}}-\frac{1}{(X+u)^{\frac{4}{3}}}\right)\right]\\
&\qquad\qquad = De(P_g-P_u)+\frac{2}{3}\gamma\int_0^X\frac{(A_{rr}-A_{\theta\theta})}{(x+u)}dx-\frac{1}{\Gamma u^{\frac{1}{3}}}, \qquad (7.48)\\
&\frac{\partial A_{rr}}{\partial t}=-\frac{4\dot{u}}{3(x+u)}A_{rr}-(A_{rr}-1), \qquad (7.49)\\
&\frac{\partial A_{\theta\theta}}{\partial t}=\frac{2\dot{u}}{3(x+u)}A_{\theta\theta}-(A_{\theta\theta}-1), \qquad (7.50)\\
&\frac{(p_a+(p_{g_0}-p_a)P_g)}{p_{g_0}}u=(1+\phi(0,t)), \qquad (7.51)\\
&\frac{\partial\phi}{\partial t}=N(x+u)^{\frac{4}{3}}\frac{\partial^2\phi}{\partial x^2}, \qquad (7.52)
\end{aligned}$$

where $N=9D\tau/u_0^{2/3}$, $\mathcal{R}=\rho u_0^{2/3}/3\mu\tau$, $De=(p_{g_0}-p_a)\tau/\mu$, $P_g=(p_g-p_a)/(p_{g_0}-p_a)$, $P_u=p_u/(p_{g_0}-p_a)$, $\gamma=G\tau/\mu$, $\Gamma=\mu u_0^{1/3}/2S\tau$ and the boundary conditions on $\phi(x,t)$ are,

$$\left.\frac{\partial\phi}{\partial x}\right|_{x=0}=\Phi\frac{(p_{g0}-p_a)}{p_{g_0}}(P_g-1), \qquad (7.53)$$

$$\left.\frac{\partial^2\phi}{\partial x^2}\right|_{x=X}=0, \qquad (7.54)$$

where $\Phi=R_gTH$. The non-dimensional initial conditions are,

$$u(0)=1, \qquad P_g(0)=1, \qquad A_{rr}(x,0)=1, \qquad A_{\theta\theta}(x,0)=1, \qquad \phi(0,0)=0.$$

For details of the non-dimensionalisation see Appendix C; individual parameter values are listed in Table C.1.

7.4 Instantaneous diffusion approximation

In order to simplify the analysis the equation in $\phi(x,t)$ can be decoupled by assuming instantaneous diffusion. In other words, by assuming that N is large so the spatial derivative dominates in (7.52) then

$$\frac{\partial^2 \phi}{\partial x^2} = 0, \tag{7.55}$$

and the boundary condition given by (7.53), at the bubble surface now applies throughout the domain. Considering the mass conservation of the gas we have

$$\frac{d}{dt}\left(\frac{p_g u}{R_g T}\right) = -\frac{d}{dt}\left(c(x,t)X\right), \tag{7.56}$$

where $c(x,t)$ is the moles of gas per unit volume, X is the fluid volume and the minus sign accounts for the fact that as the gas concentration in the fluid decreases, its concentration in the bubble increases. Integrating gives

$$\frac{p_g u}{R_g T} = -c(x,t)X + \hat{C}, \tag{7.57}$$

where $\hat{C}$ is a constant of integration retrieved by application of the initial condition

$$\frac{p_{g0} u_0}{R_g T} = -c_0 X + \hat{C}, \tag{7.58}$$

so that

$$\frac{p_g u}{R_g T} = -c(x,t)X + \frac{p_{g0} u_0}{R_g T} + c_0 X. \tag{7.59}$$

Substituting for $\partial\phi/\partial x = c(x,t) - c_0$ and non-dimensionalising as described in Appendix C we obtain

$$\left(\frac{p_a + (p_{g0} - p_a)P_g}{p_{g0}}\right) u = 1 - \frac{\partial \phi}{\partial x} X. \tag{7.60}$$

Applying the boundary condition (7.53), which is now valid throughout the domain, we have

$$\left(\frac{p_a + (p_{g0} - p_a)P_g}{p_{g0}}\right) u = 1 + \Phi \frac{p_{g0} - p_a}{p_{g0}} (1 - P_g) X. \tag{7.61}$$

By rearranging for P_g, (7.61) can be written as

$$P_g = \frac{A + Bu + \Phi X}{u + \Phi X}, \tag{7.62}$$

where $A = p_{g_0}/(p_{g_0} - p_a)$ and $B = -p_a/(p_{g_0} - p_a)$. In the following section we employ multiscale analysis and asymptotic expansions to investigate the effect of the inertia related term $\mathcal{R}$ on the inner and outer solutions. We, therefore, use asymptotic expansions to derive first an inner solution (small time) for times $t = O(\eta)$ and then construct an outer solution (large time) where η is the factor used to stretch the inner time variable.

7.5 Asymptotic analysis: Inner solution

There is a brief time which we assume to be $O(\eta)$ in which u rapidly increases from its initial value to a value that is commensurate with the outer solution derived in the following section 7.6. In this phase of the bubble growth the inertia term dominates. To allow us to study this behaviour we stretch time by introducing the inner variable,

$$T = \frac{t}{\eta},$$

where η is a scaling constant such that $0 < \eta \ll 1$. For clarity we introduce the following notation for the inner solution

$$\begin{aligned}
U(T, \eta) &= u(t, \eta), \\
AR(x, T, \eta) &= A_{rr}(x, t, \eta), \\
AQ(x, T, \eta) &= A_{\theta\theta}(x, t, \eta), \\
A(x, T, \eta) &= (A_{rr} - A_{\theta\theta})(x, t, \eta), \\
P(T, \eta) &= P_g(t, \eta), \\
\hat{\phi}(x, T, \eta) &= \phi(x, t, \eta).
\end{aligned}$$

As before we assume instantaneous diffusion so that the inner governing equations are, from (7.48), (7.49), (7.50), (7.62) and (7.61),

$$
\begin{aligned}
&\eta\frac{4}{3}\dot{U}\left(\frac{1}{U}-\frac{1}{X+U}\right)+\mathcal{R}\left(\ddot{U}\left(\frac{1}{U^{\frac{1}{3}}}-\frac{1}{(X+U)^{\frac{1}{3}}}\right)-\frac{\dot{U}^2}{6}\left(\frac{1}{U^{\frac{4}{3}}}-\frac{1}{(X+U)^{\frac{4}{3}}}\right)\right) \\
&\qquad = \eta^2\left(De(P-P_u)+\frac{2}{3}\gamma\int_0^X\frac{A}{(x+U)}dx-\frac{1}{\Gamma U^{\frac{1}{3}}}\right), \qquad (7.63)
\end{aligned}
$$

$$
\begin{aligned}
\frac{\partial AR}{\partial T} &= -\frac{4}{3}\frac{\dot{U}}{(x+U)}AR-\eta(AR-1), && (7.64)\\
\frac{\partial AQ}{\partial T} &= \frac{2}{3}\frac{\dot{U}}{(x+U)}AQ-\eta(AQ-1), && (7.65)\\
P &= \frac{A+BU+\Phi X}{U+\Phi X}, && (7.66)\\
\hat{\phi} &= \Phi\frac{p_{g_0}-p_a}{p_{g_0}}(P-1)X. && (7.67)
\end{aligned}
$$

We substitute for inner expansions of the form,

$$
\begin{aligned}
U(T,\eta) &= U_0(T)+\eta U_1(T)+O(\eta^2), && (7.68)\\
AR(x,T,\eta) &= AR_0(x,T)+\eta AR_1(x,T)+O(\eta^2), && (7.69)\\
AQ(x,T,\eta) &= AQ_0(x,T)+\eta AQ_1(x,T)+O(\eta^2), && (7.70)\\
A(x,T,\eta) &= A_0(x,T)+\eta A_1(x,T)+O(\eta^2), && (7.71)\\
P(T,\eta) &= P_0(T)+\eta P_1(T)+O(\eta^2), && (7.72)
\end{aligned}
$$

and proceed by making the appropriate Taylor series expansions where necessary to derive the momentum equation,

$$\begin{aligned}
&\frac{4}{3}\eta\left(\dot{U}_0+\eta\dot{U}_1\right)\left(\frac{1}{U_0}\left(1-\frac{\eta U_1}{U_0}\right)-\frac{1}{X+U_0}\left(1-\frac{\eta U_1}{(X+U_0)}\right)\right)\\
&+\mathcal{R}\left\{\left(\ddot{U}_0+\eta\ddot{U}_1\right)\left(\frac{1}{U_0^{\frac{1}{3}}}\left(1-\frac{\eta U_1}{3U_0}\right)-\frac{1}{(X+U_0)^{\frac{1}{3}}}\left(1-\frac{\eta U_1}{3(X+U_0)}\right)\right)\right.\\
&\qquad\left.-\frac{\left(\dot{U}_0+\eta\dot{U}_1\right)^2}{6}\left(\frac{1}{U_0^{\frac{4}{3}}}\left(1-\frac{4\eta U_1}{3U_0}\right)-\frac{1}{(X+U_0)^{\frac{4}{3}}}\left(1-\frac{4\eta U_1}{3(X+U_0)}\right)\right)\right\}\\
&\qquad\qquad=\eta^2\left[De(P_0+\eta P_1-P_u)+\frac{2}{3}\gamma\int_0^X\frac{(A_0+\eta A_1)}{x+U_0}\left(1-\frac{\eta U_1}{(x+U_0)}\right)dx\right.\\
&\qquad\qquad\qquad\left.-\frac{1}{\Gamma U_0^{\frac{1}{3}}}\left(1-\frac{\eta U_1}{U_0}\right)\right]+O(\eta^5).
\end{aligned}\tag{7.73}$$

Collecting together powers of η gives

$$\begin{aligned}
&\mathcal{R}\left(\ddot{U}_0\left(\frac{1}{U_0^{\frac{1}{3}}}-\frac{1}{(X+U_0)^{\frac{1}{3}}}\right)-\frac{\dot{U}_0^2}{6}\left(\frac{1}{U_0^{\frac{4}{3}}}-\frac{1}{(X+U_0)^{\frac{4}{3}}}\right)\right)\\
&\quad+\eta\left[\frac{4}{3}\dot{U}_0\left(\frac{1}{U_0}-\frac{1}{X+U_0}\right)+\mathcal{R}\left(\ddot{U}_1\left(\frac{1}{U_0^{\frac{1}{3}}}-\frac{1}{(X+U_0)^{\frac{1}{3}}}\right)\right.\right.\\
&\quad-\frac{\ddot{U}_0U_1}{3}\left(\frac{1}{U_0^{\frac{4}{3}}}-\frac{1}{(X+U_0)^{\frac{4}{3}}}\right)+\frac{2\dot{U}_0^2U_1}{9}\left(\frac{1}{U_0^{\frac{7}{3}}}-\frac{1}{(X+U_0)^{\frac{7}{3}}}\right)\\
&\quad\left.\left.-\frac{\dot{U}_0\dot{U}_1}{3}\left(\frac{1}{U_0^{\frac{4}{3}}}-\frac{1}{(X+U_0)^{\frac{4}{3}}}\right)\right)\right]+O(\eta^2)\\
&\qquad=0.
\end{aligned}\tag{7.74}$$

The rate equations for AR and AQ can be treated in a similar manner; starting with the non-dimensionalised rate equation in $AR(x,T)$ we have

$$\begin{aligned}
\frac{\partial(AR_0+\eta AR_1)}{\partial T} &= -\frac{4}{3(x+U_0)}(\dot{U}_0+\eta\dot{U}_1)(AR_0+\eta AR_1)\left(1-\frac{\eta U_1}{(x+U_0)}\right)\\
&\quad-\eta(AR_0+\eta AR_1-1)+O(\eta^2),
\end{aligned}\tag{7.75}$$

so that,

$$\begin{aligned}\frac{\partial AR_0}{\partial T}+\eta\frac{\partial AR_1}{\partial T} &= \left(-\frac{4\dot{U}_0AR_0}{3(x+U_0)}\right)\\ &\quad +\eta\left[-\frac{4}{3(x+U_0)}\left(\dot{U}_0AR_1-\frac{\dot{U}_0AR_0U_1}{(x+U_0)}+\dot{U}_1AR_0\right)-(AR_0-1)\right]\\ &\quad +O(\eta^2), \end{aligned} \tag{7.76}$$

and

$$\begin{aligned}\frac{\partial(AQ_0+\eta AQ_1)}{\partial T} &= \frac{2}{3(x+U_0)}(\dot{U}_0+\eta\dot{U}_1)(AQ_0+\eta AQ_1)\left(1-\frac{\eta U_1}{(x+U_0)}\right)\\ &\quad -\eta(AQ_0+\eta AQ_1-1)+O(\eta^2), \end{aligned} \tag{7.77}$$

giving

$$\begin{aligned}\frac{\partial AQ_0}{\partial T}+\eta\frac{\partial AQ_1}{\partial T} &= \left(\frac{2\dot{U}_0AQ_0}{3(x+U_0)}\right)\\ &\quad +\eta\left[\frac{2}{3(x+U_0)}\left(\dot{U}_0AQ_1-\frac{\dot{U}_0AQ_0U_1}{(x+U_0)}+\dot{U}_1AQ_0\right)-(AQ_0-1)\right]\\ &\quad +O(\eta^2), \end{aligned} \tag{7.78}$$

The pressure and diffusion equations are given by

$$P_0+\eta P_1 = \frac{A+B(U_0+\eta U_1)+\Phi X}{(U_0+\eta U_1)+\Phi X}+O(\eta^2), \tag{7.79}$$

$$\hat{\phi}_0+\eta\hat{\phi}_1 = \Phi\frac{p_{g0}-p_a}{p_{g0}}(P_0+\eta P_1-1)X+O(\eta^2), \tag{7.80}$$

so that collecting powers of η together we have

$$P_0+\eta P_1 = \frac{A+BU_0+\Phi X}{U_0+\Phi X}+\eta\left(\frac{BU_1}{U_0+\Phi X}-\frac{(A+BU_0+\Phi X)U_1}{(U_0+\Phi X)^2}\right)+O(\eta^2), \tag{7.81}$$

$$\hat{\phi}_0+\eta\hat{\phi}_1 = \Phi\frac{p_{g0}-p_a}{p_{g0}}(P_0-1)X+\eta\left(\Phi\frac{p_{g0}-p_a}{p_{g0}}P_1X\right)+O(\eta^2). \tag{7.82}$$

7.5.1 Leading order solution

If we assume that $\mathcal{R} \gg \eta$ then the leading order system, as described by (7.74), (7.76), (7.78), (7.81) and (7.82), is

$$\begin{aligned}
\ddot{U}_0\left(\frac{1}{U_0^{\frac{1}{3}}} - \frac{1}{(X+U_0)^{\frac{1}{3}}}\right) &= \frac{\dot{U}_0^2}{6}\left(\frac{1}{U_0^{\frac{4}{3}}} - \frac{1}{(X+U_0)^{\frac{4}{3}}}\right), && (7.83)\\
\frac{\partial AR_0}{\partial T} &= -\frac{4}{3}\frac{\dot{U}_0}{(x+U_0)}AR_0, && (7.84)\\
\frac{\partial AQ_0}{\partial T} &= \frac{2}{3}\frac{\dot{U}_0}{(x+U_0)}AQ_0, && (7.85)\\
P_0 &= \frac{A+BU_0+\Phi X}{U_0+\Phi X}, && (7.86)\\
\hat{\phi}_0 &= \Phi\frac{p_{g0}-p_a}{p_{g0}}P_0X. && (7.87)
\end{aligned}$$

with initial conditions $U_0(0)=1, AR_0(x,0)=1, AQ_0(x,0)=1, \hat{\phi}_0(0)=0, P_0(0)=1$ and we designate $\dot{U}_0(0)=c_v$, where we assume $c_v>0$. Multiplying the momentum equation (7.83) by $U_0^{\frac{4}{3}}(X+U_0)^{\frac{4}{3}}$ yields,

$$\ddot{U}_0U_0(X+U_0)\left((X+U_0)^{\frac{1}{3}} - U_0^{\frac{1}{3}}\right) - \frac{\dot{U}_0^2}{6}\left((X+U_0)^{\frac{4}{3}} - U_0^{\frac{4}{3}}\right) = 0, \qquad (7.88)$$

To enable an analytic solution, and since we are looking at the early time evolution of the bubble, we make the assumption that $U_0 \ll X$ and equation (7.88) reduces to

$$\ddot{U}_0U_0 - \frac{\dot{U}_0^2}{6} = 0. \qquad (7.89)$$

Figure 7.3 shows that this approximation is a reasonable one for very large X, ($> O(10^3)$) however, for values of X of the order used previously [26] ($X = 53.6$), this approximation is not very accurate. Therefore, we will study two regimes. In the first instance, the case for large X is considered, since a fully analytic solution is achievable; the semi-analytic approach for smaller X is discussed in Section 7.5.1.2.

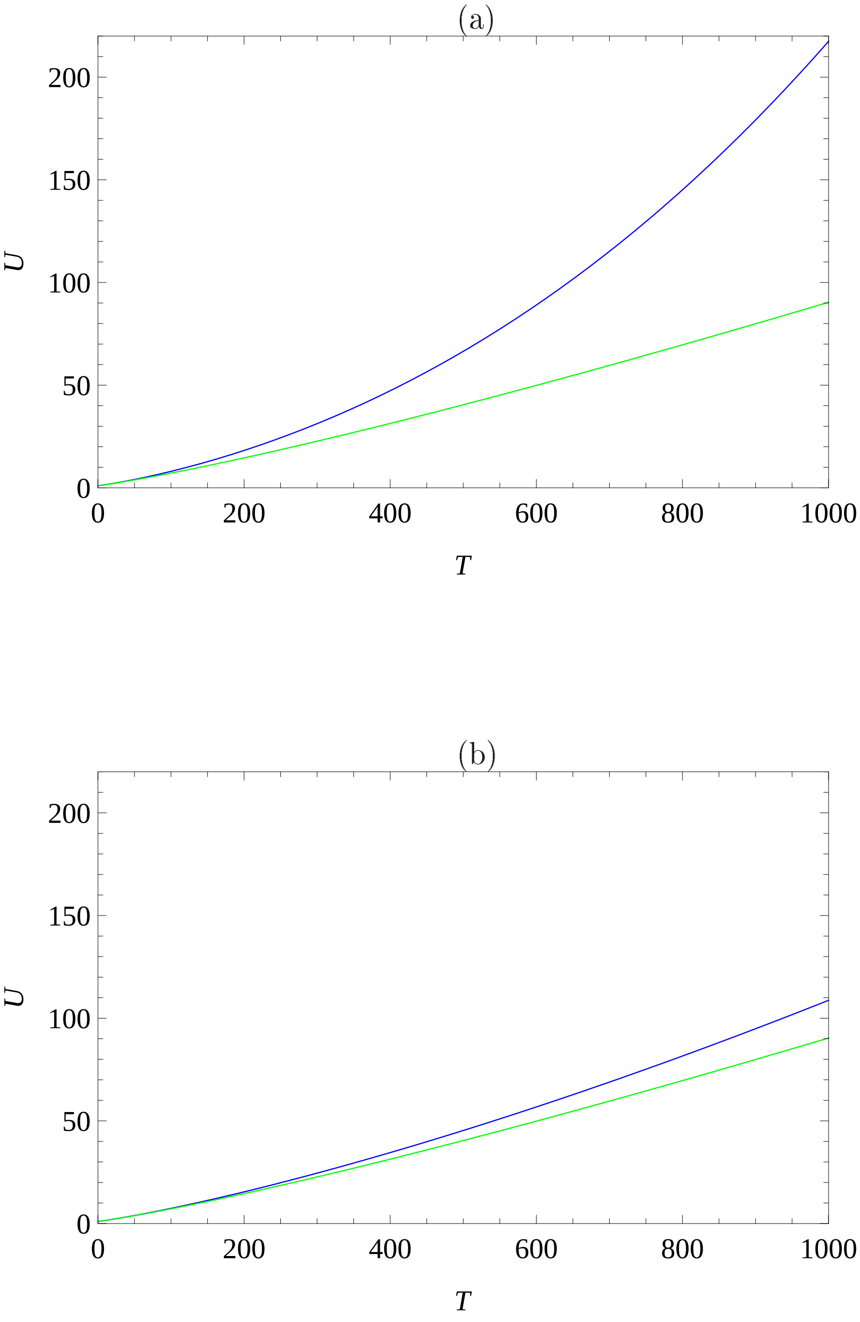

Figure 7.3: Plots of the leading order inner solution U_0 versus the inner temporal variable T illustrating the effect of X on the validity of the approximate analytic leading order solution. The figures show the numerical solution (blue line) of (7.88) and the approximate numerical solution (green line) produced by (7.89) for two values of X. In (a) $X = 50$ and in (b) $X = 1000$. The initial condition on $\dot{U}_0$ is parameterised by $c_v = 0.05$. The plots demonstrate that the approximate solution is only reasonable when X is large.

7.5.1.1 Case I: $X \gg U_0$

For $X \gg U_0$ (7.89) can be transformed using $U_0(T) = e^{az(T)}$ to give

$$\ddot{z} + \frac{5a}{6}\dot{z}^2 = 0.$$

Choosing $a = \frac{6}{5}$ for convenience results in the second order, non-linear, ODE in z,

$$\ddot{z} + \dot{z}^2 = 0. \tag{7.90}$$

Making another substitution, $y = \dot{z}$, reduces this to the first order equation

$$\frac{dy}{dT} = -y^2, \tag{7.91}$$

which can be integrated, as it is of separable type, and this leads to

$$z = \log|T + C_2| + C_3,$$

where C_2 and C_3 are arbitrary constants of integration to be determined. Hence

$$U_0 = A|T + C_2|^{\frac{6}{5}}, \tag{7.92}$$

where $A = e^{\frac{6}{5}C_3}$. Applying the initial condition $U_0(0) = 1$ allows the constant A to be expressed in terms of C_2 as follows,

$$U_0(0) = 1 = A|C_2|^{\frac{6}{5}},$$

so that,

$$A = |C_2|^{-\frac{6}{5}},$$

and

$$U_0 = \left|1 + \frac{T}{C_2}\right|^{\frac{6}{5}} \tag{7.93}$$

To determine the constant of integration C_2 we need an initial condition on the velocity $\dot{U}_0$, denoted by $\dot{U}_0(0) = c_v$. The derivative,

$$\dot{U}_0 = \frac{6}{5C_2}\left|1 + \frac{T}{C_2}\right|^{\frac{1}{5}},$$

evaluated at $t = 0$ gives,

$$\frac{6}{5C_2} = c_v.$$

Rearranging we have $C_2 = 6/5c_v$ and so

$$U_0 = \left|1 + \frac{5c_v}{6}T\right|^{\frac{6}{5}}. \tag{7.94}$$

We assume that c_v is always positive, otherwise no bubble expansion would occur. Therefore, since $T \geq 0$ we can drop the modulus requirement on $(1 + 5c_vT/6)$ so that,

$$U_0 = \left(1 + \frac{5c_v}{6}T\right)^{\frac{6}{5}}, \tag{7.95}$$

describes the leading order inner solution for non-dimensional bubble volume U_0 given by initial conditions $U_0(0) = 1$ and $\dot{U}_0(0) = c_v$ and assuming $X \gg U_0$. Figure 7.4 illustrates the form of the leading order solution $U_0(T)$, for a particular initial condition parameter c_v. This leading order solution is parameterised by c_v only, and as c_v increases so does the final volume U_0 on the given domain.

Next we turn to the zero order rate equations for the orientation tensor arising from (7.76) and (7.78)

$$\begin{aligned}
\frac{\partial AR_0}{\partial T}(x,T) &= -\frac{4\dot{U}_0}{3(x+U_0)}AR_0(x,T), \\
\frac{\partial AQ_0}{\partial T}(x,T) &= \frac{2\dot{U}_0}{3(x+U_0)}AQ_0(x,T).
\end{aligned}$$

We look first at AR_0 which can be solved by separating variables to give,

$$AR_0(x,T) = C(x)(x+U_0)^{-\frac{4}{3}},$$

where $C(x)$ is an arbitrary function of integration. Application of the initial conditions $AR_0(x,0) = 1$ and $U_0(0) = 1$ gives

$$AR_0(x,T) = \left(\frac{x+1}{x + \left(1 + \frac{5c_v}{6}T\right)^{\frac{6}{5}}}\right)^{\frac{4}{3}}. \tag{7.96}$$

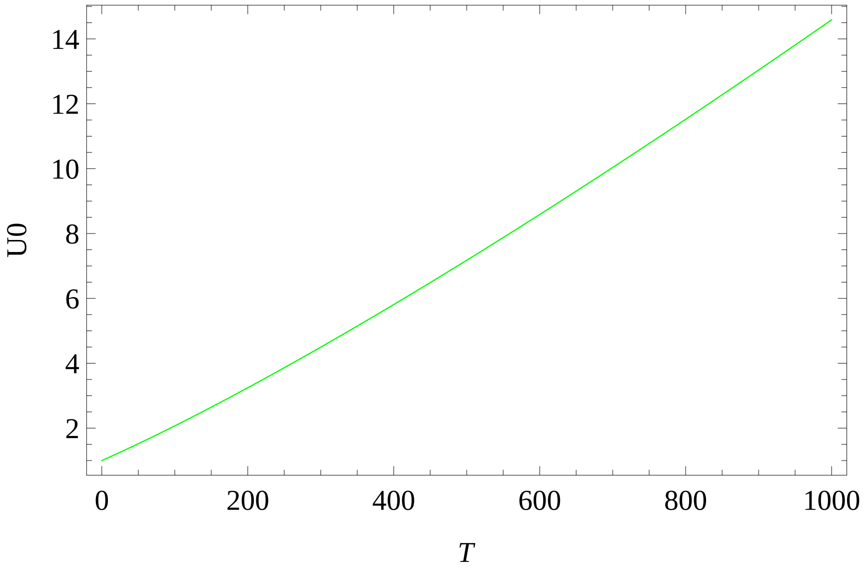

Figure 7.4: A sample plot of the leading order inner solution U_0 versus the stretched inner variable T, for $X \gg U_0$, as modelled by (7.95). In this particular case $c_v = 0.01$ and $X = 1000$.

In the same way an expression for AQ_0 can be derived in terms of U_0 and is stated below,

$$AQ_0(x,T) = \left(\frac{x + \left(1 + \frac{5c_v}{6}T\right)^{\frac{6}{5}}}{x+1} \right)^{\frac{2}{3}}. \tag{7.97}$$

The difference term $(AR - AQ)_0$ is therefore,

$$(AR - AQ)_0\,(x,T) = \left(\frac{x+1}{x + \left(1 + \frac{5c_v}{6}T\right)^{\frac{6}{5}}} \right)^{\frac{4}{3}} - \left(\frac{x + \left(1 + \frac{5c_v}{6}T\right)^{\frac{6}{5}}}{x+1} \right)^{\frac{2}{3}}. \tag{7.98}$$

Figure 7.5 illustrates the functions $AR_0(x,T)$, $AQ_0(x,T)$ and the difference term $(AR-AQ)_0(x,T)$ at a range of spatial positions in the Lagrangian fluid envelope and demonstrates that as distance from the liquid/gas interface increases these functions tend to constant values in time.

The leading order solutions P_0 and ϕ_0 are obtained by retaining only leading

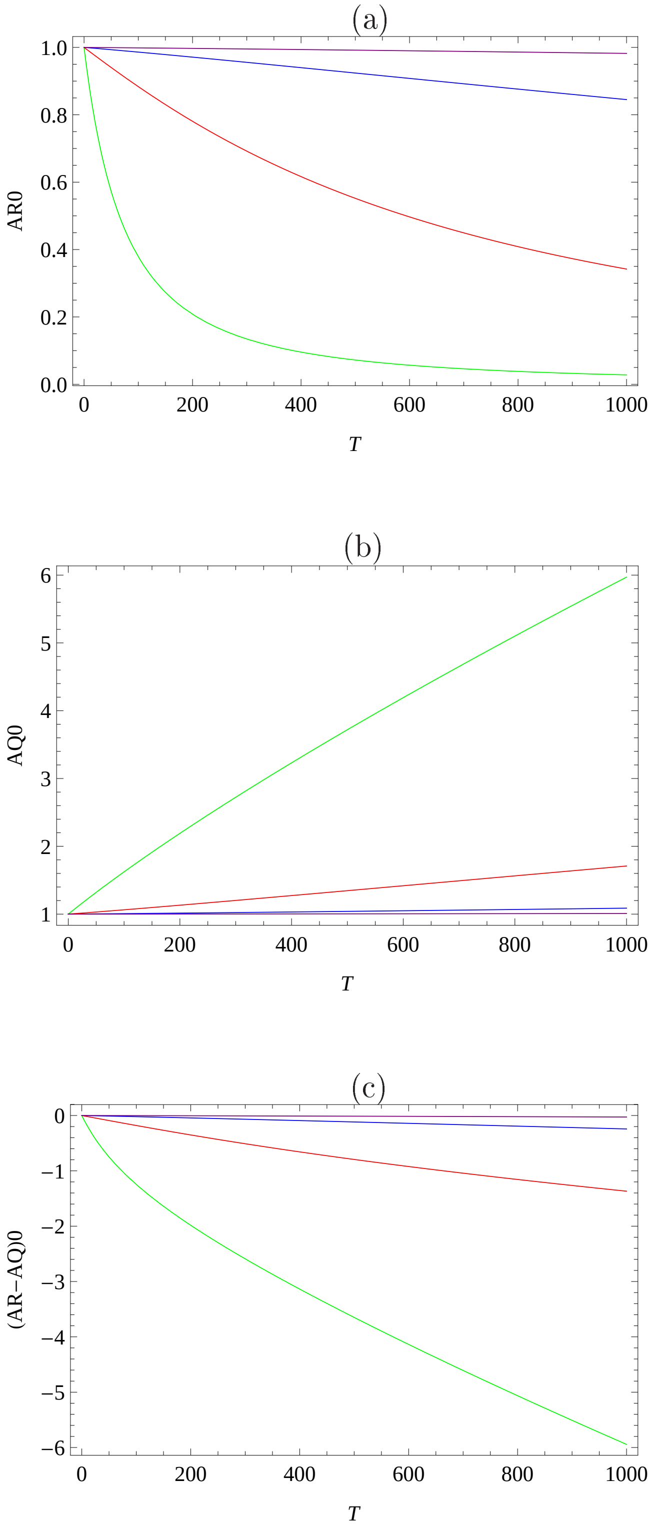

Figure 7.5: Sample plots for the inner solution forms (7.96), (7.97) and (7.98) for different spatial values x given by (a), (b) and (c), respectively. In this case $X \gg U_0$ with $c_v = 0.01$ and $X = 1000$. Green curve: $x = 0$, Red curve: $x = 10$, Blue curve: $x = 100$, Purple curve: $x = 1000$. The plots demonstrate that as we move further from the bubble boundary at $x = 0$ the first normal stress difference, $(AR - AQ)_0$, tends to zero and is constant in time.

order terms in (7.81) and (7.82) respectively and substituting for U_0 to give

$$\begin{aligned} P_0 &= \frac{A + B\left(1 + \frac{5c_v}{6}T\right)^{\frac{6}{5}} + \Phi X}{\left(1 + \frac{5c_v}{6}T\right)^{\frac{6}{5}} + \Phi X}, && (7.99) \\ \phi_0 &= \Phi \frac{p_{g0} - p_a}{p_{g0}} X P_0. && (7.100) \end{aligned}$$

These functions are shown in Figure 7.6 which clearly demonstrates that ϕ_0 is directly proportional to P_0 in this particular case of instantaneous diffusion.

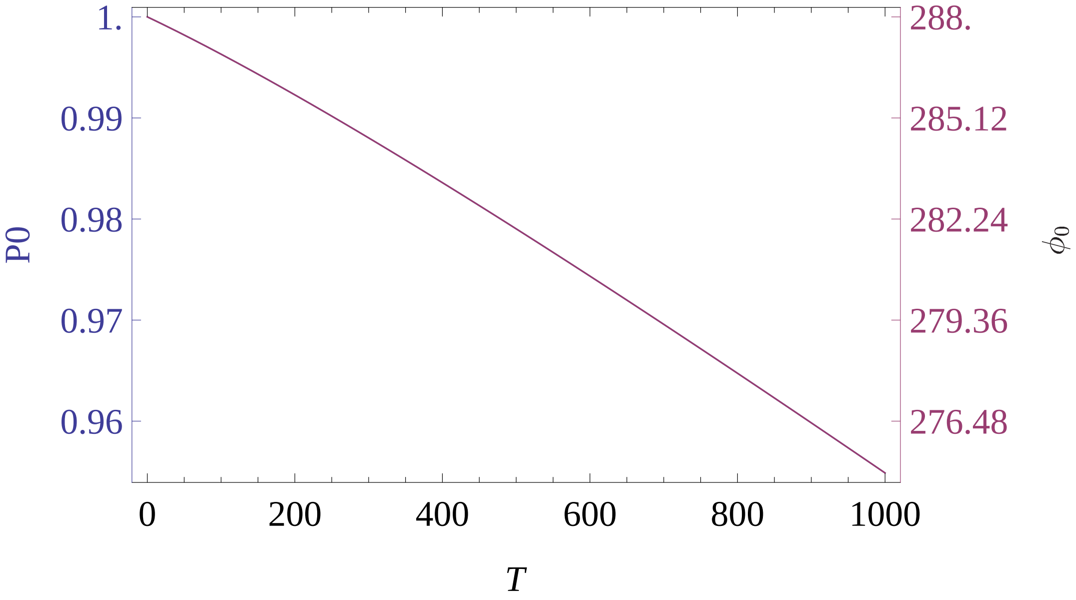

Figure 7.6: Illustration of P_0 (blue curve) and ϕ_0 (purple curve) versus the inner stretched variable T for the case of instantaneous diffusion with $X \gg U_0$. For this particular example $c_v = 0.01$ and the leading order solution U_0 is modelled by (7.95) with P_0 and ϕ_0 described by (7.99) and (7.100), respectively. As the plot and equations illustrate, the leading order concentration potential, ϕ_0, is directly proportional to the leading order bubble gas pressure, P_0, in the case of instantaneous diffusion.

7.5.1.2 Case II: $X/U_0 \sim O(1)$

For parameter sets containing $X/U_0 \sim O(1)$, the leading order inner solution, U_0, is chosen empirically in such a way as to minimise the error over the domain of interest, which in this case we take to be $T \in (0, 1000)$. In the previous section, for $X \gg U_0$, the analytic solution $U_0 = (1 + c_v T/q)^q$ where $q = 6/5$ was derived and shown to be a reasonably accurate approximation. Here a solution of the same form is assumed, that is,

$$U_0 = \left(1 + \frac{c_v}{q} T\right)^q, \tag{7.101}$$

but now the exponent q is determined numerically. The normalised error between the numerical solution of (7.88) and this ansatz is minimised by varying q. The error calculation is given by,

$$e(q) = \frac{\int_0^{T_{\text{end}}} \left| U_{\text{exact}}(T) - U_{\text{approx}}(T, q) \right| dT}{\int_0^{T_{\text{end}}} U_{\text{exact}}(T) dT}, \tag{7.102}$$

where $U_{\text{exact}}(T)$ is the numerical solution of (7.88) and $U_{\text{approx}}(T, q) = (1 + c_v T/q)^q$. Figure 7.7 shows the error plots and a sample plot of the numerical solution and the approximate analytic solution for two different values of X, for a fixed choice of parameter value c_v. Figures 7.7 (a) and (c) illustrate the case when $X = 50$ and (b) and (d) are for $X = 1000$. They demonstrate that as X increases the magnitude of the normalised error over the domain decreases and the associated value of q approaches 6/5. For values of $X/U_0 \sim O(1)$, therefore, this minimising q value is determined and the leading order solution U_0 is set to $U_0 = (1 + c_v T/q)^q$. Figure 7.8 demonstrates the improved accuracy of the semi-analytic solution derived for this second case where $X/U_0 \sim O(1)$ and compares it with the analytic approximation which assumes $X \gg U_0$. The two approximate solutions are measured against the full numeric solution of (7.83) and the semi-analytic result is clearly the most accurate although it is less useful in terms of qualitative solution analysis.

The function U_0 is then used in Section 7.5.2.2 to determine the approximate first order term U_1 in cases where $X/U_0 \sim O(1)$.

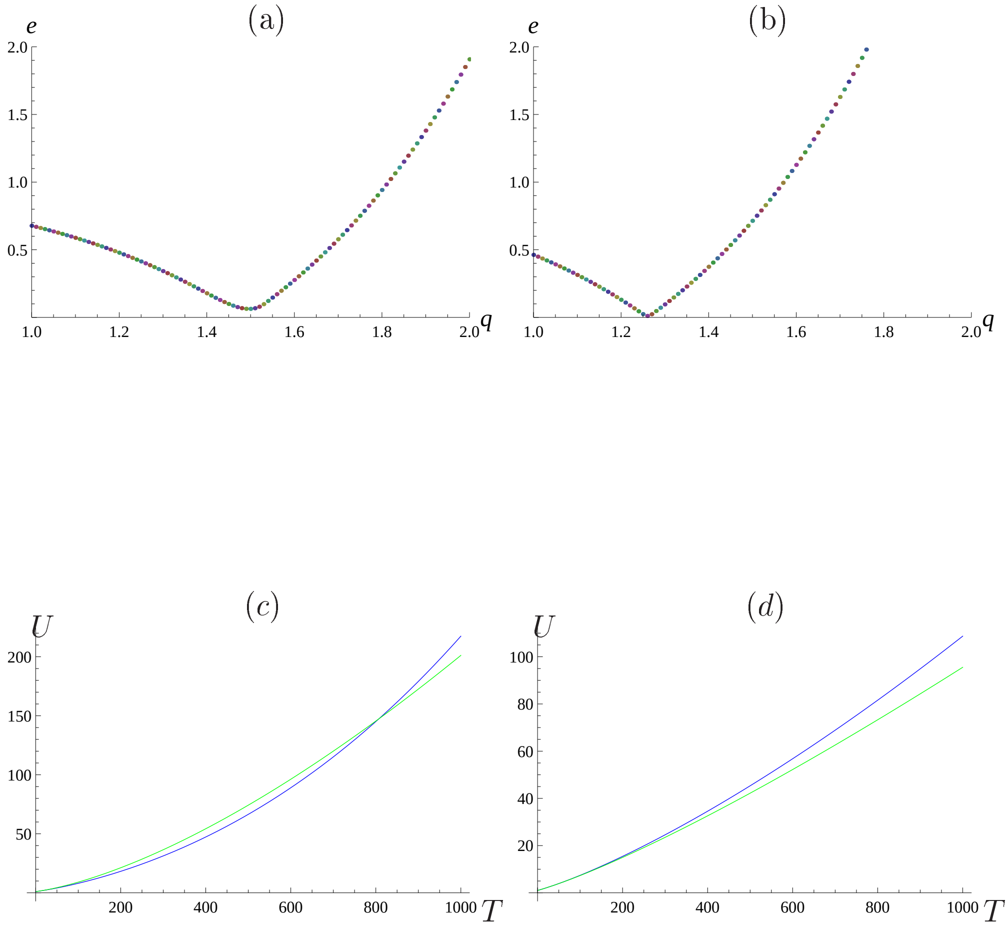

Figure 7.7: Plots (a) and (b) show the normalised error $e(q)$, given by (7.102), versus q, for $X = 50$ and $X = 1000$, respectively. They clearly illustrate an error minimising value for q for a given value of X. Plots (c) and (d) show the corresponding numerical U_{exact}, (blue line), and analytical, U_{approx}, (green line) solutions for this minimising q value which is denoted by q_{min}. In (c) $q_{\text{min}} = 1.5$ and in (d) $q_{\text{min}} = 1.26$; in both cases $c_v = 0.05$. As $X \to \infty$, $q_{\text{min}} \to 6/5$.

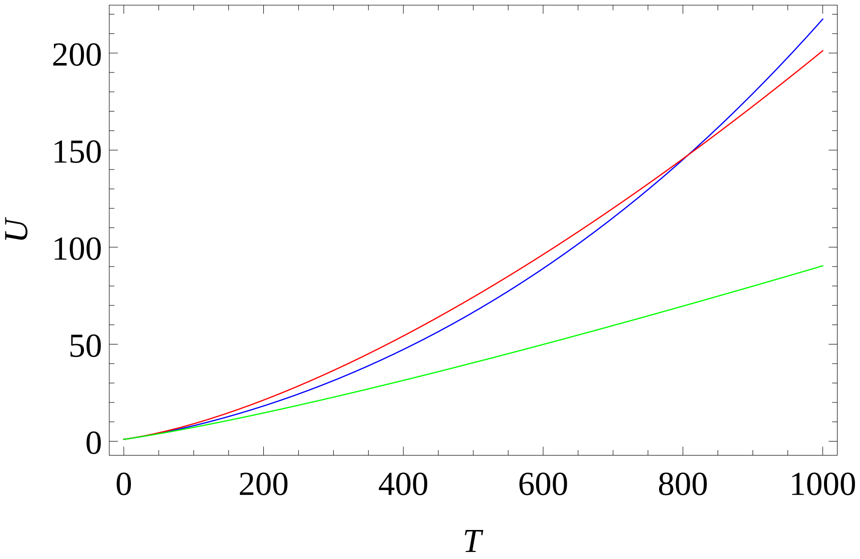

Figure 7.8: A sample plot of the leading order inner solution U_0 versus the stretched inner variable T, for $X/U_0 \sim O(1)$, as modelled by (7.95) (green line), (7.101) with $q = 1.5$ (red line) and the full numerical solution of (7.83) (blue line). In this particular case $c_v = 0.05$ and $X = 50$.

7.5.2 First order solution

Having constructed leading order solutions in the two regimes for the cases of $X \gg U_0$ and $X/U_0 \sim O(1)$, we now seek to derive the first order term U_1 and hence construct the first order asymptotic solution $U \sim U_0 + \eta U_1$. Taking terms of order η in (7.74), (7.76), (7.78), (7.81) and (7.82) results in the first order system,

$$\begin{aligned}&\ddot{U}_1\left(\frac{1}{U_0^{\frac{1}{3}}}-\frac{1}{(X+U_0)^{\frac{1}{3}}}\right)-\dot{U}_1\frac{\dot{U}_0}{3}\left(\frac{1}{U_0^{\frac{4}{3}}}-\frac{1}{(X+U_0)^{\frac{4}{3}}}\right)\\&+U_1\left(\frac{2\dot{U}_0^2}{9}\left(\frac{1}{U_0^{\frac{7}{3}}}-\frac{1}{(X+U_0)^{\frac{7}{3}}}\right)-\frac{\ddot{U}_0}{3}\left(\frac{1}{U_0^{\frac{4}{3}}}-\frac{1}{(X+U_0)^{\frac{4}{3}}}\right)\right)\\&+\frac{4\dot{U}_0}{3\mathcal{R}}\left(\frac{1}{U_0}-\frac{1}{(X+U_0)}\right)=0,\end{aligned} \tag{7.103}$$

$$\frac{\partial AR_1}{\partial T} = -\frac{4}{3(x+U_0)}\left(\dot{U}_1 AR_0 - U_1\frac{\dot{U}_0 AR_0}{(x+U_0)} + \dot{U}_0 AR_1\right) - (AR_0 - 1), \tag{7.104}$$

$$\frac{\partial AQ_1}{\partial T} = \frac{2}{3(x+U_0)}\left(\dot{U}_1 AQ_0 - U_1\frac{\dot{U}_0 AQ_0}{(x+U_0)} + \dot{U}_0 AQ_1\right) - (AQ_0 - 1), \tag{7.105}$$

$$P_1 = \frac{U_1}{U_0 + \Phi X}\left(B - \frac{A + BU_0 + \Phi X}{U_0 + \Phi X}\right), \tag{7.106}$$

$$\hat{\phi}_1 = \Phi\frac{p_{g0} - p_a}{p_{g0}}P_1 X. \tag{7.107}$$

As for the leading order solution, two separate cases are considered, namely large $X \gg U_0$ and $X/U_0 \sim O(1)$; an analytic solution can be derived in the former case while a semi-analytic solution can be found in the latter.

7.5.2.1 Case I: $X \gg U_0$

Equation (7.103) can be expressed as

$$\ddot{U}_1 + \frac{\mathbb{N}_2}{\mathbb{N}_1}\dot{U}_1 + \frac{\mathbb{N}_3}{\mathbb{N}_1}U_1 + \frac{\mathbb{N}_4}{\mathbb{N}_1} = 0, \tag{7.108}$$

where,

$$\mathbb{N}_1 = \frac{1}{U_0^{\frac{1}{3}}} - \frac{1}{(X+U_0)^{\frac{1}{3}}}, \tag{7.109}$$

$$\mathbb{N}_2 = -\frac{\dot{U}_0}{3}\left(\frac{1}{U_0^{\frac{4}{3}}} - \frac{1}{(X+U_0)^{\frac{4}{3}}}\right), \tag{7.110}$$

$$\mathbb{N}_3 = \frac{2\dot{U}_0^2}{9}\left(\frac{1}{U_0^{\frac{7}{3}}} - \frac{1}{(X+U_0)^{\frac{7}{3}}}\right) - \frac{\ddot{U}_0}{3}\left(\frac{1}{U_0^{\frac{4}{3}}} - \frac{1}{(X+U_0)^{\frac{4}{3}}}\right), \tag{7.111}$$

$$\mathbb{N}_4 = \frac{4\dot{U}_0}{3\mathcal{R}}\left(\frac{1}{U_0} - \frac{1}{X+U_0}\right), \tag{7.112}$$

and

$$\begin{aligned} U_0(T) &= \left(1+\frac{5c_vT}{6}\right)^{\frac{6}{5}}, && (7.113)\\ \dot{U}_0(T) &= c_v\left(1+\frac{5c_vT}{6}\right)^{\frac{1}{5}}, && (7.114)\\ \ddot{U}_0(T) &= \frac{c_v^2}{6}\left(1+\frac{5c_vT}{6}\right)^{-\frac{4}{5}}. && (7.115)\end{aligned}$$

The expressions for $\mathbb{N}_i, i = 1, \cdots, 4$ can be expanded in $1/X$ giving the leading order terms,

$$\begin{aligned} \frac{\mathbb{N}_2}{\mathbb{N}_1} &= -\frac{\dot{U}_0}{3U_0} = -\frac{2c_v}{(6+5c_vT)},\\ \frac{\mathbb{N}_3}{\mathbb{N}_1} &= \frac{2\dot{U}_0^2}{9U_0^2} - \frac{\ddot{U}_0}{3U_0} = \frac{6c_v^2}{(6+5c_vT)^2},\\ \frac{\mathbb{N}_4}{\mathbb{N}_1} &= \frac{4\dot{U}_0}{3\mathcal{R}U_0^{\frac{2}{3}}} = \frac{4c_v6^{\frac{3}{5}}}{3\mathcal{R}(6+5c_vT)^{\frac{3}{5}}}.\end{aligned}$$

Substitution of these coefficients into equation (7.108), transforming to the variable $z = (6 + 5c_vT)$ and multiplying by z^2 yields

$$z^2\ddot{U}_1 - \frac{2}{5}z\dot{U}_1 + \frac{6}{25}U_1 = -\frac{4z^26^{\frac{3}{5}}}{75\mathcal{R}c_vz^{\frac{3}{5}}}. \qquad (7.116)$$

This is essentially the Euler differential equation [67]

$$z^2\ddot{U}_1 + az\dot{U}_1 + bU_1 = f(z), \qquad (7.117)$$

with $a = -\frac{2}{5}, b = \frac{6}{25}, s = \frac{1-a}{2}, \nu = \frac{1}{2}|(1-a)^2-4b|^{\frac{1}{2}} > 0$, giving the complementary function

$$\begin{aligned} U_1^c(z) &= E_1z^{(s+\nu)} + E_2z^{(s-\nu)},\\ &= E_1z^{\frac{6}{5}} + E_2z^{\frac{1}{5}},\end{aligned}$$

where the constants E_1 and E_2 are to be determined from the initial conditions. Assuming a particular integral, U_1^p, of the form,

$$U_1^p(z) = Az^{\frac{7}{5}},$$

and substituting into (7.116) gives

$$A = -\frac{6^{\frac{3}{5}}2}{9\mathcal{R}c_v}, \qquad \text{and } U_1^p(z) = Az^{\frac{7}{5}}.$$

Therefore, the general solution is

$$U_1(z) = E_1 z^{\frac{6}{5}} + E_2 z^{\frac{1}{5}} - \frac{2(6^{\frac{3}{5}})}{9\mathcal{R}c_v} z^{\frac{7}{5}}. \tag{7.118}$$

The initial conditions for the first order term $U_1(T)$ are $U_1(0) = \dot{U}_1(0) = 0$ so that in the transformed system $(U_1(z))$ we have $U_1(6) = \dot{U}_1(6) = 0$ giving the following values for the arbitrary constants

$$\begin{aligned} E_1 &= \frac{8}{5\mathcal{R}c_v 6^{\frac{1}{5}}}, && (7.119) \\ E_2 &= -E_1, && (7.120) \end{aligned}$$

and so

$$U_1(z) = \frac{2}{\mathcal{R}c_v}\left(\frac{4}{5(6^{\frac{1}{5}})}\left(z^{\frac{6}{5}} - z^{\frac{1}{5}}\right) - \frac{6^{\frac{3}{5}}}{9} z^{\frac{7}{5}}\right). \tag{7.121}$$

Rewriting in the original inner variable T,

$$U_1(T) = \frac{2}{\mathcal{R}c_v}\left(\frac{4}{5(6^{\frac{1}{5}})}\left((6+5c_vT)^{\frac{6}{5}} - (6+5c_vT)^{\frac{1}{5}}\right) - \frac{6^{\frac{3}{5}}}{9}(6+5c_vT)^{\frac{7}{5}}\right). \tag{7.122}$$

Combining the result for the leading order solution from Section 7.5.1.1, with this result for U_1 the asymptotic inner solution, to first order, for instantaneous diffusion where $X \gg U_0$ can be written as

$$\begin{aligned} U(T) &= U_0(T) + \eta U_1(T), \\ &= \frac{2\eta}{\mathcal{R}c_v}\left(\frac{4}{5(6^{\frac{1}{5}})}\left((6+5c_vT)^{\frac{6}{5}} - (6+5c_vT)^{\frac{1}{5}}\right) - \frac{6^{\frac{3}{5}}}{9}(6+5c_vT)^{\frac{7}{5}}\right) \\ &\quad + \left(1 + \frac{5c_v}{6}T\right)^{\frac{6}{5}}. && (7.123) \end{aligned}$$

A sample solution is displayed in Figure 7.9, and for the parameter set given this first order solution corresponds well with that generated using the numerical solution of (7.108). Whereas the leading order solution (7.95) is parameterised by the initial condition c_v only, this first order solution is parameterised by $c_v, \mathcal{R}$, and η.

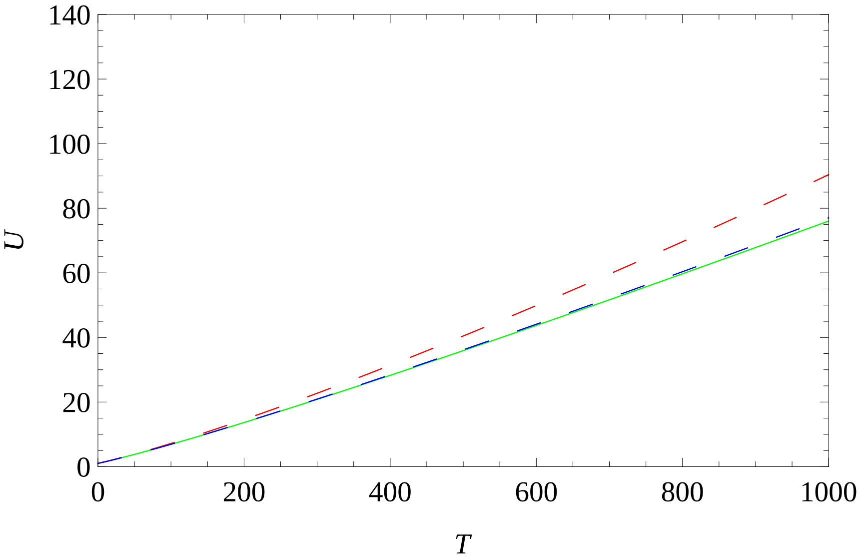

Figure 7.9: Plot of the leading order solution $U = U_0$ (red dashed curve) as modelled by (7.95) and the first order solution $U = U_0 + \eta U_1$ (blue dashed curve) as predicted by (7.123) for the case of $X \gg U_0$ with instantaneous diffusion. The green curve, for comparison, is $U = U_0 + \eta U_1$ where $U = U_0$ is modelled by (7.95) and U_1 is determined numerically from (7.108). The system parameters are given by $c_v = 0.05$, $\mathcal{R} = 1$, and $\eta = 0.001$. For the numerical solution we choose $X = 10^5$.

7.5.2.2 Case II: $X/U_0 \sim O(1)$

In this section we examine the second case which describes conditions in which evolving bubbles are closely spaced within the expanding foam so that $X/U_0 \sim O(1)$. We employ two approaches and then compare the results. A semi-analytic solution is first derived and then compared to the numerical solution of (7.103). Equation (7.103) is rewritten by substituting for the leading order solution $U_0(T) = (1 + c_v T/q)^q$, where q was determined empirically in Section 7.5.1.2.

In (7.108) we then approximate the coefficients by

$$\frac{\mathbb{N}_2(T)}{\mathbb{N}_1(T)} \approx \mathcal{S}_2(T) = \frac{\mathcal{C}_2}{\mathcal{C}_1 + T},$$
$$\frac{\mathbb{N}_3(T)}{\mathbb{N}_1(T)} \approx \mathcal{S}_3(T) = \frac{\mathcal{C}_3}{(\mathcal{C}_1 + T)^2},$$
$$\frac{\mathbb{N}_4(T)}{\mathbb{N}_1(T)} \approx \mathcal{S}_4(T) = \frac{\mathcal{C}_4}{(\mathcal{C}_1 + T)^p},$$

where $\mathcal{C}_i, i = 1, \cdots, 4$ and the exponent p are to be determined. This yields the approximate ODE in U_1

$$\ddot{U}_1 + \mathcal{S}_2(T)\dot{U}_1 + \mathcal{S}_3(T)U_1 + \mathcal{S}_4 = 0. \tag{7.124}$$

The functional forms for $\mathcal{S}_2, \mathcal{S}_3, \mathcal{S}_4$ are chosen in such a way as to make the analytic approximation more tractable, while at the same time maintaining a reasonable degree of accuracy. That is, the denominator exponents for $\mathcal{S}_2, \mathcal{S}_3$ are chosen as 1 and 2, respectively, in order to retrieve the Euler differential equation (7.133) where $z = (\mathcal{C}_1 + T)$.

First, the coefficients $\mathcal{C}_1$ and $\mathcal{C}_2$ that best describe the function $\mathbb{N}_2/\mathbb{N}_1$ given the functional form $\mathcal{C}_2/(\mathcal{C}_1 + T)$ are calculated. The following assignments are made

$$y_{2,0} = \frac{\mathbb{N}_2(0)}{\mathbb{N}_1(0)} = \frac{\mathcal{C}_2}{\mathcal{C}_1}, \tag{7.125}$$
$$y_{2,t^*} = \frac{\mathbb{N}_2(t^*)}{\mathbb{N}_1(t^*)} = \frac{\mathcal{C}_2}{(\mathcal{C}_1 + t^*)} \tag{7.126}$$

where t^* can be chosen to minimise the error of the approximation. The values for $\mathcal{C}_1, \mathcal{C}_2$ are derived from (7.125) and (7.126), respectively

$$\mathcal{C}_1 = \frac{t^* y_{2,t^*}}{(y_{2,0} - y_{2,t^*})}, \qquad \mathcal{C}_2 = \frac{t^* y_{2,0} y_{2,t^*}}{(y_{2,0} - y_{2,t^*})}$$

giving the approximate function,

$$\mathcal{S}_{2,t^*} = \frac{t^* y_{2,0} y_{2,t^*}}{t^* y_{2,t^*} + (y_{2,0} - y_{2,t^*})T}.$$

Figure 7.10 shows that the particular choice of t^* is important for the accuracy of the approximating coefficients $\mathcal{C}_1, \mathcal{C}_2$. For each choice of t^* the error was calculated by integration of the absolute value of the difference between the exact function, $\mathbb{N}_2(T)/\mathbb{N}_1(T)$, and the particular approximation, $\mathcal{S}_{2,t^*}(T)$, over the domain in T. This error value was then plotted against t^*. This is denoted by $e(t^*)$ and is defined by

$$e(t^*) = \int_0^{T_f} \left| \frac{\mathbb{N}_2(T)}{\mathbb{N}_1(T)} - \frac{t^* y_{2,0} y_{2,t^*}}{t^* y_{2,t^*} + (y_{2,0} - y_{2,t^*})T} \right| dT, \tag{7.127}$$

where the domain is given by $[0, T_f]$. Figure 7.10(a) shows the error function for the determination of $\mathcal{C}_1$ and $\mathcal{C}_2$ and indicates a minimising value of $t^* = 300$. This value is then used to construct the best approximation function $\mathcal{S}_2$ which is shown as the blue curve in Figure 7.10(c).

Having optimised and fixed $\mathcal{C}_1, \mathcal{C}_2$, the corresponding error values were calculated and plotted for $\mathcal{C}_3$ and $\mathcal{C}_4$. We designate the fixed values of $\mathcal{C}_1$ and $\mathcal{C}_2$ by $\underline{\mathcal{C}}_1$ and $\underline{\mathcal{C}}_2$ and next determine the function $\mathcal{S}_3$ as follows. We assign

$$y_{3,t^*} = \frac{\mathbb{N}_3(t^*)}{\mathbb{N}_1(t^*)}, \tag{7.128}$$

so that

$$\mathcal{S}_3 = \frac{\mathcal{C}_3}{(\underline{\mathcal{C}}_1 + T)^2}, \tag{7.129}$$

where,

$$\mathcal{C}_3(t^*) = (\underline{\mathcal{C}}_1 + t^*)^2 y_{3,t^*}. \tag{7.130}$$

The choice of t^* used to calculate this value of $\mathcal{C}_3$ will result in a particular error value given by

$$e(t^*) = \int_0^{T_f} \left| \frac{\mathbb{N}_3(T)}{\mathbb{N}_1(T)} - \frac{y_{3,t^*}(\underline{\mathcal{C}}_1 + t^*)^2}{(\underline{\mathcal{C}}_1 + T)^2} \right| dT. \tag{7.131}$$

Figure 7.10(b) shows the results of plotting this error function versus values of $t^* \in [0, T_f]$ and clearly illustrates a minimising value for the choice of t^*. This value is then used to construct the best approximation for $\mathcal{S}_3$ which is then plotted in Figure 7.10(d) with $\mathbb{N}_3/\mathbb{N}_1$ for comparison.

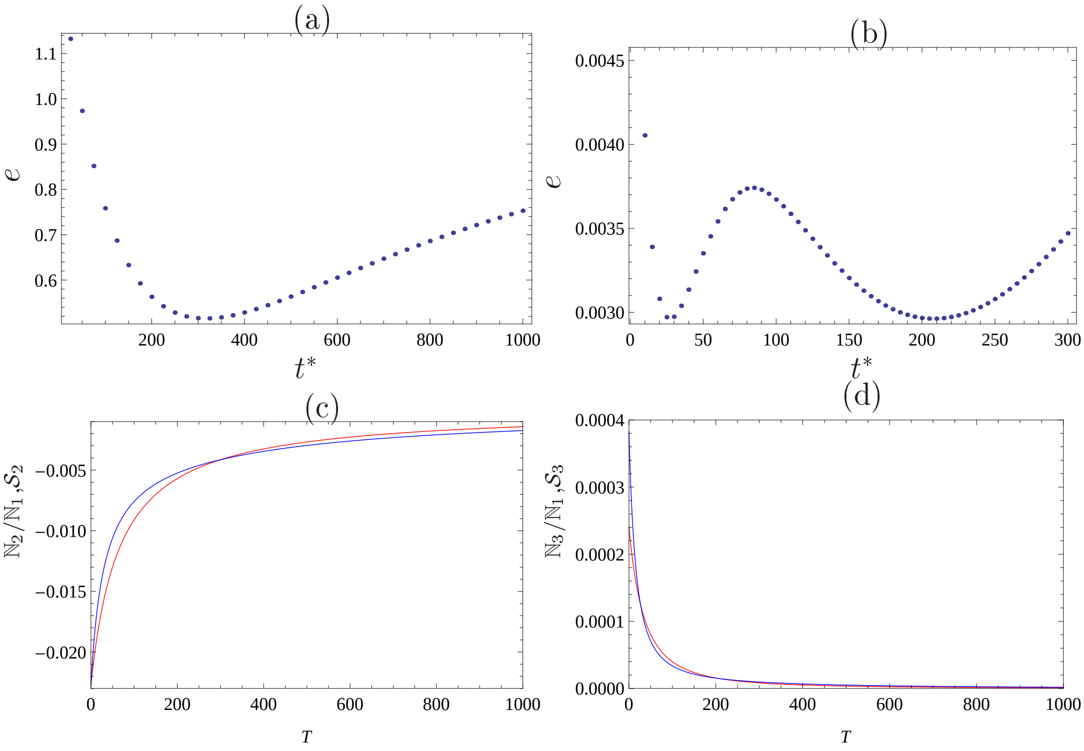

Figure 7.10: Plots showing the error functions $e(t^*)$ versus t^* in order to determine the value of t^* that minimises the error between $\mathbb{N}_i/\mathbb{N}_1$ and $\mathcal{S}_i$ for (a) $i = 2$ and (b) $i = 3$. For $i = 2$ the error function is given by (7.127); for $i = 3$ it is (7.131). As illustrated by (a), for this particular parameterisation, the minimum error for $i = 2$ occurs when $t^* = 300$ and (b) indicates that when $i = 3$ a value of $t^* = 210$ should be chosen to provide the best approximation for $\mathcal{C}_3$. Plots (c) and (d) show $\mathbb{N}_i/\mathbb{N}_1$ and $\mathcal{S}_i$ versus T, plotted using the error minimising values of t^* determined in (a) and (b) respectively. The blue curves show the exact functions $\mathbb{N}_i/\mathbb{N}_1$ (determined from (7.109) - (7.111)) that we are trying to approximate and the red curves show the closest approximation given the functional forms we require. The system parameters are $c_v = 0.05$, $q = 1.5$, $X = 50$, and $\mathcal{R} = 1$.

Note, that in order to determine $\mathcal{C}_4$ the choice of exponent p must also be optimised. We would therefore need to define an error function in terms of t^* and p and optimise over the $t^* - p$ plane. We automate this choice using a non-linear least squares algorithm and use the calculated values of p and t^* that minimise the error, to calculate $\mathcal{C}_4$ and construct S_4. Figure 7.11 shows the best approximate S_4 plotted against the exact function $\mathbb{N}_4/\mathbb{N}_1$ over the domain for a particular choice of parameters c_v, $\mathcal{R}$ and X. Having derived the functional forms for $\mathcal{S}_2, \mathcal{S}_3$ and $\mathcal{S}_4$ we can substitute them into (7.124) to give

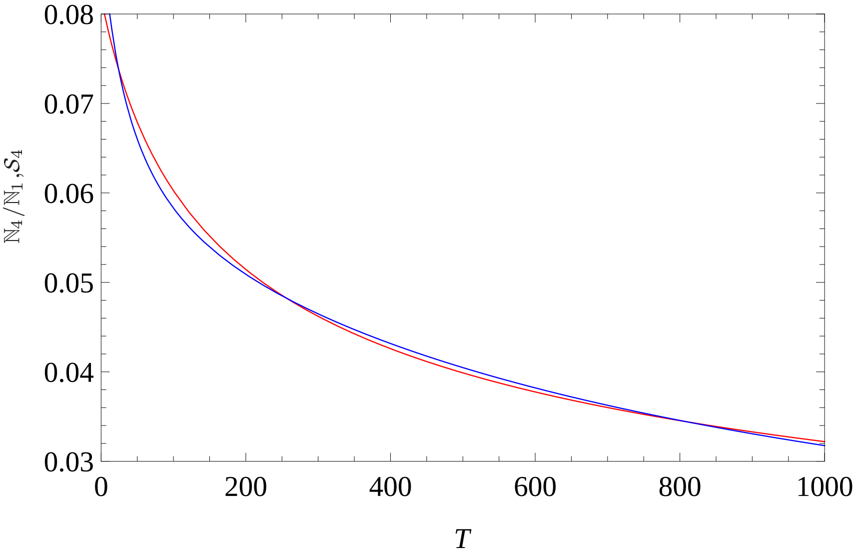

Figure 7.11: Curves of the exact functional form $\mathbb{N}_4/\mathbb{N}_1$ (blue curve) plotted alongside the best fit approximation for S_4 (red curve) as predicted using a non-linear least squares algorithm. The error of the approximation was optimised over the domain $[0, 1000]$ for the choice of t^* and exponent p. The system parameters are $c_v = 0.05$, $q = 1.5$, $X = 50$, and $\mathcal{R} = 1$.

$$\ddot{U}_1 + \frac{\mathcal{C}_2}{(\mathcal{C}_1 + T)}\dot{U}_1 + \frac{\mathcal{C}_3}{(\mathcal{C}_1 + T)^2}U_1 + \frac{\mathcal{C}_4}{(\mathcal{C}_1 + T)^p} = 0, \tag{7.132}$$

where all coefficients and exponents were approximated in Section 7.5.2.2. Transforming variables to $z = \mathcal{C}_1 + T$ and multiplying across by z^2 gives,

$$z^2\ddot{U}_1 + z\mathcal{C}_2\dot{U}_1 + \mathcal{C}_3 U_1 = -\mathcal{C}_4 z^{(2-p)}, \tag{7.133}$$

which permits a complementary function of the form [67],

$$U_1^c(z) = \begin{cases} |z|^{\frac{1-\mathcal{C}_2}{2}}\left(E_1|z|^{\nu} + E_2|z|^{-\nu}\right) & \text{if } (1-\mathcal{C}_2)^2 > 4\mathcal{C}_3, \\ |z|^{\frac{1-\mathcal{C}_2}{2}}\left(E_1 + E_2 \log|z|\right) & \text{if } (1-\mathcal{C}_2)^2 = 4\mathcal{C}_3, \\ |z|^{\frac{1-\mathcal{C}_2}{2}}\left(E_1 \sin(\nu \log|z|) + E_2 \cos(\nu \log|z|)\right) & \text{if } (1-\mathcal{C}_2)^2 < 4\mathcal{C}_3. \end{cases} \tag{7.134}$$

where $\nu = 1/2|(1-\mathcal{C}_2)^2 - 4\mathcal{C}_3|^{1/2}$. In the previous section 7.5.2.2 only the exponential solution to the associated Euler differential equation was permitted since the coefficients of $\dot{U}_1$ and U_1 were known and fixed. In this case, where C_2 and C_3 depend on X and c_v, it is not immediately obvious which branch of the Euler solution should be chosen for a given parameter set. Therefore, in this section we chose the same functional form that was used in the case of $X \gg U_0$, so that $(1-\mathcal{C}_2)^2 > 4\mathcal{C}_3$ is satisfied and the complementary functional form is therefore $U_1^c = |z|^{\frac{1-\mathcal{C}_2}{2}}\left(E_1|z|^{\nu} + E_2|z|^{-\nu}\right)$ and the particular integral is given by

$$U_1^p(z) = \frac{\mathcal{C}_4 z^{(2-p)}}{(2-p-s-\nu)(2-p-s+\nu)}, \qquad \text{where } s = \frac{1-\mathcal{C}_2}{2}. \tag{7.135}$$

The general solution is

$$U_1(z) = E_1|z|^{s+\nu} + E_2|z|^{s-\nu} + E_3 z^{2-p}, \tag{7.136}$$

where,

$$E_3 = -\frac{\mathcal{C}_4}{(2-p-s-\nu)(2-p-s+\nu)}. \tag{7.137}$$

and the constants E_1, E_2 are determined from initial conditions, $U_1(T=0) = \dot{U}_1(T=0) = 0$, in the transformed variable z, that is, $U_1(z=\mathcal{C}_1) = \dot{U}_1(z=\mathcal{C}_1) = 0$, so that

$$E_1 = \frac{\mathcal{C}_4}{2\nu(2-p-s-\nu)} C_1^{(2-p-s-\nu)}, \tag{7.138}$$

$$E_2 = -\frac{\mathcal{C}_4}{2\nu(2-p-s+\nu)} C_1^{(2-p-s+\nu)}. \tag{7.139}$$

Rewriting in the original inner variable T therefore,

$$U_1(T) = E_1(\mathcal{C}_1 + T)^{(s+\nu)} + E_2(\mathcal{C}_1 + T)^{(s-\nu)} + E_3(\mathcal{C}_1 + T)^{(2-p)} \tag{7.140}$$

and combining with the leading order solution gives the first order inner asymptotic approximate solution for finite X as,

$$U(T) = \left(1 + \frac{c_v}{q}T\right)^q + \eta\left(E_1(\mathcal{C}_1 + T)^{(s+\nu)} + E_2(\mathcal{C}_1 + T)^{(s-\nu)} + E_3(\mathcal{C}_1 + T)^{(2-p)}\right). \tag{7.141}$$

In Figure 7.12 we compare this analytic first order approximate solution (blue curve) to the first order solution (green curve) using U_1 generated via the numerical solution of the original ODE equation (7.108). The approximation is less accurate than in the case for $X \gg U_0$ (see Figure 7.9).

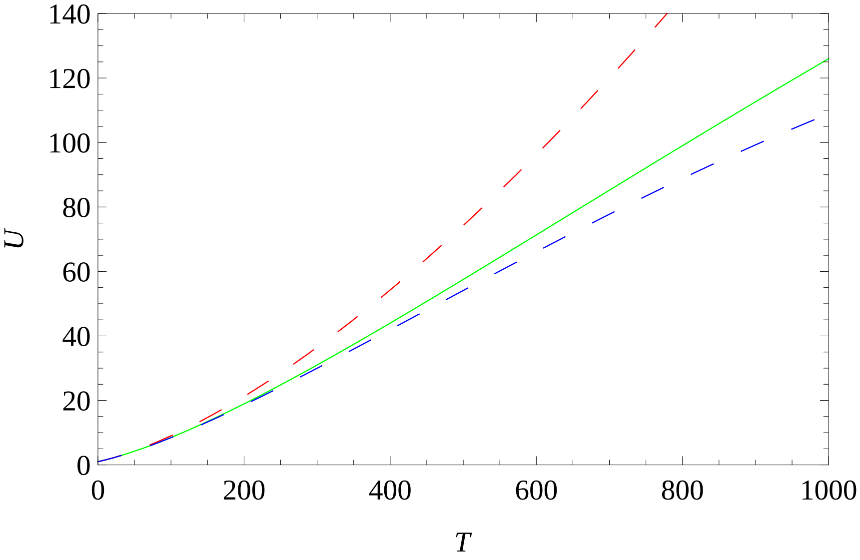

Figure 7.12: Plot comparing the leading order solution $U = U_0$ (red curve) as modelled by (7.101) and the first order solution $U = U_0 + \eta U_1$ given by (7.141). In this case X is $O(U_0)$ and an approximate analytic solution is chosen for U_0 as described in Section 7.5.1.2 and for U_1 as described in Section 7.5.2.2. The green curve, for comparison, is $U = U_0 + \eta U_1$, where U_0 is determined as described above and U_1 is the numerical solution of (7.108). The pertinent parameter values are $c_v = 0.05$, $q = 1.5$, $\mathcal{R} = 1$ and $X = 50$.

7.5.3 Discussion

In Section 7.5 we derived two possible first order inner solutions for U. The first was an analytic solution for Case I, when $X \gg U_0$, given by,

$$\begin{aligned} U(T) &= \left(1+\frac{5c_v}{6}T\right)^{\frac{6}{5}} \\ &\quad +\frac{2\eta}{\mathcal{R}c_v}\left(\frac{4}{5(6^{\frac{1}{5}})}\left((6+5c_vT)^{\frac{6}{5}}-(6+5c_vT)^{\frac{1}{5}}\right)-\frac{6^{\frac{3}{5}}}{9}(6+5c_vT)^{\frac{7}{5}}\right), \end{aligned} \tag{7.142}$$

and the second was a semi analytic approximation for Case II when $X/U_0 \sim O(1)$,

$$U(T) = \left(1+\frac{c_v}{q}T\right)^{q} + \eta\left(E_1(\mathcal{C}_1+T)^{(s+\nu)} + E_2(\mathcal{C}_1+T)^{(s-\nu)} + E_3(\mathcal{C}_1+T)^{(2-p)}\right), \tag{7.143}$$

where E_1, E_2 and E_3 are defined by (7.138), (7.139) and (7.137) respectively.

In Case I the dependence of the solution on the system parameters $c_v, \eta, \mathcal{R}$ is explicit whereas in Case II this dependence is implicit and can only be illustrated numerically which is a drawback of the semi-analytic solution.

We cannot make a direct comparison between Cases I and II, since one of the parameters X necessarily changes giving a different solution for each case. We can, however, conclude that the accuracy of the first order solutions predicted in Case I ($X \gg U_0$) is greater than observed in the semi-analytic solutions produced in Case II ($X/U_0 \sim O(1)$), when both solutions are compared to their associated numerical solution of (7.108). Since we are considering the inner solution, Case I ($X \gg U_0$) is most relevant as it describes the polymerisation at early time when small bubbles are surrounded by a large fluid volume.

For Case I we can examine the effect of inertia on the analytic first order solution by altering the grouped parameter $\mathcal{R}$ while keeping η and c_v fixed. In order to compare these results with the case of negligible inertia we solve (7.63) for $\mathcal{R} = 0$, to first order in η as follows:

$$\frac{4}{3}\dot{U}\left(\frac{1}{U} - \frac{1}{X+U}\right) = 0, \tag{7.144}$$

so that, for the stretched inner variable T, $X \gg U$ (as in Case I) we obtain the ordinary differential equation $\dot{U} = 0$ with solution $U = c_v T + 1$ where the initial conditions are given by $\dot{U}(0) = c_v$ and $U(0) = 1$. In Figure 7.13 we can see that for fixed values of η and c_v, as $\mathcal{R}$ increases the bubble volume, U, increases more rapidly as inertia increases and converges to the leading order solution $U_0 = (1 + 5c_v T/6)^{6/5}$. It is important to note that these analytic solutions are only valid for $\mathcal{R} \gg \eta$ on the timescale $t = \eta T$.

For further discussion of the significance of the relationship between $\mathcal{R}$ and η see Section 7.7.

7.6 Asymptotic analysis: Outer solution

In Section 7.5.1 we stretched the time variable t according to $T = t/\eta$ and expanded in terms of η to derive the inner solution. Then for the sake of a more convenient analysis we assumed the following relationship in scale between the inertia-type grouped parameter $\mathcal{R}$ and η such that $\mathcal{R} \gg \eta$. In this way we were able to reduce (7.74) to (7.83) and thus derive the analytic form for the solution, (7.123), for the particular case when $X \gg U_0$. For the outer solution we expand in $\mathcal{R}$ noting the scaling assumption we made for the inner solution, namely, $\mathcal{R} \gg \eta$. We, therefore, look for an expansion, in the outer temporal variable, t, of the form

$$u(t,\mathcal{R}) = u_0(t) + \mathcal{R}u_1(t) + O(\mathcal{R}^2), \tag{7.145}$$

$$A_{rr}(x,t,\mathcal{R}) = A_{rr_0}(x,t) + \mathcal{R}A_{rr_1}(x,t) + O(\mathcal{R}^2), \tag{7.146}$$

$$A_{\theta\theta}(x,t,\mathcal{R}) = A_{\theta\theta_0}(x,t) + \mathcal{R}A_{\theta\theta_1}(x,t) + O(\mathcal{R}^2). \tag{7.147}$$

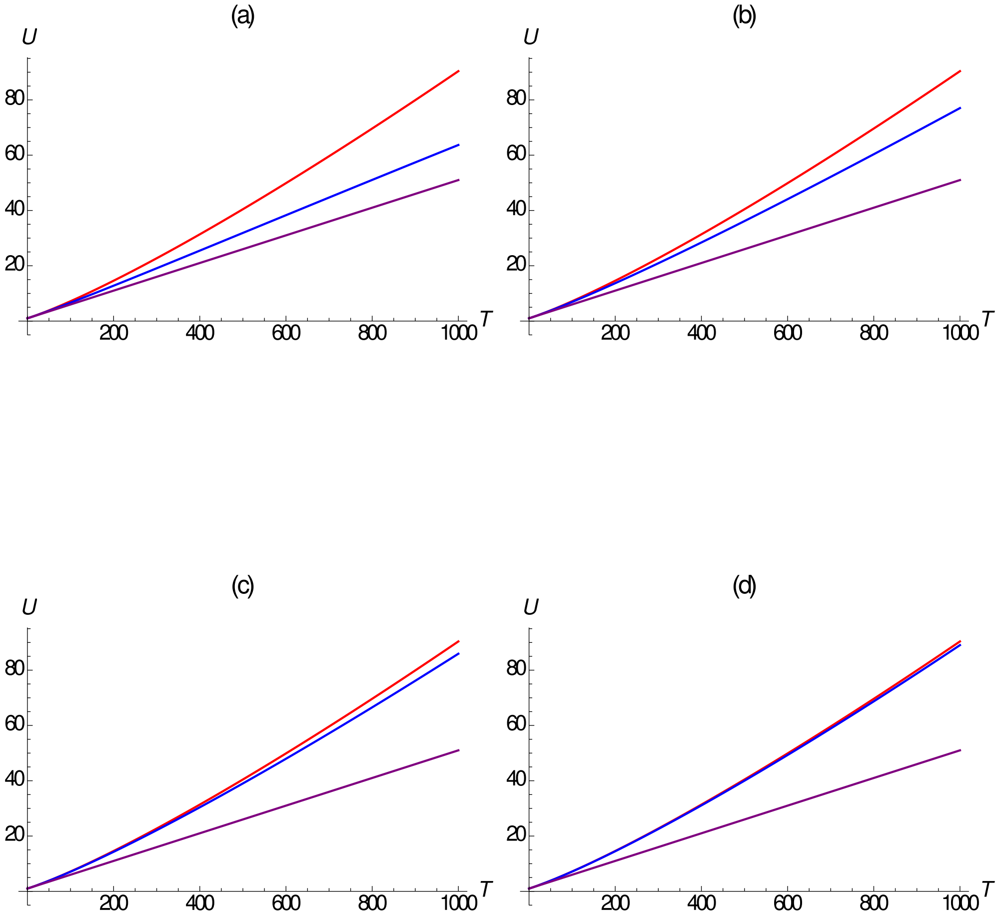

Figure 7.13: Plots illustrating the following analytic solutions for Case I ($X \gg U_0$): the leading order solution (7.95) $U = U_0$ (red curve), the first order solution $U = U_0 + \eta U_1$ (blue curve) given by (7.123) and the leading order solution in the case of negligible inertia, $U = c_v T + 1$ (purple curve). In all cases $\eta = 10^{-4}$, $c_v = 0.05$ and $\mathcal{R} \gg \eta$. The grouped parameter $\mathcal{R}$ is given by (a) $\mathcal{R} = 0.05$, (b) $\mathcal{R} = 0.1$, (c) $\mathcal{R} = 0.3$ and (d) $\mathcal{R} = 1.0$. These figures demonstrate that as $\mathcal{R}$ increases within this regime, the bubble volume increases more rapidly.

Substituting for (7.145) in (7.62) we can derive the expansion for P_g as follows

$$\begin{aligned}
P_g &= \frac{A+B(u_0+\mathcal{R}u_1)+\Phi X}{u_0+\mathcal{R}u_1+\Phi X}+O(\mathcal{R}^2),\\
&= \frac{A+Bu_0+\mathcal{R}Bu_1+\Phi X}{(u_0+\Phi X)\left(1+\mathcal{R}\frac{u_1}{u_0+\Phi X}\right)}+O(\mathcal{R}^2),\\
&= \frac{(A+Bu_0+\mathcal{R}Bu_1+\Phi X)}{u_0+\Phi X}\left(1-\frac{\mathcal{R}u_1}{u_0+\Phi X}\right)+O(\mathcal{R}^2),\\
&= \left(\frac{A+Bu_0+\Phi X}{u_0+\Phi X}\right)+\mathcal{R}\left(\frac{Bu_1}{u_0+\Phi X}-\frac{u_1(A+Bu_0+\Phi X)}{(u_0+\Phi X)^2}\right)+O(\mathcal{R}^2),\\
&= P_{g_0}+\mathcal{R}P_{g_1}+O(\mathcal{R}^2).
\end{aligned}$$

Using these in (7.48) we get the following

$$\begin{aligned}
&\frac{4}{3}(\dot{u}_0+\mathcal{R}\dot{u}_1)\left(\frac{1}{u_0+\mathcal{R}u_1}-\frac{1}{(X+u_0+\mathcal{R}u_1)}\right)\\
&+\mathcal{R}\left[(\ddot{u}_0+\mathcal{R}\ddot{u}_1)\left(\frac{1}{(u_0+\mathcal{R}u_1)^{\frac{1}{3}}}-\frac{1}{(X+u_0+\mathcal{R}u_1)^{\frac{1}{3}}}\right)\right.\\
&\left.-\frac{(\dot{u}_0+\mathcal{R}\dot{u}_1)^2}{6}\left(\frac{1}{(u_0+\mathcal{R}u_1)^{\frac{4}{3}}}-\frac{1}{(X+u_0+\mathcal{R}u_1)^{\frac{4}{3}}}\right)\right]\\
&= De(P_{g_0}+\mathcal{R}P_{g_1}-P_u)+\frac{2}{3}\gamma\int_0^X\frac{(A_{rr_0}+\mathcal{R}A_{rr_1})-(A_{\theta\theta_0}+\mathcal{R}A_{\theta\theta_1})}{(x+u_0+\mathcal{R}u_1)}dx\\
&-\frac{1}{\Gamma(u_0+\mathcal{R}u_1)^{\frac{1}{3}}}+O(\mathcal{R}^2).
\end{aligned}$$

Using a Taylor series expansion we can write this as

$$\begin{aligned}
&\frac{4}{3}(\dot{u}_0+\mathcal{R}\dot{u}_1)\left[\frac{1}{u_0}\left(1-\frac{\mathcal{R}u_1}{u_0}\right)-\frac{1}{(X+u_0)}\left(1-\frac{\mathcal{R}u_1}{(X+u_0)}\right)\right]\\
&+\mathcal{R}\left[(\ddot{u}_0+\mathcal{R}\ddot{u}_1)\left(\frac{1}{u_0^{\frac{1}{3}}}\left(1-\frac{\mathcal{R}u_1}{3u_0}\right)-\frac{1}{(X+u_0)^{\frac{1}{3}}}\left(1-\frac{\mathcal{R}u_1}{3(X+u_0)}\right)\right)\right.\\
&\left.-\frac{(\dot{u}_0+\mathcal{R}\dot{u}_1)^2}{6}\left(\frac{1}{u_0^{\frac{4}{3}}}\left(1-\frac{4\mathcal{R}u_1}{3u_0}\right)-\frac{1}{(X+u_0)^{\frac{4}{3}}}\left(1-\frac{4\mathcal{R}u_1}{3(X+u_0)}\right)\right)\right]\\
&= De(P_{g_0}+\mathcal{R}P_{g_1}-P_u)-\frac{1}{\Gamma u_0^{\frac{1}{3}}}\left(1-\frac{\mathcal{R}u_1}{3u_0}\right)\\
&+\frac{2}{3}\gamma\int_0^X\frac{(A_{rr_0}+\mathcal{R}A_{rr_1})-(A_{\theta\theta_0}+\mathcal{R}A_{\theta\theta_1})}{(x+u_0)}\left(1-\frac{\mathcal{R}u_1}{(x+u_0)}\right)+O(\mathcal{R}^2).
\end{aligned}$$

To leading order in $\mathcal{R}$, therefore, the momentum equation is

$$\frac{4}{3}\dot{u}_0\left(\frac{1}{u_0}-\frac{1}{X+u_0}\right)=De(P_{g_0}-P_u)+\frac{2}{3}\gamma\int_0^X\frac{(A_{rr}-A_{\theta\theta})_0}{x+u_0}dx-\frac{1}{\Gamma u_0^{\frac{1}{3}}}. \quad (7.148)$$

We then expand the other equations in the system in the same way, so that to leading order in $\mathcal{R}$ we have

$$\frac{\partial A_{rr_0}}{\partial t}=-\frac{4}{3}\frac{\dot{u}_0A_{rr_0}}{(x+u_0)}-(A_{rr_0}-1). \quad (7.149)$$

and

$$\frac{\partial A_{\theta\theta_0}}{\partial t}=\frac{2}{3}\frac{\dot{u}_0A_{\theta\theta_0}}{(x+u_0)}-(A_{\theta\theta_0}-1). \quad (7.150)$$

7.6.1 Leading order system for the outer solution

Assembling the leading order equations together then,

$$\dot{u}_0 = \frac{3u_0(X+u_0)}{4X}\left(De(P_{g_0}-P_u)+\frac{2}{3}\gamma\int_0^X\frac{(A_{rr}-A_{\theta\theta})_0}{x+u_0}dx-\frac{1}{\Gamma u_0^{\frac{1}{3}}}\right), \quad (7.151)$$

$$\frac{\partial A_{rr_0}}{\partial t} = -\frac{4}{3}\frac{\dot{u}_0}{(x+u_0)}A_{rr_0}-(A_{rr_0}-1), \quad (7.152)$$

$$\frac{\partial A_{\theta\theta_0}}{\partial t} = \frac{2}{3}\frac{\dot{u}_0}{(x+u_0)}A_{\theta\theta_0}-(A_{\theta\theta_0}-1), \quad (7.153)$$

$$P_{g_0} = \frac{A+Bu_0+\Phi X}{u_0+\Phi X}, \quad (7.154)$$

$$\phi_0(x,t) = \Phi\frac{p_{g_0}-p_a}{p_{g_0}}(P_{g_0}-1)X, \quad (7.155)$$

with the arbitrary initial conditions $u_0(t^*)=u_0^*$, $P_{g_0}(t^*)=P_{g_0}^*$, $A_{rr_0}(x,t^*)=A_{rr_0}^*(x)$, $A_{\theta\theta_0}(x,t^*)=A_{\theta\theta_0}^*(x)$ and $\phi_0(t^*)=\phi_0^*$.

In order to make analytical headway we need to derive an expression for the integrand in the momentum equation, that is $(A_{rr}-A_{\theta\theta})_0/(x+u_0)$. We can do this by applying the integrating factor method to the temporal integration of the rate equations in A_{rr_0} and $A_{\theta\theta_0}$. We proceed by rearranging (7.152) to give,

$$\frac{\partial A_{rr_0}}{\partial t}+\left(\frac{4}{3}\frac{\dot{u}_0}{(x+u_0)}+1\right)A_{rr_0}=1,$$

and employing the integrating factor,

$$\begin{aligned} p(x,t) &= \exp\left(\int\left[\frac{4}{3}\frac{\dot{u}_0}{x+u_0}+1\right]dt\right), \\ &= e^t(x+u_0)^{\frac{4}{3}}, \end{aligned}$$

we obtain an expression for $A_{rr_0}(x,t)$ in terms of x, $u_0(t)$ and a function of integration $C(x)$,

$$A_{rr_0}(x,t) = e^{-t}(x+u_0)^{-\frac{4}{3}}\left[\int^t e^{\hat{t}}(x+u_0)^{\frac{4}{3}}d\hat{t} + C(x)\right],$$

where $C(x)$ is given by the initial conditions as follows

$$A^*_{rr_0}(x,t^*) = A^*_{rr_0}(x) = e^{-t^*}(x+u_0^*)^{-\frac{4}{3}}\left[\int^{t^*} e^{\hat{t}}(x+u_0)^{\frac{4}{3}}d\hat{t} + C(x)\right].$$

Rearranging for $C(x)$ gives,

$$C(x) = e^{t^*}(x+u_0^*)^{\frac{4}{3}}A^*_{rr_0}(x) - \int^{t^*} e^{\hat{t}}(x+u_0)^{\frac{4}{3}}d\hat{t}$$

and therefore,

$$A_{rr_0}(x,t) = e^{-t}(x+u_0)^{-\frac{4}{3}}\int_{t^*}^t e^{\hat{t}}(x+u_0)^{\frac{4}{3}}d\hat{t} + A^*_{rr_0}(x)e^{t^*-t}\left(\frac{x+u_0^*}{x+u_0}\right)^{\frac{4}{3}}. \quad (7.156)$$

Similarly,

$$A_{\theta\theta_0}(x,t) = e^{-t}(x+u_0)^{\frac{2}{3}}\int_{t^*}^t e^{\hat{t}}(x+u_0)^{-\frac{2}{3}}d\hat{t} + A^*_{\theta\theta_0}(x)e^{t^*-t}\left(\frac{x+u_0}{x+u_0^*}\right)^{\frac{2}{3}}. \quad (7.157)$$

The function $(A_{rr} - A_{\theta\theta})_0(x)$ is obtained by simply subtracting $A_{\theta\theta_0}(x)$ from $A_{rr0(x)}$,

$$\begin{aligned} (A_{rr} - A_{\theta\theta})_0(x,t) &= e^{-t}\left[(x+u_0)^{-\frac{4}{3}}\int_{t^*}^t e^{\hat{t}}(x+u_0)^{\frac{4}{3}}d\hat{t}\right. \\ &- (x+u_0)^{\frac{2}{3}}\int_{t^*}^t e^{\hat{t}}(x+u_0)^{-\frac{2}{3}}d\hat{t} \\ &+ \left. e^{t^*}\left(A^*_{rr_0}(x)\left(\frac{x+u_0^*}{x+u_0}\right)^{\frac{4}{3}} - A^*_{\theta\theta_0}(x)\left(\frac{x+u_0}{x+u_0^*}\right)^{\frac{2}{3}}\right)\right] \end{aligned} \quad (7.158)$$

Finally, we can describe the integrand $I(u_0, x, t) = (A_{rr} - A_{\theta\theta})_0(x, t)/(x + u_0)$ as

$$\begin{aligned}
I(u_0, x, t) &= \frac{(A_{rr} - A_{\theta\theta})_0\,(x, t)}{(x + u_0)}, \\
&= I_1(u_0, x, t) - I_2(u_0, x, t) + I_3(u_0, x, t), \\
&= f_1(u_0, x, t) \int_{t^*}^{t} k_1(u_0, x, \hat{t})d\hat{t} - f_2(u_0, x, t) \int_{t^*}^{t} k_2(u_0, x, \hat{t})d\hat{t} + f_3(u_0, x, t),
\end{aligned}$$

where,

$$\begin{aligned}
f_1(u_0, x, t) &= e^{-t}(x + u_0)^{-\frac{7}{3}}, \\
f_2(u_0, x, t) &= e^{-t}(x + u_0)^{-\frac{1}{3}}, \\
f_3(u_0, x, t) &= e^{t^*-t}\left(A^*_{rr_0}(x)(x + u_0^*)^{\frac{4}{3}}(x + u_0)^{-\frac{7}{3}} - A^*_{\theta\theta_0}(x)(x + u_0^*)^{-\frac{2}{3}}(x + u_0)^{-\frac{1}{3}}\right), \\
k_1(u_0, x, \hat{t}) &= e^{\hat{t}}(x + u_0)^{\frac{4}{3}}, \\
k_2(u_0, x, \hat{t}) &= e^{\hat{t}}(x + u_0)^{-\frac{2}{3}}.
\end{aligned}$$

7.6.2 Analytic Picard iteration to determine the leading order outer solution

To leading order the momentum equation (7.151) can thus be written,

$$\dot{u}_0 = \frac{3}{4}\frac{u_0}{X}(X+u_0)\left[De\left(\frac{A + Bu_0 + \Phi X}{u_0 + \Phi X}\right) - P_u De + \frac{2}{3}\gamma\int_0^X I(u_0, x, t)dx - \frac{1}{\Gamma u_0^{\frac{1}{3}}}\right], \tag{7.159}$$

that is,

$$\begin{aligned}
\dot{u}_0 = \frac{3}{4}\frac{u_0}{X}(X + u_0)\Bigg\{&De\left(\frac{A + Bu_0 + \Phi X}{u_0 + \Phi X}\right) - P_u De - \frac{1}{\Gamma u_0^{\frac{1}{3}}} \\
&+\frac{2}{3}\gamma e^{-t}\Bigg[\int_0^X \Bigg((x + u_0)^{-\frac{7}{3}} \int^t e^{\hat{t}}(x + u_0)^{\frac{4}{3}}d\hat{t} - (x + u_0)^{-\frac{1}{3}} \int^t e^{\hat{t}}(x + u_0)^{-\frac{2}{3}}d\hat{t} \\
&+ e^{t^*}\left((x + 1)^{\frac{4}{3}}(x + 1)^{-\frac{7}{3}} - (x + 1)^{-\frac{2}{3}}(x + 1)^{-\frac{1}{3}}\right)\Bigg)dx\Bigg]\Bigg\}.
\end{aligned}$$

This is of the form,

$$\dot{u}_0 = g(u_0, t), \tag{7.160}$$

and an approximate solution can be found using the Picard iteration method [10]. We derive the first Picard iterate, $u_0^{p1}(t)$, analytically and then produce a numerical algorithm to test the accuracy of this first analytic iteration. The first iteration of the Picard method is given by,

$$u_0^{p1}(t) = u_0^* + \int_{t^*}^{t} g(u_0^*, t)dt, \tag{7.161}$$

where $u_0^* = u_0(t^*)$ so that, for example, assigning $t^* = 0$, $u_0(0) = A_{rr_0}(x, 0) = A_{\theta\theta_0}(x, 0) = 1$ we have

$$\begin{aligned} g(1,t) = \frac{3(X+1)}{4X}\Bigg\{ & De\left(\frac{A+B+\Phi X}{1+\Phi X}\right) - P_u De - \frac{1}{\Gamma} \\ & + \frac{2}{3}\gamma e^{-t}\Bigg[\int_0^X \Bigg((x+1)^{-\frac{7}{3}}\int_0^t e^{\hat{t}}(x+1)^{\frac{4}{3}}d\hat{t} - (x+1)^{-\frac{1}{3}}\int_0^t e^{\hat{t}}(x+1)^{-\frac{2}{3}}d\hat{t} \\ & + \left(A_{rr_0}^*(x)(x+u_0^*)^{\frac{4}{3}}(x+u_0)^{-\frac{7}{3}} - A_{\theta\theta_0}^*(x)(x+u_0^*)^{-\frac{2}{3}}(x+u_0)^{-\frac{1}{3}}\right)\Bigg)dx\Bigg]\Bigg\}. \end{aligned}$$

The first two integrals cancel each other out and, the spatial integral vanishes so that

$$g(1,t) = C_5,$$

where we assign

$$C_5 = \frac{3(X+1)}{4X}\left[De\left(\frac{A+B+\Phi X}{1+\Phi X}\right) - P_u De - \frac{1}{\Gamma}\right].$$

The first iterate of the Picard approximation, for the leading order outer solution is therefore,

$$\begin{aligned} u_0^{(p_1)} &= u_0^* + \int_{t^*}^{t} g(u_0^*, \hat{t})d\hat{t}, \\ &= 1 + \int_0^t C_5 d\hat{t}, \\ &= 1 + C_5 t, \end{aligned} \tag{7.162}$$

since the particular initial conditions chosen prescribe a function of integration equal to zero. Therefore,

$$u_0^{(p_1)} = 1 + C_5 t, \tag{7.163}$$

which is simply a linear solution. The second Picard iteration is given by

$$u_0^{(p_2)} = 1 + \int_0^t g(1 + C_5\hat{t}, \hat{t})d\hat{t}. \tag{7.164}$$

However, due to the complexity of the momentum equation and the form of the first Picard iterate, the analytic form for the second iteration would be cumbersome and unwieldy. So in order to assess the accuracy of the first Picard iterate, (7.159) was solved numerically, in Section 7.6.3.

Plots of this leading order analytic Picard approximation are illustrated in Figures 7.14 (a) and (b), for a range of values of P_u and De, respectively. The grouped parameter De is the ratio of the bubble growth rate in the solvent to the relaxation rate of the polymer and is inversely proportional to the viscosity value μ. We can see from Figure 7.14 (b) that as viscosity decreases, for a constant initial gas pressure difference across the bubble wall, the initial bubble growth rate increases as expected. However, we will see in the next section that, although the numerical solution predicts the same qualitative increase it asymptotes to a steady state value whereas the Picard solution does not. This is not unexpected since we have only carried out one iteration of the Picard scheme and have retrieved the leading order linear solution (7.163). This leading order solution is relatively accurate near to the inital bubble volume but as t increases this solution is no longer accurate, as illustrated in Figure 7.15. The Picard method is a function wise iteration and would require several more iterations to produce a reasonable approximation over a larger domain interval. Theoretically this is possible but due to the complexity of the system and the integro-differential momentum equation we do not proceed down this analytical path.

The relationship between the irradiating acoustic standing wave pressure amplitude, P_u, and the final bubble volume can be observed in Figure 7.14 (a) and implies that increasing this amplitude suppresses the speed of bubble volume growth at early time. Since this linear approximation does not asymptote as we would expect the numerical solution to do, we cannot predict the effect of the pressure amplitude on the steady state bubble volume. We will investigate this effect in the following section when we perform a numerical analysis for the outer solution in the case of instantaneous diffusion.

7.6.3 Numerical solution of the leading order momentum equation

The momentum equation (7.159) contains an integral in t within an integral over x. For the temporal integrals within the integrand $I(u_0, x, t)$ we use a quadrature rule with weightings α_k, where $u_{0k} = u_0(\hat{t}_k), \hat{t}_1 = t^*, \hat{t}_j = t_j$ and $t_j \in [t^*, t]$ to give,

$$\begin{aligned}
I_1(t_j) &= e^{-t_j}(x+u_{0j})^{-\frac{7}{3}} \sum_{k=1}^{j} \alpha_k e^{\hat{t}_k} (x+u_{0k})^{\frac{4}{3}}, \\
I_2(t_j) &= e^{-t_j}(x+u_{0j})^{-\frac{1}{3}} \sum_{k=1}^{j} \alpha_k e^{\hat{t}_k} (x+u_{0k})^{-\frac{2}{3}}, \\
I_3(t_j) &= e^{t^*-t_j} \left(A^*_{rr_0}(x)(x+u^*_{0_j})^{\frac{4}{3}}(x+u_0)^{-\frac{7}{3}} - A^*_{\theta\theta_0}(x)(x+u^*_0)^{-\frac{2}{3}}(x+u_{0j})^{-\frac{1}{3}} \right).
\end{aligned}$$

The spatial integral can be written as

$$\hat{I} = \hat{I}_1 - \hat{I}_2 + \hat{I}_3, \qquad \text{where } \hat{I}_i = \int_0^X I_i dx, \qquad i = 1, 2, 3,$$

so that, for example,

$$\hat{I}_1(t_j) = \int_0^X e^{-t_j}(x+u_{0j})^{-\frac{7}{3}} \sum_{k=1}^{j} \alpha_k e^{\hat{t}_k}(x+u_{0k})^{\frac{4}{3}} dx.$$

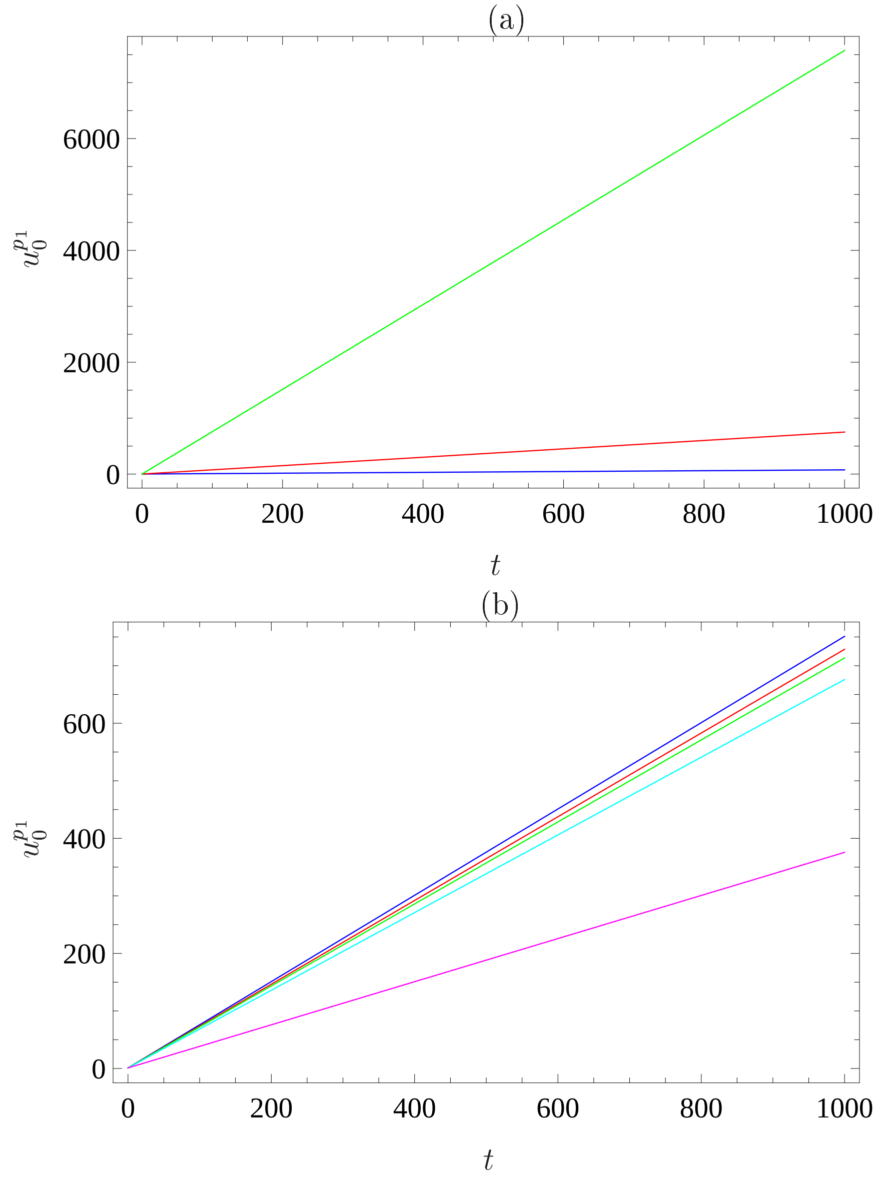

Figure 7.14: Plots of the first Picard iterate solution, u_0^{p1} for a range of values of (a) De (which is inversely proportional to viscosity) and (b) P_u, the non-dimensional value for the pressure amplitude of the irradiating acoustic standing wave. The initial conditions and parameters common to both plots are as follows: $t^* = 0$, $u^* = 1$, $X = 1000$, $p_a = 10^5$, $p_{g_0} = 10p_a$, $\Phi = 0.32$, $\Gamma = 1000$. In (a) $P_u = 0$ and the range of values for De are 0.1 (blue line), 1 (red line), 10 (green line), and in (b) the non-dimensional pressure amplitude values, P_u, are zero (blue line), 0.03 (red line), 0.05 (green line), 0.10 (cyan line), 0.50 (magenta line), with De fixed at 1.

We introduce a quadrature in x via the weightings α_L to give,

$$\begin{aligned}
\hat{I}_1(t_j) &= e^{-t_j}\sum_{L=1}^{m}\alpha_L(x_L+u_{0j})^{-\frac{7}{3}}\sum_{k=1}^{j}\alpha_k e^{\hat{t}_k}(x_L+u_{0k})^{\frac{4}{3}},\\
\hat{I}_2(t_j) &= e^{-t_j}\sum_{L=1}^{m}\alpha_L(x_L+u_{0j})^{-\frac{1}{3}}\sum_{k=1}^{j}\alpha_k e^{\hat{t}_k}(x_L+u_{0k})^{-\frac{2}{3}},\\
\hat{I}_3(t_j) &= e^{t^*-t_j}\sum_{L=1}^{m}\alpha_L A^*_{rr_0}(x)(x_L+u_{0j})^{-\frac{7}{3}}(x_L+u_0^*)^{\frac{4}{3}}\\
&\quad -e^{t^*-t_j}\sum_{L=1}^{m}\alpha_L A^*_{\theta\theta_0}(x)(x_L+u_{0j})^{-\frac{1}{3}}(x_L+u_0^*)^{-\frac{2}{3}}.
\end{aligned}$$

So we have discretised the leading order momentum equation for the outer solution via

$$\frac{du_{0j}}{dt}=\frac{3u_{0j}}{4X}(X+u_{0j})\left(De\left(\frac{A+Bu_{0j}+\Phi X}{u_{0j}+\Phi X}\right)-P_uDe-\frac{1}{\Gamma u_{0j}^{\frac{1}{3}}}+\frac{2}{3}\gamma\hat{I}(u_{0j},t_j)\right). \tag{7.165}$$

We use the following Euler iterative scheme to then integrate in time this nonlinear system of ODEs, to give

$$\begin{aligned}
u_{0j+1} &= u_{0j}+\delta t\frac{3u_{0j}}{4X}(X+u_{0j})\left(De\frac{A+Bu_{0j}+\Phi X}{u_{0j}+\Phi X}-P_uDe\right.\\
&\qquad \left.-\frac{1}{\Gamma(u_{0j})^{\frac{1}{3}}}+\frac{2}{3}\gamma\hat{I}(u_{0j},t_j)\right),
\end{aligned}$$

with initial conditions $u_0(t^*)=u_0^*$, $A_{rr_0}(x,t^*)=A^*_{rr_0}(x)$ and $A_{\theta\theta_0}(x,t^*)=A^*_{\theta\theta_0}(x)$. For the purpose of constructing Figure 7.15 we choose $t^*=0$ and $u^*=A^*_{rr_0}(x)=A^*_{\theta\theta_0}(x)=1$. We use the Composite Simpson rule with quadrature weightings,

$$\alpha_1=\alpha_m=\frac{h}{3},\qquad \alpha_j=\begin{cases}\frac{4}{3}h, & j \text{ even}\\ \frac{2}{3}h, & j \text{ odd}\end{cases},$$

where $h=\delta x,\delta t$ and the accuracy is $O(h^4)$.

Figure 7.15 shows an example solution using this numerical analysis. As for the analytic Picard method, we look at the effect of altering the viscosity via the dimensionless grouped parameter, De and the dimensionless applied acoustic pressure amplitude, P_u; the results of this are shown in Figure 7.16. In the case of instantaneous diffusion we can see, from Figure 7.16 (a), that an increase in P_u results in a decrease in the final bubble volume though the time to achieve this steady state solution is unaffected. In (b) we see the converse effect due to increasing viscosity; that is, the steady state bubble volume is unaffected but the time required to reach this steady state volume is increased.

7.7 Discussion

In this Chapter we derived a governing system of coupled equations to describe the evolution of a non-reacting polymer foam incorporating the effects of inertia and an irradiating acoustic signal. Having made an assumption of instantaneous diffusion we were then able to partially decouple the system.

An asymptotic analysis was performed to derive inner solutions in the scaled temporal variable, T. Both leading and first order solutions, for the non dimensional bubble volume were derived in two different regimes; the first described the case when the ratio of the bubble volume to surrounding fluid volume is very small and the second pertains to the case when they are of the same order. The first instance describes the non-reacting foam at early time when the bubbles have just nucleated and individual bubbles are located at large distances from neighbouring bubbles; the second case describes a time nearer to completion when the bubbles are closely spaced and the fluid volume surrounding individual bubbles is smaller.

In Case I, $X \gg U_0$, we were able to derive an analytic solution to leading order and first order. The leading order solution was parameterised by the initial condition only and described the relationship between bubble volume and time as $U \propto t^{6/5}$. The leading order solution in the case of negligible inertia was linear so the effect of inertia is to increase the bubble growth rate to leading

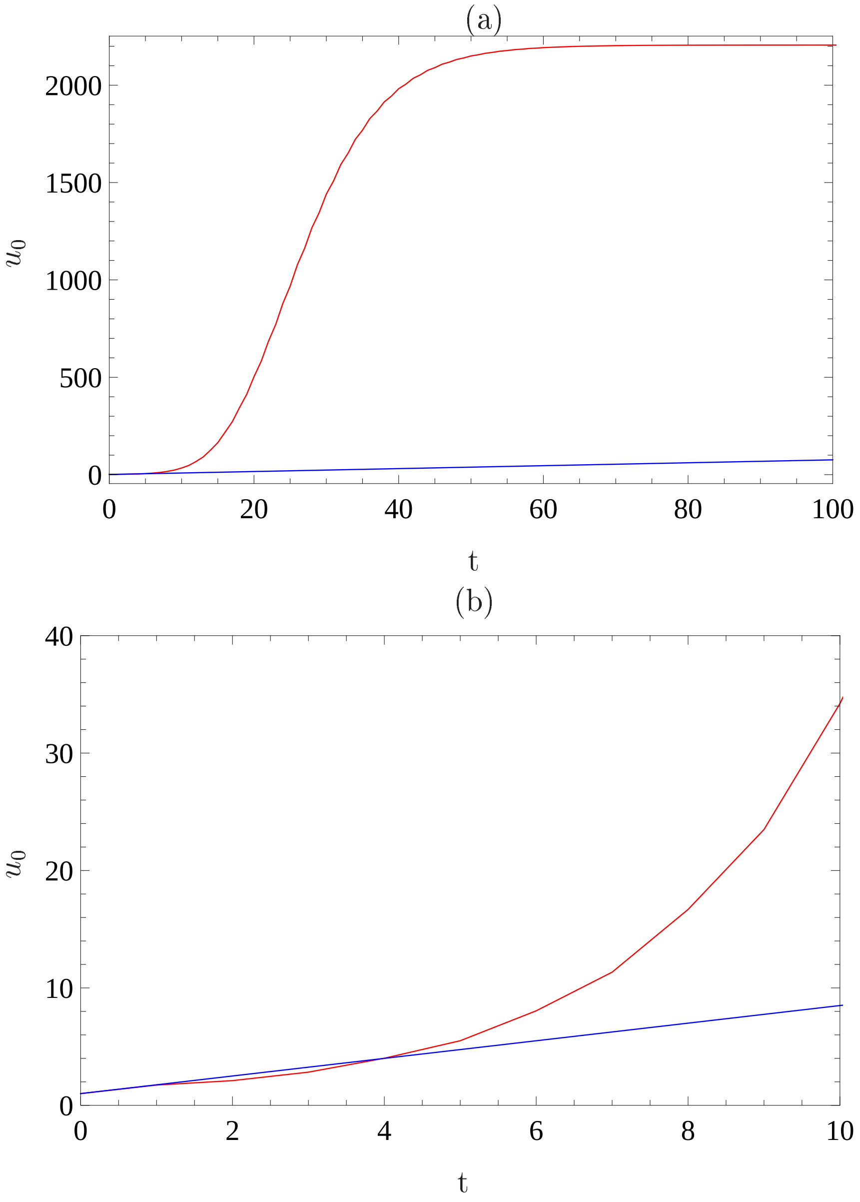

Figure 7.15: (a) The first iterate, u_0^{p1}, for the analytic Picard solution (red line) given by (7.163) and the associated numerical solution calculated using the Euler iterative scheme as desribed in Section 7.6.3. The zoomed in plot (b) shows that this first iterate is only reasonably accurate close to the initial condition at $t^* = 0$ and does not provide a good description of u_0 as $t > t^*$. The initial conditions and parameters common to both plots are as follows: $t^* = 0$, $u^* = 1$, $X = 1000$, $p_a = 10^5$, $p_{g_0} = 10p_a$, $\Phi = 0.32$, $\Gamma = 1000$, $\gamma = 1$, $P_u = 0$ and $De = 1$.

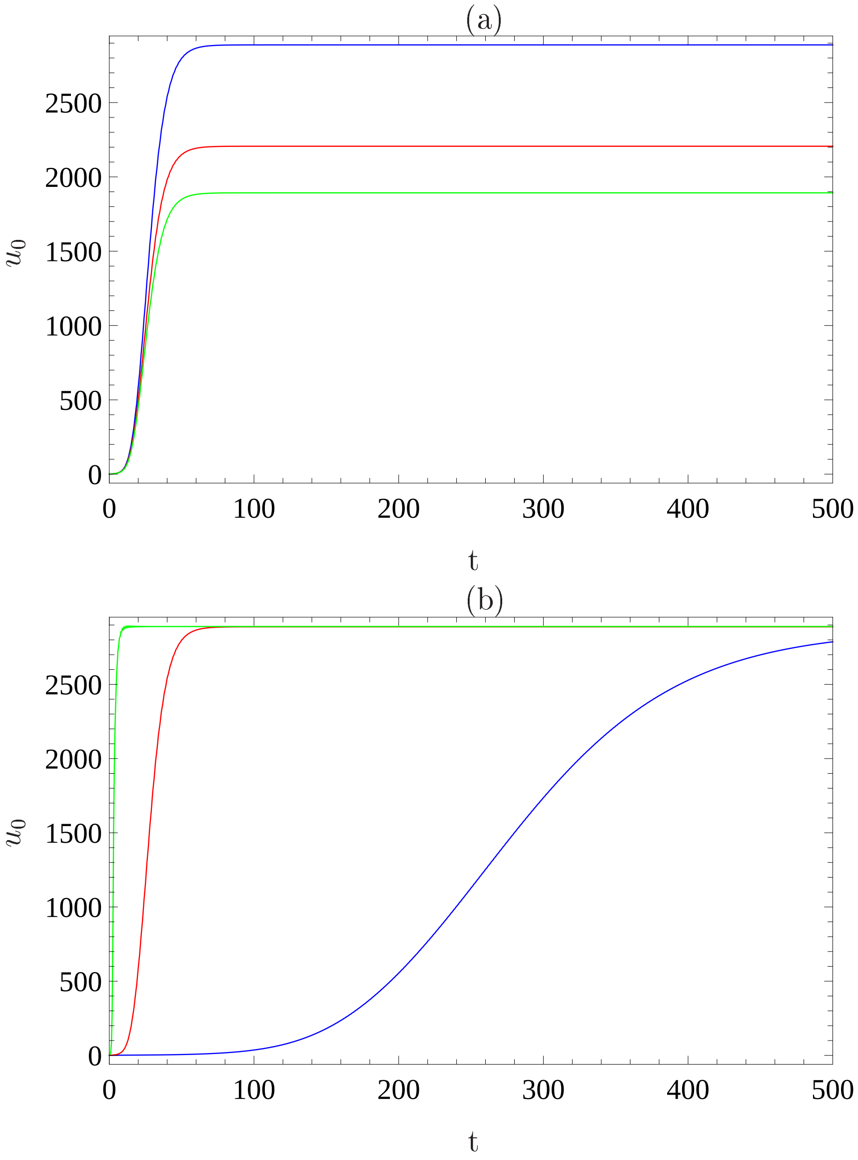

Figure 7.16: The numerical solution of (7.165) and how it is affected by (a) acoustic pressure amplitude, P_u, and (b) viscosity via the dimensionless grouped parameter De. In (a) the values of P_u are zero (blue line), 0.03 (red line) and 0.05 (green line). The Deborah numbers, De, in (b) are 0.1 (blue line), 1.0 (red line) and 10.0 (green line), corresponding to viscosity values of 9×10^6, 9×10^5 and 9×10^4, respectively. These are all realistic viscosity values for polymer foams. The initial conditions and parameters common to both plots are as described in Figure 7.15 except for those parameter values detailed above for (a) and (b). Note that these $P_u = 0.03$ and $P_u = 0.05$ relate to acoustic pressure amplitude values of $p_u = 2.7 \times 10^4$ Pa and 4.5×10^4, respectively, and reflect instrumental values. The actual pressure amplitude, *in situ* would be much lower due to the effects of attenuation as we shall see in Chapter 8.

order. The first order solution was parameterised by the initial condition and the parameter describing inertia, $\mathcal{R}$. However, this solution is only accurate for large X. As $\mathcal{R}$ increases, with other parameters fixed, the first order inner solution predicts an increase in bubble growth rate with increasing inertia, as illustrated in Figure 7.13.

In Case II, $X/U_0 \sim O(1)$, we were able to derive a semi-analytic solution, for the leading and first order cases, by consideration of the normalised error functions over the domain of interest. Although these solutions had to be derived, in part, numerically, they did provide improved accuracy for smaller values of X. Their dependence on the system parameters is implicit and therefore they cannot be used to predict the effect of individual parameters on the final solution. Further work in this area would involve deriving the second order inner solutions, which would include a greater number of parameters in the solution since the right hand side of (7.63) is of order η^2. This would give greater qualitative and quantitative insight into the effects of the acoustic pressure amplitude, P_u, for example.

In Section 7.6.1 we investigated the outer asymptotic solution, which essentially describes the case assuming no inertia. The outer problem is defined by a complex system of five coupled equations, one of which is an integro-differential equation. This makes an analytic solution very hard to obtain. The assumption of instantaneous diffusion allowed us to decouple the concentration potential equation from the system and we were further able to produce an explicit form for the integrand, $(A_{rr} - A_{\theta\theta})_0/(x + u_0)$. It was thus possible to use this to describe the bubble volume evolution via a single integro-differential equation, (7.159).

The inner and outer asymptotic solutions have been derived as described above. The inner asymptotic expansion is in η and the outer asymptotic expansion is in $\mathcal{R}$ with the following prescribed relationship of scale between them:

$\mathcal{R} \gg \eta$. We have not attempted to match the inner and outer solutions as we are interested in the early time behaviour only. However, it is important to note that if matching were necessary then we must define quantitatively the relationship between η and $\mathcal{R}$ so that we could match the inner solution, as the inner temporal variable, $T \to \infty$, to the outer solution as the outer temporal variable, $t \to 0$.

The Picard iteration method was then chosen to derive a leading order analytic solution. The leading order solution was linear in the outer temporal variable t (7.163) and would not be expected therefore to asymptote as the numerical solution predicts; this is illustrated in Figure 7.15 where the Picard solution (blue line) is compared to the numerical solution (red line). Although the leading order Picard solution is not accurate over the whole domain of interest it is reasonably close to the numerical solution for early time. It must also be remembered that it is just a leading order solution and further iterations would need to be performed to improve the accuracy of this analytic approximation. The Picard iteration method converges vector wise as opposed to the pointwise convergence of other schemes e.g. the Euler scheme, although convergence can often be a problem [10]. Theoretically, it is possible to derive higher order terms for this system, however, due to the complexity of the integro-differential momentum equation we did not perform further iterations and instead employed a numerical algorithm to measure the accuracy of the Picard iterate (as discussed above) and to investigate certain parameter effects such as acoustic amplitude, P_u, and viscosity via the grouped parameter De. We demonstrated that an increase in the acoustic pressure amplitude of the standing wave irradiating the system results in a reduced steady state bubble volume but does not affect the time taken to reach this steady state value. Increasing viscosity, on the other hand, does not affect the final bubble volume but does result in a longer time before the steady state is achieved. This effect was also described by Everitt *et* *al.* [26] who demonstrated two distinct phases of bubble growth in the case of instantaneous diffusion; an initial rapid expansion in bubble volume followed by a slower second phase. In Figure 7.16 (b) we observe the analytic inner solution which describes the bubble growth at early time and it agrees qualitatively with the results reported by Everitt *et al.* [26] for their numerical solution at early time.

Both these factors, P_u and De, could have an effect on a bubble size distribution within an expanding polymer foam and in the following chapter we investigate the effect of the acoustic pressure amplitude of the irradiating standing wave used, by Torres-Sanchez *et al.* [93], to tailor the bubble size distribution in a reacting polymer foam. Torres-Sanchez *et al.* reported a correlation between the acoustic pressure amplitude at a given spatial point and the porosity value at that point with porosity directly proportional to the pressure amplitude. The porosity value is related to bubble volume and in the following chapter we develop a mathematical model in order to track the bubble growth of a homogeneous distribution of bubbles under the influence of an acoustic standing wave, in order to demonstrate mathematically the same relationship observed by [93] between porosity/bubble size and acoustic pressure amplitude. First we will look at the extra factors that need to be considered in the reacting system as opposed to the non-reacting system and derive a scheme to describe the evolution of a single bubble in an expanding reacting polymer foam. We neglect the effects of inertia and describe the evolving rheology of the fluid using a multi-mode Oldroyd B system as first proposed by Everitt *et al.* [26]. Having thus produced solutions for single bubbles evolving under the influence of a given acoustic pressure amplitude value, P_u, we then define a framework within which to describe the bubble-bubble interaction of a homogeneous bubble distribution across the sample.

Chapter 8

Modelling the effect of ultrasound on the porosity profile in a reacting polymer

In the previous chapter inertia was introduced into a model for the dynamics of a single bubble in a non-reacting polymer foam. By assuming instantaneous diffusion and large fluid volume X, an analytic inner solution was derived using an asymptotic expansion. This chapter is motivated by the experimental work carried out by Torres-Sanchez *et al.* [92, 93], to produce the first model of their observations, namely, that porosity varies in direct proportion to the acoustic pressure magnitude of the ultrasound signal [93, 94]. To this end, the second reacting model proposed by Everitt *et al.* [26], which incorporates gas production and evolving fluid rheology, was extended to include the effects of ultrasound. Due to the extra level of complexity in this reacting system, and the particular parameterisation of the model, inertia was assumed to be negligible. In order to illustrate the effects that an ultrasound standing wave can have on the polymer foam density, a simulation of the differential growth dynamics of a series of adjacent bubbles was performed.

The original work in this chapter, which builds on the model derived by Everitt *et al.* is contained in the following sections: the effect of the acoustic pressure amplitude term, P_u, incorporated into the momentum equation (8.1) is illustrated in Section 8.4. As opposed to Everitt *et al.* [26] we derive the analytic solution for the extent of reaction, α, in Section 8.1. Although we had the reacting model as published by Everitt *et al.* no numerical code was available and therefore we developed one from scratch. The results from our numerical scheme were validated by comparison with plots produced in [26] to ensure that it was working correctly. The model was then applied to the experiment described by Torres Sanchez *et al.* [93] and the results can be seen in Section 8.2. Sections 8.5 and 8.6 outline the development of a new model to track the bubble size distribution profile for a given number of post nucleated bubbles sited at different spacing intervals across the sample, and two metrics are proposed to quantify the heterogeneity in the resultant distribution. Some of this derivation was based on data produced and published by Torres-Sanchez *et al.* [92] and is presented in Section 8.5. An explanation of the derivation of the elastic modulus term, $G(t)$, published in [26] is given in Section 8.1.2 in order to aid understanding of the model.

The corresponding reacting model is developed, in this chapter, to describe the experimental system of Torres-Sanchez [93]; however, due to its added layer of complexity, the reacting model will be given a numerical treatment.

The reader is directed to Everitt *et al.* [26] for a full description and non-dimensionalisation of the governing system of equations and boundary and initial conditions. Here we simply restate the non-dimensionalised system proposed by [26] and explain the origin and derivation of the additional terms due to the reaction.

$$\frac{4}{3}\dot{u}\left[\frac{1}{u}-\frac{1}{X+u}\right]=(P_g-P_u)M+\frac{2}{3}\gamma\sum_{\epsilon=\epsilon_{ch}}^{\epsilon_x}\frac{G(\epsilon)}{G_0}\int_0^X\frac{(A_{rr}-A_{\theta\theta})}{x+u}dx-\frac{1}{\Gamma\left(u\right)^{\frac{1}{3}}}, \tag{8.1}$$

$$\frac{\partial A_{rr}}{\partial t}=-\frac{4\dot{u}}{3\left(x+u\right)}A_{rr}-\frac{\epsilon}{c_\alpha}\left(A_{rr}-1\right), \tag{8.2}$$

$$\frac{\partial\left(A_{rr}-A_{\theta\theta}\right)}{\partial t}=\frac{2\dot{u}}{3(x+u)}\left[(A_{rr}-A_{\theta\theta})-3A_{rr}\right]-\frac{\epsilon}{c_\alpha}\left(A_{rr}-A_{\theta\theta}\right), \tag{8.3}$$

$$\left(\frac{p_a+(p_{g0}-p_a)P_g}{p_{g0}}\right)u=1+\xi\Phi\frac{p_a}{p_{g0}}X\left(\phi(0,t)+(\alpha-\alpha_0)\right), \tag{8.4}$$

$$\frac{\partial\phi}{\partial t}=N(x+u)^{\frac{4}{3}}\frac{\partial^2\phi}{\partial x^2}-\frac{1}{X}\frac{d\alpha}{dt}(X-x). \tag{8.5}$$

Boundary conditions

$$\frac{\partial\phi}{\partial x}=\frac{1}{\xi X}\frac{p_{g0}-p_a}{p_a}(P_g-1), \qquad x=0, \tag{8.6}$$

$$\frac{\partial^2\phi}{\partial x^2}=0, \qquad x=X. \tag{8.7}$$

Initial conditions

$A_{rr}(0)=1, \qquad \left(A_{rr}-A_{\theta\theta}\right)(0)=0, \qquad u(0)=1, \qquad P_g(0)=1, \qquad \phi(0)=0,$

where the dependent variables are as follows: $u(t)$ is the dimensionless bubble volume, $P_g(t)$ is the dimensionless bubble gas pressure, $A_{rr}(x,t)$ and $A_{\theta\theta}(x,t)$ are the diagonal components of the orientation tensor $\mathbf{A(x,t)}$ and $\phi(x,t)$ is the dimensionless gas concentration potential through in the liquid. The independent variables are x, t. The parameters are as follows: X is the dimensionless outer fluid volume, P_u is the dimensionless acoustic pressure amplitude, M is the ratio of the rate of bubble growth to the reaction rate and is defined in Table 8.1, G_0 is the elastic modulus of the fully developed gel, γ is the ratio of polymer to solvent contributions to the steady shear viscosity and is defined in Table 8.1, Γ is the ratio of viscous force to surface tension defined in Table 8.1, $G(\epsilon)$ is the relaxation modulus for a molecule with relaxation rate ϵ and c_α is the reaction rate constant. The remaining parameters are defined and quantified in Table 8.2.

The non-dimensional grouped parameters differ slightly from those of the non-reacting model, due to the inclusion of a reaction rate constant c_α, and are listed in Table 8.1. Individual parameters for the reacting system are described and quantified in Table 8.2. The construction of the evolving relaxation modulus term, $G(\epsilon)$, is detailed in Section 8.1.2 and the effect of the reaction kinetics on (8.4) and (8.5) is described in Section 8.1.1. The only change to the orientation tensor rate equations, (8.2) and (8.3), is the non-dimensionalisation of the temporal variable by the reaction rate constant, c_α, rather than the relaxation time, τ, as in the non-reacting system.

$M = (p_{g0} - p_a)/\mu c_\alpha$

$\gamma = G_0/\mu c_\alpha$

$\Gamma = u_0^{\frac{1}{3}} \mu c_\alpha / 2S$

$N = 9D\tau / u_0^{\frac{2}{3}} c_\alpha$

$\Phi = R_g T H$

Table 8.1: Dimensionless groups in the non-dimensional formulation for the reacting model (8.1) - (8.5).

Comparing the reacting momentum equation (8.1), (with $\mathcal{R} = 0$) to the non-reacting case (7.48), we can see that the relaxation moduli for individual modes coming into existence at time t need to be calculated. This derivation is expounded in Section 8.1.2 and elucidates work published by Everitt *et al.* [26]. The non reacting bubble gas pressure equation (7.49) only considers the gas dissolved, initially, in the fluid volume. An extra term is therefore included in the reacting case (8.4) to account for the additional bubble gas pressure due to the generation of gas by the polymerisation reaction. Finally, the non reacting diffusion equation (7.52) becomes a reaction diffusion equation in the reacting

Parameter	Value	Units	Comments
p_a	1×10^5	$\mathrm{Nm^{-2}}$	Pressure outside liquid layer
R_g	8.31	$\mathrm{Jmol^{-1}K^{-1}}$	Gas constant
T	323	K	Temperature
H	10.5×10^{-5}	$\mathrm{molN^{-1}m^{-1}}$	Henry's law constant
D	1.6×10^{-9}	$\mathrm{m^2s^{-1}}$	Diffusivity [15][1]
ρ	1088	$\mathrm{kgm^{-3}}$	Liquid density[2]
ν	2.2		Molecular weight distribution exponent
σ	0.45		Largest molecular weight scaling exponent
d_f	2.5		Fractal dimension of the equilibrium coil size of a molecule [16, 26, 87]
m_x	0.32	$\mathrm{kgmol^{-1}}$	Molar mass of initial polymers
p_{g0}	2×10^5	$\mathrm{Nm^{-2}}$	Initial bubble gas pressure
μ	1×10^4	$\mathrm{Nsm^{-2}}$	Solvent viscosity
u_0	1×10^{-18}	$\mathrm{m^3}$	Initial bubble volume
S	0.02	$\mathrm{Nm^{-1}}$	Surface tension
ξ	10		Maximum gas concentration produced by reaction/background gas concentration
α_0	0.1		Extent of reaction at nucleation
t_0	0	s	Time of reaction at nucleation
α_c	0.91		Extent of reaction at the gel point
c_α	0.04	$\mathrm{s^{-1}}$	Reaction rate calculated from data[3]
ϵ_x	750	$\mathrm{s^{-1}}$	Relaxation rate of initial polymers
X	50		Dimensionless fluid volume

Table 8.2: Parameters used to construct Figure 8.5. [1]The parameter range for the diffusion constant of CO_2 is based on the diffusion constant for CO_2 in water ($1.6 \mathrm{x} 10^{-9} \mathrm{m^2s^{-1}}$). [2]Determined experimentally by author of [93]. [3]For details of this calculation and a discussion on the reaction kinetics see Section 8.3. Unless stated otherwise, parameters values have been taken from [26].

case (8.5) and contains a source term in addition to the diffusion term.

8.1 Reacting model

There are two major differences which need to be accounted for in the reacting model. Firstly, as well as the dissolved gas already present in the fluid at $t = 0$, the gas produced as a by-product of the polymerisation reaction must also be accounted for in the governing equations. Secondly, the relaxation modulus, G, is no longer a constant and the effective relaxation modulus, $G(t)$, of the polymer changes as the reaction proceeds. These effects are both mediated by the reaction kinetics of the polymerisation. The polymer is normally formed from two reacting species, but here the model is simplified by assuming a single reacting species that forms self-similar molecules of increasing molecular weights that ultimately form a gel [26].

The reaction is followed via the variable α, where α gives the ratio of the number of chemical bonds to the total number of possible chemical bonds. That is, α is a dimensionless quantity measuring the extent of reaction with $0 \leq \alpha < 1$. As in [26] the reaction is assumed to follow second order kinetics with a reaction rate, c_α so that,

$$\frac{d\alpha}{dt} = c_\alpha(1-\alpha)^2. \tag{8.8}$$

This admits the analytic solution,

$$\alpha(t) = 1 - \frac{(1-\alpha_0)}{c_\alpha(t-t_0)(1-\alpha_0)+1}, \tag{8.9}$$

where $\alpha(t_0) = \alpha_0$ is the extent of reaction at nucleation. The effect of the reaction rate constant, c_α, is illustrated in Figure 8.1 and demonstrates that as c_α increases the reaction extent approaches (but never reaches) unity at a faster rate. Scaling time, t, by $1/c_\alpha$ we obtain the non-dimensional form

$$\alpha(\hat{t}) = 1 - \frac{(1-\alpha_0)}{(1-\alpha_0)(\hat{t}-\hat{t}_0)+1}, \tag{8.10}$$

where $\hat{t} = t/c_\alpha$. The extent of reaction, α, at time t will dictate the additional dissolved gas concentration potential and bubble gas pressure due to the reaction as well as govern the molecular weight distribution, and hence the relaxation modulus, within a cluster at any given time.

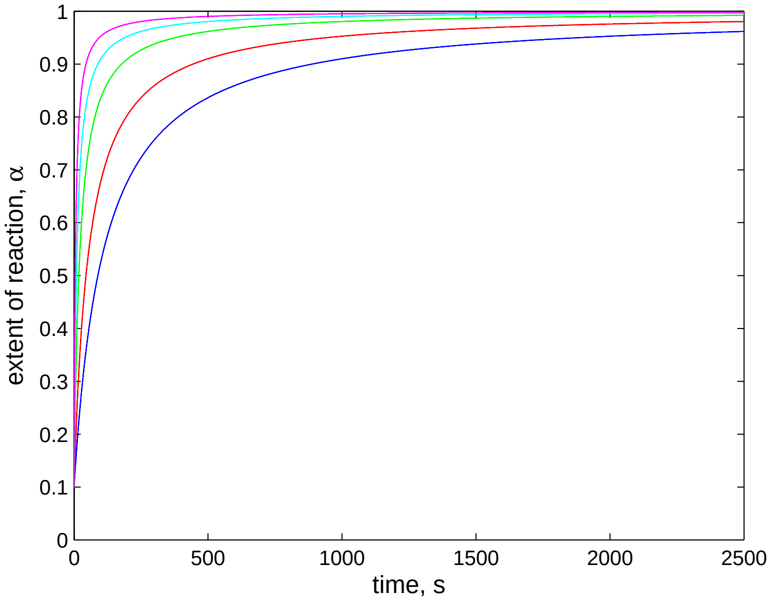

Figure 8.1: Plots showing the extent of reaction, α, versus time for a second order reaction, for a range of values of the reaction rate constant c_α. The reaction rate constants are as follows: $c_\alpha = 0.01$ (blue line), $c_\alpha = 0.02$ (red line), $c_\alpha = 0.05$ (green line), $c_\alpha = 0.10$ (cyan line), $c_\alpha = 0.20$ (magenta line). The initial condition is given by $\alpha(0) = 0.1$. As c_α increases the extent of reaction, α, approaches unity more quickly.

8.1.1 Gaseous phase

Due to the generation of gas as the reaction proceeds, the non reacting equations (7.51) and (7.52) need to be amended to account for this source. The modified gas diffusion equation is now a reaction diffusion equation with the total gas produced by the reaction in the fluid volume X at time t assumed to be proportional to $d\alpha/dt$ [26] so that at a given volume co-ordinate, x, the fraction of this contribution can be added to the diffusion term to give,

$$\frac{\partial \phi}{\partial t} = N(x+u)^{\frac{4}{3}}\frac{\partial^2 \phi}{\partial x^2} - \frac{1}{X}\frac{d\alpha}{dt}(X-x). \tag{8.11}$$

As in the previous section, the boundary conditions at the inner ($x = 0$) and outer ($x = X$) boundaries are derived via application of Henry's law and the zero flux condition, respectively.

8.1.2 Liquid/Gel phase

The second effect on the effective relaxation rate of the polymer occurs in the liquid/gel phase. In the previous chapter the relaxation modulus of the polymer, G, was assumed to be constant throughout the bubble expansion phase but with the reacting system the effective relaxation modulus is constantly changing through the different stages of the reaction. In this section an expression for $G(t)$ is derived by considering the behaviour, at a molecular level, during the different phases of the polymerisation reaction.

As the polymerisation reaction proceeds the molecules in the monomer solution start to react and bond to form molecules with a range of molecular weights. Before the gel point ('pre-gelation') the cross-linking polymer is a distribution of finite clusters called a 'sol'. Once the gel point has been passed ('post-gelation') it is called a 'gel' and is an infinitely large macromolecule which can only swell, but not dissolve, in a solvent even though low molecular weight molecules (sol fraction) are still extractable from the gel [104]. As a result, polymeric materials relax with a broad spectrum of modes; longer modes belong to the motion of entire molecules or large chain segments, while shorter modes characterise small scale details of the molecules. Extra long relaxation modes herald the onset of the liquid-solid transition, which in chemical polymerisation is known as the 'gel point'. At this critical point in the reaction the material is neither a liquid or a solid (see Figure 8.2). At and near the gel point, the molecular motions slow down while they correlate with motions of other molecules over longer and longer distances; relaxation modes are now coupled over a wide range of time scales. The result is a self-similar relaxation spectrum which is governed by a power law relationship. This critical extent of reaction, α_c, is characterised by the divergence of the molecular weight of the largest molecule to infinity and an infinitely broad molecular weight distribution [104]. The combination of liquid and solid behaviour at the gel point requires unusual regularity in the relaxation pattern. Furthermore, there is a critical region in the neighbourhood of the gel point where all properties can be expanded in powers of the distance from the gel point, $|\alpha - \alpha_c|$. Outside this critical region the behaviour loses its simplicity. In order to derive an expression for the effective relaxation modulus, $G(t)$, it is necessary to consider the molecular structure of the molecule and its dynamics in a fluid. Everitt *et al.* [26] developed a scheme to calculate the relaxation modulus of individual modes both pre and post gelation, and then, by considering the distribution of molecular weights within evolving clusters, they derived a function for the effective relaxation modulus, $G(t)$, of the fluid. What follows in the remainder of this section is a detailed explanation of Everitt *et al.*'s derivation as well as further clarification.

When a polymer molecule is put into a homogeneous flow it assumes the aspect of a statistically spherical coil with average size (radius of gyration) r. Due to the self similar nature of the polymer molecule the radius of gyration is related to the molecule mass via its fractal dimension d_f [104]

$$r \propto m^{1/d_f}. \tag{8.12}$$

In Rouse dynamics [20] the friction on a molecular segment is proportional to the number of monomers so that the diffusion coefficient is inversely proportional to molecular weight. The longest relaxation time for a molecule of molecular mass

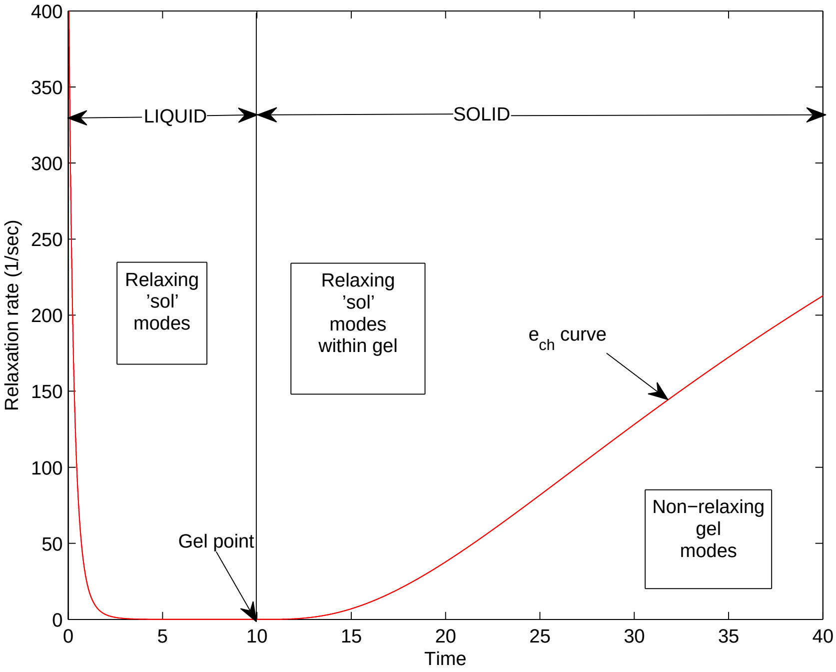

Figure 8.2: Before the gel point, when the longest relaxation time $\tau_{ch} \to \infty$ and $\epsilon_{ch} \to 0$, the polymer is in a liquid state. At the gel point, $t = t_c$, it is neither liquid nor solid and for $t > t_c$ it is a solid. Before the gel point the crosslinking polymer is a distribution of finite clusters and we call it a 'sol' since it is still soluble in good solvents; at this stage all the modes can relax. Once the gel point has been passed it is called a gel; an infinitely large macromolecule which can only swell but not dissolve in a solvent even though low molecular weight molecules (sol fraction) are still extractable from the gel [104]. The infinite cluster cannot dissolve although the finite clusters in the sol fraction can still relax and account for the 'relaxing sol modes within the gel' in the diagram. As $t \to \infty$ (8.47) predicts that $\epsilon_{ch} \to \epsilon_x$.

m therefore scales as

$$\epsilon_m \propto \frac{1}{mr^2}. \tag{8.13}$$

The polymer molecules in the fluid at $t = 0$ are assumed to be self-similar chains with molecular weight m_x and slowest relaxation rate ϵ_x, so that

$$\epsilon_m = \epsilon_x \left(\frac{m_x}{m}\right)^{\left(2/d_f+1\right)} \tag{8.14}$$

The relaxation rates for all the other possible modes for the molecule of mass m, from $k = 1$ to $k = m/m_x$, are

$$\epsilon = \epsilon_m(k) = \epsilon_x \left(\frac{m_x}{m}k\right)^{2/d_r}, \tag{8.15}$$

where $2/d_r = 1 + 2/d_f$. For each molecular weight, m, there is an associated Rouse spectrum of relaxation modes [20] approximated as a continuous spectrum $\epsilon_m(k)$, so that the relaxation modulus $G_m(t)$ for molecules of mass m can be obtained by integration over the modes $k = 1$ to $k = m/m_x$ via

$$G_m(t) = \frac{\rho_m RT}{m} \int_1^{m/m_x} e^{-\epsilon_m(k)t} dk, \tag{8.16}$$

where k is the mode number, $\rho_m = mn(m)\rho$, $n(m)$ is the number density of molecules of molecular weight m, R is the universal gas constant and T is the temperature. Rearranging equation (8.15) for k we have,

$$k = \frac{m}{m_x}\left(\frac{\epsilon}{\epsilon_x}\right)^{d_r/2}, \tag{8.17}$$

so that substituting for,

$$dk = \frac{\frac{m}{m_x}\left(\frac{\epsilon}{\epsilon_x}\right)^{d_r/2} d\epsilon}{(2\epsilon/d_r)}, \tag{8.18}$$

in (8.16) and changing the integration limits from k to ϵ we obtain,

$$G_m(t) = mn(m)G_0 \frac{d_r}{2} \int_{\epsilon_m}^{\epsilon_x} \left(\frac{\epsilon}{\epsilon_x}\right)^{d_r/2} e^{-\epsilon t} \frac{d\epsilon}{\epsilon}, \tag{8.19}$$

where $G_0 = \rho RT/m_x$. Next, the function describing the distribution of molecular weights of the clusters, $n(m)$, must be derived. At the gel point $n(m)$ scales with the molecular weight of the cluster, so that a cluster or molecule of molecular weight m will have a number density which is related by a power law to its molecular weight. That is,

$$n(m) \sim m^{-\nu}, \qquad \text{at } \alpha = \alpha_c. \tag{8.20}$$

In the vicinity of the gel point a cutoff function, $f\left(\frac{m}{m_{ch}}, \frac{m_x}{m}\right)$, is introduced,

$$n(m) \sim m^{-\nu} f\left(\frac{m}{m_{ch}}, \frac{m_x}{m}\right), \tag{8.21}$$

defining the two limits of the scaling regime, where m_{ch} (molecular weight of the largest finite polymer molecule) scales according to

$$m_{ch} \sim |\alpha - \alpha_c|^{-1/\sigma}. \tag{8.22}$$

Away from these limits (i.e. $m \ll m_{ch}$ and $m \gg m_x$) the cutoff function $f(0,0) = \chi$, where χ is a constant, and in this case $n(m)$ follows the simple power law,

$$n(m) = \chi m^{-\nu}. \tag{8.23}$$

Near the two ends of the scaling region the distribution $n(m)$ is more complicated and is controlled by the cutoff function f. However, the analytical form of the cutoff function at these two ends is unknown [74]. Randrianantoandro *et al.* [72] used Monte Carlo simulations to obtain a more accurate exponential cutoff function, however, we retain the double step cutoff function proposed by Rubenstein *et al.* [74] and used by Everitt *et al.* [26]. Throughout the reaction, therefore,

$$f\left(\frac{m}{m_{ch}}, \frac{m_x}{m}\right) = \begin{cases} \chi, & m_x < m < m_{ch} \\ 0, & m > m_{ch} \text{ or } m < m_x. \end{cases} \tag{8.24}$$

The value of this constant can be determined from the following normalisation condition

$$\int n(m) m dm = \text{sol fraction} = \begin{cases} 1 & \text{for } \alpha < \alpha_c, \\ 1 - \text{gel fraction} & \text{for } \alpha > \alpha_c. \end{cases} \tag{8.25}$$

Up until the gelation point $\alpha = \alpha_c$

$$n(m) = \begin{cases} 0 & 0 < m < m_x, \\ \chi m^{-\nu} & m_x < m < m_{ch}, \\ 0 & m > m_{ch} \end{cases}$$

where χ is the constant that we are trying to determine. Integrating over all mass from 0 to m_∞

$$\begin{aligned} \int n(m) m dm &= \int_0^{m_x} 0 dm + \int_{m_x}^{m_{ch}} \chi m^{-\nu} m dm + \int_{m_{ch}}^{m_\infty} 0 dm, \\ &= \chi \left[\frac{m^{2-\nu}}{2-\nu} \right]_{m_x}^{m_{ch}}, \\ &= \frac{\chi}{(\nu-2) m_x^{\nu-2}} \left[1 - \left(\frac{m_x}{m_{ch}} \right)^{\nu-2} \right], \end{aligned} \tag{8.26}$$

and applying the normalisation condition (8.25) for $\alpha < \alpha_c$ we can obtain the constant χ

$$\chi = \frac{(\nu-2) m_x^{\nu-2}}{\left[1 - \left(\frac{m_x}{m_{ch}} \right)^{\nu-2} \right]}. \tag{8.27}$$

By the same method we have for the post gelation period,

$$\frac{\chi}{(\nu-2) m_x^{\nu-2}} \left[1 - \left(\frac{m_x}{m_{ch}} \right)^{\nu-2} \right] = 1 - \text{gel fraction},$$

where the remaining $\left(\frac{m_x}{m_{ch}} \right)^{\nu-2}$ makes up the gel fraction [26], so that for $\alpha > \alpha_c$

$$\chi = (\nu-2) m_x^{\nu-2}. \tag{8.28}$$

Therefore, a full description of the cutoff function $f(\frac{m}{m_{ch}}, \frac{m_x}{m})$ is given by

$$f\left(\frac{m}{m_{ch}}, \frac{m_x}{m} \right) = \begin{cases} 0 & 0 < m < m_x, & \alpha_0 < \alpha < 1, \\ \frac{(\nu-2) m_x^{\nu-2}}{\left[1 - \left(\frac{m_x}{m_{ch}} \right)^{\nu-2} \right]} & m_x < m < m_{ch}, & \alpha_0 < \alpha < \alpha_c, \\ (\nu-2) m_x^{\nu-2} & m_x < m < m_{ch}, & \alpha_c < \alpha < 1, \\ 0 & m_{ch} < m < m_\infty, & \alpha_0 < \alpha < 1, \end{cases} \tag{8.29}$$

and the number density for molecules of molecular weight m is

$$n(m) = \begin{cases} 0 & 0 < m < m_x, \quad \alpha_0 < \alpha < 1, \\ \frac{(\nu-2)m_x^{\nu-2}}{\left[1-\left(\frac{m_x}{m_{ch}}\right)^{\nu-2}\right]}m^{-\nu} & m_x < m < m_{ch}, \quad \alpha_0 < \alpha < \alpha_c, \\ (\nu-2)m_x^{\nu-2}m^{-\nu} & m_x < m < m_{ch}, \quad \alpha_c < \alpha < 1, \\ 0 & m_{ch} < m < m_\infty, \quad \alpha_0 < \alpha < 1. \end{cases} \tag{8.30}$$

Prior to the gel point ($\alpha_0 < \alpha < \alpha_c$) all molecular weights in the sol lie within the range $m_x < m < m_{ch}$ and all existing modes are relaxing modes with a relaxation rate lying within $\epsilon_x < \epsilon < \epsilon_{ch}$. Their contribution to $G(t)$ is given by (8.19).

After the gel point, $\alpha > \alpha_c$, the gel is made up of a gel fraction and a sol fraction (see Figure 8.2). The sol fraction contains only relaxing modes with $\epsilon_x < \epsilon < \epsilon_{ch}$ and their contribution to G is determined via (8.19). The gel fraction, quantified by $(m_x/m_{ch})^{\nu-2}$, contains both relaxing ($\epsilon_x < \epsilon < \epsilon_{ch}$) and non-relaxing modes ($0 < \epsilon < \epsilon_{ch}$).

The functions G_{pre} and G_{post} are assigned to define the evolution of the relaxation modulus pre- and post-gelation respectively so that throughout the polymerisation reaction the relaxation modulus can be described by

$$G(t) = \begin{cases} G_{\text{pre}}(t) & \alpha_0 < \alpha < \alpha_c, \\ G_{\text{post}}(t) & \alpha_c < \alpha < 1. \end{cases} \tag{8.31}$$

First G_{pre} is derived by integration of (8.19) over all molecular weights from m_x to m_{ch},

$$G_{\text{pre}}(t) = G_0 \frac{d_r}{2} \int_{\epsilon_{ch}}^{\epsilon_x} \int_{m_\epsilon}^{m_{ch}} mn(m) \left(\frac{\epsilon}{\epsilon_x}\right)^{d_r/2} \frac{e^{-\epsilon t}}{\epsilon} dm d\epsilon, \tag{8.32}$$

and bearing in mind the following relations derived from (8.14)

$$\begin{aligned}\left(\frac{1}{m_\epsilon}\right)^{\nu-2} &= \left(\frac{1}{m_x}\right)^{\nu-2}\left(\frac{\epsilon}{\epsilon_x}\right)^{(\nu-2)d_r/2}, \\ \left(\frac{1}{m_{ch}}\right)^{\nu-2} &= \left(\frac{1}{m_x}\right)^{\nu-2}\left(\frac{\epsilon_{ch}}{\epsilon_x}\right)^{(\nu-2)d_r/2}, \\ \left(\frac{m_x}{m_{ch}}\right)^{\nu-2} &= \left(\frac{\epsilon_{ch}}{\epsilon_x}\right)^{(\nu-2)d_r/2}, \qquad (8.33)\end{aligned}$$

the pre-gelation relaxation modulus can be stated as,

$$G_{\text{pre}}(t) = \frac{G_0\frac{d_r}{2}}{1-\left(\frac{\epsilon_{ch}}{\epsilon_x}\right)^{(\nu-2)\frac{d_r}{2}}}\int_{\epsilon_{ch}}^{\epsilon_x}\left(\left(\frac{\epsilon}{\epsilon_x}\right)^{(\nu-1)\frac{d_r}{2}} - \left(\frac{\epsilon_{ch}}{\epsilon_x}\right)^{(\nu-2)\frac{d_r}{2}}\left(\frac{\epsilon}{\epsilon_x}\right)^{\frac{d_r}{2}}\right)e^{-\epsilon t}\frac{d\epsilon}{\epsilon}. \qquad (8.34)$$

Post gelation, when $\alpha > \alpha_c$, there are three contributions to the relaxation modulus

$$G_{\text{post}}(t) = G_{\text{sol}}(t) + G^{\text{r}}_{\text{gel}}(t) + G^{\text{nr}}_{\text{gel}}(t) \qquad (8.35)$$

where $G_{\text{sol}}(t)$ is the contribution due to the relaxing modes in the sol fraction, $G^{\text{r}}_{\text{gel}}(t)$ is the contribution due to the relaxing modes in the gel fraction and $G^{\text{nr}}_{\text{gel}}(t)$ is the contribution due to the non-relaxing gel mode. The limits of integration for ϵ and m are set out in Table 8.3 so that, integrating over the relevant limits, we have, for $\alpha > \alpha_c$,

	G_{sol}	$G^{\text{r}}_{\text{gel}}$	$G^{\text{nr}}_{\text{gel}}$
ϵ	$\epsilon_{ch} < \epsilon < \epsilon_x$	$\epsilon_{ch} < \epsilon < \epsilon_x$	$0 < \epsilon < \epsilon_{ch}$
m	$m_x < m < m_{ch}$	$m_{ch} < m < \infty$	$m_{ch} < m < \infty$

Table 8.3: Limits of integration for ϵ and m for $\alpha > \alpha_c$.

$$\begin{aligned}G_{\text{post}}(t) &= G_0\frac{d_r}{2}\int_{\epsilon_{ch}}^{\epsilon_x}\int_{m_\epsilon}^{m_{ch}} mn(m)\left(\frac{\epsilon}{\epsilon_x}\right)^{\frac{d_r}{2}}\frac{e^{-\epsilon t}}{\epsilon}dmd\epsilon \qquad \Big(G_{\text{sol}}(t)\Big) \\ &+ G_0\frac{d_r}{2}\int_{\epsilon_{ch}}^{\epsilon_x}\int_{m_{ch}}^{\infty} mn(m)\left(\frac{\epsilon}{\epsilon_x}\right)^{\frac{d_r}{2}}\frac{e^{-\epsilon t}}{\epsilon}dmd\epsilon \qquad \Big(G^{r}_{\text{gel}}(t)\Big) \\ &+ G_0\frac{d_r}{2}\int_{0}^{\epsilon_{ch}}\int_{m_{ch}}^{\infty} mn(m)\left(\frac{\epsilon}{\epsilon_x}\right)^{\frac{d_r}{2}}\frac{1}{\epsilon}dmd\epsilon \qquad \Big(G^{nr}_{\text{gel}}(t)\Big) \qquad (8.36)\end{aligned}$$

Each contribution is determined individually as follows: $G_{\mathrm{sol}}(t)$ is obtained via integration of the first term in (8.36) from m_x to m_{ch} with $n(m) = (\nu - 2)m_x^{\nu-2}m^{-\nu}$ from (8.30) and so

$$\begin{aligned} G_{\mathrm{sol}}(t) &= G_0\frac{d_r}{2}\int_{\epsilon_{ch}}^{\epsilon_x}\int_{m_\epsilon}^{m_{ch}} mn(m)\left(\frac{\epsilon}{\epsilon_x}\right)^{\frac{d_r}{2}}\frac{e^{-\epsilon t}}{\epsilon}dmd\epsilon, \\ &= G_0\frac{d_r}{2}\int_{\epsilon_{ch}}^{\epsilon_x}\left(\left(\frac{\epsilon}{\epsilon_x}\right)^{\frac{d_r}{2}(\nu-1)} - \left(\frac{\epsilon_{ch}}{\epsilon_x}\right)^{\frac{d_r}{2}(\nu-2)}\left(\frac{\epsilon}{\epsilon_x}\right)^{\frac{d_r}{2}}\right)e^{-\epsilon t}\frac{d\epsilon}{\epsilon}. \end{aligned} \tag{8.37}$$

To calculate the contributions $G_{\mathrm{gel}}^{\mathrm{r}}(t)$ and $G_{\mathrm{gel}}^{\mathrm{nr}}(t)$ we substitute for the gel fraction [26] given by

$$\int_{m_{ch}}^{\infty} mn(m)dm = \left(\frac{m_x}{m_{ch}}\right)^{\nu-2}, \tag{8.38}$$

so that, in (8.36)

$$\begin{aligned} G_{\mathrm{gel}}^{\mathrm{r}}(t) &= G_0\frac{d_r}{2}\int_{\epsilon_{ch}}^{\epsilon_x}\left(\frac{m_x}{m_{ch}}\right)^{\nu-2}\left(\frac{\epsilon}{\epsilon_x}\right)^{\frac{d_r}{2}}\frac{e^{-\epsilon t}}{\epsilon}d\epsilon, \\ &= G_0\frac{d_r}{2}\int_{\epsilon_{ch}}^{\epsilon_x}\left(\frac{\epsilon_{ch}}{\epsilon_x}\right)^{\frac{d_r}{2}(\nu-2)}\left(\frac{\epsilon}{\epsilon_x}\right)^{\frac{d_r}{2}}\frac{e^{-\epsilon t}}{\epsilon}d\epsilon. \end{aligned} \tag{8.39}$$

And similarly, from (8.33)

$$\begin{aligned} G_{\mathrm{gel}}^{\mathrm{nr}}(t) &= G_0\frac{d_r}{2}\int_{0}^{\epsilon_{ch}}\left(\frac{m_x}{m_{ch}}\right)^{\nu-2}\left(\frac{\epsilon}{\epsilon_x}\right)^{\frac{d_r}{2}}\frac{d\epsilon}{\epsilon}, \\ &= G_0\frac{d_r}{2}\int_{0}^{\epsilon_{ch}}\left(\frac{\epsilon_{ch}}{\epsilon_x}\right)^{\frac{d_r}{2}(\nu-2)}\left(\frac{\epsilon}{\epsilon_x}\right)^{\frac{d_r}{2}}\frac{d\epsilon}{\epsilon}. \end{aligned} \tag{8.40}$$

The limits of integration are the same for $G_{\mathrm{sol}}(t)$ and $G_{\mathrm{gel}}^{\mathrm{r}}(t)$ so that they can be combined to give the sum of the contributions of the relaxing modes in the sol and gel fractions post gelation as

$$G_{\mathrm{sol}}(t) + G_{\mathrm{gel}}^{\mathrm{r}}(t) = G_0\frac{d_r}{2}\int_{\epsilon_{ch}}^{\epsilon_x}\left(\frac{\epsilon}{\epsilon_x}\right)^{\frac{d_r}{2}(\nu-1)}e^{-\epsilon t}\frac{d\epsilon}{\epsilon}. \tag{8.41}$$

Post gelation, the total contribution to the relaxation modulus due to the gel fraction is,

$$G_{\text{post}}(t) = G_0 \frac{d_r}{2} \left(\underbrace{\int_{\epsilon_{ch}}^{\epsilon_x} \left(\frac{\epsilon}{\epsilon_x}\right)^{\frac{d_r}{2}(\nu-1)} e^{-\epsilon t} \frac{d\epsilon}{\epsilon}}_{\text{relaxing modes}} + \underbrace{\int_0^{\epsilon_{ch}} \left(\frac{\epsilon_{ch}}{\epsilon_x}\right)^{\frac{d_r}{2}(\nu-2)} \left(\frac{\epsilon}{\epsilon_x}\right)^{\frac{d_r}{2}} \frac{d\epsilon}{\epsilon}}_{\text{non-relaxing mode}} \right) \tag{8.42}$$

or on integration of the non-relaxing mode,

$$G_{\text{post}}(t) = G_0 \frac{d_r}{2} \int_{\epsilon_{ch}}^{\epsilon_x} \left(\frac{\epsilon}{\epsilon_x}\right)^{\frac{d_r}{2}(\nu-1)} e^{-\epsilon t} \frac{d\epsilon}{\epsilon} + G_0 \left(\frac{\epsilon_{ch}}{\epsilon_x}\right)^{\frac{d_r}{2}(\nu-1)}. \tag{8.43}$$

Hence (8.31) can be written

$$G(t) = \begin{cases} \int_{\epsilon_{ch}(t)}^{\epsilon_x} G_{\text{pre}}(\epsilon) e^{-\epsilon t} \frac{d\epsilon}{\epsilon}, & \alpha < \alpha_c \\ G_e + \int_{\epsilon_{ch}(t)}^{\epsilon_x} G_{\text{post}}(\epsilon) e^{-\epsilon t} \frac{d\epsilon}{\epsilon}, & \alpha > \alpha_c \end{cases} \tag{8.44}$$

where from (8.34) and (8.43),

$$G_{\text{pre}}(\epsilon) = \frac{G_0 \left(\frac{d_r}{2}\right)}{1 - \left(\frac{\epsilon_{ch}(t)}{\epsilon_x}\right)^{\frac{d_r}{2}(\nu-2)}} \left[\left(\frac{\epsilon}{\epsilon_x}\right)^{\frac{d_r}{2}(\nu-1)} - \left(\frac{\epsilon_{ch}(t)}{\epsilon_x}\right)^{\frac{d_r}{2}(\nu-2)} \left(\frac{\epsilon}{e_x}\right)^{\frac{d_r}{2}} \right], \tag{8.45}$$

$$G_{\text{post}}(\epsilon) = G_0 \frac{d_r}{2} \left(\frac{\epsilon}{\epsilon_x}\right)^{\frac{d_r}{2}(\nu-1)} \quad \text{and} \quad G_e = G_0 \left(\frac{\epsilon_{ch}(t)}{\epsilon_x}\right)^{\frac{d_r}{2}(\nu-1)}. \tag{8.46}$$

For the purposes of our model the continuous spectrum is discretised to obtain a series of i single modes, as illustrated in Figure 8.3, with relaxation rate ϵ_i and relaxation modulus $G(\epsilon_i)$. The integrals in (8.44) are thus replaced by summations. Each mode is treated as an individual mode in a multimode Oldroyd B fluid. Details of the logarithmic sampling scheme used to discretise the system can be found in Section 8.2 and the $G(\epsilon_i)$ can be determined for $\epsilon_{ch} < \epsilon < \epsilon_x$ from (8.45) and (8.46) for pre-gelation and post-gelation, respectively.

At each time point the range of the integration/discretisation is from ϵ_{ch} to ϵ_x but since ϵ_{ch} is not constant this interval is changing with time according to

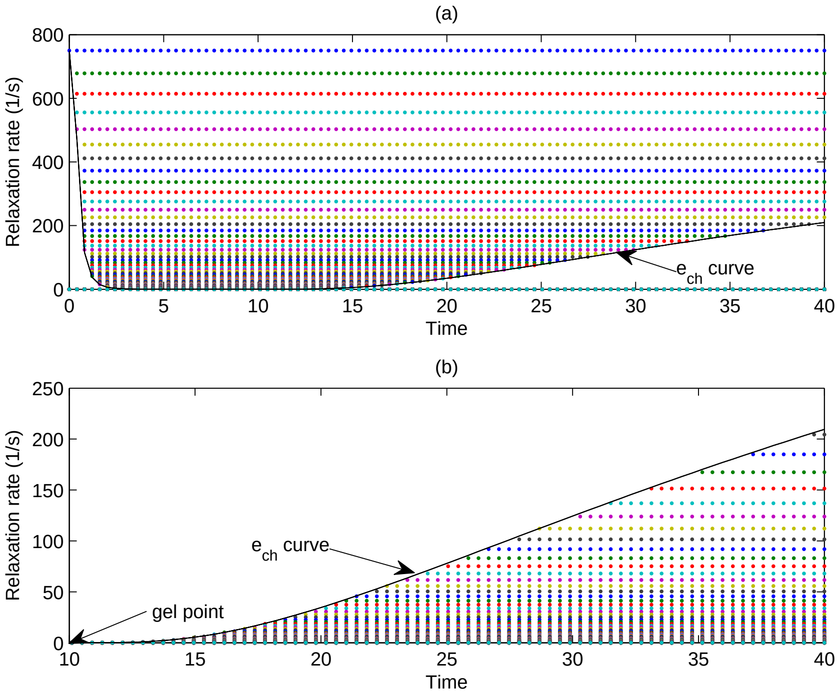

Figure 8.3: Schematic diagram illustrating the logarithmic sampling of relaxation modes ϵ_i for (a) both the pre-gelation and post-gelation stage and (b) the post-gelation stage of the reaction. Modes above the ϵ_{ch} curve are relaxing modes; before the gel point they belong to the sol fraction and after the gel point they belong to the gel fraction. Modes below the ϵ_{ch} curve are non-relaxing gel modes and contribute to the relaxation modulus of the gel.

the reaction rate α. Near the gel point, percolation theory predicts the cluster mass distribution scales with the distance from the gel point $|\alpha - \alpha_c|$ according to (8.22). Due to the fractal nature of the molecule it can be shown that the relaxation rate $\epsilon_{ch} \sim |\alpha - \alpha_c|^{2/\sigma d_r}$ [16,87]. Therefore the characteristic relaxation rate (i.e. the relaxation rate of the largest molecule at time t) can be stated as

$$\epsilon_{ch}(t) = \begin{cases} \epsilon_x \left| \frac{\alpha(t) - \alpha_c}{\alpha_c} \right|^{\frac{2}{\sigma d_r}}, & \alpha(t) < \alpha_c \\ \beta \epsilon_x \left| \frac{\alpha(t) - \alpha_c}{\alpha_c} \right|^{\frac{2}{\sigma d_r}}, & \alpha(t) > \alpha_c \end{cases} \tag{8.47}$$

where $\alpha(t)$ is defined by equation (8.9). The factor β is included to allow for the fact that $\epsilon_{ch}(t)$ is not symmetric about the gel point. Everitt *et al.* [26] derived a value for this parameter ($\beta = 0.0049$) based on prefactors determined in an earlier paper [72]. However, for the sake of simplicity they use $\beta = ((1 - \alpha_c)/\alpha_c)^{2/\sigma d_r}$, as will we, so that as t tends to infinity, ϵ_{ch} tends to ϵ_x. Having fully described the relaxation modulus, $G(t)$, of the polymer over the duration of the reaction, and discretised it into a series of i modes, we can now use this information to augment the non-reacting system, ((7.48) - (7.50)), with $\mathcal{R} = 0$, and derive results for the reacting model. A summary of the non-dimensionalised reacting model is now given. The non-dimensional variables are as for the non-reacting case and are detailed in Appendix C, with the exception of the temporal variable, which in the reacting case is scaled by $1/c_\alpha$. The variables are assigned indices i, j, n, to denote modal, spatial and temporal discretisation, respectively, with $i = 1 \cdots I, j = 1 \cdots J$ and $n = 1 \cdots N$. The resultant non-dimensional grouped parameters are tabulated in Table 8.1 and the individual parameter values pertinent to the reacting model are listed in Table 8.2.

$$\frac{4}{3}\dot{u}^n \left[\frac{1}{u^n} - \frac{1}{X + u^n} \right] = (P_g^n - P_u)M + \frac{2}{3}\gamma \sum_{\epsilon_i = \epsilon_{ch}(n)}^{\epsilon_x} \frac{G(\epsilon_i)}{G_0} \sum_{j=1}^{J} \frac{(A_{rr} - A_{\theta\theta})_{i,j}^n}{x_j + u^n} - \frac{1}{\Gamma\,(u^n)^{\frac{1}{3}}}, \tag{8.48}$$

$$\frac{\partial A^n_{rr_{i,j}}}{\partial t} = -\frac{4\dot{u}^n}{3\left(x_j + u^n\right)} A^n_{rr_{i,j}} - \frac{\epsilon_i}{c_\alpha}\left(A^n_{rr_{i,j}} - 1\right), \tag{8.49}$$

$$\frac{\partial\left(A_{rr} - A_{\theta\theta}\right)^n_{i,j}}{\partial t} = \frac{2\dot{u}^n}{3(x_j + u^n)}\left[(A_{rr} - A_{\theta\theta})^n_{i,j} - 3A^n_{rr_{i,j}}\right] - \frac{\epsilon_i}{c_\alpha}\left(A_{rr} - A_{\theta\theta}\right)^n_{i,j}, \tag{8.50}$$

$$\left(\frac{p_a + (p_{g0} - p_a)P^n_g}{p_{g0}}\right) u^n = 1 + \xi\Phi\frac{p_a}{p_{g0}} X\left(\phi^n_j(0,t) + (\alpha^n - \alpha_0)\right), \tag{8.51}$$

$$\frac{\partial\phi^n_j}{\partial t} = N(x_j + u^n)^{\frac{4}{3}}\frac{\partial^2\phi^n_j}{\partial x^2} - \frac{1}{X}\frac{d\alpha^n}{dt}(X - x_j). \tag{8.52}$$

Boundary conditions

$$\frac{\partial\phi^n_j}{\partial x} = \frac{1}{\xi X}\frac{p_{g0} - p_a}{p_a}(P^n_g - 1), \qquad x = 0, \tag{8.53}$$

$$\frac{\partial^2\phi^n_j}{\partial x^2} = 0, \qquad x = X. \tag{8.54}$$

Initial conditions

$$A^1_{rr_{i,j}} = 1, \qquad (A_{rr} - A_{\theta\theta})^1_{i,j} = 0, \qquad u^1 = 1, \qquad P^1_g = 1, \qquad \phi^1_j = 0.$$

It is important to note that contrary to the non-reacting model in the previous chapter, inertia is assumed to be negligible here and diffusion is no longer assumed to be instantaneous.

Before the gelation point, as the molecular weight distribution is continually broadening, new modes come into existence, i.e. are ‘switched on’, at each time step (see Figure 8.3(a)). As each new mode is ‘switched on’ it has initial orientation tensor $\mathbf{A} = \mathbf{I}$. However, at each time step n we determine $\mathbf{A}^{n+1}$ via (8.49) and (8.50). It can be seen from the right hand side of these equations, that this $\mathbf{A}^{n+1}$, is calculated from ϵ^n_i modes rather than ϵ^{n+1}_i modes. For example, if we have three modes $\{\epsilon_1, \epsilon_2, \epsilon_3\}$ existing at $t(n)$ and an extra two modes are ‘switched on’ at $t(n+1)$, so that we now have five modes $\{\epsilon_1, \epsilon_2, \epsilon_3, \epsilon_4, \epsilon_5\}$, the equation will calculate $A^{n+1}_{rr_{1,j}}$, $A^{n+1}_{rr_{2,j}}$, and $A^{n+1}_{rr_{3,j}}$ correctly but the terms $A^{n+1}_{rr_{4,j}}$ and $A^{n+1}_{rr_{5,j}}$ will be calculated based on $\epsilon_4, \epsilon_5 = 0$ instead of the actual values of these modes at $t(n+1)$. If left untreated, this would mean that the stress $G\mathbf{A}$ would not be conserved from one time step to the next and so in order to account for this discrepancy we ensure that stress is conserved by adjusting $\mathbf{A}$ for each mode in the following way

$$(G + \Delta G)\hat{\mathbf{A}} = G\mathbf{A} + \Delta G\mathbf{I}, \tag{8.55}$$

where $\hat{\mathbf{A}}$ is the adjusted orientation tensor at time step n determined from the output, $\mathbf{A}$, of (8.49) and (8.50). This leads to the following step in the numerical scheme,

$$\begin{aligned} \hat{A}^n_{rr_{i,j}} &= \frac{\left(\sum_i G^n_i\right) A^n_{rr_{i,j}} + \left[\sum_i G^{n+1}_i - \sum_i G^n_i\right]}{\sum_i G^{n+1}_i}, & (8.56) \\ \left(\hat{A}_{rr} - \hat{A}_{\theta\theta}\right)^n_{i,j} &= \frac{\left(\sum_i G^n_i\right) \left(\hat{A}_{rr} - \hat{A}_{\theta\theta}\right)^n_{i,j}}{\sum_i G^{n+1}_i}. & (8.57) \end{aligned}$$

where $G_i = G(\epsilon_i)$. The picture is slightly different post-gelation; now an infinite cluster exists along with a distribution of finite clusters [16]. At the gel point the material is neither liquid nor solid [104]; it has a viscosity which diverges to infinity and an elastic modulus, G_{gel}, equal to zero. Proceeding past the gel point the elastic modulus begins to grow with time as the larger finite clusters attach to the infinite cluster and become frozen (that is, no longer able to relax). These modes, which we refer to as 'switched off', can be observed below the ϵ_{ch} curve in Figure 8.3(b). Again, because $\mathbf{A}^{n+1}$ is determined from ϵ^n_i we need to adjust this single gel mode according to

$$\left(G_{\text{gel}} + \Delta G_{\text{gel}} + \Delta G_{\text{off}}\right) \hat{\mathbf{A}} = G_{\text{gel}}\mathbf{A} + \Delta G_{\text{gel}}\mathbf{I} + \Delta G_{\text{off}}\mathbf{A}_{\text{off}}, \tag{8.58}$$

that is,

$$\begin{aligned} A^n_{rr_j} &= \frac{G^n_{\text{gel}} A^n_{rr_j} + \left(G^{n+1}_{\text{gel}} - G^n_{\text{gel}}\right) + \sum_i G^{n+1}_{\text{off}_\text{i}} A^n_{rr_{i,j}}}{G^{n+1}_{\text{gel}}}, & (8.59) \\ \left(\hat{A}_{rr} - \hat{A}_{\theta\theta}\right)^n_j &= \frac{G^n_{\text{gel}} \left(\hat{A}_{rr} - \hat{A}_{\theta\theta}\right)^n_j + \sum_i G^{n+1}_{\text{off}_\text{i}} \left(\hat{A}_{rr} - \hat{A}_{\theta\theta}\right)^n_j}{G^{n+1}_{\text{gel}}}, & (8.60) \end{aligned}$$

where $G_{\text{off}}(\epsilon_i)$ is the value of the stress modulus for modes $\epsilon_i < \epsilon_{ch}$ at a given time point. The combined modulus, $\Delta G_{\text{off}} = \sum_i G_{\text{off}_\text{i}}$, and stress, $\Delta G_{\text{off}}\mathbf{A}_{\text{off}} =$

$\sum_i G^{n+1}_{\mathrm{off_i}} A^n_{rr_i}$, of these 'switched off' modes is added to the single gel mode, at each time step, after the gelation point.

8.2 Numerical scheme and results

A fourth order Runge-Kutta method was used to solve the stress equations (8.49) and (8.50). The momentum equation, (8.48), was solved by a forward Euler method with a time step less than the shortest relaxation time ($1/\epsilon_x$). The solutions to the gas diffusion equation (8.52) and gas pressure equation (8.51) were obtained via the Crank-Nicolson method [84], choosing the spatial discretisation so that $\Delta t/(\Delta x)^2 < 1/2$, thus ensuring spurious oscillations do not occur. The spatial integration in (8.48) was carried out using the composite Simpson's rule. Due to the discretisation of the relaxation modulus into individual modes, (8.49) and (8.50) are solved for each modal index $i = 1, 2, .., I$ and spatial index $j = 1, 2, .., J$ which are then summed over both the i and j indices in the momentum equation (8.48). The relaxation spectrum is discretised by $\epsilon_i = \epsilon_x e^{-di(i-1)}$, where $di = 0.2$ and $I = 100$.

The non-dimensionalised system, (8.48) - (8.52), was solved numerically for the parameterisation described in [26] and the numerical code was validated against results published in the same paper. We then examined the output using the parameterisation described in Table 8.2 which pertains to conditions, described in [92, 93], that we seek to model. For this analysis we continue to use the non-dimensional system as we are only concerned with single bubbles. In particular, we investigate the effect of the reaction rate constant, c_α, and the pressure amplitude of the acoustic irradiation, on the non-dimensional bubble volume, u, and the dimensionless bubble gas pressure, P_g, as illustrated in Figures 8.4 and 8.5. As c_α increases the bubble volume reaches steady state more quickly and the initial gradient is steeper as shown in Figure 8.4. The steady state bubble volume is, itself, unaffected by the reaction rate constant. The bubble gas pressure peaks sooner for lower reaction rates (see Figure 8.5 (b)) but as c_α increases the magnitude of this peak gas pressure is larger. The initial bubble growth is controlled, via diffusion, by the concentration of gas already dissolved in the fluid and the diffusion timescale is quantified by $9D/(u_0X)^{2/3}$. The second source for gas into the bubble is its production as a by product of the reaction, at a rate given by c_α. For larger c_α values, therefore, we see a larger peak in bubble gas pressure as shown in Figure 8.5 (b). In our parameterisation (see Table 8.2) gas diffusion is relatively fast compared to the initial, viscosity controlled bubble expansion rate, given by $\xi p_a \alpha_0/\mu$. For each value of c_α in Figure 8.5, therefore, the bubble gas pressure initially increases and only begins to fall as the reaction rate decreases and gas concentration in the fluid begins to fall. Comparing Figures 8.5 (a) and (b) we can see that as the bubble gas pressure decays towards its steady state value, the initial steep bubble growth gradient decreases to a lower value.

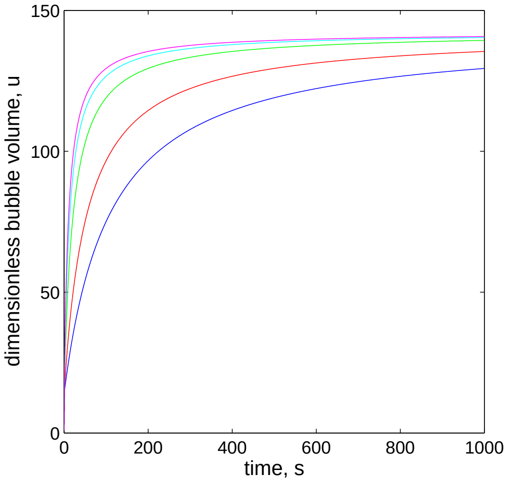

Figure 8.4: The effect of reaction rate constant coefficient, c_α, on dimensionless bubble growth rate. Blue line: $c_\alpha = 0.01$; Red line: $c_\alpha = 0.02$; Green line: $c_\alpha = 0.05$; Cyan line: $c_\alpha = 0.08$; Magenta line: $c_\alpha = 0.10$; Data obtained from the numerical integration of (8.48) - (8.52) using parameter values in Table 8.2

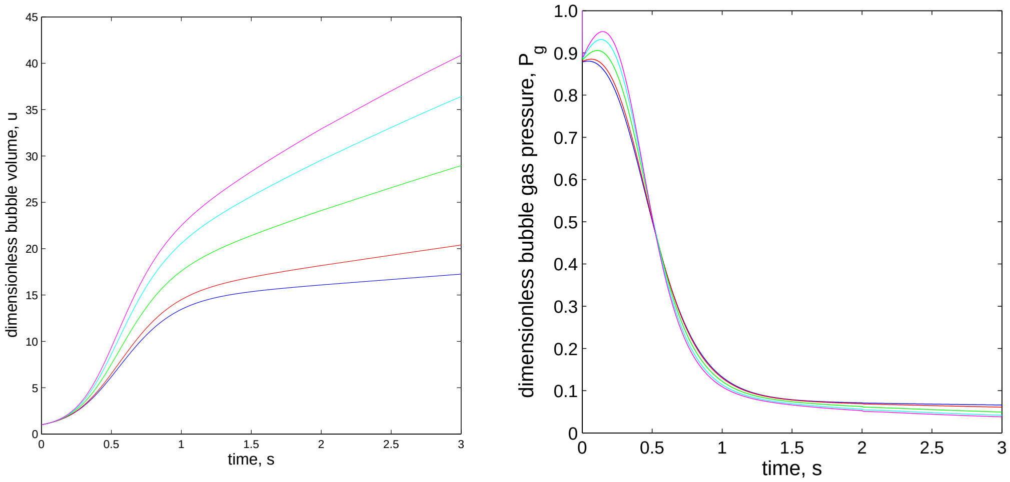

Figure 8.5: The effect of reaction rate constant coefficient, c_α, on (a) dimensionless bubble growth rate, and (b) dimensionless bubble gas pressure. Blue line: $c_\alpha = 0.01$; Red line: $c_\alpha = 0.02$; Green line: $c_\alpha = 0.05$; Cyan line: $c_\alpha = 0.08$; Magenta line: $c_\alpha = 0.10$; Data obtained from the numerical integration of (8.48) - (8.52) using parameter values in Table 8.2. Note that (a) is effectively a scaling of Figure 8.4.

When we go on to examine bubble distributions in Section 8.6 we need to redimensionalise the temporal variable in order to compare neighbouring bubble radii at consecutive time points.

8.3 Calculation of reaction rates from experimental observations

Having developed a numerical code, to track the growth of a single bubble in a polymerising polymer foam, we now turn to the experimental work described in [93] and develop a model to measure a bubble size distribution within a polymerising sample. First we detail the experimental set up used by Torres-Sanchez *et al.* and then propose a model for this system.

A schematic of the experimental set up used in [93] is shown in Figure 8.6. The reactants were placed in a cylindrical vessel in the middle of a water bath lined with acoustic absorbers to minimise wave reflection. The water bath maintained a constant temperature in order to prevent overheating. The sample container and transducer were aligned along the longitudinal axis of the bath and the sonotrode tip was immersed 2cm below the free surface on the same plane as that of the central plane of the container. The container was perpendicular to the sonicating probe and had the opposite 180 degrees of its surface shielded by absorbent material to minimise reflections. Thermocouples and conductivity probes were held in the middle of the mixture to monitor the reaction. To start the reaction the blowing agent was added to the mixture which was then irradiated for 20 minutes with a 2 min on/1 min off cycle. When irradiation was complete the curing foam was left in the bath for 30 minutes until rigid. Examining the polymerisation reaction itself, the chemical reaction to form polyurethane occurs between polyols and diisocyanate groups with distilled water employed

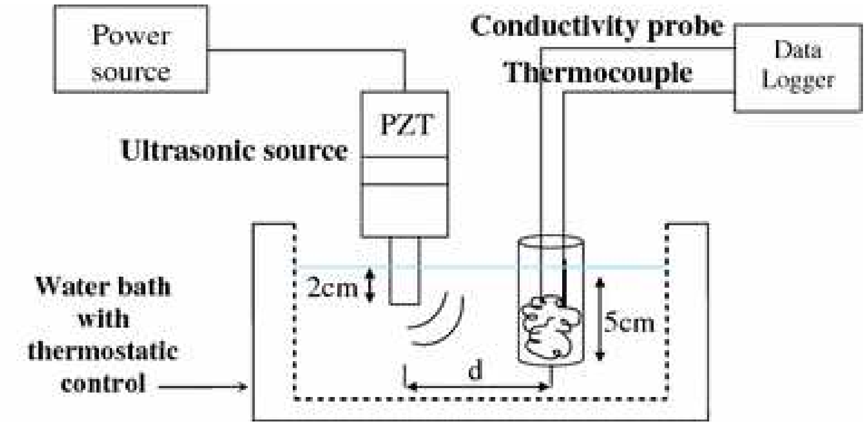

Figure 8.6: Schematic of the experimental rig as published in [93] and reprinted with the permission of the author.

as a blowing agent and can be written

$$\text{polyol} + \text{diisocyanate} \rightarrow \text{polyurethane} + CO_2.$$

In [93] the reaction is assumed to be of first order and can be described by the reaction kinetics

$$\frac{d\alpha}{dt} = c_\alpha(1-\alpha), \tag{8.61}$$

so that

$$\alpha^{(1)}(t) = 1 - (1-\alpha_0)e^{-c_\alpha(t-t_0)}, \tag{8.62}$$

where $\alpha^{(1)}(t)$ is the extent of the first order reaction. Everitt *et al.* [26] assume second order reaction kinetics described by (8.8) and (8.9) where we assign $\alpha^{(2)}$ as the extent of the second order reaction. In [92] the time to gelation point, $t_c = 253s$, for samples irradiated at 20Hz, can be calculated as an average of the three experimental plots obtained by irradiating the samples at different acoustic pressure amplitudes (see Table 8.4 and Figure 8.7).

Assuming this value for t_c and using the values in Table 8.2 for the parameters α_0, t_0 and α_c we can calculate the approximate reaction rates, $c_\alpha^{(1)}$ and $c_\alpha^{(2)}$, required for the first and second order reaction kinetics, respectively. For the

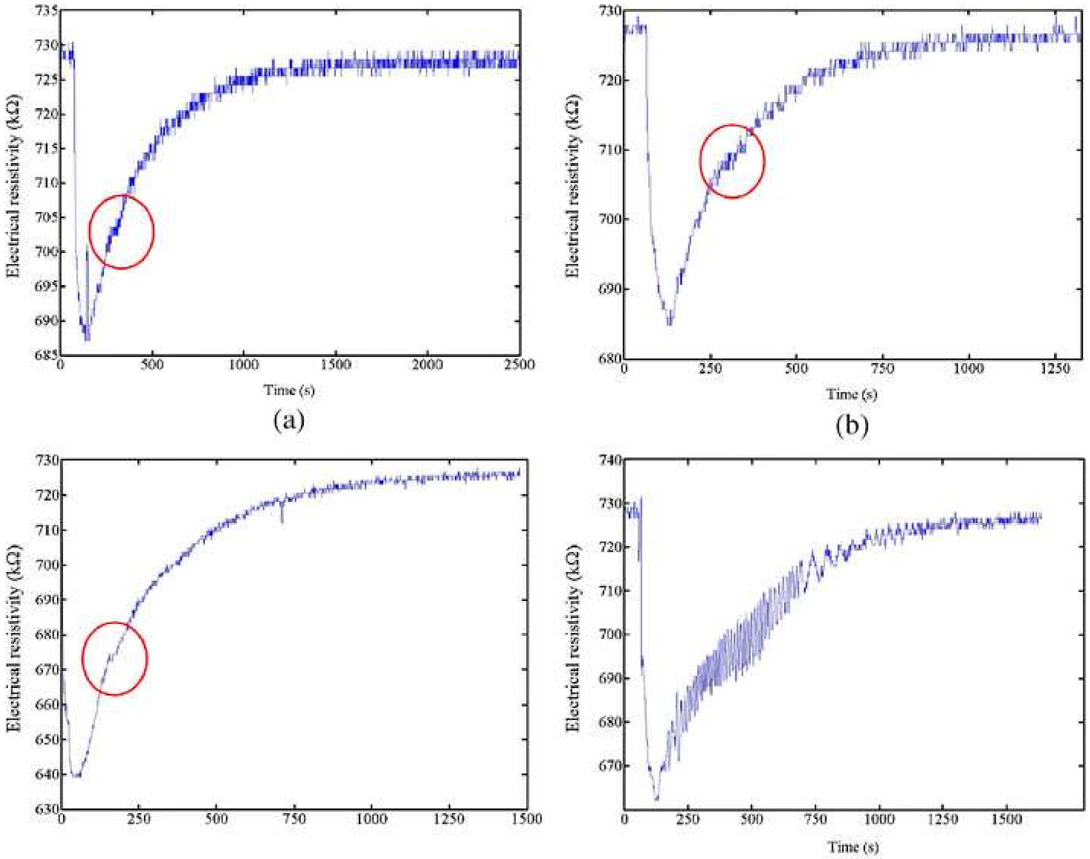

(a) (b)

(c) (d)

Figure 8.7: Experimental plots of electrical resistivity lines obtained from foams sonicated at 20kHz and different acoustic pressures: (a) 7 kPa, (b) 10 kPa, (c) 17 kPa, (d) 28 kPa. The start of the ‘gelation stage’ has been circled. Data from these plots are used to construct Table 8.4. Reprinted with the permission of the author [92].

Reference [92]	Amplitude (kPa)	$t_c(s)$	$c_\alpha(s^{-1})$
Figure 5(a)	7	300	0.034
Figure 5(b)	10	260	0.040
Figure 5(c)	17	200	0.053

Table 8.4: Data values approximated from plots (a), (b) and (c) in Figure 5 of [92]. From these plots we can approximate the time of the gelation point, t_c, in samples irradiated at 20Hz and acoustic pressure amplitudes of 7kPa, 10kPa and 17kPa, respectively. This gelation time is approximately identified, in Figure 8.7, as the first small plateau in the plots of electrical resistance versus time reproduced here. The c_α values for this second order reaction are calculated via (8.64).

first order case,

$$c_\alpha^{(1)} = \frac{1}{(t_0 - t_c)} \log\left(\frac{1-\alpha_c^{(1)}}{1-\alpha_0}\right), \tag{8.63}$$

so that, with $\alpha_c^{(1)} = 0.91$, $\alpha_0 = 0.1$, $t_c = 253$s and $t_0 = 10$s (see Table 8.2), $c_\alpha = 9 \times 10^{-3}\text{s}^{-1}$. For the second order reaction,

$$c_\alpha^{(2)} = \frac{(\alpha_c^{(2)} - \alpha_0)}{(t_c - t_0)(1-\alpha_0)(1-\alpha_c)}, \tag{8.64}$$

so that $c_\alpha = 0.04\text{s}^{-1}$. The model that we employ for numerical simulations assumes second order reaction kinetics and we will therefore use this latter value of c_α to model the experimental set up used in [93] even though they assumed first order reaction kinetics with a measured reaction rate of $c_\alpha = 1 \times 10^{-3}s^{-1}$.

8.4 The direct effect of pressure amplitude on bubble volume evolution

We first consider the experimental system in two dimensions only with the left hand side lower corner of the container positioned at the origin and the sonotrode in line with the vertical plane through the centre of the cylinder positioned at a vertical distance $h/2$ from the origin, where h is the height of the sample cylinder (see Figure 8.8).

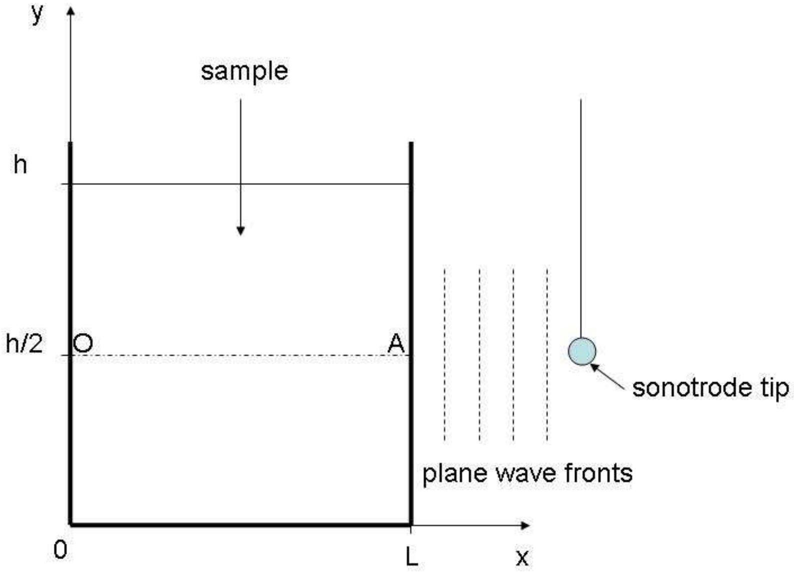

Figure 8.8: Schematic illustrating a 2D vertical segment, in the $x - y$ plane, of the 3D sample container with height, h and width, L. The reacting sample within the container is irradiated by an acoustic signal from the sonotrode tip which is positioned a sufficient distance from the sample container so that plane wave irradiation may be assumed. The 1D horizontal line ‘OA’ is situated at the sample half height, $h/2$. In order to simplify the mathematical model it is assumed that the sample height remains constant throughout the reaction; this is not the case in the experimental setup.

There are a number of assumptions that we deploy to simplify the situtation. At the point of acoustic irradiation we assume that the polymerising sample is a homogeneous dispersion of post nucleated bubbles of a given initial radius. We also assume that the height of the sample is h and remains so for the duration of the sample irradiation which is continuous. This does not reflect the experiment described above as the upper surface rises as the reaction progresses. We assume that the sonotrode tip is so small, and the wavelength and distance from the sample such, that the irradiating wave may be assumed to be planar throughout the sample. Choosing the line OA (see Figure 8.8) at $y = h/2$ we can therefore reduce the pressure distribution to one dimension only.

Acoustic pressure, P_u, is the local pressure deviation from the ambient atmospheric pressure, p_a, caused by an acoustic wave. The instantaneous sound pressure, $P_u(x,t)$ is the deviation from the local ambient pressure due to the insonifying wave at a given point in space and time. In order to determine the effective acoustic pressure at a spatial point over a given time interval we can calculate the root mean square (RMS) value. For a periodic sinusoidal waveform given by,

$$P(x,t) = p_1 + p_2 \cos(2\pi f t)\sin(kx),$$

where f is the frequency and k the wavenumber, the RMS pressure is,

$$P_{\text{rms}}(x) = p_1 + (p_2/\sqrt{2})\sin(kx).$$

The waveform set up in [93] is a standing wave resulting from the superposition of an incident and reflected wave of equal acoustic pressure amplitude and frequency and described by,

$$P_s(x,t) = p_1 + 2p_2 \cos(2\pi f t)\sin(kx),$$

with an RMS spatial distribution,

$$P_{\text{rms}}(x) = p_1 + \sqrt{2}p_2 \sin(kx).$$

The total pressure, P_{total}, is the sum of the ambient and effective acoustic pressure so that in the case of the standing wave,

$$P_u(x) = p_1 + \sqrt{2}p_2 \sin(kx), \tag{8.65}$$

the total pressure is given by,

$$P_{\text{total}}(x) = p_a + p_1 + \sqrt{2}p_2 \sin(kx). \tag{8.66}$$

The *in situ* pressure field, $\bar{P}$, proposed by [93] was quoted in decibels, dB, and had approximate minimum and maximum levels of 143dB and 151dB, respectively. The conversion equation

$$P = 2 \times 10^{\left(\bar{P}/20-5\right)}, \tag{8.67}$$

was applied to obtain the corresponding minimum and maximum values of P in Pascals, which were then used to derive a mathematical function to model the insonifying signal. This resulted in the following parameter values for the signal modelled by (8.65): $p_1 = 500Pa$, $p_2 = 200/\sqrt{2}Pa$, $k = \pi/L$, where $L = 50$ is the sample width in mm. The schematic in Figure 8.9 demonstrates the effective pressure field in Pascals (green line) and shows bubbles nucleated homogeneously across the one dimensional x domain. The corresponding field in decibels is also plotted (blue line) and is calculated via

$$\bar{P} = 20\log_{10}\left(\frac{P}{2 \times 10^{-5}}\right). \tag{8.68}$$

The *in situ* pressure amplitude values proposed by Torres-Sanchez *et al.* [93] are attenuated by the water bath and polymerising sample. Thus, although the instrumental value for the pressure amplitude of the standing wave is of the order 10^4Pa, the actual amplitude in situ is only of order 10^2Pa. Substituting for the values of p_1 and p_2, described above, in the acoustic pressure amplitude term, p_u, gives non-dimensional minimum and maximum P_u values of 0.0014

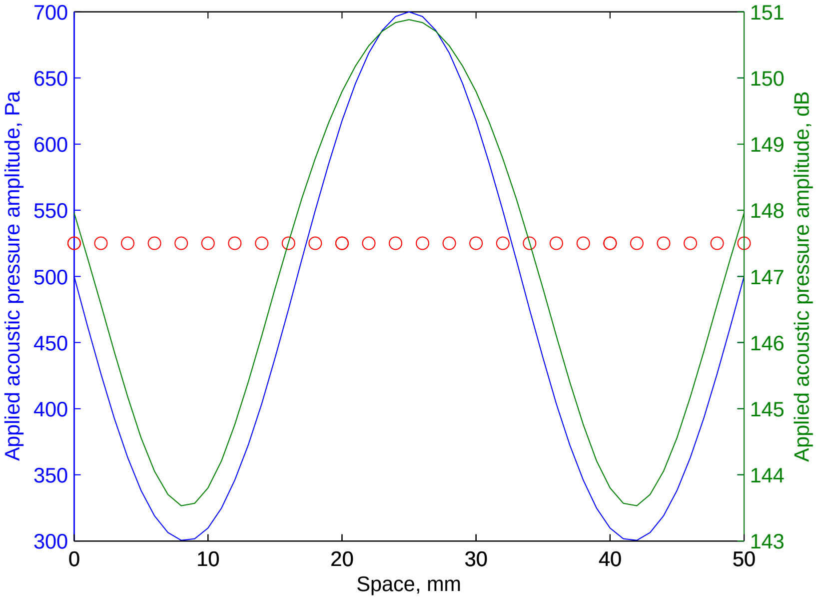

Figure 8.9: Schematic illustrating the idealised sinusoidal waveform used to model the effective acoustic pressure distribution in the sample described in [93]. The waveform is described by (8.65) with $p_1 = 500$ Pa, $p_2 = 200/\sqrt{2}$ Pa, $k = \pi/L$ where $L = 50$ mm. The values for p_1 and p_2 were derived via consideration of the minimum and maximum pressure values in dB proposed in [93]. The green line gives the pressure in Pascals and the blue line gives the pressure in decibels (dB) using the conversion equation (8.68). The circles illustrate a series of homogeneously spaced nucleated bubbles across the one dimensional sample domain.

and 0.0050, respectively. These P_u values were entered in (8.1) and plots of the evolving dimensionless bubble volume, u, are shown in Figure 8.10. This figure illustrates that, at this level of pressure amplitude, the effect on the expanding bubble volume is negligible. Therefore, because of the attenuation of the pressure amplitude we look instead at the indirect effect of the pressure amplitude on the polymerisation reaction rate constant, c_α, in the next section.

8.5 The effect of pressure amplitude on reaction rate

Motivated by Torres-Sanchez *et al.* [92] we decided to investigate the effect of pressure amplitude on reaction rate. In [26] the reaction rate is a non-varying constant and only a single bubble is considered. We propose that due to the local pressure amplitude distribution we can describe a local reaction rate distribution across the sample so that for a series of bubbles each one evolves under the influence of its local reaction rate. In order to examine this effect in isolation we have set the acoustic pressure amplitude, P_u, in the momentum equation (8.1) to zero for the remainder of this Chapter. Before looking at the bubble size distribution across such a sample we first examine the sensitivity of the model to the reaction rate constant, c_α. The evolution of a single bubble under a number of different reaction rates of the order used in [92] is illustrated in Figure 8.5 (a); the parameter values are described in Table 8.2. We can see that the effect of different c_α is significant, given that the plot in Figure 8.5 is non-dimensional, and that it is worth investigating this further and extending the result from the single bubble case to the multibubble case and including bubble-bubble interaction.

First we derived an empirical relationship between the pressure amplitude applied to the sample and the resultant reaction rate constant, c_α. This was done by examining the experimental data used to construct Figure 8.11 in [92].

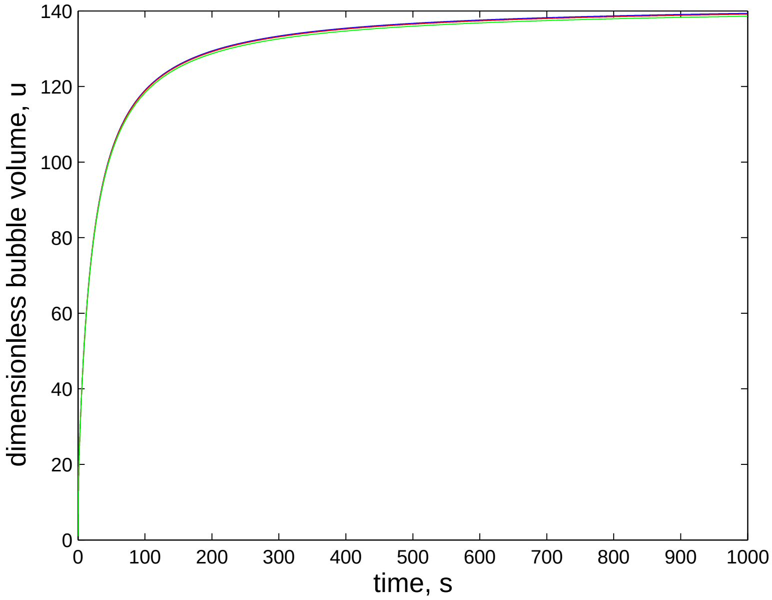

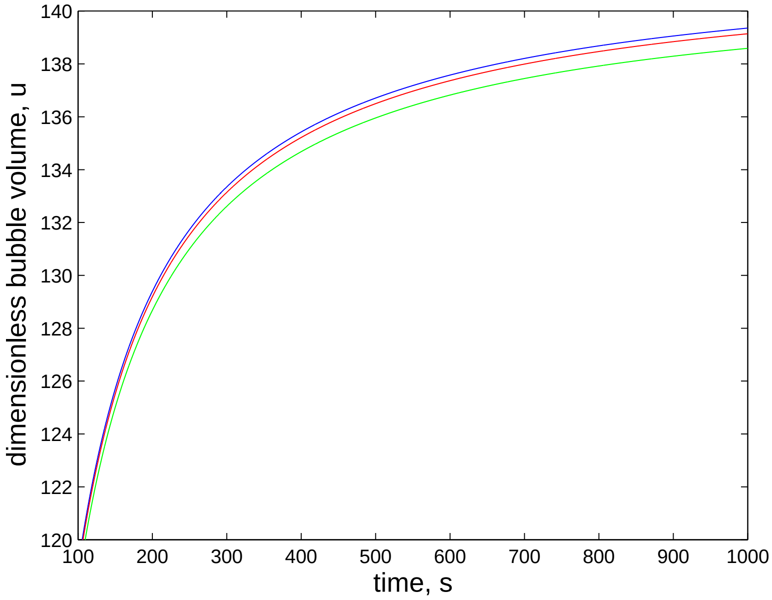

Figure 8.10: Plots demonstrating the effect of the *in situ* acoustic pressure amplitude levels on the bubble volume evolution. In both cases $P_u = 0$ (blue line), $P_u = 0.0014$ (red line) and $P_u = 0.0050$ (green line) are compared. The lower plot is a zoomed in version of that on the left to quantify the magnitude of the difference in each case.

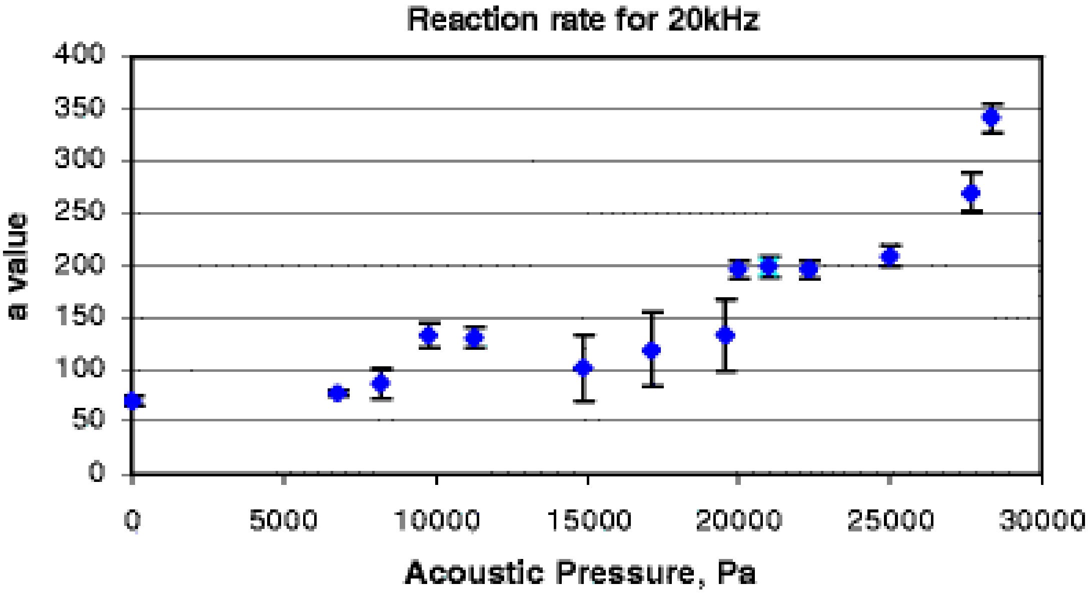

Figure 8.11: Slope constant ‘a’ value for different samples irradiated at 20 kHz as published in [92]. Data from this plot were extracted to construct Table 8.5. Reprinted with the permission of the author [92].

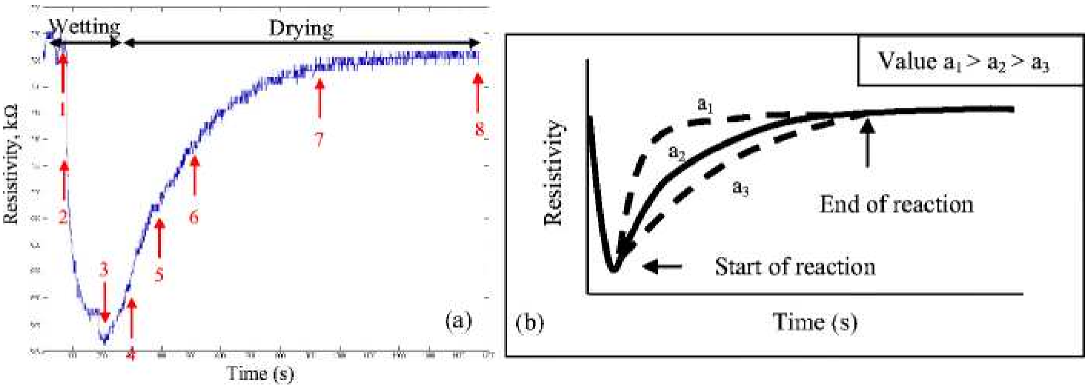

Figure 8.12: (a) Electrical resistance data collected by DAQ; (b) The corresponding logarithmic phase of the resistivity with different slope constant ‘a’. Reprinted with the permission of the author [92].

The data values are shown in Table 8.5. The parameter a is the coefficient of the curve $y = a\log(x) + b$ fitted to the resistivity-pressure amplitude data (see Figure 8.7) and gives a measure of the reaction rate constant as illustrated by Figure 8.12 (b) from the same paper. Taking the second order reaction rate, $c_\alpha = 0.04$, as determined in Section 8.3, and correlating it directly with the value of $a = 68$ in the absence of an acoustic signal (see Figure 8.11) we determined the constant of proportionality $k = 1700$. In other words, $c_\alpha = a/k$; this can then be used to calculate the remaining c_α values tabulated in Table 8.5. We then fitted a linear function to the experimentally observed relationship between pressure amplitude and reaction rate (see Figure 8.13) to give

a	$c_\alpha, 10^{-2}s^{-1}$	Pressure amplitude, P_a
68	4.0	0
75	4.4	6750
86	5.1	8250
132	7.8	9750
129	7.6	11250
100	5.9	15000
121	7.1	17250
132	7.8	19500
196	11.5	20000
200	11.8	21000
196	11.5	22500
204	12.0	25000
268	15.8	27750
343	20.2	28500

Table 8.5: Data table showing the a values and acoustic pressure amplitude values (in Pa) extracted from Figure 8.11 [92] and the corresponding c_α value calculated using the direct correlation given by $c_\alpha = a/1700$, with units of $10^{-2}s^{-1}$. The plot, in Figure 8.13, of reaction rate constant versus pressure amplitude was constructed using this data.

$$c_\alpha = 3.571 \times 10^{-4} + 5.513 \times 10^{-6} P_a. \tag{8.69}$$

A theoretical irradiating acoustic signal, (8.70), was proposed to approximate

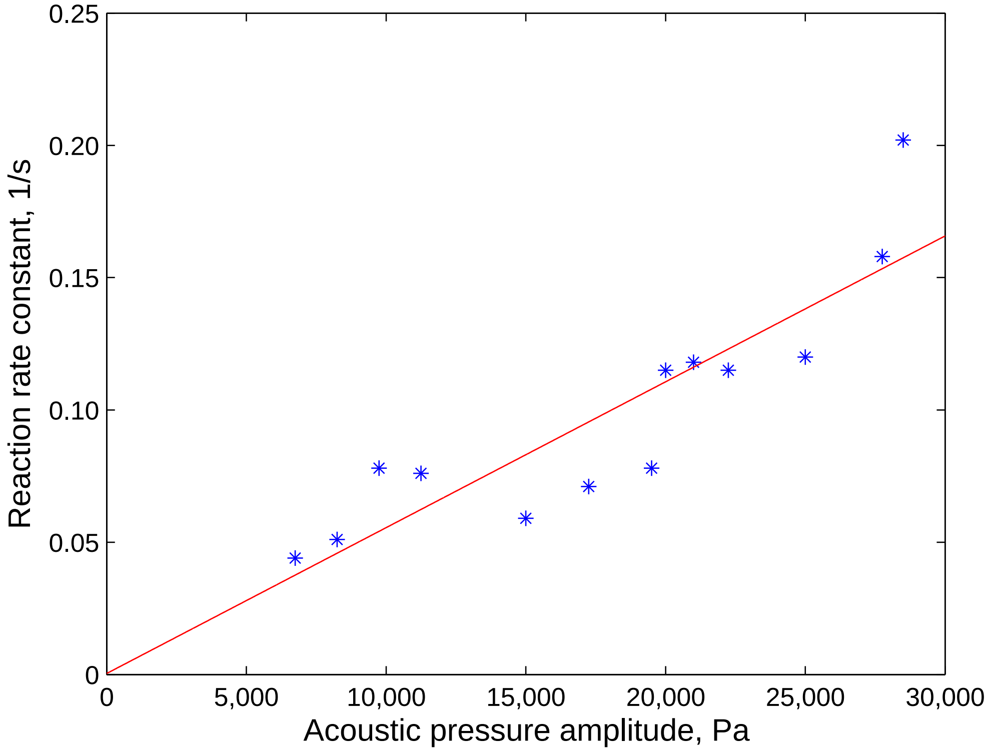

Figure 8.13: Plot of reaction rate constant, c_α (s^{-1}) versus pressure amplitude (Pa) from data quoted in Table 8.5. The pressure amplitude values were extracted from Figure 8.11 [92] and the reaction rate constant values determined by the direct correlation given by $c_\alpha = a/1700$ as described in the text.

that described in [93]. The signal is a sine wave with one and a half wavelengths across the sample width and a maximum amplitude value at half the sample width. The maximum pressure amplitude is 30kPa and the minimum is 5kPa. This reflects approximately the instrumental range of values used to irradiate the sample. The irradiating signal is defined by

$$P_a = 17500 - 12500 \sin\left(\frac{3\pi x}{L}\right), \tag{8.70}$$

where $L = 50$mm is the width of the sample and x, the spatial co-ordinate within the sample, is also measured in the same units. We can then substitute for this form of P_a into (8.69) to plot the resultant reaction rate distribution across the sample.

8.6 Simulation of the foam porosity profile

Having tailored a pre-existing model to track the evolution of a single bubble in an expanding reacting polymer foam we now examine how a one dimensional series of bubbles, spread homogeneously across the sample domain, evolve under the influence of an ultrasound standing wave (expressed as a local reaction rate) and the influence of their nearest neighbours. These post nucleation bubbles were initially placed across the sample domain with a number of different spacings to analyse the effect of the density of bubbles on the heterogeneity of the final sample. It is important to note that since we are now comparing results for different reaction rate constants we must re-dimensionalise the temporal variable. The remaining results in this section, therefore, refer to the dimensional temporal variable. Since the reaction rate distribution across the sample is symmetric we can reduce the computational cost by reducing the domain to half the sample width, that is $L/2$. A discrete set of c_α values (see Figure 8.14) was obtained for each 0.25mm spatial point and the bubbles were initially spaced at 0.25mm intervals. Having determined the local reaction rates for each bubble

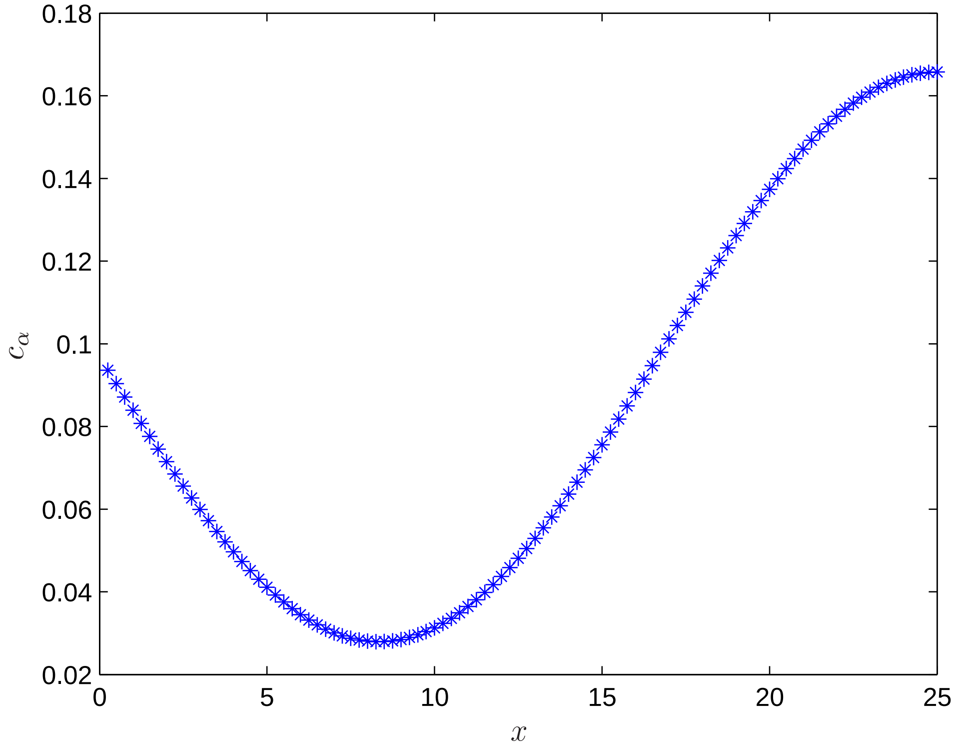

Figure 8.14: Plot showing the discretised form of the continuous spatial distribution curve for local reaction rate constant, c_α, with discrete spatial interval $\delta x = 0.25$mm. Due to the symmetry of the sample domain we are only interested in the spatial region up to $L/2$, where in this case $L = 50$mm.

we evolve them independently (they are initially unhindered by neighbouring bubbles) so that we have a vector of radii for each time point during the expansion. We further assume that the bubbles do not translate during the reaction, that is the bubble centre positions are fixed. The parameterisation for this analysis is described in Table 8.6. For each bubble in the domain we then append its vector to produce a matrix, $r(t_n, m)$, of radii for $m = 1, \cdots, N$ bubbles at $t_n = 1, \cdots, T$ time points. At each time point we need to assess whether or not a given bubble is touching either of its neighbours and to this end at each timepoint t_n, $M(t, :) = R(t, 1 : N-1) - L(t, 2 : N)$ is calculated, where $R(t, N)$ and $L(t, N)$ give the right and left hand bubble positions, respectively. If any of the entries in the vector M are not strictly positive then the bubbles associated with those entries are touching and so their growth is stopped. The schematic in Figure 8.15 demonstrates this. At the end of the temporal loop therefore we will have a matrix of right and left position vectors and hence the final radius of each of the N bubbles at $t = T$. We use these values to construct the schematics in Figures 8.16 - 8.18 and the plots in Figures 8.19 - 8.22. Table 8.6 shows the maximum and minimum bubble radii for each initial bubble spacing value δx.

Parameter	Value	Units	Comments
D	1	$10^{-2}\mathrm{m}^2\mathrm{s}^{-1}$	essentially instantaneous diffusion
p_{g0}	10	$10^5\mathrm{Nm}^{-2}$	$p_{g0} = p_a(1 + \xi\alpha_0)$ [26]
u_0	9	$10^{-12}\mathrm{m}^3$	
S	1	$10^{-6}\mathrm{Nm}^{-1}$	negligible surface tension
ξ	90		
X	500		
c_α	$0.028 - 0.166$	s^{-1}	calculated from data in [92]*

Table 8.6: Parameter values used to construct Figures 8.16 to 8.20. The remaining parameter values, not already listed in this table are as detailed in Table 8.2. * For details of this calculation and a discussion on the reaction kinetics see Section 8.3.

The schematics in Figures 8.16 - 8.18 were constructed by taking the final

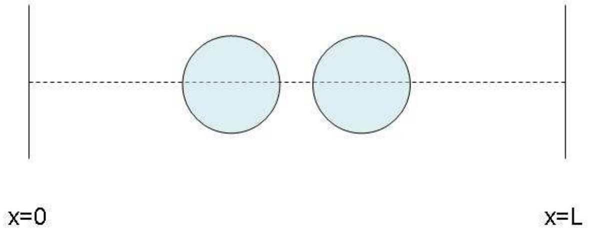

Time point: t-1

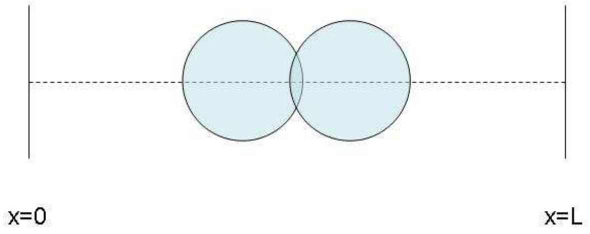

Time point: t

Figure 8.15: Schematic illustrating the simple rule for bubble-bubble interaction. At time point $t-1$ the position and radii of the neighbouring bubbles are such that they are not touching and bubble evolution is continued until the next time step when the bubble position and radii are checked again. In this case, at the subsequent time point t the bubble evolution means that the corresponding entry in the vector M (see text) is not strictly positive and therefore the growth of these bubbles in the mathematical code is stopped and their positions frozen for the duration of the time loop.

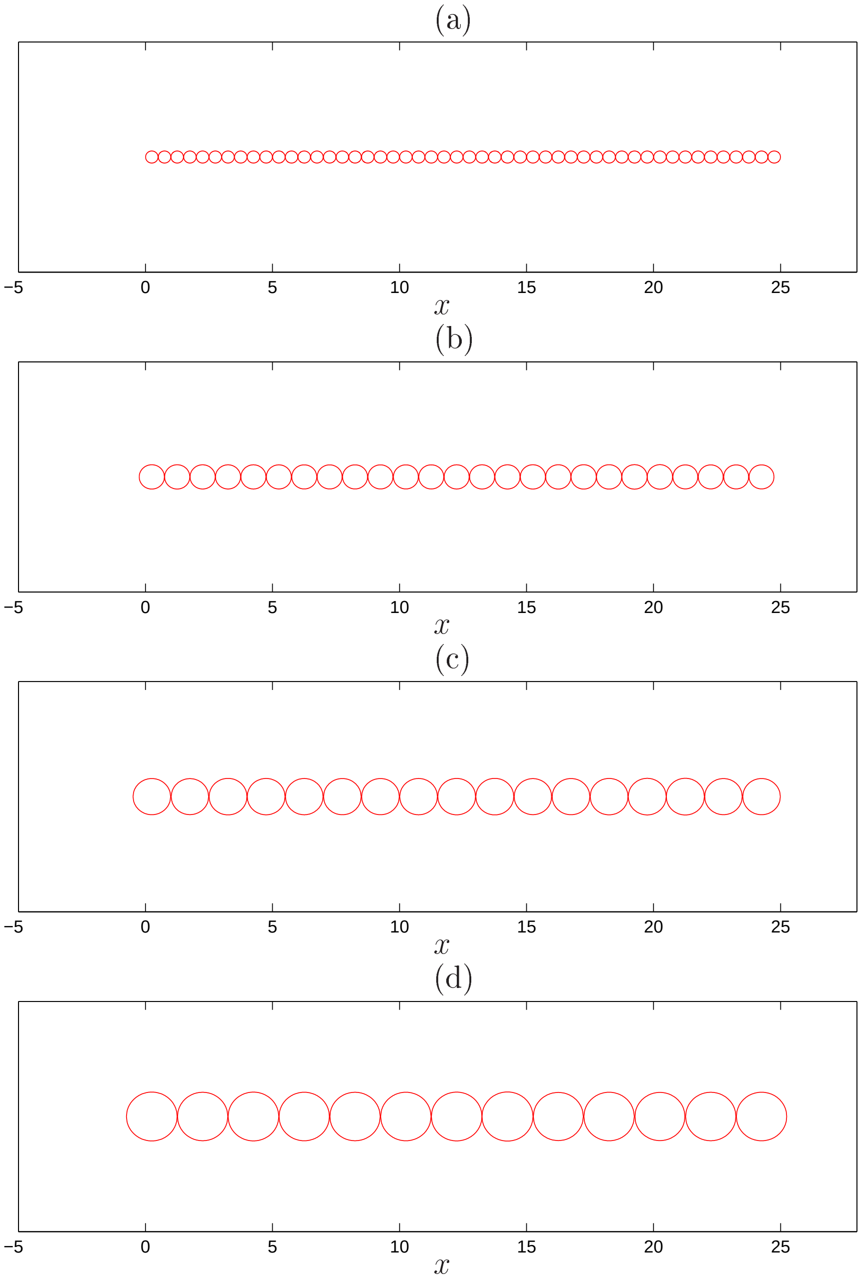

Figure 8.16: Illustrative plots showing the final bubble size distribution, across the half sample domain, given the local reaction rate constant profile prescribed in Figure 8.14, for (a) 50, (b) 25, (c) 17 and (d) 13 bubbles. The bubbles are positioned homogeneously across the domain at 0.5, 1.0, 1.5 and 2.0 mm intervals, respectively, and each bubble is allowed to evolve, given the local reaction rate constant value prescribed at its central position, until the reaction ceases or it touchs a neighbouring bubble. x is the horizontal co-ordinate, in the sample, in millimetres and the parameter values used are listed in Table 8.6.

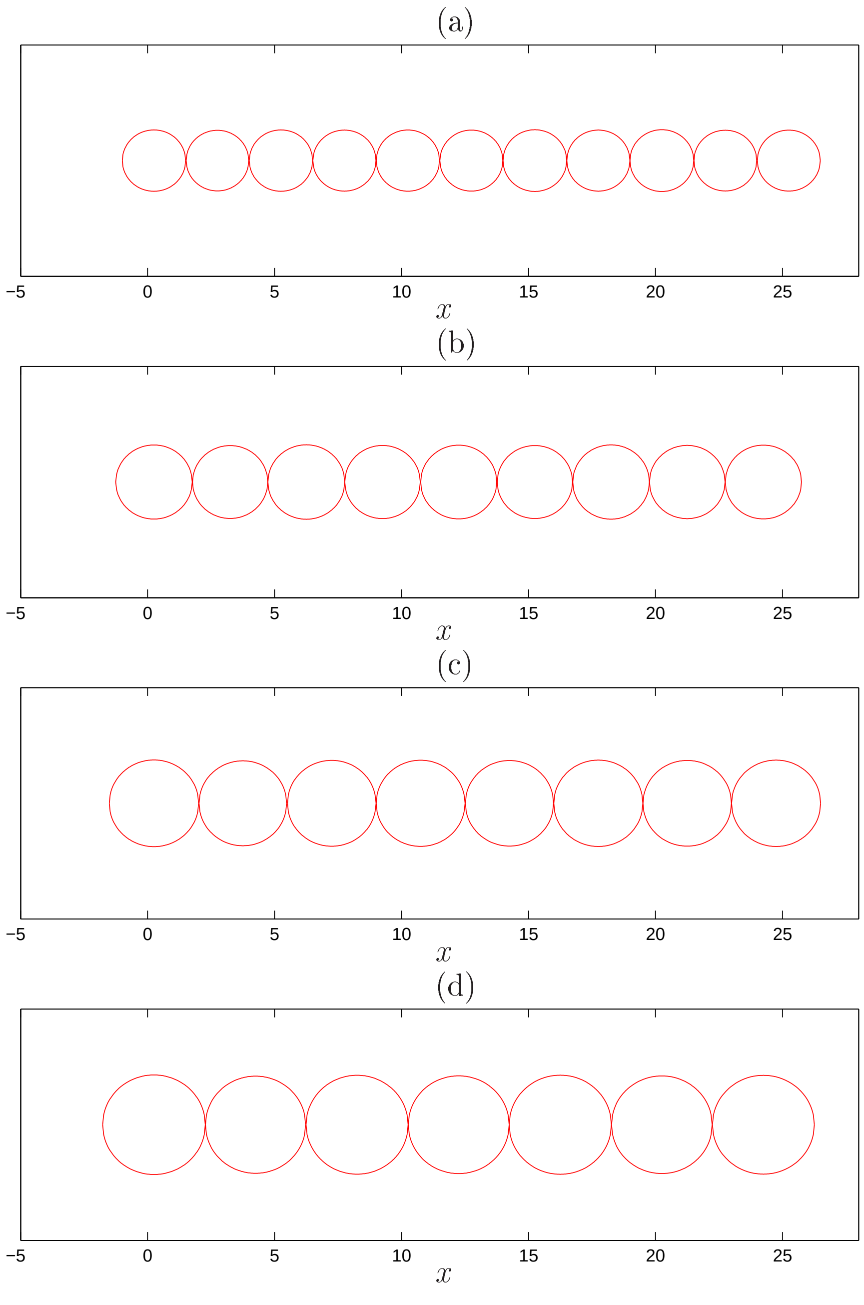

Figure 8.17: Illustrative plots showing the final bubble size distribution, across the half sample domain, given the local reaction rate constant profile prescribed in Figure 8.14, for (a) 11, (b) 9, (c) 8 and (d) 7 bubbles. The bubbles are positioned homogeneously across the domain at 2.5, 3.0, 3.5 and 4.0 mm intervals, respectively, and each bubble is allowed to evolve, given the local reaction rate constant value prescribed at its central position, until the reaction ceases or it touchs a neighbouring bubble. x is the horizontal co-ordinate, in the sample, in millimetres and the parameter values used are listed in Table 8.6.

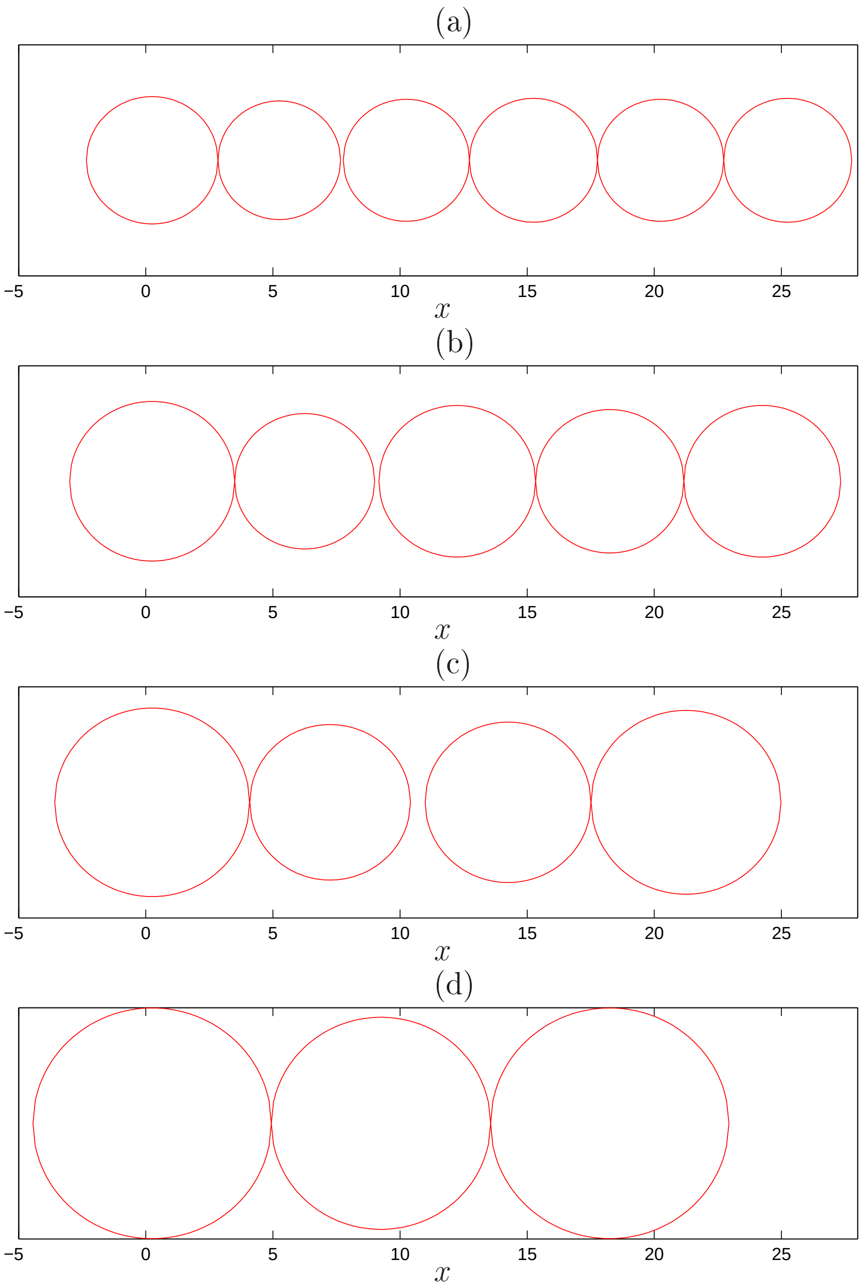

Figure 8.18: Illustrative plots showing the final bubble size distribution, across the half sample domain, given the local reaction rate constant profile prescribed in Figure 8.14, for (a) 6, (b) 5, (c) 4 and (d) 3 bubbles. The bubbles are positioned homogeneously across the domain at 5.0, 6.0, 7.0 and 9.0 mm intervals, respectively, and each bubble is allowed to evolve, given the local reaction rate constant value prescribed at its central position, until the reaction ceases or it touchs a neighbouring bubble. x is the horizontal co-ordinate, in the sample, in millimetres and the parameter values used are listed in Table 8.6.

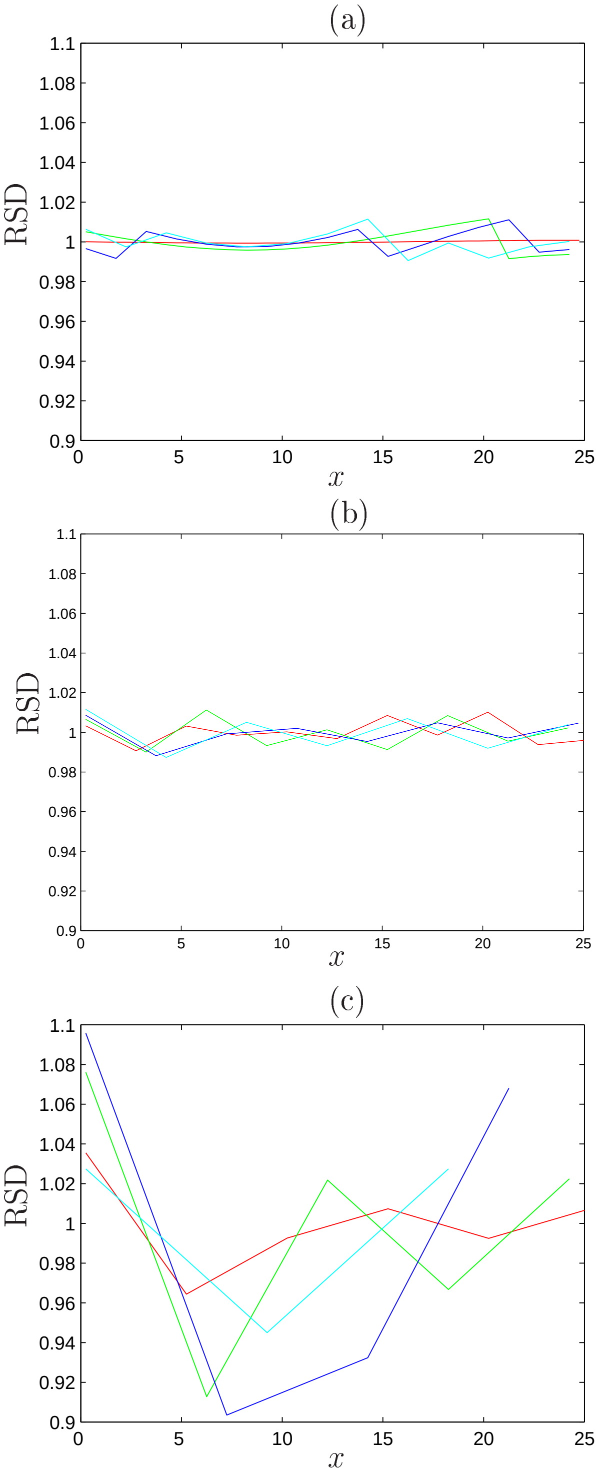

Figure 8.19: Plots illustrating the relative size distribution (RSD) calculated by dividing each bubble radius by the average bubble radius for a given bubble separation. (a), (b) and (c) relate to Figures 8.16, 8.17 and 8.18, respectively, with line colour order of red, green, blue and cyan ranging from the smallest δx value to the largest in each case. A quick visual inspection indicates that as we increase bubble separation the bubble size heterogeneity increases. We measure this heterogeneity in Figure 8.20 using two different metrics Θ_1 and Θ_2 given by (8.71) and (8.72), respectively.

δx, mm	N	min radius, mm	max radius, mm	% difference
0.5	50	0.2453	0.2456	0.12
1.0	25	0.4893	0.4992	2.02
1.5	17	0.7345	0.7489	1.96
2.0	13	0.9819	1.0026	2.11
2.5	11	1.2310	1.2552	1.97
3.0	9	1.4801	1.5119	2.15
3.5	8	1.7251	1.7608	2.07
4.0	7	1.9737	2.0222	2.46
5.0	6	2.4110	2.5887	7.37
6.0	5	2.7529	3.2455	17.89
7.0	4	3.1599	3.8321	21.27
9.0	3	4.3118	4.6881	8.73

Table 8.7: The final maximum and minimum bubble radii, in an N bubble distribution across a sample domain of length $L/2$ (where $L = 50$mm) with bubble spacing given by δx. The percentage difference is calculated with reference to the minimum bubble radius. The maximum percentage difference occurs with $N = 4$ bubbles and a bubble spacing of 7mm. Parameter values used to construct this table are detailed in Tables 8.2 and 8.6.

bubble radius for each ith bubble in the distribution and plotting a circle of the given radius centred on the bubble position x_i. These figures cover a range in δx of 0.5mm to 9.0mm. The larger the number of bubbles, the smaller the steady state bubble volume due to interaction with neighbouring bubbles before the natural steady state volume is achieved. In Figure 8.16 (a) and (b), in particular, it is hard to discern any heterogeneity in bubble size with the naked eye. As the number of bubbles decreases below 17 we can observe heterogeneity in the bubble size distributions due to the spatial reaction rate profile across the sample. This is easiest to observe in Figure 8.18 as the reduced number of bubbles means larger final volumes are achieved before bubble-bubble interaction halts further growth.

To aid the illustration of the heterogeneity through each of the distributions shown in Figures 8.16 - 8.18 we plot the relative size distribution (RSD) with respect to the average bubble radius in each case. The results are displayed in

Figure 8.19 (a) - (c) and appear to show that heterogeneity of bubble size distribution through the sample increases as δx increases. In the following section we derive two metrics to quantify this observed heterogeneity and look for a bubble spacing value, δx, to maximise it.

8.6.1 Definition and analysis of bubble size heterogeneity

We looked at two different metrics to capture the final bubble size heterogeneity across the sample domain. The first definition takes into consideration the difference in bubble size for adjacent bubbles through the sample and is defined thus

$$\Theta_1 = \left(\sum_{j=L}^{N} |r(T,j) - r(T,j-1)| \right) \Bigg/ \left(\sum_{j=1}^{N} r(T,j)/N \right). \tag{8.71}$$

The second definition considers only the difference between the largest and smallest bubbles in the sample so that,

$$\Theta_2 = \left(\max_{j\in(1,N)}\{r(T,j)\} - \min_{j\in(1,N)}\{r(T,j)\} \right) \Bigg/ \left(\sum_{j=1}^{N} r(T,j)/N \right). \tag{8.72}$$

These two values were calculated for each initial bubble spacing and the results are plotted in Figure 8.20. We can see that qualitatively both definitions show the same trends for heterogeneity versus bubble spacing. There appears to be an optimal bubble spacing that results in increased heterogeneity in final bubble radii through the sample and this occurs at a bubble spacing of approximately 6-7mm.

Figure 8.21 shows the results of the same analysis as described here and in Section 8.6 with the exception that the value of the fluid volume surrounding the bubble is $X = 150$ as opposed to $X = 500$. In this case the value for the bubble spacing interval, δx, decreases so that the maximum heterogeneity in bubble size distribution is achieved when $\delta x = 5$mm, as opposed to 7mm in the case when $X = 500$.

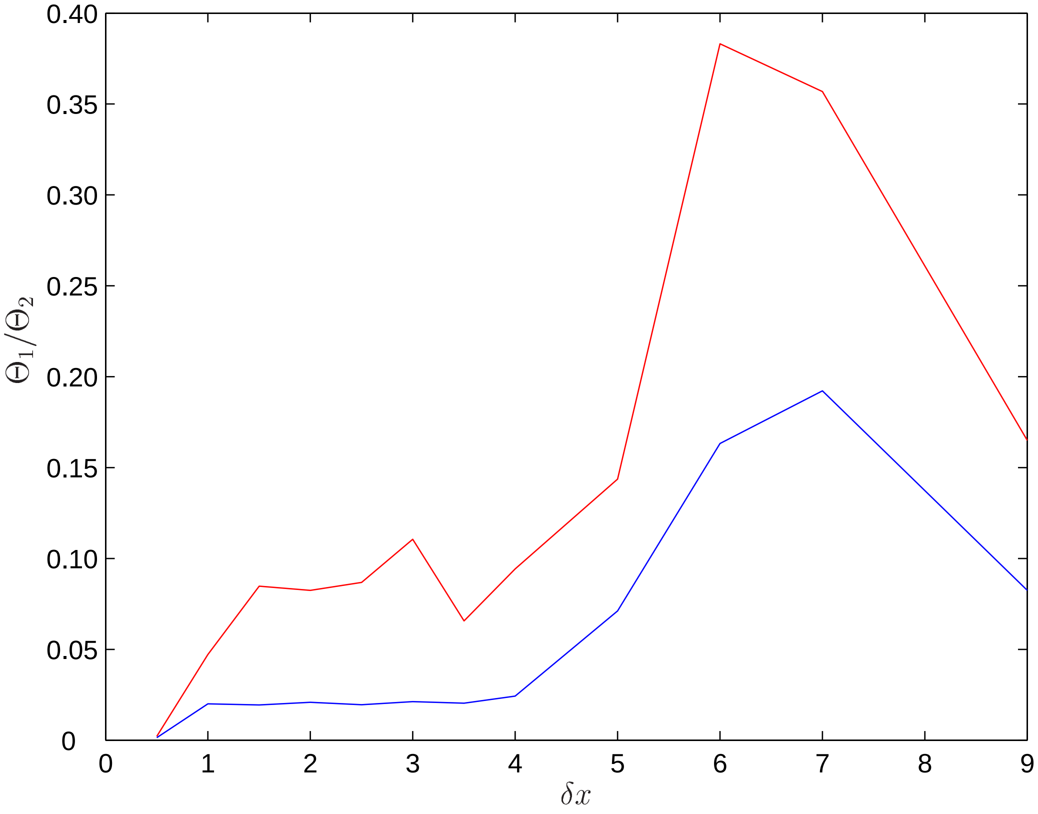

Figure 8.20: Plot illustrating the results for bubble size heterogeneity versus the bubble spacing, δx (mm), through the sample, given by the metrics Θ_1 (8.71) and Θ_2 (8.72). Curves for Θ_1 (red curve) and Θ_2 (blue curve) agree qualitatively if not quantitatively. They both suggest that the initial bubble spacing interval required to acheive the maximum bubble size heterogeneity across the sample is approximately $\delta x = 6$. The metric Θ_1 also suggests a local maxima at $\delta x = 2$ but this is not observed using Θ_2. The parameter values used to construct this figure are listed in Table 8.6 with $X = 500$.

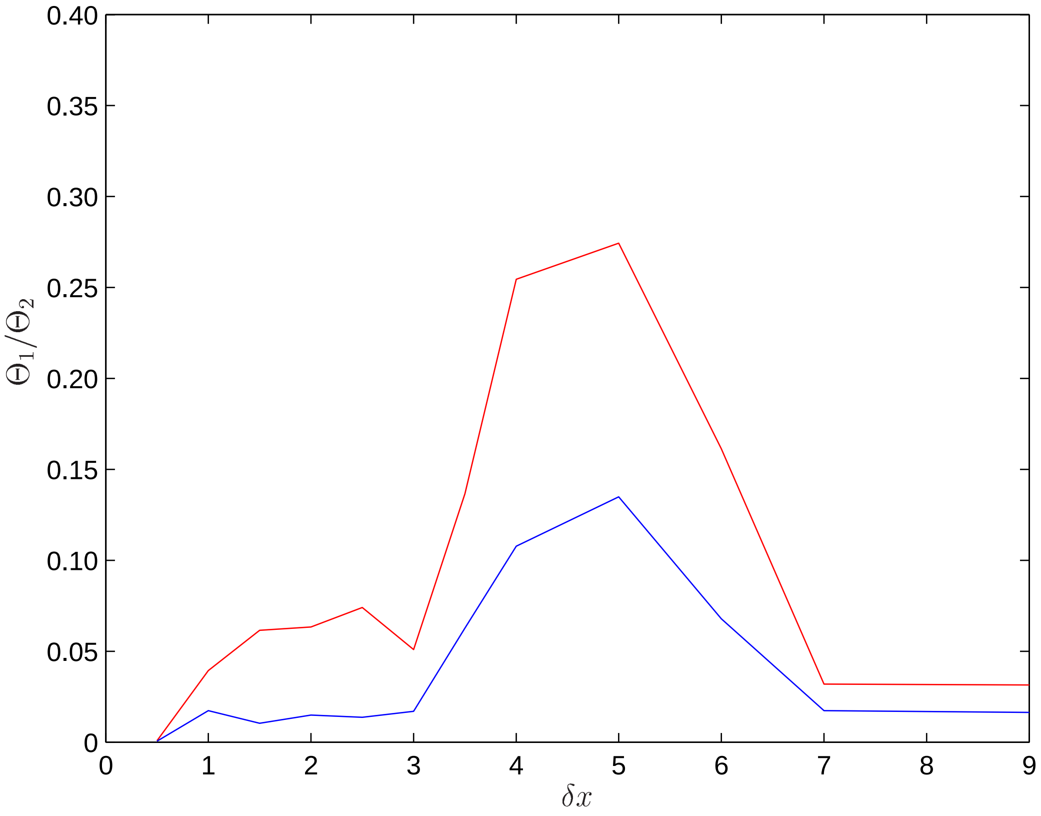

Figure 8.21: Plot illustrating the results for bubble size heterogeneity versus the bubble spacing, δx (mm), through the sample, given by the metrics Θ_1 (8.71) and Θ_2 (8.72). Curves for Θ_1 (red curve) and Θ_2 (blue curve) agree qualitatively if not quantitatively. They both suggest that the initial bubble spacing interval required to acheive the maximum bubble size heterogeneity across the sample is approximately $\delta x = 6$. The metric Θ_1 also suggests a local maxima at $\delta x = 2$ but this is not observed using Θ_2. The parameter values used to construct this figure are listed in Table 8.6 with the exception that $X = 150$.

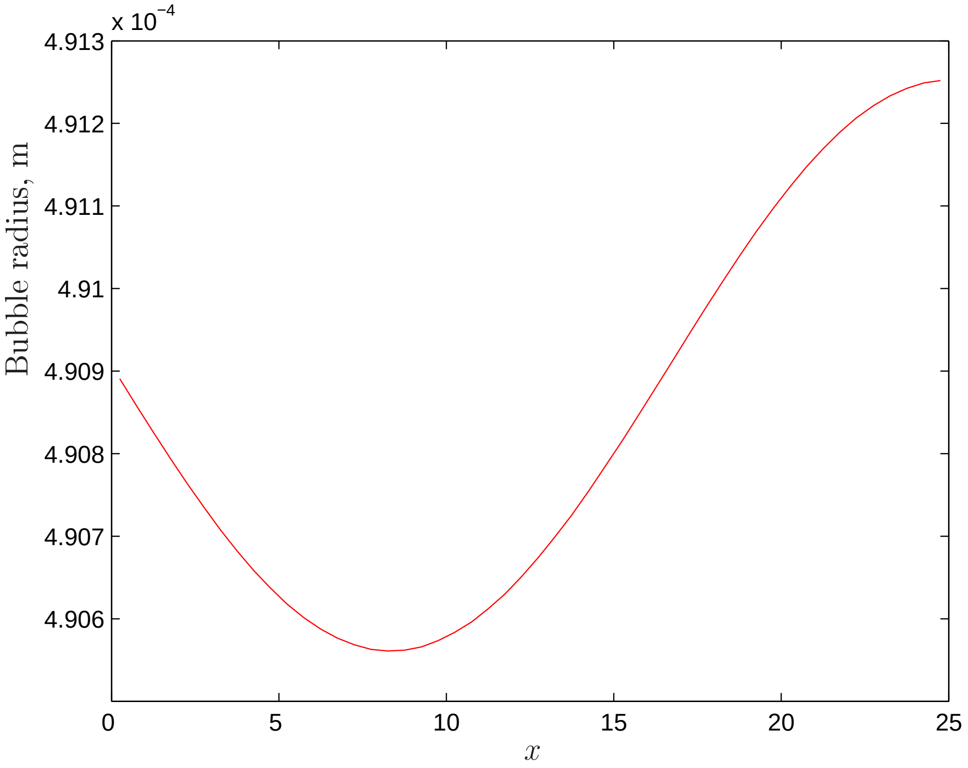

Figure 8.22: Plot illustrating the final bubble radius distribution for 50 bubbles in the sample domain. The profile of this size distribution is qualitatively similar to the reaction rate distribution profile in Figure 8.14, however, as demonstrated by the vertical axis, the magnitude of this effect is small.

Having isolated the effect of pressure amplitude on reaction rate and examined the resultant effects in the model, we have shown that the pressure amplitude of the irradiating acoustic standing wave, can effect bubble size distribution through its effects on reaction rate. The reaction rate distribution across the sample does lead to spatial heterogeneity in final bubble sizes. However, as Figure 8.19 demonstrates, the bubble size does not necessarily correlate with the local pressure amplitude profile as illustrated in Figure 8.14. An exception to this is the case for $\delta x = 0.5$mm and we can observe by comparing Figure 8.14 to 8.22 that bubble volume is indeed proportional to the pressure amplitude although the magnitude of this effect is small. This is the same qualitative effect reported by Torres-Sanchez *et al.* in [93]. The magnitude of the experimentally observed effect of acoustic pressure amplitude on bubble size reported in their paper is more significant than that produced by our model and therefore another mechanism, or perhaps several mechanisms, may be responsible and these will be discussed in the next section.

For a given steady state bubble volume, our model can predict a homogeneous bubble spacing value, δx, that produces maximum heterogeneity through the sample. Figure 8.21 demonstrates analysis of heterogeneity under the same conditions as in Figure 8.20 with the exception of a lower dimensionless fluid volume, $X = 150$. This results in a reduced steady state volume for each bubble in the scheme and, as Figure 8.21 illustrates, the spacing interval required to optimise heterogeneity in bubble size distribution is reduced.

Mathematically we can choose any bubble spacing we like but experimentally this is not possible and initial bubble spacing will depend on many factors governing nucleation. Furthermore, bubble spacing will also change as new bubbles nucleate at subsequent timepoints.

8.7 Discussion

In this chapter we extended a model, introduced by Everitt *et al.* [26], for the growth of a single bubble within a reacting polymer foam, to include the effects of an irradiating acoustic standing wave. First we developed a numerical code to solve the coupled system of five PDEs, and validated our results by comparing with those of Everitt *et al.* in the case of no insonifying acoustic signal. Satisfied that the numerical code was producing the right results we then looked to apply this model to the experiment described by Torres-Sanchez *et al.* [93]. Before considering a multibubble distribution we first examined the effect of this new parameterisation, and in particular, the role played by the pressure amplitude of the acoustic standing wave. Due to the attenuating effect of the sample, on the acoustic standing wave, this pressure amplitude was shown to have no direct effect on the bubble volume (see Figure 8.10). However, the value of the reaction rate constant, c_α was demonstrated to have a much more significant effect as illustrated in Figure 8.1. In another related paper by Torres-Sanchez *et al.* [92] the authors point to a relationship between the reaction rate of the polymerisation and the pressure amplitude of the acoustic standing wave. We extracted, from their data, a relationship between the local acoustic pressure amplitude and the localised reaction rate constant c_α, and used this to propose a spatial reaction rate profile across the sample, that correlates with the pressure amplitude profile.

Having developed a numerical code to track the evolution of an individual bubble insonified at a given acoustic pressure amplitude we then considered a one-dimensional distribution of nucleated bubbles 'seeded' homogeneously across the sample. An empirical set of rules was defined in order to describe bubble-bubble interaction and, for a given steady state bubble volume, the effect of different bubble spacings across the sample was examined. Two heterogeneity metrics were defined and both agreed qualitatively, predicting an optimum bubble spacing interval to acheive maximum bubble heterogeneity.

Although the reaction rate distribution did increase the heterogeneity of the final bubble size distribution, it did not consistently predict the correlation between bubble size and pressure amplitude value measured across the sample as was so clearly illustrated in the experimental work carried out by Torres-Sanchez *et al.* [93]. They demonstrate, experimentally, that for realistic in situ acoustic pressure amplitudes across the sample domain the porosity value correlates with the pressure amplitude. RMS pressure amplitudes ranged from 0 to 600 Pa and the dimensionless porosity values (as defined in [94]) were in the range 0 to 160 where porosity increases with porosity value. We have shown, theoretically, that in cases of high bubble number density it is possible to illustrate a bubble size distribution profile that correlates with the acoustic pressure amplitude distribution across the sample (compare Figures 8.9 and 8.22), as demonstrated by [93], although the magnitude of this correlation is smaller. We have further demonstrated that the initial bubble spacing can affect the final bubble size distribution and heterogeneity of the sample. Optimum initial bubble spacing values can be determined, for a given parameter set, that will result in the maximum heterogeneity for the final bubble size distribution. This effect of initial bubble spacing could be considered in the future modelling of nucleation effects on the final bubble size distribution through the sample.

Chapter 9

Conclusions and Further Work

9.1 Conclusions

The main motivation for this section of the thesis was a problem proposed, at the MMSG 2010 [1], by Dr Carmen Torres-Sanchez [93] regarding the tailoring of the porosity gradients within a cured sample of a polymerising foam under the influence of an acoustic standing wave. This is a very complex process involving many interacting factors and effects, for example, rectified diffusion, Ostwald ripening and nucleation, all of which are affected by the variations in pressure amplitude that comes with an acoustic standing wave. Due to the complexity of the problem we decided to investigate the direct effect of the applied acoustic pressure amplitude on the system, in the first instance, and then latterly its effect on the bubble size distribution via the reaction rate constant, c_α. We added an acoustic amplitude to the right hand side of the momentum equation published in [26] to examine the direct effect of the standing wave. However, although the insonifying acoustic signal has amplitude of order 10^4Pa, the attenuating nature of the water bath surrounding the sample and the sample medium itself, mean that the actual amplitude in situ is only of order 10^2Pa and has no observable effect on the bubble size. We can therefore conclude that this is not a mechanism responsible for the bubble size heterogeneity observed in [93].

An indirect effect of the acoustic pressure amplitude is demonstrated through the reaction rate constant, c_α. This link has been proposed in previous publications [69, 92] and we decided to examine whether or not it could be responsible for the porosity profiles reported by [93]. We parameterised the system for the conditions reported in [92, 93] and defined a spatial reaction rate profile due to the acoustic standing wave. Individual bubbles were allowed to grow under the influence of their local reaction rate constant and a simple scheme for bubble-bubble interaction was proposed so that final bubble distributions could be obtained. We were thus able to demonstrate that the acoustic pressure amplitude effect on reaction rate was responsible for introducing heterogeneity in the bubble size distribution across the sample domain. In certain cases this bubble size distribution correlated with the pressure amplitude profile across the sample, that is, larger bubble sizes occurred at spatial points with a larger local pressure amplitude.

The bubble spacing required to acheive the maximum heterogeneity in the bubble size distribution was shown to depend, through the non-dimensional fluid volume, X, on the steady state volume of the individual bubbles. That is, the smaller the unimpeded steady state volume of individual bubbles, the smaller the spacing interval required to acheive the maximum heterogeneity.

Although we have demonstrated that the acoustic standing wave used to irradiate the polymerising sample in [93] is indeed responsible for a certain degree of bubble size heterogeneity across the domain, the bubble size distribution does not always correlate with the applied pressure amplitude profile as reported in [93]. Furthermore, the magnitude of the heterogeneity observed in [93] was much more significant than that demonstrated here. This is not unexpected when we consider the number of interacting effects involved in this process and the fact that we have examined, in isolation, only one such mechanism. Avenues of further investigation are suggested in the next section.

In Chapter 7 we produced a model to track the growth of a bubble in a free rising, non-reacting polymer foam incorporating the effects of inertia. We partially decoupled the system by assuming instantaneous diffusion and were able to derive, first and leading order, inner and outer asymptotic solutions, respectively. The dimensionless fluid volume, X, played an important role in the form and derivation of the leading and first order inner solutions, with improved solution accuracy for large X. The leading order bubble volume was exponential with respect to the inner temporal variable. By a variable transformation, we were able to reduce the first order system to the Euler differential equation and solve for the particular branch defined by our parameterisation. Two separate regimes were considered; the first described the case when the fluid volume was much larger than the bubble volume and the second pertained to volumes of the same order.

The outer asymptotic solution essentially relates to the scheme with zero inertia. We were able to reduce the coupled five equation PDE system to a single integro-differential equation to describe bubble volume evolution for the outer asymptotic problem. This essentially describes the case of negligible inertia which we investigated further in Chapter 8. This was achieved by assuming instantaneous diffusion to decouple the gas concentration potential, as well as deriving an explicit form for the integrand, $(A_{rr}-A_{\theta\theta})_0/(x+u_0)$. We attempted to derive an analytic approximation using the Picard iterative scheme but because of the complexity of the equation, only the first iterate was derived. A numerical code was developed instead and this provided a must faster tool for analysing the bubble evolution than the full numerical analysis performed as in [26]. However, it must be remembered that many assumptions and approximations have been made along the way so that fewer mechanisms and parameters are considered.

Given the parameterisation of the system, in the absence of an insonifying acoustic standing wave, inertia would in fact be negligible. However, if we were to add an acoustic forcing term to the right hand side of the momentum equation to model the effects of the irradiating standing wave, then in a scaled temporal variable, the effects of inertia would be significant due to the phenomenon of rectified diffusion caused by the oscillatory motion of the bubble. Although, in this instance, we only look at the time averaged RMS signal for the acoustic wave and derive inner asymptotic solutions to leading and first order, we have produced a scheme that can be employed in the future to examine the effects of the acoustic pressure amplitude on rectified diffusion.

9.2 Further Work

Suggestions for further work include, but are not limited to, the following areas. The basic rules for bubble-bubble interaction described in Chapter 8 could be improved in various ways, possibly coupling bubbles through the stress evolution in the surrounding fluid. In our basic scheme the bubbles interact as if no fluid was present and the only variable considered is the bubble radius.

The nucleation process, which continues for some time after the polymerisation reaction has commenced, has not been considered here. It would be possible to model the effect of this aspect of nucleation using our scheme, by assuming a function to describe nucleation so that different bubbles nucleate at different times during the reaction. These results could be compared with the same nucleation function in the absence of an acoustic pressure amplitude. This additional mechanism would be likely to introduce further heterogeneity through the sample. It is important to note that this version of the nucleation effect does not consider the direct effect of the acoustic pressure amplitude on the actual nucleation rate of bubbles.

The phenomenon of Bjerknes forces is another pressure sensitive mechanism that organises bubbles according to size; bubbles less than the resonance size migrate to pressure antinodes and bubbles larger than the resonance size to pressure nodes. The Bjerknes force is directly proportional to the applied acoustic pressure amplitude as well as depending on bubble size. Rather than governing bubble growth it acts to translate bubbles and as such may be partially responsible for the heterogeneity in bubble size distributions observed experimentally.

The work done in Chapter 7, to include the inertia term could be extended to include an investigation into the effect of the acoustic standing wave on the pumping effects of the acoustic signal on mass transfer into the bubble by rectified diffusion.

The inner asymptotic solutions, in Chapter 7, were derived to leading and first order. The construction of higher order asymptotic solutions would enable the effects of a greater number of parameters to be investigated. Due to the large number of parameters involved in the reacting scheme, a sensitivity analysis would prove useful in identifying which key factors are driving the process, and thus help to inform the direction of any future analysis.

The ability to tailor the porosity profiles within polymerising materials will lead to significant improvements in a range of manufactured products such as artificial bone. Given the complexity of the physics involved it is essential that mathematical modelling is used to design the manufacturing process. This thesis is the first step in this direction and it is hoped that it will inspire other researchers to take up the baton and develop the model to fully explain this fascinating problem.

Appendix A

Numerical scheme for the spatially heterogeneous host-parasite model

Spatial discretisation

The spatial domain $[0, L]$ is divided into N intervals of length dx and we use the standard notation $P_j(t)$ as an approximation of $P(j\,dx, t)$ for $j = 0, 1, \cdots, N$. $H_j(t)$ is defined in a similar manner.

Treatment of the hare equation

The PDE is a standard reaction-diffusion equation and is discretised using a second order accurate central difference scheme,

$$\frac{\partial H}{\partial t} = D_H \frac{H_{j+1} - 2H_j + H_{j-1}}{dx^2} - b(H + P) + \frac{aH^2}{c_1 P + H}, \qquad j = 0, 1, \cdots, N.$$

In order to satisfy the prescribed no flux boundary conditions and to maintain second order accuracy, we set the following values $H_{-1} = H_1$ and $H_{N+1} = H_{N-1}$.

Treatment of the parasite equation

The parasite equation has a reaction term and an advection term since the parasite lives in the host and travels with the host velocity. A first order upwind semidiscretisation could be used that would maintain positivity but could introduce a large amount of numerical diffusion, unless the spatial discretisation is sufficiently fine. On the other hand, high order spatial discretisations often lead to oscillations in solutions which may break the positivity requirement when the solution values are small. Instead we use *flux limiters* which are designed to limit the spatial derivatives to realistic, or physically realisable values. They tend to be favoured when sharp wave fronts are present. The flux limiter scheme for our problem is constructed as follows. We denote the velocity of the advective flux at grid point j by

$$w_j = \frac{D_H}{H}\frac{\partial H_j}{\partial x}, \qquad j = 0, 1, \cdots, N.$$

We define the derivative of H at grid point j using central differences as standard and let f_j denote the semidiscretised advective flux at grid point j, i.e.

$$f_j = w_j P_j, \qquad j = 0, 1, \cdots, N.$$

We then introduce the semidiscretised general flux function $F_{j+1/2}$ which is a function of the fluxes f surrounding the grid point j. Using a central difference approximation for the spatial derivative, the advection term can be approximated by the expression

$$\frac{1}{dx}\left(F_{j+1/2} - F_{j-1/2}\right), \qquad j = 0, 1, \cdots, N.$$

The semidiscretisation of the parasite equation then yields

$$\frac{\partial P}{\partial t} = \frac{1}{dx}\left(F_{j+1/2} - F_{j-1/2}\right) + P\left[\frac{\lambda H}{1+H} - (\mu + b + \alpha) - \frac{2bP}{H}\right]$$

We set $F_{-1/2} = F_{N+1/2} = 0$ to ensure that the no-flux boundary conditions are satisfied. It only remains to choose the flux functions $F_{j+1/2}$. To this end, we define the function

$$r_j = \frac{f_{j+1} - f_j + \epsilon}{f_j - f_{j-1} + \epsilon}, \qquad j = 0, 1, \cdots, N,$$

which encapsulates the ratio of the gradients of fluxes about grid point j. Note that the quantity ϵ is a small number that ensures that r_j is well defined even when the fluxes surrounding grid point j are identical. We set $\epsilon = 10^{-30}$. Consistent with the boundary conditions, we set $f_{-1} = f_{N+1} = 0$. Finally we introduce a *limiter function* $\phi(r)$ and define the general flux function for a non-negative velocity as

$$F_{j+1/2} = f_j + \frac{1}{2}\phi(r_j)(f_j - f_{j-1}), \qquad j = 0, 1, \cdots, N-1.$$

However, for a negative velocity $w_j < 0$ we reflect all the indices about $j + 1/2$ to obtain

$$F_{j+1/2} = f_{j+1} + \frac{1}{2}\phi\left(\frac{1}{r_{j+1}}\right)(f_{j+1} - f_{j+2}), \qquad j = 0, 1, \cdots, N-1.$$

We choose a symmetric, van Leer flux limiter function, namely

$$\phi(r) = \frac{r + |r|}{1 + |r|},$$

which tends to 2 as $r \to \infty$ and has the following symmetry property

$$\frac{\phi(r)}{r} = \phi\left(\frac{1}{r}\right),$$

which ensures that the limiting action operates in the same way for forward and backward gradients. Note that $\phi(r) = 0$ would be equivalent to a first-order upwind discretisation.

Numerical integration of the ODE system

The spatial discretisation described above reduces the PDE system to a system of ODEs which we solve using a fourth order Runge-Kutta method.

Appendix B

Rescaling of Mountain hare, *Trichostrongylus-retortaeformis* system

The continuous growth equations for a host population of density, H interacting with a parasite population, P in a spatially heterogeneous system are stated below. The original reaction-kinetic system is augmented by a spatial term related to the rate of hare flux J_H. The population densities are therefore dependent on a one-dimensional spatial component, x as well as time, t and evolve according to

$$\frac{\partial H}{\partial t} = -\alpha P - bH + \frac{aH^2}{(\delta P + H)} - \frac{\partial J_H}{\partial x}, \tag{B.1}$$

$$\frac{\partial P}{\partial t} = P\left[\frac{\lambda H}{H_0 + H} - (\mu + \alpha + b) - \frac{2\alpha P}{H}\right] - \frac{\partial}{\partial x}\left(\frac{P J_H}{H}\right), \tag{B.2}$$

where x,$t \in \mathbb{R}$, $H = H(x,t)$, $P = P(x,t)$, $J_H = -D_H \partial H/\partial x$ and D_H is the diffusion coefficient for the hare population.

We introduce the dimensionless constants h and p and substituting into (B.1) for $H = h\bar{H}$ and $P = p\bar{P}$ gives

$$\frac{\partial}{\partial t}(h\bar{H}) = -\alpha p\bar{P} - bh\bar{H} + \frac{a(h\bar{H})^2}{\delta p\bar{P} + h\bar{H}} - h\frac{\partial \bar{J}_H}{\partial x}, \tag{B.3}$$

$$\rightarrow h\frac{\partial \bar{H}}{\partial t} = -\alpha p\bar{P} - bh\bar{H} + \frac{h^2 a\bar{H}^2}{\delta p\bar{P} + h\bar{H}} - h\frac{\partial \bar{J}_H}{\partial x}. \tag{B.4}$$

Dividing through by h and rearranging we have

$$\frac{\partial \bar{H}}{\partial t} = -\frac{p}{h}\alpha \bar{P} - b\bar{H} + \frac{a\bar{H}^2}{\frac{p}{h}\delta \bar{P} + \bar{H}} - \frac{\partial \bar{J}_H}{\partial x}. \tag{B.5}$$

Assigning $\bar{\alpha} = \frac{p}{h}\alpha$ and $\bar{\delta} = \frac{p}{h}\delta$ we can rewrite (B.5) as

$$\frac{\partial \bar{H}}{\partial t} = -\bar{\alpha}\bar{P} - b\bar{H} + \frac{a\bar{H}^2}{\bar{\delta}\bar{P} + \bar{H}} - \frac{\partial \bar{J}_H}{\partial x}. \tag{B.6}$$

We non-dimensionalise (B.2) in the same way,

$$\frac{\partial}{\partial t}(p\bar{P}) = p\bar{P}\left[\frac{\lambda h\bar{H}}{H_0 + h\bar{H}} - \mu - \alpha - b - \frac{2\alpha p\bar{P}}{h\bar{H}}\right] - \frac{\partial}{\partial x}\left(\frac{ph\bar{P}\bar{J}_H}{h\bar{H}}\right). \tag{B.7}$$

Dividing through by p and setting $h = H_0$ and $p = P_0$ we obtain

$$\frac{\partial \bar{P}}{\partial t} = \bar{P}\left[\frac{\lambda \bar{H}}{1 + \bar{H}} - \mu - \alpha - b - \frac{P_0}{H_0}2\alpha\frac{\bar{P}}{\bar{H}}\right] - \frac{\partial}{\partial x}\left(\frac{\bar{P}\bar{J}_H}{\bar{H}}\right). \tag{B.8}$$

Defining the parameter $\epsilon = \frac{H_0}{P_0}$ the above equation can be rewritten as

$$\frac{\partial \bar{P}}{\partial t} = \bar{P}\left[\frac{\lambda \bar{H}}{1 + \bar{H}} - \mu - \bar{\alpha}\epsilon - b - 2\bar{\alpha}\frac{\bar{P}}{\bar{H}}\right] - \frac{\partial}{\partial x}\left(\frac{\bar{P}\bar{J}_H}{\bar{H}}\right), \tag{B.9}$$

and our rescaled system can now be presented

$$\begin{aligned} \frac{\partial \bar{H}}{\partial t} &= -\bar{\alpha}\bar{P} - b\bar{H} + \frac{a\bar{H}^2}{\bar{\delta}\bar{P} + \bar{H}} - \frac{\partial \bar{J}_H}{\partial x}, && \text{(B.10)} \\ \frac{\partial \bar{P}}{\partial t} &= \bar{P}\left[\frac{\lambda \bar{H}}{1 + \bar{H}} - \mu - \bar{\alpha}\epsilon - b - 2\bar{\alpha}\frac{\bar{P}}{\bar{H}}\right] - \frac{\partial}{\partial x}\left(\frac{\bar{P}\bar{J}_H}{\bar{H}}\right), && \text{(B.11)} \end{aligned}$$

where the non-dimensional parameters are given by

$\bar{\alpha} = \frac{\alpha P_0}{H_0} = 0.0209$, $\bar{\delta} = \frac{\delta P_0}{H_0} = 0.2618$, $\epsilon = \frac{H_0}{P_0} = 3.82 \times 10^{-4}$,

and $P_0 = 1 \times 10^8$.

Appendix C

Non dimensionalisation of non-reacting system of equations

All lengths are scaled with $u_0^{\frac{1}{3}}$ and volumes with u_0, we scale time with the relaxation time of the polymer τ, p_g according to

$$P_g = \frac{p_g - p_a}{p_{g0} - p_a}, \tag{C.1}$$

and ϕ with $p_{g0}u_0/R_gT$, that is, the initial number of moles of gas. The following substitutions are made in the governing equations, boundary and initial conditions:

$$\begin{aligned} t &= \tau\hat{t}, & u &= u_0\hat{u}, & p_g &= (p_{g0} - p_a)P_g + p_a, \\ x &= u_0\hat{x}, & \dot{u} &= \tfrac{u_0}{\tau}\hat{\dot{u}}, & p_u &= (p_{g0} - p_a)P_u, \\ X &= u_0\hat{X}, & \ddot{u} &= \tfrac{u_0}{\tau^2}\hat{\ddot{u}}, \text{ and} & \phi &= \tfrac{p_{g0}u_0}{R_gT}\hat{\phi}. \end{aligned}$$

Starting with the momentum equation (7.32)

$$\begin{aligned} \frac{4}{3}\mu\dot{u}\left(\frac{1}{u} - \frac{1}{X+u}\right) + \rho\left[\frac{\ddot{u}}{3}\left(\frac{1}{u^{\frac{1}{3}}} - \frac{1}{(X+u)^{\frac{1}{3}}}\right) - \frac{\dot{u}^2}{18}\left(\frac{1}{u^{\frac{4}{3}}} - \frac{1}{(X+u)^{\frac{4}{3}}}\right)\right] \\ = p_g - p_a - p_u + \frac{2}{3}G\int_0^X \frac{(A_{rr} - A_{\theta\theta})}{(x'+u)}dx' - \frac{2S}{u^{\frac{1}{3}}}, \end{aligned} \tag{C.2}$$

$$\frac{4}{3}\frac{\mu}{\tau}u_0\hat{u}\left(\frac{1}{u_0\hat{u}}-\frac{1}{u_0(\hat{X}+\hat{u})}\right)$$
$$+\rho\left[\frac{u_0}{\tau^2}\frac{\hat{\ddot{u}}}{3}\left(\frac{1}{u_0^{\frac{1}{3}}\hat{u}^{\frac{1}{3}}}-\frac{1}{u_0^{\frac{1}{3}}(\hat{X}+\hat{u})^{\frac{1}{3}}}\right)-\frac{u_0^2}{\tau^2}\frac{\hat{\dot{u}}^2}{18}\left(\frac{1}{u_0^{\frac{4}{3}}\hat{u}^{\frac{4}{3}}}-\frac{1}{u_0^{\frac{4}{3}}(\hat{X}+\hat{u})^{\frac{4}{3}}}\right)\right]$$
$$=(p_{g0}-p_a)P_g-(p_{g0}-p_a)P_u+\frac{2}{3}G\int_0^{u_0\hat{X}}\frac{(A_{rr}-A_{\theta\theta})}{u_0(\hat{x}+\hat{u})}d(u_0\hat{x})-\frac{2S}{u_0^{\frac{1}{3}}\hat{u}^{\frac{1}{3}}}.$$

Dividing by μ/τ and collecting powers of u_0 together gives

$$\frac{4}{3}\hat{\dot{u}}\left(\frac{1}{\hat{u}}-\frac{1}{(\hat{X}+\hat{u})}\right)+\mathcal{R}\left[\hat{\ddot{u}}\left(\frac{1}{\hat{u}^{\frac{1}{3}}}-\frac{1}{(\hat{X}+\hat{u})^{\frac{1}{3}}}\right)-\frac{\hat{\dot{u}}^2}{6}\left(\frac{1}{\hat{u}^{\frac{4}{3}}}-\frac{1}{(\hat{X}+\hat{u})^{\frac{4}{3}}}\right)\right]$$
$$= De(P_g-P_u)+\frac{2}{3}\gamma\int_0^{\hat{X}}\frac{(\hat{A}_{rr}-\hat{A}_{\theta\theta})}{(\hat{x}+\hat{u})}d\hat{x}-\frac{1}{\Gamma\hat{u}^{\frac{1}{3}}}, \quad \text{(C.3)}$$

where the following non dimensional grouped parameters are defined by,

$$\mathcal{R}=\frac{\rho u_0^{\frac{2}{3}}}{3\mu\tau}, \qquad De=\frac{(p_{g0}-p_a)\tau}{\mu}, \qquad \gamma=\frac{G\tau}{\mu}, \qquad \Gamma=\frac{\mu u_0^{\frac{1}{3}}}{2S\tau}.$$

Substitution for the non-dimensional variables into (7.37) and (7.39) gives,

$$\frac{\partial A_{rr}}{\tau\partial\hat{t}} = -\frac{4u_0\hat{\dot{u}}}{3\tau u_0(\hat{x}+\hat{u})}A_{rr}-\frac{1}{\tau}(A_{rr}-1),$$
$$\frac{\partial A_{rr}}{\partial\hat{t}} = -\frac{4\hat{\dot{u}}}{3(\hat{x}+\hat{u})}A_{rr}-(A_{rr}-1), \quad \text{(C.4)}$$

and,

$$\frac{\partial(A_{rr}-A_{\theta\theta})}{\tau\partial\hat{t}} = \frac{2u_0\hat{\dot{u}}}{3\tau u_0(\hat{x}+\hat{u})}\left[(A_{rr}-A_{\theta\theta})-3A_{rr}\right]-\frac{1}{\tau}(A_{rr}-A_{\theta\theta}),$$
$$\frac{\partial(A_{rr}-A_{\theta\theta})}{\partial\hat{t}} = \frac{2\hat{\dot{u}}}{3(\hat{x}+\hat{u})}\left[(A_{rr}-A_{\theta\theta})-3A_{rr}\right]-(A_{rr}-A_{\theta\theta}), \quad \text{(C.5)}$$

respectively. We can re-write (7.47) as

$$p_g u_0\hat{u}=p_{g0}u_0+R_gT\hat{\phi}(0,t)\frac{p_{g0}u_0}{R_gT}.$$

Dividing through by u_0 and rearranging gives,

$$(p_a+(p_{g0}-p_a)P_g)p_{g0}\hat{u}=(1+\hat{\phi}(0,t)). \quad \text{(C.6)}$$

For the diffusion equation (7.45) we have

$$\begin{aligned} \frac{p_{g0}u_0}{R_gT\tau}\frac{\partial\hat{\phi}}{\partial\hat{t}} &= 9D(u_0(\hat{x}+\hat{u}))^{\frac{4}{3}}\frac{p_{g0}u_0}{R_gT}\frac{\partial^2\hat{\phi}}{u_0^2\partial\hat{x}^2}, \\ \frac{\partial\hat{\phi}}{\partial\hat{t}} &= N(\hat{x}+\hat{u})^{\frac{4}{3}}\frac{\partial^2\hat{\phi}}{\partial\hat{x}^2}, \qquad \text{where } N = \frac{9D\tau}{u_0^{\frac{2}{3}}}. \end{aligned} \tag{C.7}$$

Finally we need to non-dimensionalise the boundary condition on ϕ at the bubble surface, that is,

$$\left.\frac{\partial\phi}{\partial x}\right|_{x=0} = (p_g - p_{g0})H,$$

so that,

$$\begin{aligned} \frac{\partial}{\partial(u_0\hat{x})}\left(\frac{p_{g0}u_0}{R_gT}\hat{\phi}\right)\Bigg|_{(u_0\hat{x})=0} &= [(p_a + (p_{g0}-p_a)P_g) - p_{g0}]H, \\ \left.\frac{\partial\hat{\phi}}{\partial\hat{x}}\right|_{\hat{x}=0} &= \Phi\frac{(p_{g0}-p_a)}{p_{g0}}(P_g - 1), \end{aligned} \tag{C.8}$$

where $\Phi = R_gTH$.

Parameter	Value	Units
Pressure outside the fluid layer, p_a	1	10^5Nm^{-2}
Initial bubble gas pressure, p_{g0}	10	10^5Nm^{-2}
Elastic modulus, G	$1-10$	10^5Nm^{-2}
Solvent viscosity, μ	$1,6$	10^5Nsm^{-2}
Polymer relaxation time, τ	1	s
Initial bubble volume, u_0	1	10^{-18}m^3
Surface tension, S	$0-5$	10^{-1}Nm^{-1}
Gas constant, R_g	8.31	$\text{Jmol}^{-1}\text{K}^{-1}$
Temperature, T	370	K
Henry's law constant, H	10.5	$10^{-5}\text{molN}^{-1}\text{m}^{-1}$
Diffusivity, D	$0.1-100$	$10^{-12}\text{m}^2\text{s}^{-1}$
Fluid density, ρ	1200	kgm^{-3}

Table C.1: Parameters required for bubble expansion in the non-reacting system (7.48) - (7.52).

Bibliography

[1] *Uk mathematics-in-medicine study groups.* http://www.maths-in-medicine.org/uk/. Accessed October 2010.

[2] A. Adamson, *A Textbook of Physical Chemistry*, 2nd Ed. Elsevier, 2012.

[3] I. Akhatov, R. Mettin, C. Ohl, U. Parlitz, and W. Lauterborn, *Bjerknes force threshold for stable single bubble sonoluminescence*, Physical Review E, 55 (1997), pp. 3747–3750.

[4] M. Amon and C. Denson, *A study of the dynamics of foam growth: Analysis of the growth of closely spaced spherical bubbles*, Polymer Engineering Science, 24 (1984), pp. 1026–1034.

[5] R. Anderson, *The regulation of host population growth by parasitic species*, Parasitology, 76 (1978), pp. 119–157.

[6] R. Anderson and R. May, *Regulation and stability of host-parasite interactions: I. Regulatory processes*, Journal of Animal Ecology, 47 (1978), pp. 219–247.

[7] A. Arefmanesh and S. Advani, *Diffusion-induced growth of a gas bubble in a viscoelastic fluid*, Rheologica Acta, 30 (1991), pp. 274–283.

[8] N. Aziz, *Bone grafts and bone substitutes: Basic science and clinical applications*, World Scientific Publishing Company, 2005.

[9] N. Bacaer, *A short history of mathematical population dynamics*, Springer London, 2011, ch. Lotka, Volterra and the predator-prey system (1920-1926), pp. 71–76.

[10] N. Bali and N. Narayana Iyengar, *A Textbook of Engineering Mathematics*, Laxmi Publications, 2004.

[11] J. Bruchon and T. Coupez, *A numerical strategy for the direct 3d simulation of the expansion of bubbles into a molten polymer during a foaming process*, International Journal for Numerical Methods in Fluids, 57 (2008), pp. 977–1003.

[12] S. Cai and J. Xi, *A control approach for pore size distribution in the bone scaffold based on the hexahedral mesh refinement*, Computer-Aided Design, 40 (2008), pp. 1040–1050.

[13] L. Crum, *Measurements of the growth of air bubbles by rectified diffusion*, Journal of the Acoustical Society of America, 68 (1980), pp. 203–211.

[14] ——, *Rectified diffusion*, Ultrasonics, 22 (1984), pp. 215–223.

[15] E. Cussler, *Diffusion: Mass Transfer in Fluid Systems*, 3rd Ed. Cambridge; New York: Cambridge University Press, 2009.

[16] P. De Gennes, *Scaling Concepts in Polymer Physics*, Cornell University Press, Ithaca, 1979.

[17] O. Diekmann and M. Kretzschmar, *Patterns in the effects of infectious diseases on population growth*, Journal of Mathematical Biology, 29 (1991), pp. 539–570.

[18] A. Dobson and P. Hudson, *Regulation and stability of a free-living host-parasite system: Trichostrongylus tenuis in red grouse. II. Population models*, Journal of Animal Ecology, 61 (1992), pp. 487–498.

[19] E. Doedel, R. Paffenroth, A. Champneys, T. Fairgrieve, Y. Kuznetsov, B. Sandstede, and X. Wang, *Auto 2000: Continuation and bifurcation software for ordinary differential equations.* http://www.dam.brown.edu/people/sandsted/publications/auto2000.pdf. Accessed November 2009.

[20] M. Doi and S. Edwards, *Theory of polymer dynamics*, Oxford Science Publications/Clarendon Press, Oxford, 1986.

[21] R. Edwards, *Grouse moor owners driving mountain hares to the brink.* http://www.heraldscotland.com/news/environment/grouse-moor-owners-driving-mountain-hares-to-the-brink.22648639. Accessed December 2013.

[22] A. Eller, *Effects of diffusion on gaseous cavitation in bubbles*, Journal of the Acoustical Society of America, 57 (1975), pp. 1374–1378.

[23] A. Eller and H. Flynn, *Rectified diffusion during nonlinear pulsations of cavitation bubbles*, Journal of the Acoustical Society of America, 37 (1965), pp. 493–503.

[24] S. Everitt, O. Harlen, and H. Wilson, *Bubble growth in a two-dimensional viscoelastic foam*, Journal of Non-Newtonian Fluid Mechanics, 137 (2006), pp. 46–59.

[25] ——, *Competition and interaction of polydisperse bubbles in polymer foams*, Journal of Non-Newtonian Fluid Mechanics, 137 (2006), pp. 60–71.

[26] S. Everitt, O. Harlen, H. Wilson, and D. Read, *Bubble dynamics in viscoelastic fluids with application to reacting and non-reacting polymer*

foams, Journal of Non-Newtonian Fluid Mechanics, 114 (2003), pp. 83–107.

[27] M. Favelukis, *Dynamics of foam growth: Bubble growth in a limited amount of liquid*, Polymer Engineering and Science, 44 (2004), pp. 1900–1906.

[28] J. Feng and C. Bertelo, *Prediction of bubble growth and size distribution in polymer foaming based on a heterogeneous nucleation model*, Journal of Rheology, 48 (2004), pp. 439–462.

[29] J. Fisher, A. Mikos, and J. Bronzino, *Tissue Engineering*, CRC Press, 2007.

[30] J. Flux, *Life history of the Mountain hare in north-east Scotland*, Journal of Zoology, 161 (1970), pp. 75–123.

[31] H. Fogler and J. Goddard, *Oscillations of a gas bubble in viscoelastic liquids subject to acoustic and impulsive pressure variations*, Journal of Applied Physics, 42 (1971), pp. 259–263.

[32] Game and Wildlife Conservation Trust, *Mountain hare cycles.* http://www.gwct.org.uk/research_surveys/species_research/mammals/mountain-hare/1155.asp. Accessed April 2010.

[33] Hare Preservation Trust, *The mountain hare.* From Electronic Materials. http://www.hare-preservation-trust.co.uk/mountain.html. Accessed December 2009.

[34] S. Harris, P. Morris, S. Wray, and D. Yalden, *A review of british mammals: population estimates and conservation status of british mammals other than cetaceans.*, tech. report, Joint Nature Conservation Committee, Peterborough., 1995.

[35] A. Harrison, S. Newey, L. Gilbert, D. Haydon, and S. Thirgood, *Culling wildlife hosts to control disease: mountain hares, red grouse and louping ill virus*, Journal of Applied Ecology, 47 (2010), pp. 926–930.

[36] R. Hewson, *A population study of mountain hares (lepus timidus) in north-east scotland from 1956-1969*, Journal of Animal Ecology, 45 (1976), pp. 395–414.

[37] B. Hornfeldt, *Synchronous population fluctuations in voles, small game, owls, and tularemia in northern sweden*, Oecologia (Berl.), 32 (1978), pp. 141–152.

[38] P. Hudson, A. Dobson, and D. Newborn, *Prevention of population cycles by parasite removal*, Science, 282 (1998), pp. 2256–2258.

[39] P. Hudson, D. Newborn, and A. Dobson, *Regulation and stability of a free-living host-parasite system: Trichostrongylus tenuis in red grouse. I. Monitoring and parasite reduction experiments*, Journal of Animal Ecology, 61 (1992), pp. 477–486.

[40] S. Ishaug, G. Crane, M. Miller, A. Yasko, M. Yaszemski, and A. Mikos, *Bone formation by three-dimensional stromal osteoblast culture in biodegradable polymer scaffolds*, Journal of Biomedical Materials Research, 36 (1997), pp. 17–28.

[41] D. Kay, *Schaum's Outline of Tensor Calculus*, McGraw Hill Professional, 1998.

[42] L. Keith, *Herbivore-plant interactions at northern latitudes*, Oikos, 40 (1983), pp. 385–395.

[43] V. Kinrade, J. Ewald, A. Smith, S. Newey, G. Iason, S. Thirgood, and R. Raynor, *The distribution of mountain hare (*Lepus

timidus*) in scotland (2006/07)*, tech. report, Scottish National Heritage, 2008. Commissioned Report No. 278 (ROAME No. R07AC308).

[44] Y. Kojima, S. Koda, and H. Nomura, *Effect of ultrasonic frequency on polymerization of styrene under sonication*, Ultrasonics Sonochemistry, 8 (2001), pp. 75–79.

[45] N. Kopell and L. Howard, *Plane wave solutions to reaction-diffusion equations*, Studies in Applied Mathematics, 52 (1973), pp. 291–328.

[46] C. Krebs, R. Boonstra, S. Boutin, and A. Sinclair, *What drives the 10-year cycle of snowshoe hares?*

[47] X. Lambin, D. Elston, S. Petty, and J. MacKinnon, *Spatial asynchrony and periodic travelling waves in cyclic populations of field voles*, Proceedings of the Royal Society London B, 265 (1998), pp. 1491–1496.

[48] X. Lambin, S. Petty, and J. MacKinnon, *Cyclic dynamics in field vole populations and generalist predation*, Journal of Animal Ecology, 69 (2000), pp. 106–118.

[49] T. Leighton, *Bubble population phenomena in acoustic cavitation*, Ultrasonics Sonochemistry, 2 (1995), pp. S123–S136.

[50] T. Leong, S. Wu, S. Kentish, and M. Ashokkumar, *Growth of bubbles by rectified diffusion in aqueous surfactant solutions*, Journal of Physical Chemistry C, 114 (2010), pp. 20141–20145.

[51] P. Lewin and L. Bjorno, *Acoustic pressure amplitude thresholds for rectified diffusion in gaseous microbubbles in biological tissue*, Journal of the Acoustical Society of America, 69 (1981), pp. 846–852.

[52] J. Logan, *Applied Partial Differential Equations*, Springer-Verlag New York, 2004.

[53] O. Louisnard and F. Gomez, *Growth by rectified diffusion of strongly acoustically forced gas bubbles in nearly saturated liquids*, Physical Review E, 67 (2003), p. 12pp.

[54] A. Markworth, *Comments on foam stability, ostwald ripening, and grain growth*, Journal of Colloid and Interface Science, 107 (1985), pp. 569–571.

[55] I. Martin, V. Shastri, R. Padera, J. Yang, A. Mackay, R. Langer, G. Vunjak-Novakovic, and L. Freed, *Selective differentiation of mammalian bone marrow stromal cells cultured on three-dimensional polymer foams*, Journal of Biomedical Materials Research, 55 (2001), pp. 229–235.

[56] R. May and R. Anderson, *Regulation and stability of host-parasite interactions: II. Destabilizing processes*, Journal of Animal Ecology, 47 (1978), pp. 249–267.

[57] J. McGradySteed, P. Harris, and P. Morin, *Biodiversity regulates ecosystem predictability*, Nature, 390 (1997), pp. 162–165.

[58] E. Mora, L. Artavia, and C. Macosko, *Modulus development during reactive urethane foaming*, Journal of Rheology, 35 (1991), pp. 921–940.

[59] R. Moss, D. Elston, and A. Watson, *Spatial asynchrony and demographic traveling waves during red grouse population cycles*, Ecology, 81 (2000), pp. 981–989.

[60] J. Murray, *Mathematical Biology*, Springer-Verlag, 1989.

[61] A. Naji Meidani and M. Hasan, *Mathematical and physical modelling of bubble growth due to ultrasound*, Applied Mathematical Modelling, 28 (2004), pp. 333–351.

[62] S. Newey, F. Dahl, T. Willebrand, and S. Thirgood, *Unstable dynamics and population limitation in mountain hares*, Biol. Rev., 82 (2007), pp. 527–549.

[63] S. Newey, D. Shaw, A. Kirby, P. Montieth, P. Hudson, and S. Thirgood, *Prevalence, intensity and aggregation of intestinal parasites in mountain hares and their potential impact on population dynamics*, International Journal for Parasitology, 35 (2005), pp. 367–373.

[64] S. Newey and S. Thirgood, *Parasite-mediated reduction in fecundity of mountain hares*, in Proceedings of the Royal Society London B, vol. 271, 2004, pp. S413–S415.

[65] S. Newey, T. Willebrand, D. Haydon, F. Dahl, N. Aebischer, A. Smith, and S. Thirgood, *Do mountain hare populations cycle?*, Oikos, 116 (2007), pp. 1547–1557.

[66] D. Niyogi, R. Kumar, and K. Gandhi, *Modeling of bubble-size distribution in free rise polyurethane foams*, AIChE Journal, 38 (1992), pp. 1170–1184.

[67] A. Polyanin and V. Zaitsev, *Handbook of Exact Solutions for Ordinary Differential Equations*, Chapman & Hall, 2003.

[68] G. Potts, S. Tapper, and P. Hudson, *Population fluctuations in red grouse: analysis of bag records and a simulation model*, Journal of Animal Ecology, 53 (1984), pp. 21–36.

[69] G. Price, E. Lenz, and C. Ansell, *The effect of high intensity ultrasound on the synthesis of some polyurethanes*, European Polymer Journal, 38 (2002), pp. 1531–1536.

[70] A. Prosperetti, *Bubble phenomena in sound fields: part one*, Ultrasonics, 22 (1984), pp. 69–77.

[71] ——, *Bubble phenomena in sound fields: part two*, Ultrasonics, 22 (1984), pp. 115–124.

[72] H. Randrianantoandro, T. Nicolai, D. Durand, and F. Prochazka, *Slow dynamics in gels*, Journal of Non-Newtonian Fluid Mechanics, 67 (1996), pp. 311–323.

[73] Raptor Persecution Scotland, *Snh still licensing mountain hare culls.* https://raptorpersecutionscotland.wordpress.com/2013/12/11/SNH-still-licensing-mountain-hare-culls/.

[74] M. Rubenstein, R. Colby, and J. Gillmor, *Springer Series in Chemical Physics: Space-Time Organization in Macromolecular Fluids*, vol. 51, Springer-Verlag Berlin, 1989, ch. Dynamic Scaling for Polymer Gelation, pp. 66–74.

[75] J. Schmelzer and F. Schwietzer, *Ostwald ripening of bubbles in liquid-gas solutions*, Journal of Non-Equilibrium Thermodynamics, 12 (1987), pp. 255–270.

[76] M. Shafi and R. Flumerfelt, *Initial bubble growth in polymer foam processes*, Chemical Engineering Science, 52 (1997), pp. 627–633.

[77] M. Shafi, K. Joshi, and R. Flumerfelt, *Bubble size distributions in freely expanded polymer foams*, Chemical Engineering Science, 52 (1997), pp. 635–644.

[78] J. Sherratt, *On the evolution of periodic plane waves in reaction-diffusion systems of* $\lambda - \omega$ *type*, Society for Industrial and Applied Mathematics, 54 (1994), pp. 1374–1385.

[79] ——, *On the speed of amplitude transition waves in reaction-diffusion systems of $\lambda - \omega$ type*, IMA Journal of Applied Mathematics, 52 (1994), pp. 79–92.

[80] ——, *Periodic travelling waves in cyclic predator-prey systems*, Ecology Letters, 4 (2001), pp. 30–37.

[81] ——, *Periodic travelling wave selection by dirichlet boundary conditions in oscillatory reaction-diffusion systems*, SIAM Journal of Applied Mathematics, 63 (2003), pp. 1520–1538.

[82] ——, *A comparison of periodic travelling wave generation by robin and dirichlet boundary conditions in oscillatory reaction-diffusion equations*, IMA Journal of Applied Mathematics, 73 (2008), pp. 759–781.

[83] J. Sherratt and M. Smith, *Periodic travelling waves in cyclic populations: field studies and reaction-diffusion models*, Journal of the Royal Society Interface, 5 (2008), pp. 483–505.

[84] G. Smith, *Numerical solution of partial differential equations: Finite difference methods*, 3rd Ed. Oxford: New York: Clarendon Press; Oxford University Press, 1985.

[85] M. Smith and J. Sherratt, *The effects of unequal diffusion coefficients on periodic travelling waves in oscillatory reaction-diffusion systems*, Physica D, 236 (2007), pp. 90–103.

[86] M. Smith, J. Sherratt, and X. Lambin, *The effects of density-dependent dispersal on the spatiotemporal dynamics of cyclic populations*, Journal of Theoretical Biology, 254 (2008), pp. 264–274.

[87] D. Stauffer and A. Ahaony, *Introduction to Percolation Theory (Revised second edition)*, Taylor and Francis, London, 1994.

[88] C. Stewart, *Nucleation and growth of bubbles in elastomers*, Journal of Polymer Science, 8 (1970), pp. 937–955.

[89] J. Street, A. Fricke, and L. Reiss, *Dynamics of phase growth in viscous non-newtonian liquids*, Ind. Eng. Chem. Fundam., 10 (1971), pp. 54–64.

[90] H. Tai, M. Mather, D. Howard, W. Wang, L. White, J. Crowe, S. Morgan, A. Chandra, D. Williams, S. Howdle, and K. Shakesheff, *Control of pore size and structure of tissue engineering scaffolds produced by supercritical fluid processing*, European Cells and Materials, 14 (2007), pp. 64–77.

[91] Y. Ting, *Viscoelastic effect of polymers on single bubble dynamics*, AIChE Journal, 21 (1975), pp. 810–813.

[92] C. Torres-Sanchez and J. Corney, *Identification of formation stages in a polymeric foam customised by sonication via electrical resistivity measurements*, Journal of Polymer Res, 16 (2009), pp. 461–470.

[93] ——, *Porosity tailoring mechanisms in sonicated polymeric foams*, Smart Materials and Structures, 18 (2009), p. 104001 (13pp).

[94] ——, *Towards functionally graded cellular microstructures*, Journal of Mechanical Design, 131 (2009), pp. 091011–091018.

[95] S. Townsend, *The stability of model ecosystems*, PhD thesis, University of Glasgow, 2009.

[96] S. Townsend, S. Newey, S. Thirgood, and D. Haydon, *Dissecting the drivers of population cycles: Interactions between parasites and mountain hare demography*, Ecological Modelling, 222 (2011), pp. 45–56.

[97] S. Townsend, S. Newey, S. Thirgood, L. Matthews, and D. Haydon, *Can parasites drive population cycles in mountain hares?*, in Proceedings of the Royal Society B, vol. 276, 2009, pp. 1611–1617.

[98] P. Turchin, *Complex population dynamics: A theoretical empirical synthesis*, vol. Monographs in population biology, Princeton University Press, 2003, ch. Red Grouse, pp. 272–295.

[99] D. Venerus, *Diffusion-induced bubble growth in viscous liquids of finite and infinite extent*, Polymer Engineering and Science, 41 (2001), pp. 1390–1398.

[100] D. Venerus, N. Yala, and B. Bernstein, *Analysis of diffusion-induced bubble growth in viscoelastic liquids*, Journal of Non-Newtonian Fluid Mechanics, 75 (1998), pp. 55–75.

[101] S. Webb and J. Sherratt, *Oscillatory reaction-diffusion equations with temporally varying parameters*, Mathematical and Computer Modelling, 39 (2004), pp. 45–60.

[102] J. Williams, *Statistical analysis of fluctuations in red grouse bag data*, Oecologia, 65 (1985), pp. 269–272.

[103] Wilson, H.J., *Graduate lectures: Polymeric fluids.* http://www.ucl.ac.uk/ ucahhwi/GM05. Accessed March 2011.

[104] H. Winter and M. Mours, *Rheology of polymers near liquid-solid transitions*, Advances in Polymer Science, 134 (1997), pp. 165–234.

[105] T. Woodfield and J. Malda, *Design of porous scaffolds for cartilage tissue engineering using a three-dimensional fiber-deposition technique*, Biomaterials, 25 (2004), pp. 4149–4161.

[106] P. Yue, J. Feng, C. Bertelo, and H. Hu, *An arbitrary lagrangian-eulerian method for simulating bubble growth in polymer foaming*, Journal of Computational Physics, 226 (2007), pp. 2229–2249.

[107] W. Zhai, J. Yu, and J. He, *Ultrasonic irradiation enhanced cell nucleation: An effective approach to microcellular foams of both high cell density and expansion ratio*, Polymer, 49 (2008), pp. 2430–2434.